UNIVERSITY OF LJUBLJANA
FACULTY OF MATHEMATICS AND PHYSICS

Andrej Gorišek

Cross section measurement of D^0 and D^{*+} meson production in inelastic collisions of $920\ \mathrm{GeV}$ protons with nuclei

DOCTORAL THESIS

SUPERVISOR: PROF. DR. PETER KRIŽAN
CO-SUPERVISOR: AS. PROF. DR. SAMO KORPAR

Ljubljana, December 2002

UNIVERZA V LJUBLJANI
FAKULTETA ZA MATEMATIKO IN FIZIKO

Andrej Gorišek

Meritev preseka za tvorbo mezonov D^0 in D^{*+} v neelastičnih trkih protonov energije $920\ \mathrm{GeV}$ z jedri

DISERTACIJA

MENTOR: PROF. DR. PETER KRIŽAN
SOMENTOR: DOC. DR. SAMO KORPAR

Ljubljana, december 2002

Marjetki

Za podporo bi se na prvem mestu rad zahvalil svojemu mentorju Petru Križanu, zlasti za mnogokratno branje, včasih še nedokončanega besedila. Maretu Stariču gre zahvala, ker je najbolj med nami vsemi verjel v poskus HERA-B, pomagal pa mi je še s številnimi nasveti in kritikami. S Samom Korparjem sva uspešno sodelovala pri umeritvah merske naparve HERA-B. Alešu Stanovniku sem hvaležen za njegove nasvete pri pisanju disetracije. Brez Tomija Živka in Roka Pestotnika, ki poleg omenjenih sestavljata ljubljansko skupino pri HERA-B, ne bi bilo pravega vzdušja. V dolgem času, ki sem ga preživel v Hamburgu, sem dobil veliko znancev, med katerimi bi še posebej omenil Patricijo, Vascota in Danija, s katerimi je 'poslovno' znanstvo preraslo v pravo prijateljstvo. Marjetki sem hvaležen, ker je potrpežljivo prenašala moje nezanimanje za medčloveške odnose v zadnjem obdobju.

Abstract

The subject of the present thesis is the alignment and calibration of the HERA-B spectrometer and the analysis of acquired data. Three different methods used for the overall alignment of the spectrometer are explained, two of which use the curved individual tracks and the third one which employs the tracks from two body decays, where an additional information about the momentum is available. The convergence of the methods was tested on the MC data set, and the improvement was shown on the acquired data. The performance of the Ring Imaging Cherenkov counter (RICH) was then investigated and it was shown that the performance improves with better alignment. At the end a measurement of the production cross section for D^0 and D^{*+} mesons is presented, measured at two different target materials. The value of D^0 meson production cross section is also used to determine the $c\bar{c}$ quark pair production cross section and the nuclear effects in the D^0 production.

Povzetek

V doktorski disertaciji obravnavam krajevno umeritev merilne naprave HERA-B in analizo zajetih podatkov. Najprej so predstavljeni trije različni postopki, ki so bili uporabljeni za krajevno umeritev merilne naprave. Prva dva postopka uporabljata posamezne ukrivljene sledi delcev, medtem ko so pri tretjem postopku uporabljene sledi, ki nastanejo pri razpadih delcev, kjer je na voljo dodatna informacija o gibalni količini posameznega delca. Postopke sem preiskusil na simuliranih podatkih in jih nato uporabil za izboljšavo krajevne umeritve merilne naprave. Preiskusil sem delovanje detektorja obročev Čerenkova, kjer sem pokazal, da se identifikacija delcev izboljša z izboljšano krajevno umeritvijo. Na koncu sem izmeril presek za tvorbo mezonov D^0 in D^{*+} pri dveh tarčah narejenih iz različnih materialov. Vrednost preseka za tvorbo mezonov D^0 je bila uporabljena še za določitev preseka za tvorbo parov kvarkov $c\bar{c}$ ter za določitev jedrskih vplivov na tvorbo mezonov D^0.

Physics and Astronomy Classification Scheme:

- 13.85.Ni Inclusive production with identified hadrons
- 14.40.Lb Charmed mesons
- 25.40.Ep Inelastic proton scattering
- 29.40.-n Radiation detectors
- 29.40.Ka Cherenkov detectors
- 29.85.+c Computer data analysis

Contents

1 Introduction

The study of rare processes in the decays of hadrons with b and c quarks has proven to be one of the most important tools in elementary particle physics. In order to carry out such measurements one needs, however, large samples of recorded decays of B and D mesons. One way to arrive at such samples is to collide high energy protons with a fixed target, and such scheme was employed by the HERA-B spectrometer at the proton ring of the HERA collider at the DESY institute in Hamburg.

This thesis is a part of the advanced commissioning stage of the HERA-B spectrometer. After finding the working conditions for operation of the individual components of the spectrometer in the hostile environment of the HERA-B experiment, the calibration and alignment have to be carried out, and test measurements are performed. In my thesis, three issues of this sort are discussed, overall alignment of the whole spectrometer, the calibration of one of the crucial components, the Ring Imaging Cherenkov Counter (RICH), and finally, a measurement of the D^0 and D^{*+} production cross section.

1.1 The structure of the thesis

The thesis is organized as follows. I will first give a brief overview of the HERA-B experiment. All the major components will be discussed, including the data acquisition system with the trigger systems. An overview of analysis software and the Monte Carlo simulation software will be presented.

In the next section I will discuss the alignment of the HERA-B spectrometer. The analysis is based on the data sample, taken with the spectrometer with the magnet field turned on, thus the paths of the particles are curved, which additionally complicates the procedure of alignment. The work is divided into two parts. First, the alignment based on geometrical considerations of individual tracks is presented. Since it turns out that not all parameters of the detector positions can be fixed based on the geometry alone, also two body decays (such as J/Ψ meson decay into muon pair) were considered. The improvement is shown on the sample of the J/Ψ meson muonic decays. In the year 2002 a data sample taken without magnetic field became available. There the alignment procedure is much easier, which will be mentioned at the end of the section.

In the next section the final calibration of the Ring Imaging Cherenkov Counter (RICH) will be discussed. Special emphasis will be on showing the improvement of RICH performance with improved alignment which was used for later reprocessing of the 2000 data.

Section 5 describes the measurement of the production cross section of neutral D^0 and charged D^{*+} mesons. The measurement is based on the recently collected data, with much

larger statistics compared to the year 2000 data sample. The new data are also taken in the mode of 'interaction' trigger, where the systematic errors due to trigger efficiency and enhancement estimation are small. The resulting value of the measured cross section for the $c\bar{c}$ quark pair production is also given and compared to the theoretical predictions and other existing measurements. Since also data taken with multiple targets inserted simultaneously were analyzed, a new wire following procedure, for reconstructing the target positions, was developed. This very important technical detail is described in App. E.

At the end of the thesis a short summary and further outlook is given.

2 The HERA-B experiment

2.1 The HERA accelerator

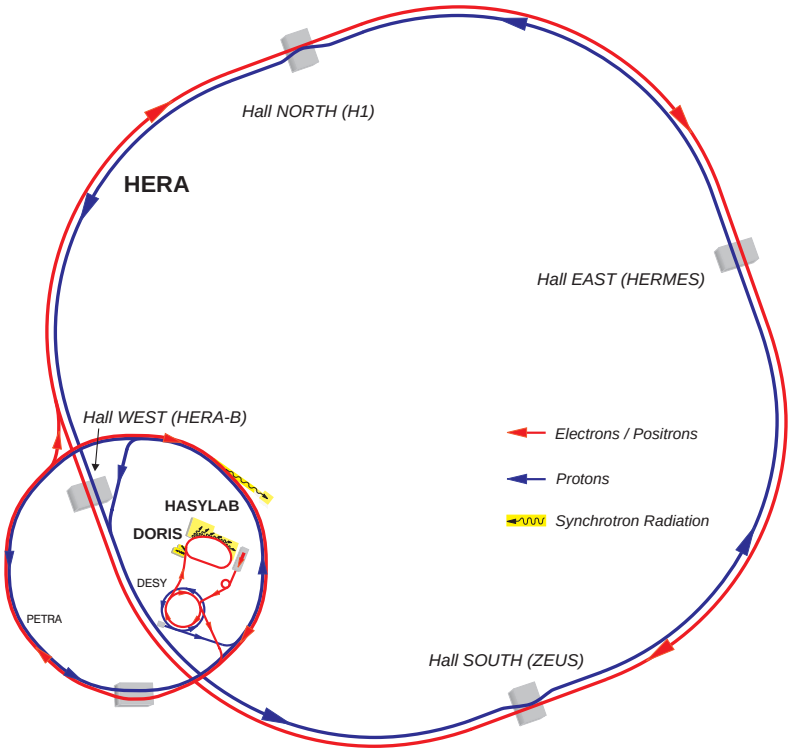

Figure 2.1: Layout of the HERA rings with the location of the four experimental areas.

The HERA (Hadron Elektron Ring Anlage) accelerator is a double storage ring built at DESY institute in Hamburg, Germany. It is designed for colliding $920\ \mathrm{GeV}$ protons against $30\ \mathrm{GeV}$ electrons. Both rings are $6335.8\ \mathrm{m}$ long. Their multi-step injection chain and their four interaction regions are shown in Fig. 2.1. The particles in each beam are grouped in 220 bunches, separated by $96\ \mathrm{ns}$. As a result the bunches pass the experiments at a rate slightly above $10\ \mathrm{MHz}$.

Amongst the four interaction points two of them are used by collider type experiments H1 and ZEUS, that are studying the collisions of protons with electrons, and are placed in the North and the South Hall. The other two experiments, HERMES and HERA-B, are using only single

beams and stationary targets. The HERMES experiment, installed in the East hall, studies the collisions of electrons with a gas target. Finally, the HERA-B experiment which is situated in the West hall, uses the proton beam collisions with fixed solid targets made of different materials.

2.2 The HERA-B experiment

The HERA-B experiment was originally designed to search for CP violation in decays of neutral B mesons [1, 2]. The decay $\mathrm{B}^0 \to \mathrm{J}/\psi\,\mathrm{K_s} \to \ell^+\,\ell^-\,\pi^+\,\pi^-$, with leptons in the final state, is accepted as the best candidate, both theoretically and experimentally, for the study of CP asymmetries [3]. The HERA-B spectrometer is optimized to detect such, so called "gold plated" decays schematically shown on Fig 2.2. In HERA-B the neutral B meson decaying into the signal channel $\mathrm{J}/\psi\,\mathrm{K_S^0}$ has an average momentum of 120 GeV/c and decays after an average flight distance of about 9 mm. J/ψ promptly decays into two leptons, either e^+e^-or $\mu^+\mu^-$, while $\mathrm{K_S^0}$ decays after a typical flight distance of about 1.1 m. The most powerful tagging methods for the beauty content of the decaying neutral B meson make use of the second beauty particle, i.e. charged or neutral meson or baryon. The cleanest tag, although occurring with rather small probability, is provided by the charge of a lepton with high transverse momentum from the semileptonic decays of the associated B meson. Less clean but more frequent is the tag provided by the charge of a kaon, produced in the subsequent charm decay.

Furthermore, the HERA-B detector allows to perform a number of other valuable physics measurements in particular in the fields of quantum chromodynamics and charm physics [4]. Among the most competitive are the measurements of $\sigma_{b\bar{b}}$ [5] and $\sigma_{c\bar{c}}$ cross section and measurement of J/ψ, ψ' and χ_c production.

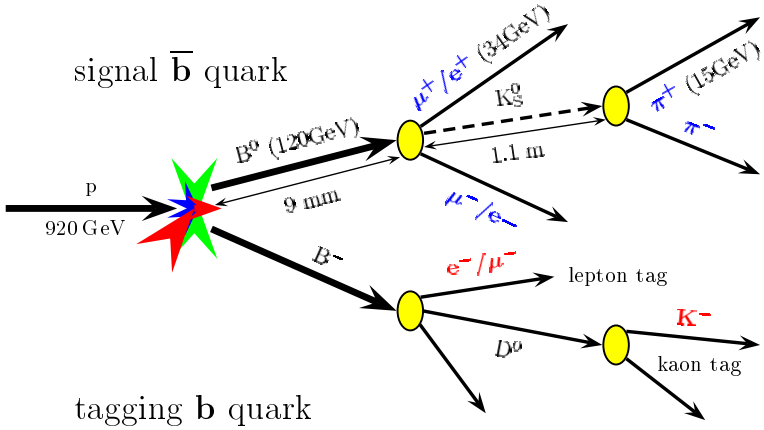

Figure 2.2: The "gold platted" $\mathrm{B}^0 \to \mathrm{J}/\psi\,\mathrm{K_s}$ decay with some kinematical quantities at the HERA-B experiment.

At the HERA-B proton beam energy the production cross section of B mesons is approximately one million times smaller than the inelastic scattering cross section. Taking into account the branching fractions of the decays Br($\mathrm{B}^0 \to \mathrm{J}/\psi\ \mathrm{K}^0_\mathrm{S}$) $= 5 \times 10^{-4}$, $Br(J/\psi \to l^+l^-) = 0.06$, and $Br(K^0_s \to \pi^+\pi^-) = 0.69$, it appears that there is only one event of interest in every 25000 events containing B mesons. The key issue of the experiment is thus the effective trigger system able to select these rare events. The interaction frequency that is required to collect enough B mesons in a reasonable time of 3 years is 40 MHz. To achieve this extremely high interaction rate there has to be on average four superimposed interactions in a single crossing of proton bunches. For that purpose a target system with 8 targets that can be operated simultaneously was designed

The HERA-B spectrometer was designed to cope with very high interaction rates, where each bunch crossing generates tracks in the detector with extremely high particle densities (see Fig. 2.4). This requires fast track detectors which provide high precision in the decay reconstruction. To achieve the necessary precision, the detector elements with sufficiently high granularity and high rate capabilities are required to be as close as 1 cm from the proton beam, where they are hit by some $10^7\ \mathrm{particles/cm^2 s}$. Leptons from B decays have to be identified with high purity in order to suppress backgrounds from the inelastic proton nucleus interactions

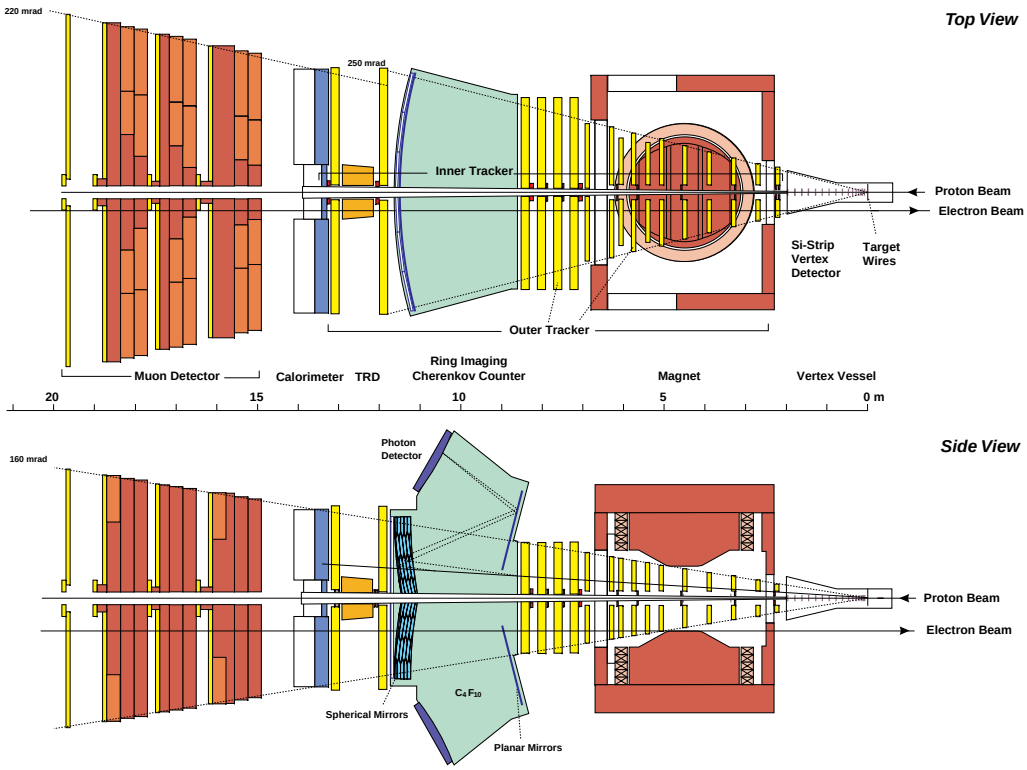

Figure 2.3: The HERA-B spectrometer with the silicon vertex detector, the main tracking system, the dipole magnet, the transition radiation detector, the ring imaging Cherenkov counter, the electromagnetic calorimeter and the muon system. In the 2002 setup the main tracking system in the region of the dipole magnet was removed.

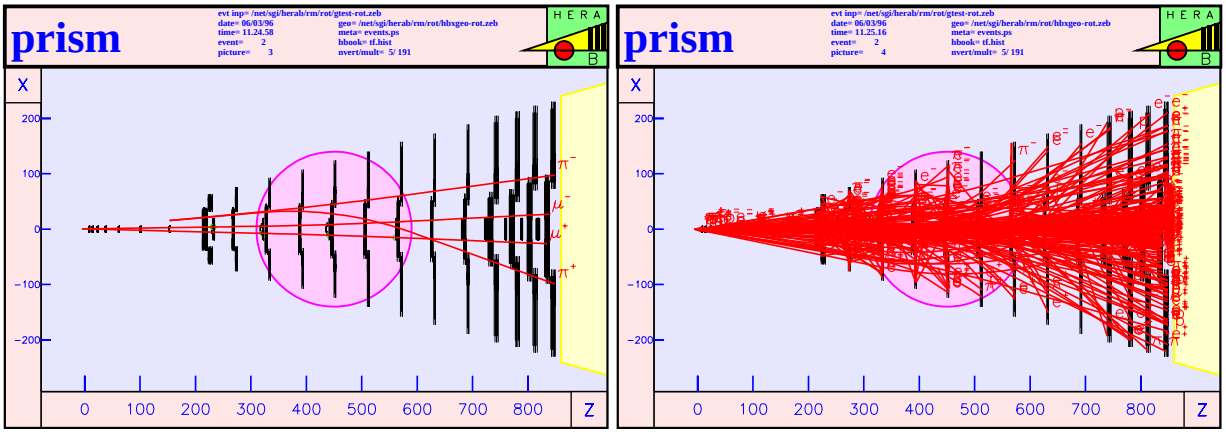

Figure 2.4: Simulated tracks due to one bunch crossing in the HERA-B spectrometer. The ”gold plated” events (left) lay in a huge background of other particles produced in the same event.

and charm decays. Also the identification of the tagging kaon with its momentum between a few GeV/c and 50 GeV/c should be performed. Due to restricted access to the detector, HERA-B had to be designed such that even the components very close to the beam have a minimum lifetime of about 10^7 seconds operating at full target rate. Furthermore the detector has to provide a good B meson decay vertex resolution and multiple event reconstruction per bunch crossing. To meet these requirements, the spectrometer consists of several detector subsystems which can logically divided into tracking and particle identification systems. The tracking system consists of the magnet, the vertex detector (VDS), and the inner and outer tracker detectors, while the transition radiation detector (TRD), the ring imaging Cherenkov detector (RICH), the electromagnetic calorimeter (ECAL) and the muon identification system (MUON) compose the particle identification system. The HERA-B spectrometer (Fig. 2.3) reflects the fixed target nature of the experiment, with finer detector granularity for small production angles, where higher particle densities are expected. Its outer dimensions are approximately $9\ \mathrm{m} \times 7\ \mathrm{m} \times 20\ \mathrm{m}$, and the angular acceptance of the detector is from 10 mrad to 160 mrad vertically and from 10 mrad to 220 mrad horizontally. This is equivalent to 90% of the solid angle in the proton nucleus center of mass frame.

In the following sections, each HERA-B detector subsystem design shall be briefly described and its main tasks presented.

2.3 The target

In the HERA-B detector, B and D mesons are produced in interactions of protons with nuclei in thin wire targets surrounding the HERA proton beam. In order not to disturb other experiments on the storage ring, HERA-B uses the protons from the beam halo, which would be lost, anyhow. The basic idea is to bring halo protons to interact in the target before they hit any aperture limitation in the beam tube. An efficient competition of the target with collimators, which define the aperture of the beam, is thus needed.

The target mechanics is mounted inside a conical extension of the beam pipe, which houses

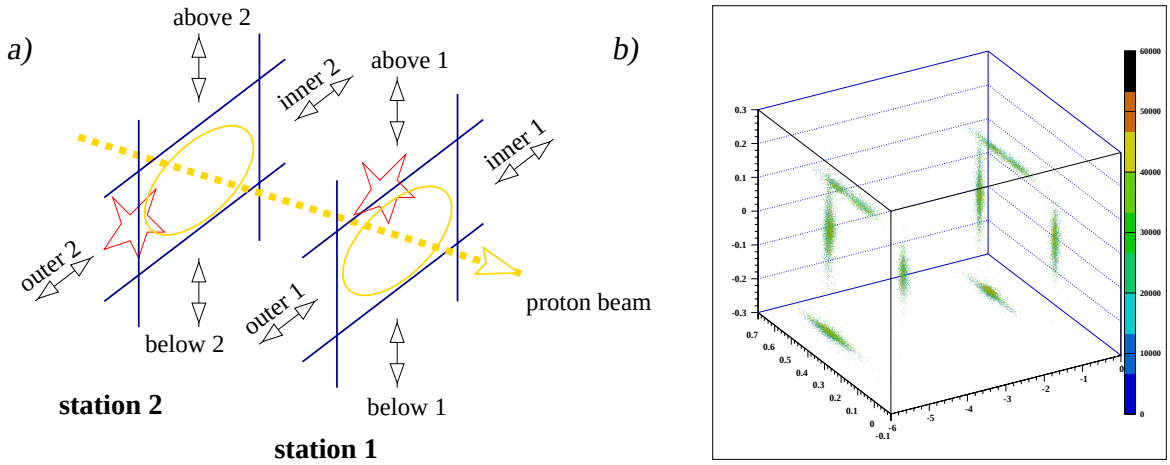

Figure 2.5: a) setup of the eight target wires surrounding the HERA proton beam with the names of the wires. b) Reconstructed vertices with all eight target wires operating simultaneously in the beam [7].

the retractable parts of the vertex detector. The target consists of a set of eight movable ribbons with $50\ \mu\mathrm{m}$ width perpendicular to the beam, $500\mu\mathrm{m}$ thickness along the beam and of 30 mm length (Fig. 2.5). Same of the ribbons have been replaced by a circular wires in the 2002 setup. The ribbons are positioned at a distance of $4\ \sigma$ to $6\ \sigma$ from the beam center with σ being the r.m.s. width of the beam. The ribbons are grouped in two stations separated by 4 cm along the beam direction. Within one station four ribbons approach the beam from four different sides (see Fig. 2.6). Each ribbon is mounted on a ceramic fork, which can be independently moved with a nominal step size of 50 nm. A constant target interaction rate with equal sharing among ribbons can be achieved by an automatic feedback system which continuously adjusts the wire positions via stepping motors [6].

As already mentioned, four proton interactions with the target are required per bunch crossing which should be compared with the natural loss rate of the proton beam. With a typical proton bunch current of 100 mA (i.e. 1.4×10^{13} protons in 220 bunches circulating with the frequency of 45 kHz) and a lifetime of 100 hours, the HERA proton beam looses 40×10^6 protons per second. This indicates that the target has to collect the protons before they get lost with high efficiency in order to arrive at an interaction rate of 40 MHz.

The described target system allows multiple interactions in a single bunch crossing, which are distributed among different ribbons, to allow separation. The target system has celebrated itself with a robust and reliable operation.

2.4 The dipole magnet

To determine the momentum of particles which are produced in the collisions of protons with the internal target, the spectrometer uses a dipole magnet characterized by the magnetic field integral of $e\int_{Z_{min}}^{Z_{max}} B \cdot dz = 0.635\mathrm{GeV/c}$. It consists of two iron poles, an iron flux return yoke and two cylindrical copper coils. The momentum is calculated from the curvature of the particle trajectories in the magnetic field. The magnet position presents a compromise between

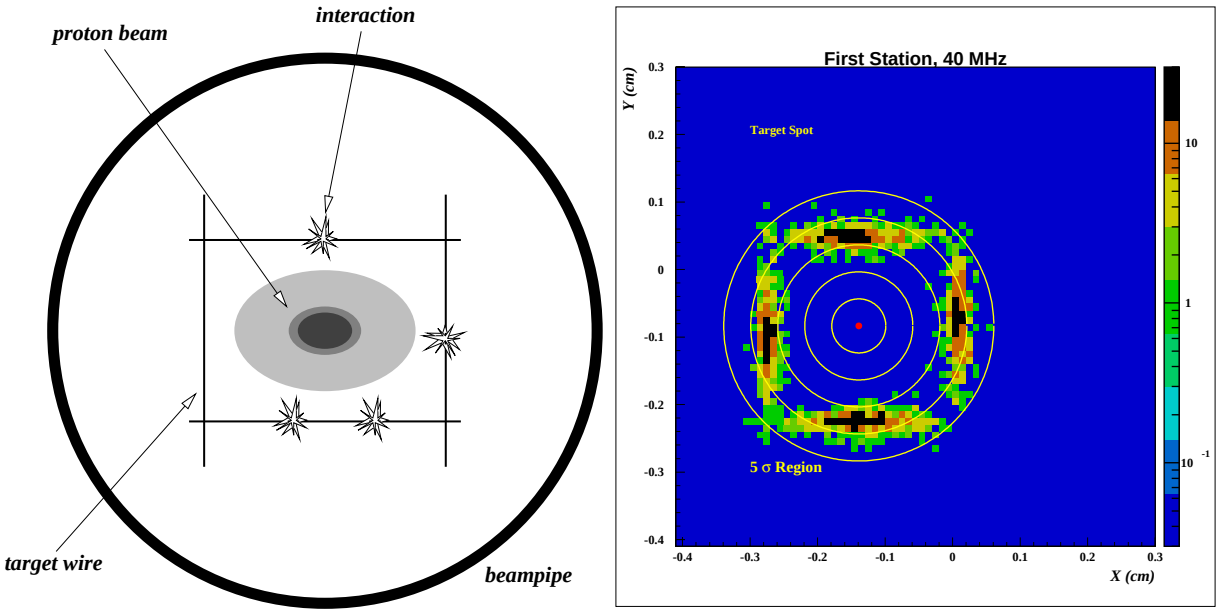

Figure 2.6: The basic idea of a halo target is shown. Protons leaving the beam core interact in the target. The right plot shows the vertices reconstructed with four target wires simultaneously inserted [7].

the acceptance for late decaying K_s and magnet aperture for fixed solid angle coverage. The location of the magnet center is fixed at 4.5 m downstream from the target, which determines the vertical magnet aperture to 160 mrad and the horizontal aperture to about 250 mrad.

2.5 The tracking system

The tracking of charged particles is performed by a vertex detector, followed by a main tracking system which is divided into an inner tracker (ITR) closer to the proton beam and an outer tracker (OTR) at distances larger than 20 cm from the proton beam.

2.5.1 The vertex detector system

The vertex detector system provides the track coordinates information for reconstruction of the decay vertices and the impact parameters of all tagging particles. From the reconstructed tracks, the primary interaction is reconstructed in the primary vertex. The secondary reactions in the chain produce secondary vertices. In Fig. 2.7 a longitudinal distribution of $J/\psi \to \mu^+\mu^-$ reconstructed vertices is shown. The information of the vertex detector is also used at the trigger level in order to reject events, where the two leptons do not form a common vertex which is displaced from the target wire.

The vertex detector system consists of eight layers with four modules in each of them (Fig. 2.8). The eight layer is contrary to the others situated outside the beam vacuum vessel just in front of the magnet. Each module carries two double sided silicon detectors and the front end electronics. The first three modules in a quadrant are integrated in one roman pot. Layers four to seven have each module mounted in a separate roman pots. All detectors are mounted

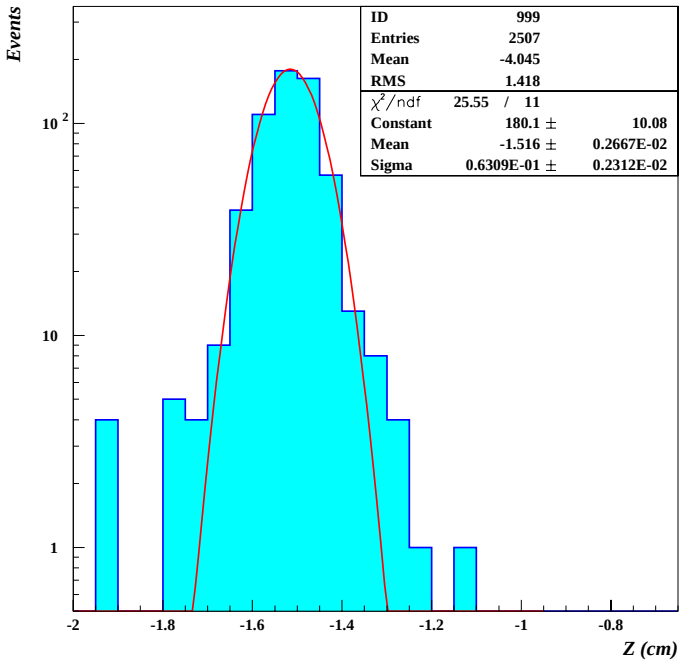

Figure 2.7: Longitudinal distribution of vertices of $J/\psi \to \mu^+\mu^-$ candidates from the "below-1" titanium wire as reconstructed in the vertex detector system [7].

perpendicular to the beam. The vertex detector system uses $300\ \mu\mathrm{m}$ thick double sided n type bulk silicon strip detectors. Each detector of an overall size of $53 \times 73\ \mathrm{mm}^2$ has an active area of $50 \times 70\ \mathrm{mm}^2$. On the two detector sides the strips are orthogonal. The two detectors in a module are mounted back to back (Fig. 2.9) with a relative stereo angle of 5^0. Electronics and detectors are mounted on separate plates to establish different cooling paths. The vertex detectors have to be replaced once per year due to the radiation damage.

The vertex detector system acceptance is from 10 mrad up to 250 mrad vertically and horizontally. The minimum distance between the active area of the silicon detectors and the beam is 1 cm. The overall detector system length is 2.5 m. The resolution of the vertex detector is limited by multiple scattering in the material between track vertex and the point of the first track measurement [8]. The roman pots are mounted inside a cone shaped vacuum vessel (Fig. 2.3). Each roman pot provides a secondary vacuum of $10^{-6}\ \mathrm{mbar}$, smaller than the primary HERA vacuum of $10^{-8}\ \mathrm{mbar}$. Individual modules have a $150\ \mu\mathrm{m}$ thin aluminum cap separating the primary from the secondary vacuum. The detectors can be retracted during the beam injection or adjustment.

2.5.2 The inner tracker

The main tracking system is divided into parts of different granularity, in order to keep occupancies below a level of 20%. In accordance with the increasing particle densities towards small

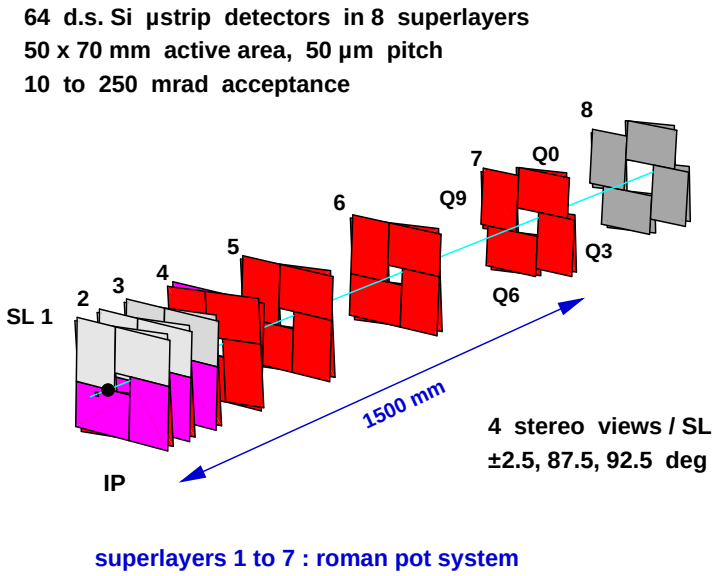

Figure 2.8: Isometric view of the arrangement of detector wafers in the VDS. The first seven superlayers are mounted inside the beam shroud, while the structurally same superlayer 8 is positioned outside the beam shroud and functionally belongs to the magnet tracker.

polar angles the system is divided into an inner and an outer section. Besides track information it also provides momentum measurements.

The inner tracker (ITR) is covering the inner part of the main tracking system from aproximatelly 10 mrad and up to a radial distance of $20 - 30$ cm from the proton beam. Half of all tracks in a typical event pass trough inner tracker, which has to cope with particle rates of up to $10^4 \mathrm{mm}^{-2}\mathrm{s}^{-1}$. The inner tracker detector consists of low gain micro strip gas chambers (MSGC) operated with $Ar - CO_2$ gas mixture and combined with a gas electron multiplier (GEM) [9].

The micro strip gas chamber cover consists of a G10 plate to ensure mechanical stability and a kapton foil covered with copper, which serves as the drift cathode (Fig. 2.10). Below the drift gap the gas electron multiplier foil is mounted. It consists of a 50 μm thick kapton foil, which is covered with 7 μm copper on each side. The holes in the kapton are staggered with a pitch of 140 μm and have a diameter of about 55 μm. The charge produced in the GEM foil is transfered by an electrical field through the transfer gap of 2.8 mm to the standard MSGC substrate. A gold layer is deposited onto a glass wafer and the electrode structure which consists of 10 μm wide anodes and 170 μm wide cathode strips, with a gap of 60 μm in between (see Fig. 2.10). The micro strip gas chambers pitch of 300μm provides maximum occupancies of about 5% and the spatial resolution better than 80μm. The momentum resolution is limited by multiple scattering, while photon conversions represent a significant background source. Single detector layer thickness is thus minimized and presents less than 0.35 % of a radiation length.

The inner tracker has 48 detector layers, each being composed of four independent L shaped detector planes (see Fig. 2.10). Three stereo strip orientations, vertical strips (0°) and strips with $(\pm 5^\circ)$ orientation, are used, which allow reconstruction also in y direction. Several layers with different strip orientation, mounted together in a common support structure form eleven super-

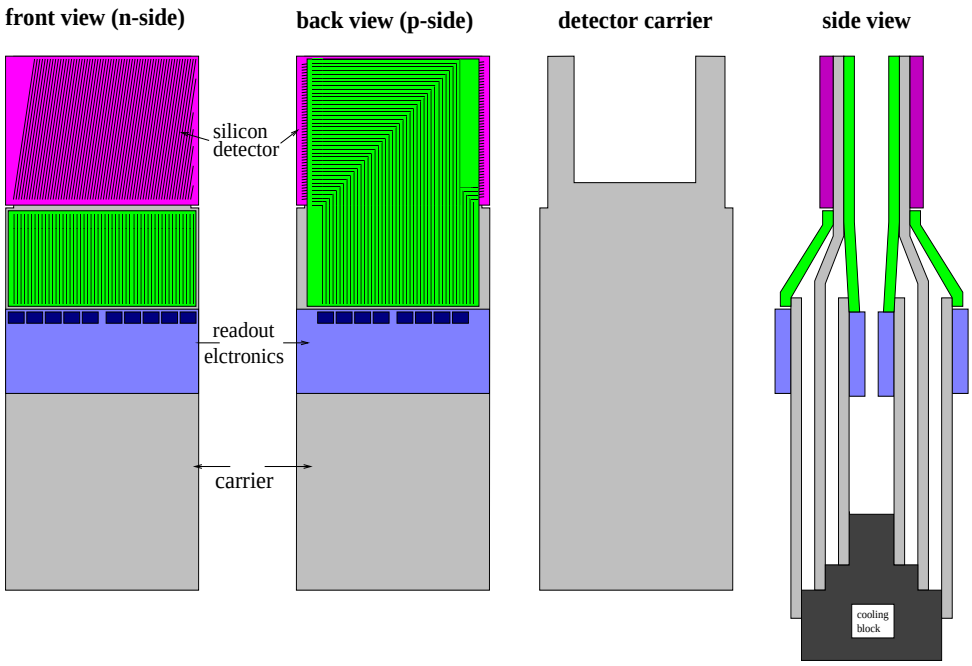

Figure 2.9: Schematic view of the vertex detector module.

layers. Two superlayers in front of the calorimeter are used for triggering. Four superlayers between the magnet and the RICH are used to start track finding and pattern recognition. They provide three dimensional hit information. Six layers of these superlayers are also used for triggering. The remaining superlayers near the vertex detector and in the magnet are used to extrapolate the tracks to the vertex detector (see Fig. 2.3).

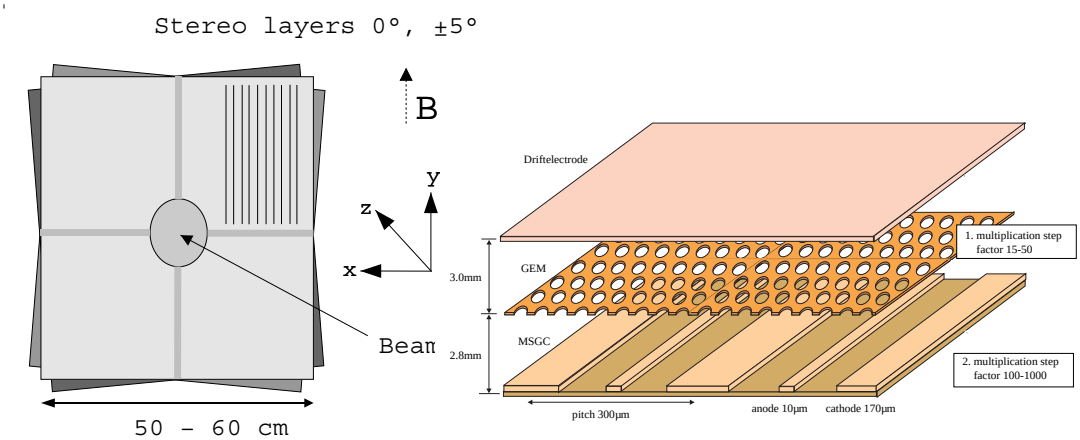

Figure 2.10: Geometry of the inner tracker detector in front of the RICH detector and a schematic view of a low gain micro strip gas chamber combined with a gas electron multiplier foil.

2.5.3 The outer tracker

The purpose of the outer tracker is to measure charged particle tracks in the outer part of geometrical acceptance of the experiment, down to a distance of $20\ \mathrm{cm}$ from the proton beam. The outer limit of the spectrometer acceptance is at 250 mrad in the horizontal plane and at 220 mrad in the vertical plane. This translates to lateral dimensions of about $6\ \mathrm{m}$ by $4.5\ \mathrm{m}$ for the sensitive area of the largest subdetectors.

A modular design has been adopted in the construction of the superlayers. Each detector plane consists of an array of independent honeycomb modules which are fixed to a common support. These modules have a standard width of 32 cm, whereas their length differs from superlayer to superlayer. The basic drift cell in an honeycomb drift chamber is a tube of hexagonal cross section with a signal wire strung along its center (Fig. 2.11, right). The tube is made of conductive foil which acts as the cathode. In order to minimize the number of readout channels while keeping the cell occupancy at an acceptable level, two different cell sizes are used. Modules with a cell size of 5 mm are placed in the regions closer to the proton beam pipe, while the outer regions are covered by modules with 10 mm cell size (see Fig. 2.11, left).

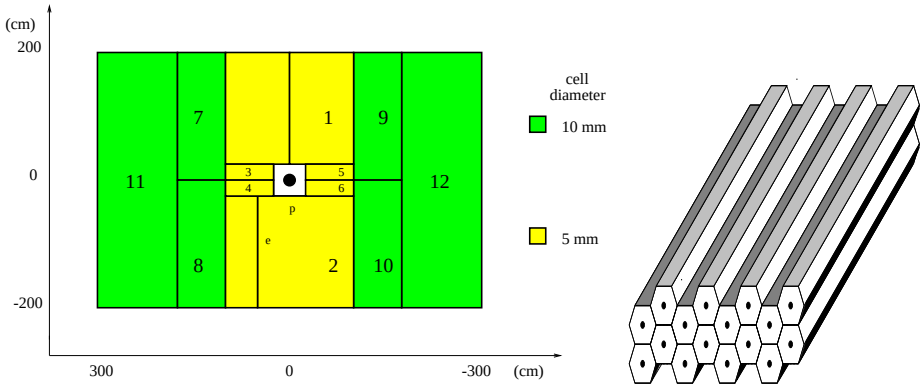

Figure 2.11: A lateral segmentation of a superlayer superlayer into twelve sections (left). Each section consists of modules of honeycomb drift chambers, shown in the right plot.

The basic superlayer design consists of detector planes with wire dirrections at 0 mrad, +80 mrad and -80 mrad with respect to the vertical direction. The coincidence of hits in the three layers assures spatial resolution of the order of $150\mu\mathrm{m}$ per superlayer in the horizontal direction and about $150\mu m/80\ \mathrm{mrad} = 1.9\ \mathrm{mm}$ in the vertical direction.

The outer tracker consists of fifteen planar drift tube superlayers oriented perpendicularly to the beam direction and at distances from about 2 m up to 13 m downstream from the target (see Fig. 2.3). In the region from the end of the target vessel to the end of the magnet nine chambers are positioned. They are used for finding and fitting the curved continuations of already found straight track sections. Four layers in the region from the end of the magnet up to the front side of the RICH vessel are used for pattern recognition of straight tracks and for trigger decisions. The remaining two superlayers in the region between the RICH and the electromagnetic calorimeter are used by the trigger and to extrapolate tracks to the calorimeter and the muon system.

2.5.4 The 2002 tracking system

When it become clear that it will not be possible to compete with the other two experiments dedicated to measure the CP violation in the system of B mesons, the HERA-B spectrometer layout was slightly altered. The major difference is that the tracking system (inner as well as outer) was removed from the magnet area.

2.6 The ring imaging Cherenkov counter

The design requirement for the HERA-B Ring Imaging Cherenkov counter is to identify hadrons, particularly kaons from B decays, in the momentum range up to about 50 GeV/c. This task has to be performed in high multiplicity of several hundred charged particles per beam crossing each 96 ns in the solid angle of ± 160 mrad vertically and ± 250 mrad horizontally.

Radiator The best hadron separation at high momenta is obtained with low refractive index gas radiators. The refractive index of the gas however, has to be sufficiently high to permit detection down to a few GeV/c. Normal temperature and pressure perfluorobutane gas (C_4F_{10}, n = 1.00137) was chosen, with $\theta_c = 52.4$ mrad at $\beta = 1$, with $\pi - K$ separation of 0.9 mrad at 50 GeV/c and with pion and kaon thresholds of 2.7 GeV/c and 9.6 GeV/c respectively. The relatively low dispersion of 5% variation in n-1 between 300 nm and 600 nm, contributes 0.33 mrad to the r.m.s. angular spread of a single photon. In order to obtain sufficient resolution in the high charged particle multiplicity environment, many photons per ring are needed, which in turn requires a gas radiator thickness of several meters.

Since some of the freons are known to scintillate considerably, as e.g. CF_4, scintillations in the C_4F_{10} gas were studied [10]. It was found that their contribution to background is less than 0.2 detected photons per charged particle.

The C_4F_{10} gas is contained in the radiator vessel, made from stainless steel plates, with 1 mm aluminum particle entrance and exit windows (see Fig. 2.12), is placed about 8.5 m downstream of the target (see Fig. 2.3). Two Kapton-reinforced plastic beam shrouds close the gas volume around the two beam pipes for protons and electrons. After reflection from spherical and planar mirrors, the Cherenkov light exits the vessel through 2 mm thick UV grade Plexiglass windows. The vessel is filled with 108 m^3 of C_4F_{10} gas, which is being circulated in a closed system with liquefaction stages for cleaning and buffering. Requirements on impurities are moderate due to operation in the visible and near UV part of the Cherenkov spectrum.

Mirrors The Cherenkov photons are focused onto the photon detector with spherical mirrors, which should have a large focal length f, permitting larger granularity Δx of the photon detector ($\sigma_\theta \propto \Delta x / f$). It is also desirable that the mirror center of curvature be near the target in order to reduce spherical aberration errors. This then leads to the conclusion, that a suitable position for the RICH is downstream of the bending magnet, about 10 m from the targets. The necessary solid angle coverage at this distance demands a large detector.

In order to reduce multiple Coulomb scattering and background, the photon detector should be placed outside of the main charged particle flux. This was achieved by tilting the upper and

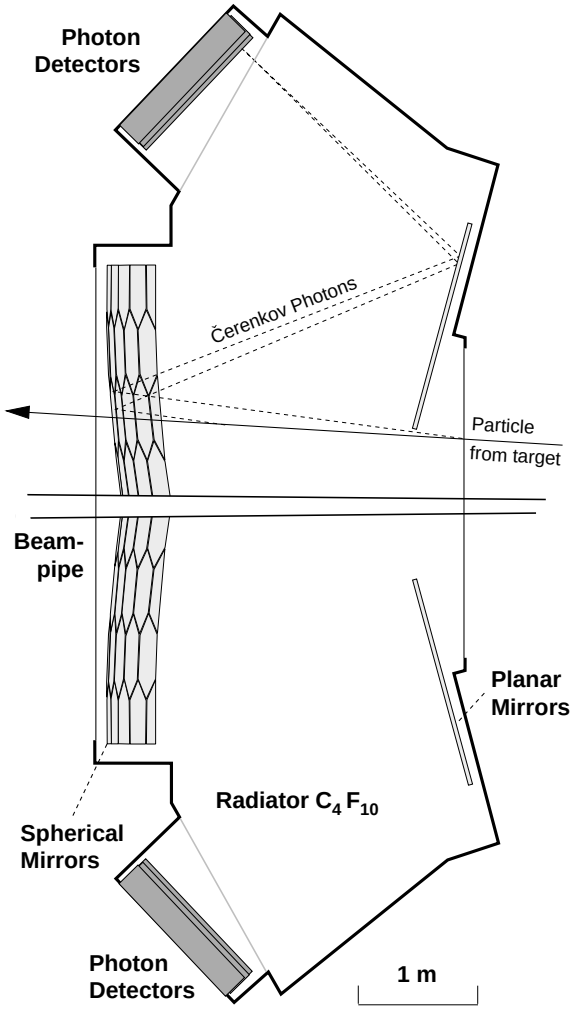

Figure 2.12: Scheme of the RICH. Rays emitted by a particle and their paths to the photon detector are indicated.

lower halves of the spherical mirror in opposite directions. Additional reflections on planar mirrors enable a more compact overall shape of the detector.

In the actual design this is realized by a spherical mirror, placed inside the radiator vessel, with the center of the sphere near the target and a radius of curvature of 11.4 m. The mirror, a 6 m by 4 m rectangular cutout from the sphere, consists of 80 full or partial, 7 mm thick, hexagons made from Pyrex glass, coated with 200 nm of aluminum and 30 nm of MgF_2 (see Fig. 2.13). To be able to place the focal surface outside the particle flux ($\pm$160 mrad vertically), the mirror is split horizontally and both halves are tilted by 9° away from the proton beam direction. Two planar mirrors, each composed of 18 rectangular elements, translates the focal surface to the photon detector area above and below the radiator vessel (see Fig. 2.12). The planar mirrors are made of float glass, thus being significantly cheaper than Pyrex mirrors at the required optical quality. All 80 spherical and 36 planar mirrors are mounted on a rigid low mass support structure inside the radiator volume and can be individually adjusted by stepper

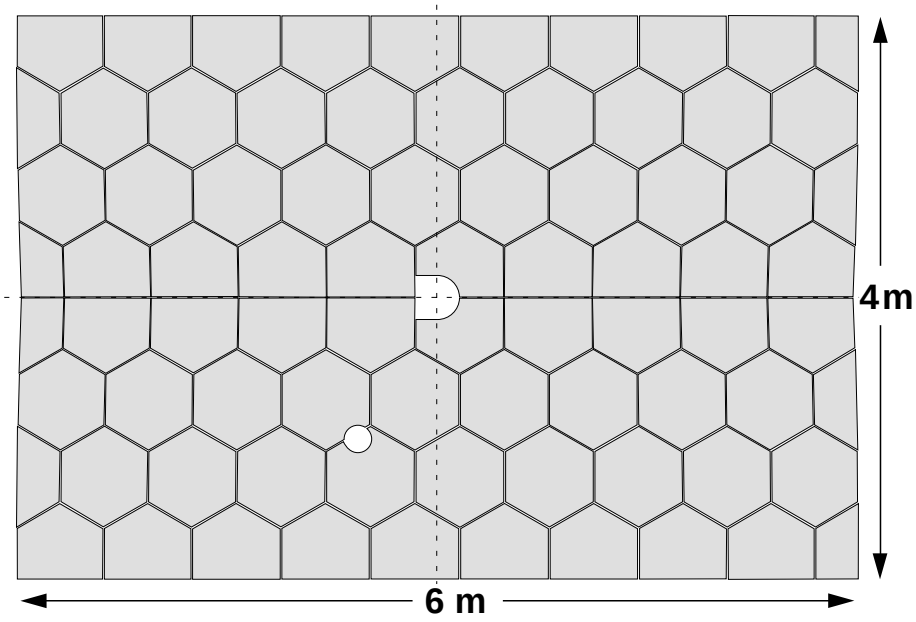

Figure 2.13: Distribution of spherical mirror multigons. The holes in the center are for the proton and electron beam pipes.

motors from the outside.

The mirror quality was determined upon delivery by measuring for each segment the radius of curvature and the fraction of reflected light, and by recording a Ronchi image to check the homogeneity of the mirror surface [13]. The reflectivity was required to exceed 85% in the wavelength interval from 250 nm to 600 nm. From the data acquired, the mirror segments were grouped in a tiling scheme according to their optical quality and resolution requirements [11].

All mirrors were aligned to better than the required precision by surveying them inside the vessel. An off-line data based algorithm was developed for monitoring of the positions of the mirror segments during the measurement [12].

Photon detector The RICH photon detector consists of an array of Hamamatsu multi-anode R5900-00-M16 and R5900-03-M4 photomultiplier tubes (PMTs). In what follows they are denoted by M16 and M4. The M16 version has 16 pads of 4.5 x 4.5 mm^2 each, with a 12-stage, metal-foil dynode system [14]. The M4 version has 4 pads of 9 x 9 mm^2 each, and 10 dynodes. The quantum efficiency of the M16 photocathode with borosilicate window has a broad plateau in the wavelength region between 300 nm to 500 nm and a maximum value about 20%. The M4 tubes have a UV transparent window, which shifts the low wavelength cut-off to about 250 nm. The other PMT characteristics such as the required cathode high voltage ($\leq$ 1000 V), the current amplification (10^7), dark current ($\sim$ 1 nA), pulse rise time (0.8 ns), transit time spread (0.3 ns) are also satisfactory [14]. In the initial set of on-the-bench measurements [15], the single photon counting properties of the photomultiplier tube were investigated, in particular the efficiency for single photon detection as well as the background count rate. It was established that the PMT allows for a good single photoelectron detection efficiency (above 98%), with very small

cross talk (below 0.2%), low background rate (few Hz per channel, Fig. 2.14), and acceptable uniformity as shown in Figs. 2.15 and 2.16 [16].

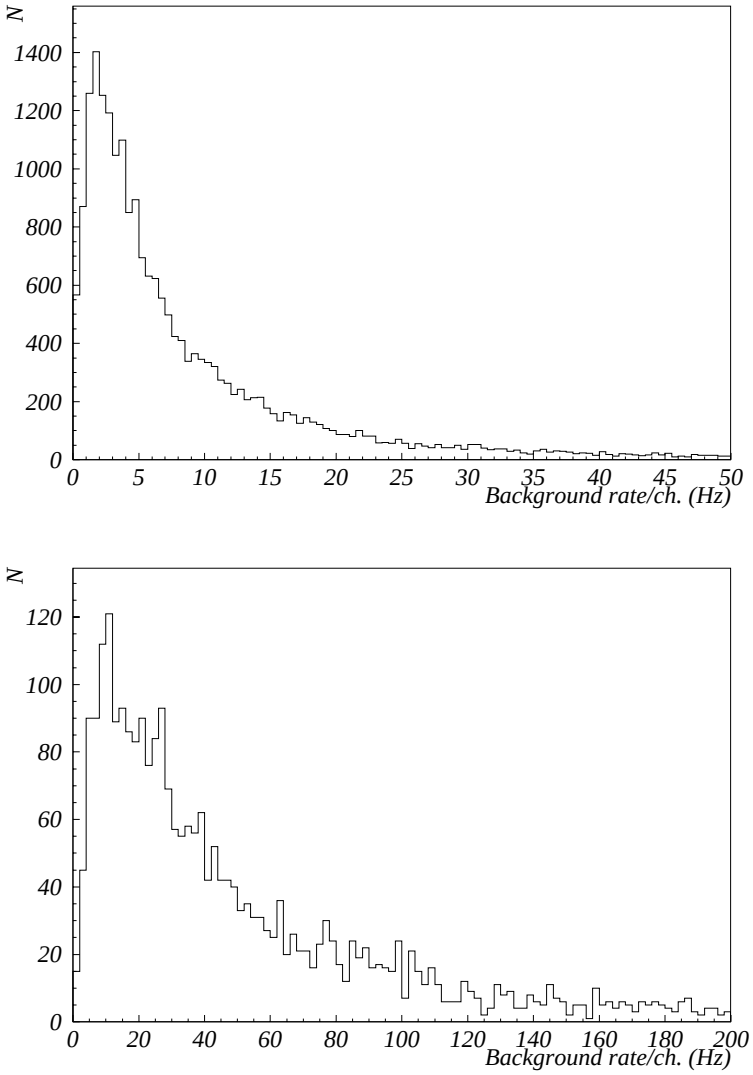

Figure 2.14: Distribution of the number of PMT channels as a function of the background rate per channel for M16 (top) and M4 (bottom) PMTs.

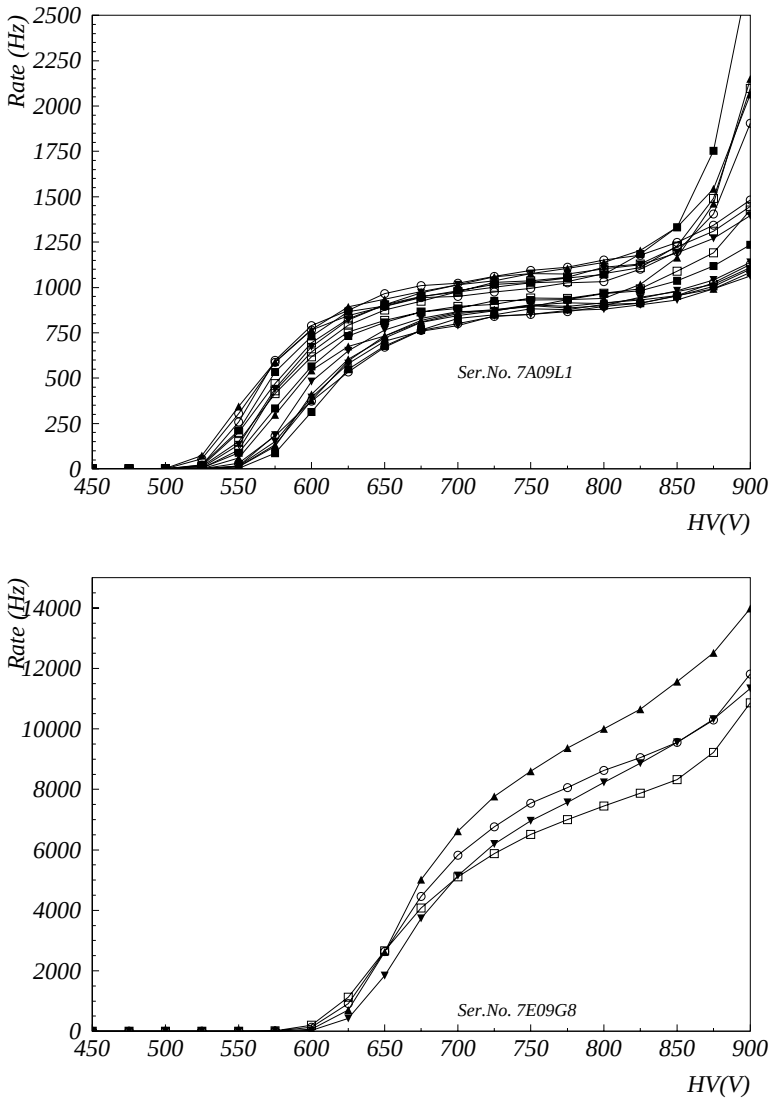

Figure 2.15: The plateau curves i.e., the dependence of measured rate as a function of the high voltage for all channels of a representative M16 (above) and M4 (below) photomultiplier tube.

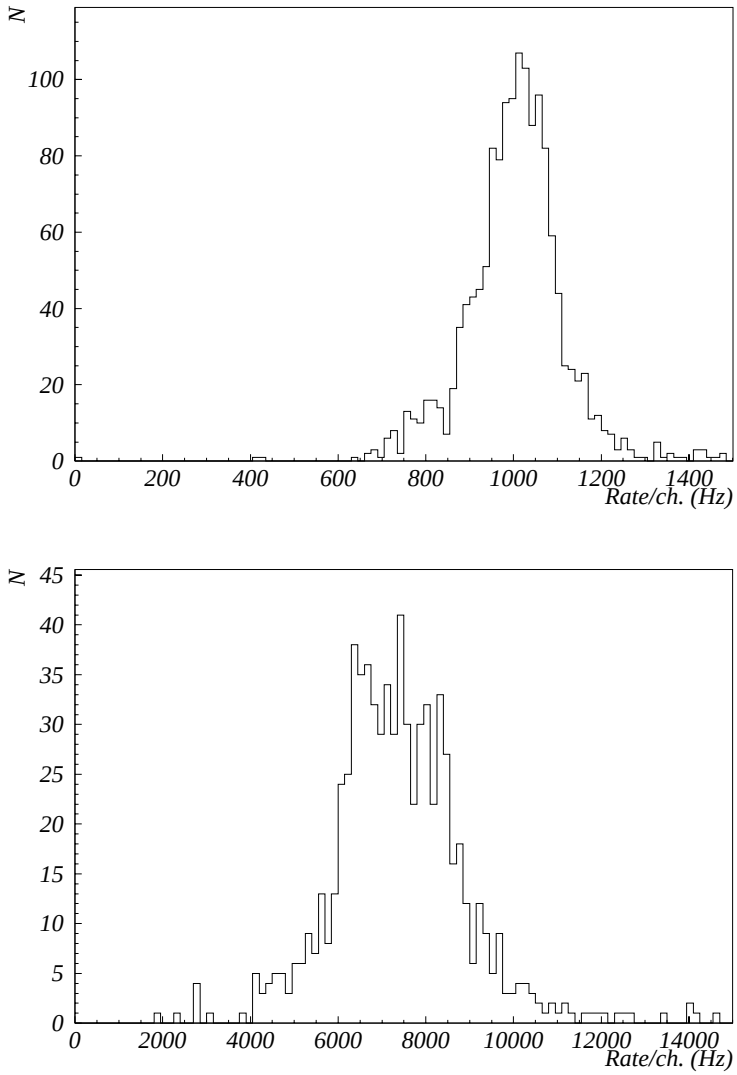

Figure 2.16: Distribution of the number of PMT channels as a function of the rate per channel for the M16 (top) and M4 (bottom) PMTs at optimum high voltage, as determined in the quality assessment tests.

2.7 The transition radiation detector

The transition radiation detector (TRD) was designed to be a part of the electron identification system. It efficiently separates electrons from hadrons in the region where the angular density of secondary particles and occupancy are highest. The transition radiation detector is positioned between the last two outer tracker super layers and covers the region around the proton beam pipe in transverse dimensions of $(134 \times 89\ \mathrm{cm}^2)$.

The detector consists of transition radiator interleaved with planes of straw proportional drift chambers as detecting elements (Fig. 2.17). The radiator consists of polypropylene fibers with a diameter of 20 μm resulting in a total radiator thickness of 1.6 cm per layer. The active detector elements of the TRD are straws made of thin multilayer (Kapton, carbon load Kapton, aluminum) cylindrical drift tubes. The straws of two different lengths (65 and 135 cm) and a diameter of 6 mm are used. The detector is operating with a gas mixture of Xe:CF_4:CO_2 70:20:10 at a gas gain of $2.5{\times}10^4$. This mixture combines the advantages of efficient transition radiation absorption, short total drift time and stability with respect to discharge. The total drift time for 6 mm straws is 64 ns.

The TRD consists of 2 superlayers with straw planes tilted by ± 30 degrees relative to the horizontal axes. Each superlayer contain 16 planes of straws interlayered with a radiator.

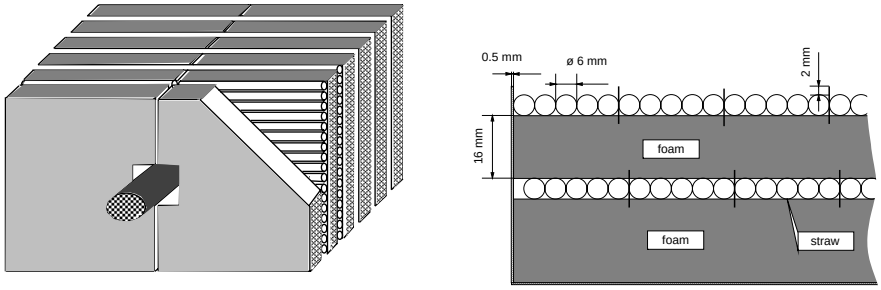

Figure 2.17: The isometric view of the transition radiation tracker (left) and the cross section of a block of the transition radiation detector (right).

2.8 The electromagnetic calorimeter

The electromagnetic calorimeter (ECAL) was originally designed to provide the pretrigger signals on electron and positron candidates of $\mathrm{J}/\psi \to \mathrm{e}^+\mathrm{e}^-$ decays, a good hadron electron separation as well as energy and position measurements, mainly used at the first trigger level. The calorimeter is positioned at about 13 m from the target (Fig. 2.3 and Fig. 2.18). In order to have high detection efficiency both for the electrons produced in J/ψ decays and for tagging electrons, the calorimeter covers the range of 310 cm horizontally and 235 cm vertically. The geometrical acceptance to detect both the electron and the positron from J/ψ is 70% [1, 2]. The corresponding acceptance loss is caused mainly by the inner hole of the calorimeter, where the proton beam pipe goes through.

The calorimeter has modular structure with a basic unit of $11 \times 11\mathrm{cm}^2$ transverse dimensions (as shown in Fig. 2.19). The modules were built using shashlik technology with a sampling plastic scintillator and absorber sandwich. The scintillator and absorber plates are perforated to let plastic wavelength shifting fibers penetrate perpendicular through the plates. The light is collected by these wavelength shifter fibers which are joined in bundles arriving at a photomultiplier face.

The granularity of the detector is increasing with decreasing distance from the beam axis (see Fig. 2.18). Thus the inner, middle and outer modules comprise twenty five, four and one calorimeter basic cell respectively. The schematic view of the inner calorimeter module is

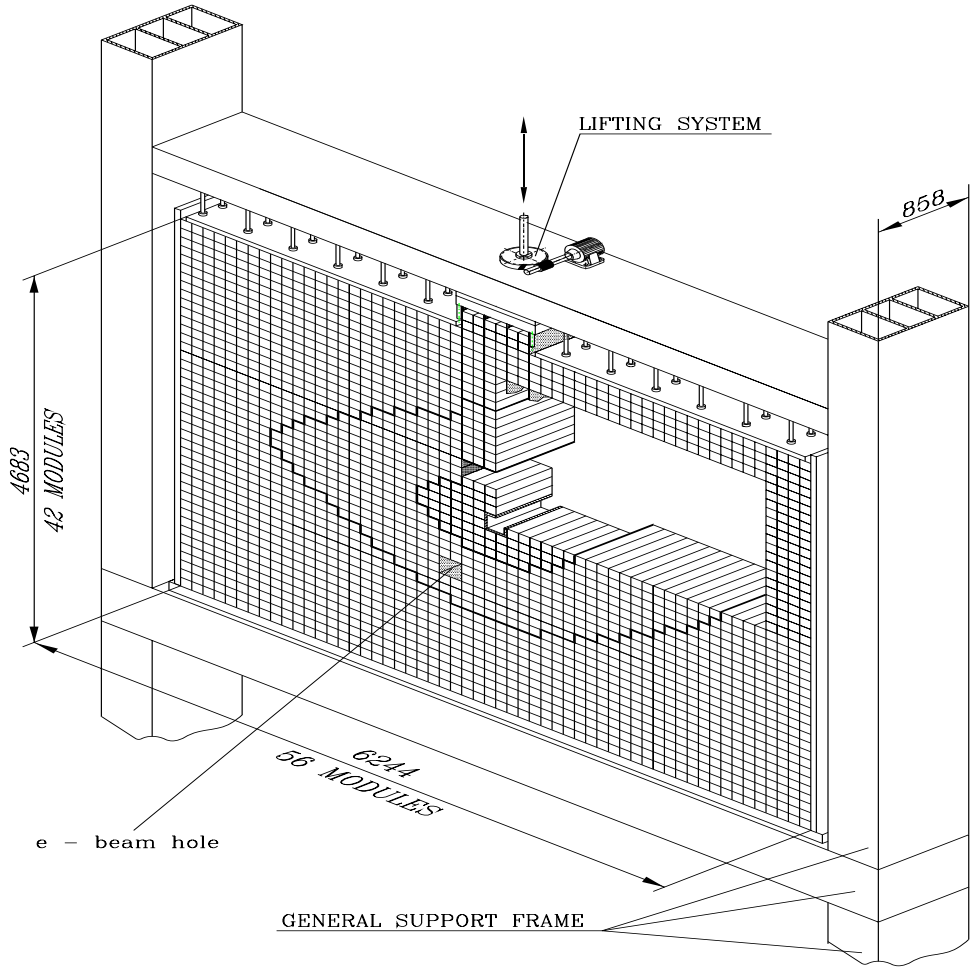

Figure 2.18: The electromagnetic calorimeter geometry. The 84 modules of the inner section are composed of 25 channels, the 532 ones of the middle section of 4 channels, while each of 1728 outer modules represent one channel.

shown in Fig. 2.19. Each module is made of alternating perforated tungsten and scintillator

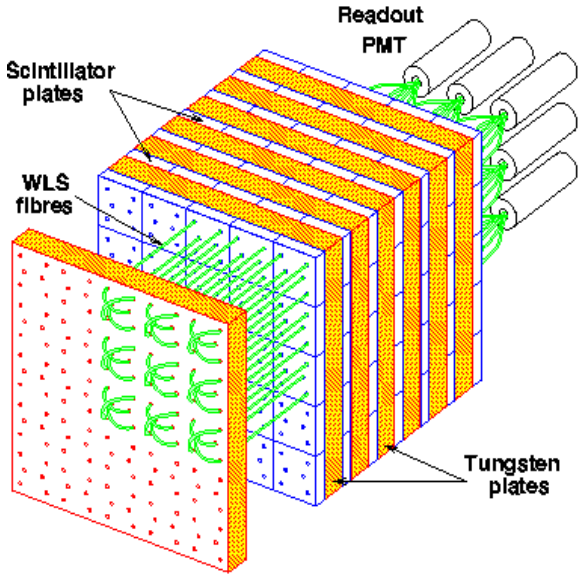

Figure 2.19: Schematic view of the inner module. The scintillator and absorber plates are perforated to let plastic wavelength shifting fibers penetrate perpendicular through the plates. The light is collected by the photomultipliers at the back.

plates being $2\ \mathrm{mm}$ and $1\ \mathrm{mm}$ thick respectively. Altogether there are 40 tungsten and scintillator layers resulting in a total thickness of 23 radiation lengths. Each module has a transverse segmentation of 5×5 basic cells. Each basic cell employs its own photomultiplier tube. The middle and outer calorimeter modules consist of 37 layers of 3 mm thick lead and 6 mm thick scintillator plates resulting in a 20 radiation length depth. The outer calorimeter module consists of one individual basic cell, while the middle module is subdivided into 2×2 basic cells. In total there are 84 modules for the inner, 532 for the middle and 1728 modules for the outer calorimeter sections.

Using the ECAL information for triggering on the lepton pairs a clear J/Ψ meson signal can be reconstructed from the decay $J/\psi \rightarrow e^+e^-$. Electrons loose some energy with Bremsstrahlung in the magnetic field of the dipole magnet. Some of the Bremsstrahlung photons can be reconstructed in ECAL and the invariant mass (i.e. the mass of the electron positron pair[†]) can be partially corrcted (Fig. 2.20).

The performance of the electromagnetic calorimeter is illustrated also in Fig. 2.21. In the analysis it was assumed that π^0 decayed in the target wire to two γ photons. In the histogram only pairs, where each of the clusters had transverse energy E_T[‡] above $0.3\ GeV$ are registered. A clear π^0 peak with the width of $\sigma(m)/m \sim 7\%$ is seen. When events with two clusters with $E_T \geq 0.6\ GeV$ are selected with additional cuts on distance between clusters (more than 4 ECAL cells), E_T of cluster pair above $2\ GeV$, a very clear η peak can be seen. In this case the mass resolution is about $\sigma(m)/m \sim 5\%$ which is better than for π^0, as expected.

[†] $m = (\sqrt{m_1^2 + \vec{p_1}^{\,2}} + \sqrt{m_2^2 + \vec{p_2}^{\,2}})^2 - |\vec{p_1} + \vec{p_2}|^2$
[‡] $E_T = E\frac{p_T}{p}$

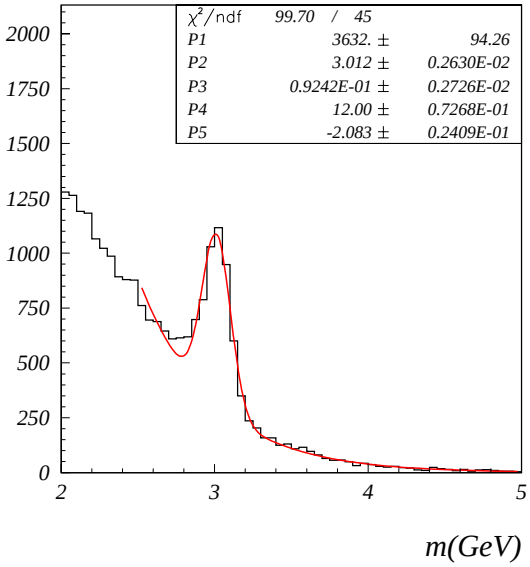

Figure 2.20: Invariant mass distribution for the e^+e^- pairs. The J/ψ resonance can be clearly seen. The condition was used that at least one Bremsstrahlung cluster candidate was found.

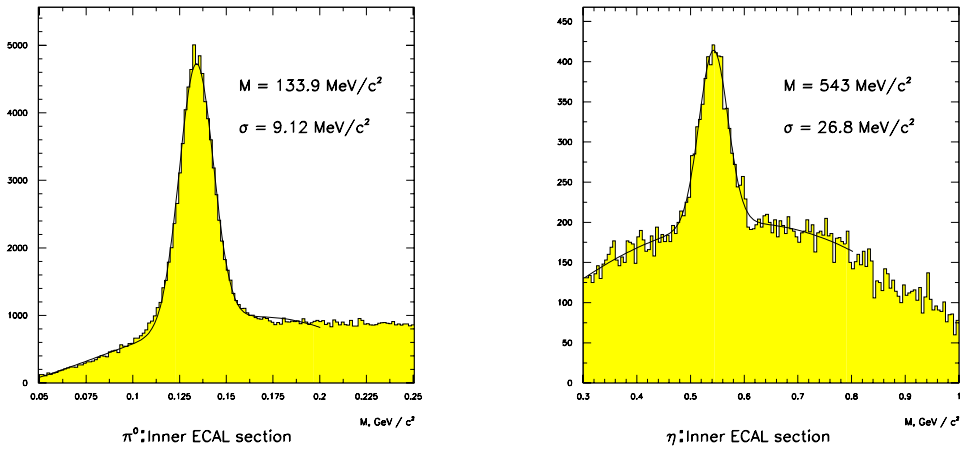

Figure 2.21: Two-cluster invariant mass spectrum [7]: π^0 (left) and η signal (right) in two-cluster invariant mass spectrum, Inner ECAL.

Fitting the π^0 mass peak allowed to extract information on energy and position resolutions. As shown in [18] energy resolution was estimated to be $\sigma(E)/E = (22.5\pm0.5)\%/\sqrt{E} \bigoplus (1.7\pm 0.3)\%$ in the region $12-60\ GeV$, comparable to design values $17\%/\sqrt{E} \bigoplus \pm 1\%$ [1, 2]. Spatial resolution was estimated to be $\sigma_{x,y} = 0.2\ cm$ and linearity better than 0.5% in the $12-80\ GeV$ range.

2.9 The muon system

The muon system (MUON) detects muons in the momentum range between a few GeV up to about 200 GeV/c. Identified muon pairs with an invariant mass in the region of the J/ψ meson provide the trigger signal for $\mathrm{B}^0 \to \mathrm{J}/\psi \mathrm{K_s}$ decays. The muon system also serves to select additional single muons from semileptonic decays, which provide a tag of B meson flavor. Angular detector acceptance is 250 mrad horizontally and 160 mrad vertically. The geometrical acceptance for detection of the $\mu^+\mu^-$ pairs with momenta above $5\ \mathrm{GeV/c}$ from J/ψ decays is 71%, while the acceptance for the tagging muon is 81% [1, 2].

The higher penetration capability of muons compared to hadrons is used for their separation. The muon system consists of the three hadron absorber segments, built of iron and armored concrete blocks, alternate with three detector superlayers (Fig. 2.3). A fourth superlayer is added at the and without an additional absorber to provide (together with the third superlayer) a clean measurement of track directions, which is not affected by multiple scattering in the material.

The muon detection superlayers are composed of three different chamber types: tube chambers, pad chambers and gas pixel chambers. In the outer regions of the first two superlayers of the muon system the tube chambers are used, while the last two employ pad chambers. In the region around the beam pipe gas pixel chambers in all four layers are used.

The tube chamber is a closed-cell proportional wire chamber made of an aluminum profile with a large drift cell cross section of $14 \times 12\ \mathrm{mm}^2$. A 3 m long and $40\mu m$ thick gold plated tungsten anode wire is stretched in the center. To ensure a high efficiency, each chamber consists of two layers of 16 cells shifted one against the other for half a cell width (Fig. 2.22).

The pad chamber is a proportional wire chamber assembled from an open aluminum profile and closed with the copper phenolic board. Again, the pad chambers consist of two monolayers shifted for half a cell width with respect to each other and a 3 m long anode wire is stretched inside each cell.

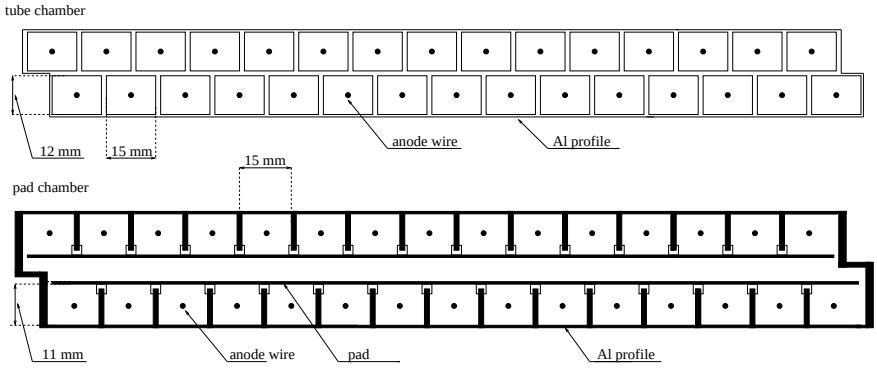

Figure 2.22: Schematic drawing of the tube chamber and pad chamber construction.

Gas pixel chambers, single-layer multiwire proportional chambers, are composed of square cells formed by one signal wire and four potential wires with the length of about 3 cm, oriented along the beam direction. Cells of a size of $9 \times 9\ \mathrm{mm}^2$ are used in the first three superlayers, while cell size of $9.4 \times 9.4\ \mathrm{mm}^2$ is chosen for the last superlayer in order to approximately

follow the projective geometry. The cell sizes of the muon chambers are determined by the maximum allowed drift time because the accuracy for the measurement of the track position is limited by multiple scattering in the calorimeter and in the absorber.

The first and the second superlayers consist of three layers of muon tube chambers, with anode wires perpendicular to the horizontal plane in one layer and wires oriented by $\pm 20^0$ with respect to the vertical line in the other two (Fig. 2.23). The third and fourth superlayer consist of one layer with pad and wire readout.

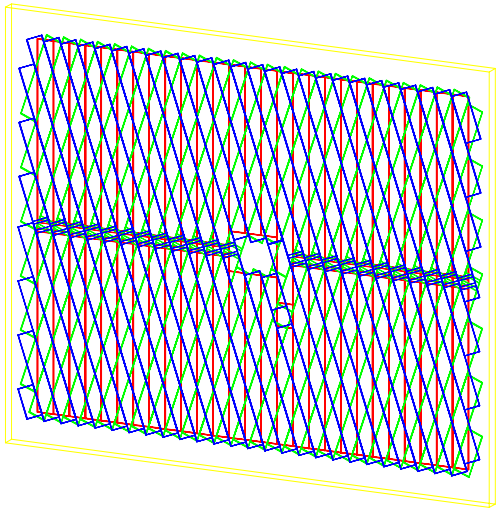

Figure 2.23: View of the superlayer with three layers of muon tube chambers.

In the recent data the yield of J/Ψ mesons is about thousand per hour of data acquisition. Portion of online reconstructed J/Ψ mesons is shown in Fig. 2.24.

2.10 The data acquisition system and the triggering system

To extract the highly unlikely ”gold platted” events from the majority of inelastic interactions a complicated data acquisition system (DAQ) and a multilevel trigger system was designed [19]. The HERA-B data acquisition system must cope with more than half a million of detector channels, a 10 MHz bunch crossing rate and a signal to background ratio of 10^{-10}. The physics program of the experiment determines the trigger algorithms. Since the signal to background ratio is very small, the event selection scheme is divided into four sequential triggering levels. There are two constraints to the DAQ of the HERA-B system, the logging rate and the processing power. A typical HERA-B event has a size of 100 kbyte, which corresponds to a data flow rate of 1 Tbyte/s at an event rate of 10 MHz. Such a high data flow rate cannot be accommodated by the available storage logging systems. In addition, the complete event reconstruction takes a few seconds on the state of the art processors. As the required processing power cannot be implemented, events must be selected before they are saved on tape or disk.

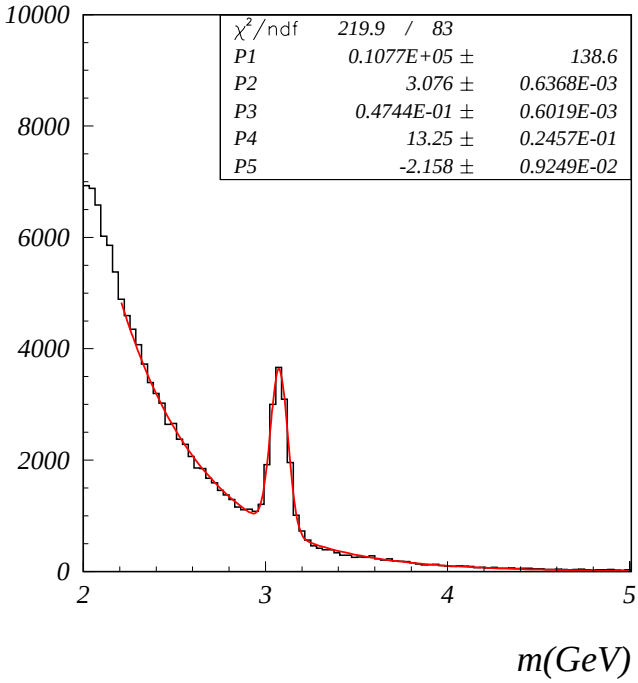

Figure 2.24: Reconstructed $J/\Psi \to \mu\mu$ decays. The muon system was used for triggering on muon pair candidates.

The DAQ and the triggering system architecture is presented in Fig. 2.25 and will be briefly described in the following. Each of the trigger levels has a characteristic data flow and rate requirement. At the first level, the calorimeter and the muon chambers are used to separate regions in the tracking system in which a lepton may pass and a search of such tracks is carried out. After the tracks are found, the invariant mass of the l^+l^- pair is calculated, which is matched with the mass of the J/ψ particle. Specially designed processors are used to carry out all these operations in maximal time of 12 μs, suppressing the background by a factor of 200 and retaining more than 60% of all the useful events. During the processing of the triggers, the data is stored in the front end electronics pipeline buffers, to reduce dead time. At the second level tracking is refined, and an information about the secondary vertex is used, which suppresses the background by an additional factor of 25. Finally, at the third level, the complete reconstruction of the event is done, which enables an additional rejection factor of 20. In the final analysis, the separation of the $B \to J/\psi K^0_S$ decay is achieved primarily by calculating the invariant mass of the candidate for the B meson and by imposing the requirement that the vertex of the decayed B meson is several millimeters away from the primary vertex.

The signals recorded are fed into the different types of front end electronics. The signals are amplified, shaped and digitized already at the detector. The signal wires are connected to a Front End Driver (FED) system. There are four different types of front end drivers for different types of the measurements needed: analog type FED for the inner tracker and the silicon vertex

detector, hit type FED for the muon system, the RICH, the High-Pt system and the TRD, timing type FED for the outer tracker, and a pulse height type FED for the electromagnetic calorimeter.

The Fast Control System is designed to synchronize the detector, assign the detector signals to events and identify events. Therefore it distributes signals to the FED's. Among these signals are the bunch clock, the FED specific delay between bunch clock and detector signals, the current event number and event numbers of First Level Trigger (FLT) accepted events. The Fast Control System consists of one central "mother" unit, a signal distribution system and a "daughter" board in each Front End Driver crate. There are 210 daughters in the HERA-B detector all together.

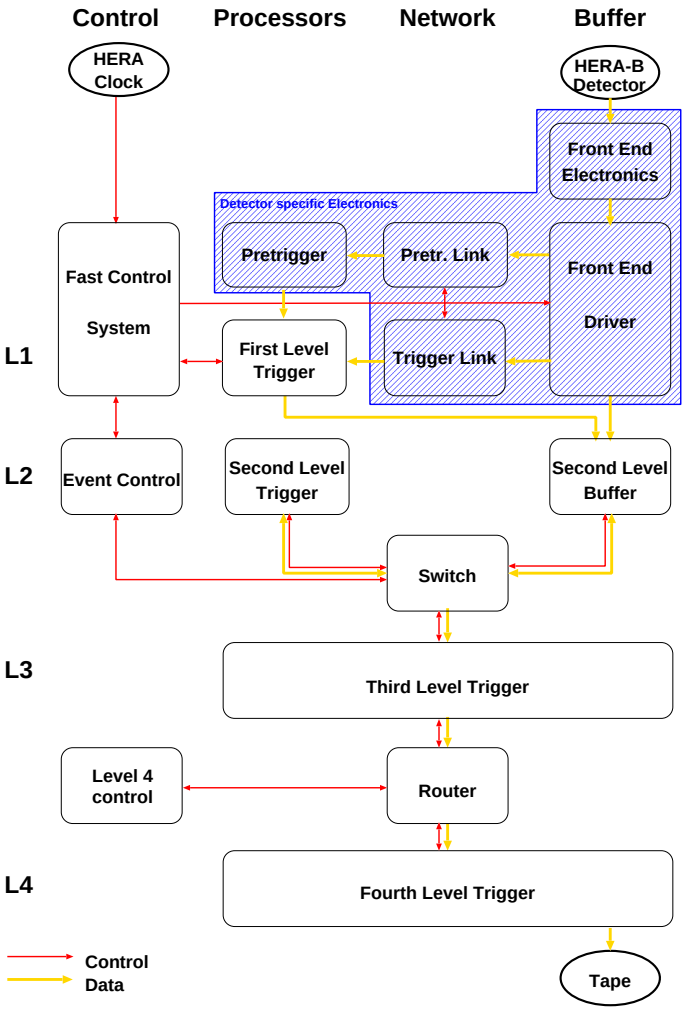

Figure 2.25: Data acquisition and triggering system architecture used in the HERA-B experiment.

The first level trigger processes only part of the event information with data stream of 150 Gbyte/s and delivers its result after a delay not longer than $12\ \mu$s. The first level trigger is expected to reduce the input event rate by a factor of 200. After an event is accepted by the first level, all data belonging to this event are read out of the pipelines and pushed into a second level buffer, which is implemented with the SHARC cluster VME boards. The same

SHARC cluster board is used to implement a switch which carries the event control traffic, the dialog between second level trigger and second level buffer and runs the event controller. The second level trigger operates only on selected data information at 50 kHz to 100 kHz input rate and therefore digests 50 Mbyte/s. More than hundred dedicated second level trigger PC processors repeats the first level trigger algorithm with a higher precision. It adds more hits with the full chamber resolution in the tracking layers behind the magnet and projects tracks through the magnet and vertex detector. The silicon tracker data is used to reject di-leptons generated in different interactions during the same bunch crossing and to enhance J/ψ candidates from secondary vertices downstream of the target. A rejection factor of 10 should be obtained by eliminating events which do not contain reconstructed tracks of acceptable quality and an additional rejection of factor 10 is expected after the vertex cuts are applied. Events surviving the second level trigger cuts are passed to the third level trigger. It is the first trigger level which does not use only selected information, but requires a complete event data assembled and available in processor memory. The third step operates at a rate below 1 kHz which amounts to a data rate of 100 Mbyte/s. The third level trigger does the full track and vertex fitting with high precision. More stringent cuts on particle mass and vertex positions for all the tracks in the event should reduce the data stream by a factor of 10. Accepted events are routed to the fourth level trigger. It actually does not act as a real trigger because it performs the full event reconstruction which calls for the entire detector alignment and calibration data. The fourth step works at the event input rates smaller than 50 Hz which presents a data stream of moderate 5 Mbyte/s. A few seconds of computing time per event is needed on one of more than one hundred dedicated processors, where pattern recognition and event reconstruction procedures are running. A reduction of a factor 2.5 is expected such that the event data would be routed to the storage media at a moderate event rate of 20 Hz as a final step of the DAQ and triggering system procedure.

The actual trigger setup differ slightly from the design described above. This resulted in few different types of data that were taken so far, which are as follows,

- minimum bias data sample, where no trigger was used at all,
- interaction trigger sample, where the trigger was set to reject the empty events. Typically it was required that there is more than 20 hits reconstructed in RICH detector,
- single lepton trigger, where only one lepton candidate with reconstructed transverse momentum above threshold (usually set to $1\ \mathrm{GeV}$) was required,
- di-lepton trigger, where a pair of leptons was required to have transverse momenta above threshold.

Different trigger demands, such as the cuts on the transverse momentum (p_T) of the lepton candidate varied slightly in different data sets.

2.11 Monte Carlo simulation

The complete simulation in the HERA-B experiment is divided into two steps. The first step is the simulation of physical processes, also called event generation. In the target of the HERA-B experiment the protons collide into nuclear target. Thus beside hard generation processes also nuclear effects have to be simulated, and a combination of two event generator packages had to be implemented [20]. PYTHIA package [21] is used for simulating various scattering subprocesses of importance for the HERA-B physics program, like heavy quark production. PYTHIA internally utilizes the JETSET package [21] for simulating the jet fragmentation. The nuclear effects are generated by FRITIOF package [22].

The next step is the simulation of the detector response to the event generated and is implemented in HBGEAN package [23] which is based on GEANT [24] the standard package for the detector description and simulation. This part itself is divided in multiple steps. First the interactions of particles with the detector material, such as multiple scattering or pair production were simulated. All the intersections of generated tracks with the spectrometer material are then calculated and stored. Then the detector hits are generated by taking into account the smearing of the position due to detector resolution and imperfect detector efficiencies.

3 Alignment of the HERA-B spectrometer

3.1 Introduction

As already discussed in the introduction, an essential part of the commissioning of a spectrometer is its alignment. In this chapter methods for an overall alignment of the HERA-B spectrometer will be presented, in which the positions of individual detector components are determined (see also [25]). Such an overall alignment will be in what follows referred to as 'global alignment' to distinguish it from the 'internal alignment', which deals with the detector components internally. I will first introduce the aim of global alignment. and describe different methods. Two methods are based on single tracks and the third one uses the measured two-body particle decays. The single track based methods all use fitting of two-dimensional distributions, which will also be described briefly. The results are divided into two parts: the results using the simulated MC data, which serve in case of track based methods to estimate the achievable accuracy and systematics, and the results on the data accumulated in the year 2000. At the end the results of alignment obtained using the data acquired without magnetic field will be shown.

The procedure of alignment in the HERA-B spectrometer is divided into two parts. The first step is the internal alignment of the individual detector components:

- the vertex detector (VDS), which is located upstream from the magnet,
- the magnet, used for determining the charged particle momenta. It is characterized with the magnetic field integral: $e \int_{Z_{min}}^{Z_{max}} B \cdot dz = 0.635 \mathrm{GeV/c}$,
- the main tracker, which consists of outer tracker (OTR) and inner tracker (ITR), and was further divided as discussed in the next section,
- the ring imaging Cherenkov counter (RICH),
- the electromagnetic calorimeter (ECAL) and
- the muon chambers (MUON).

The parameters of the global alignment of components can not be determined by the internal alignment procedure. The determination of these parameters is the task of global alignment. The assumption of global alignment is that the components are internally aligned.

The global alignment is carried out in several steps which are illustrated in Fig. 3.1. The first plot represents the state of the internally aligned detector, before the global alignment procedure is started. The second plot shows the effect of two steps which are carried out using

single tracks. First the parts behind the magnet and the parts in front of the magnet are aligned separately. This is done by comparing the straight portions of tracks linking given two components both on the same side of the magnet. Both parts are then connected to meet in the central plain of the magnet. In these two steps it is not possible to determine the absolute momentum scale. A kink in the center of the magnet only changes the momentum of each track, as may be seen on the second plot. The fit of the track to the measured points doesn't degrade. These two steps of global alignment are called geometry based alignment and described in Sections 3.3.1 and 3.3.2.

The third plot represents the momentum based part of the global alignment. There are a couple of ways to determine the kink of the spectrometer. For example by studying the tracks coming from decaying particles an additional constraints can be made on the momenta of the two tracks which have to combine into the mass of the decaying particle. This method is described in Section 3.3.3. There exist also alternative possibilities, such as converted gammas or early bremsstrahlung photons, where some information downstream from the magnet is obtained which is not effected by the magnetic field. All these possibilities require very large statistics, i.e. a large number of recorded events.

At the end the whole HERA-B spectrometer has to be positioned. Because the number of shifts applied so far in the global alignment procedure is large, due to many components and their degrees of freedom, the sum of all the shifts can be required to be minimal. This step, fit to the nominal position, is represented on the last plot.

Note that in this chapter the standard HERA-B coordinate system is used, i.e. the incidence proton beam direction is along the z axis, y is vertical, and x points inside of the proton accelerator ring.

3.2 Implementation

3.2.1 Global alignment transformations

At the stage when the global alignment procedure is started, each component of the HERA-B spectrometer can be considered as a bulk which is internally aligned. On the other hand, the internal alignment is not sensitive to several transformations, i.e. linear transformations such as shear, stretching, rotation and, in addition, the translations in all directions. Several of these transformations produce similar effects, when angles or displacements are small. For example the rotation around an axis parallel to the x axis is approximately the same as the effect of shear deformation in the yz plane (Fig. 3.2). This means that a subset of all possible transformations has to be made for which parameters can eventually be determined. In addition, the stretching in x and y directions is highly unlikely due to the fact that the distances between wires/strips in the detector plane are accurately known, and therefore these degrees of freedom are not considered.

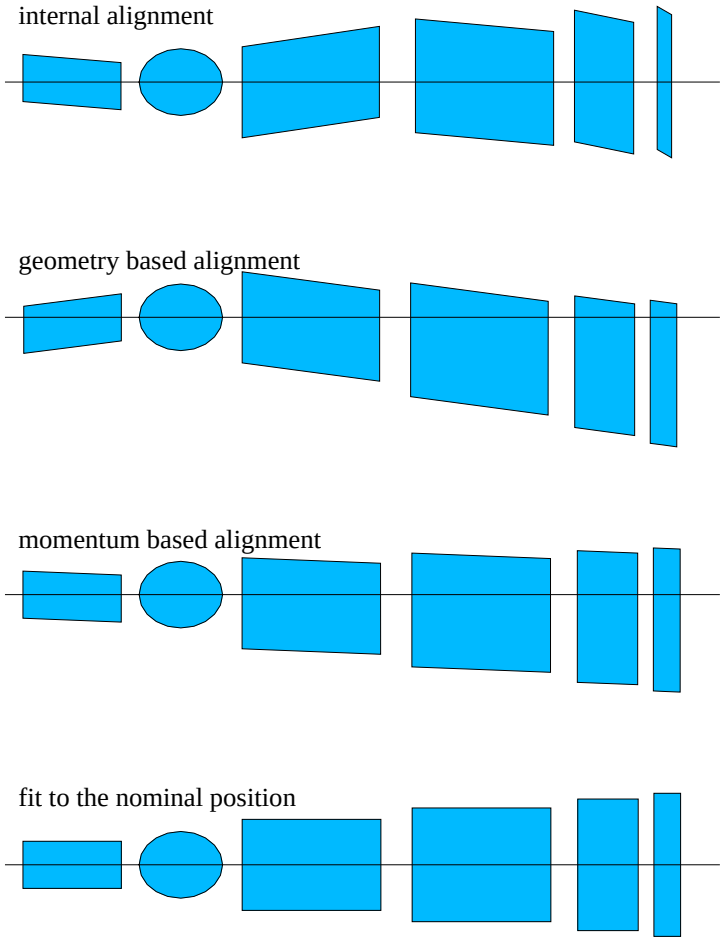

Figure 3.1: Symbolic representation of steps of the alignment procedure for the HERA-B spectrometer. The oval part designates the magnet, which divides the spectrometer into two parts: the left-hand part in front of the magnet (the vertex detector and the target) and the right-hand part behind the magnet (the trackers and the particle identification devices). Note that the determined shifts are only taken into account in the reconstruction (the components are not physically shifted).

The chosen set of global transformations is as follows:

- translations in x, y and z directions
- shear in xz and yz planes relative to a reference z, keeping the planes perpendicular to z axis.
- stretching in the z direction with respect to a reference z.
- rotation around the z axis for an angle φ.

The reference position on the z axis was chosen to be common to shearing transformations and stretching transformation. For its value the central plane of the magnet was chosen, where the track segments from the vertex detector (VDS) and main tracker (OTR), intersect in the

linear approximation. This point is offering itself as the most natural one. If some other reference z value was chosen the shearing or stretching transformations can still be decomposed into shearing or stretching around the middle of the magnet and a certain translation.

Using a single track based comparison of two components, one in front of the magnet and the other behind the magnet, only 5 among these 7 parameters can be determined: all shifts (x, y, z), shear in yz plane and rotation around z. In addition, by comparing two components only the relative shifts can be determined of one component compared to the other. The shear in xz and the stretching in z direction cannot be determined on the track basis only. To determine these, the physical signals were used, e.g. two body decay of J/Ψ meson (see Section 3.3.3).

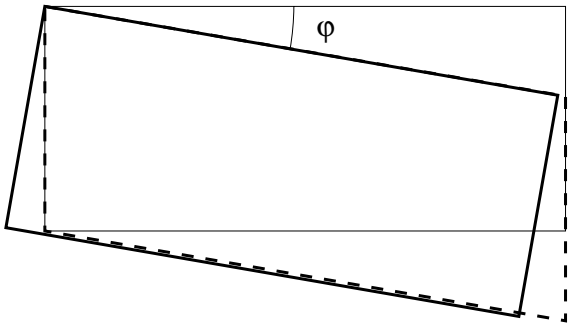

Figure 3.2: Similarity of shear (dashed line) and rotation for small angles (thick line).

3.2.2 Subdivision of HERA-B into components

Naturally HERA-B, when operating in magnet-on mode, is divided in three parts: the part in front of the magnet (vertex detector, for which an abbreviated term VDS will be used, and the target), the part in the magnet and the tracking system and particle identification devices behind the magnet. These parts have to be considered separately. The parts of the tracking system behind the magnet are further divided into several parts, which can be adjusted separately. This was done due to a lack of overlap between separate parts. For example, each superlayer of the outer tracker (OTR) is divided into two halves which are mounted on separate frames and can be moved individually. The + halve consists of the modules that occupy most of the +x (i.e. $x > 0$) side of the superlayer. The − halve is a bit larger and occupies besides −x (i.e. $x < 0$) also a part of the +x side of the superlayer (see Fig. 3.3, where an example a superlayer division is shown). There are not enough tracks coming from +OTR to −OTR and vice versa (i.e. tracks that crosses the some superlayers in the + halve and some in the − halve), to do a reliable relative internal alignment. The inner tracker is divided into 4 quadrants: +x+y, +x−y, −x+y and −x−y. In this case there is sufficient overlap between the quadrants to do the internal alignment using the space point method, thus for the ITR all quadrants are adjusted simultaneously.

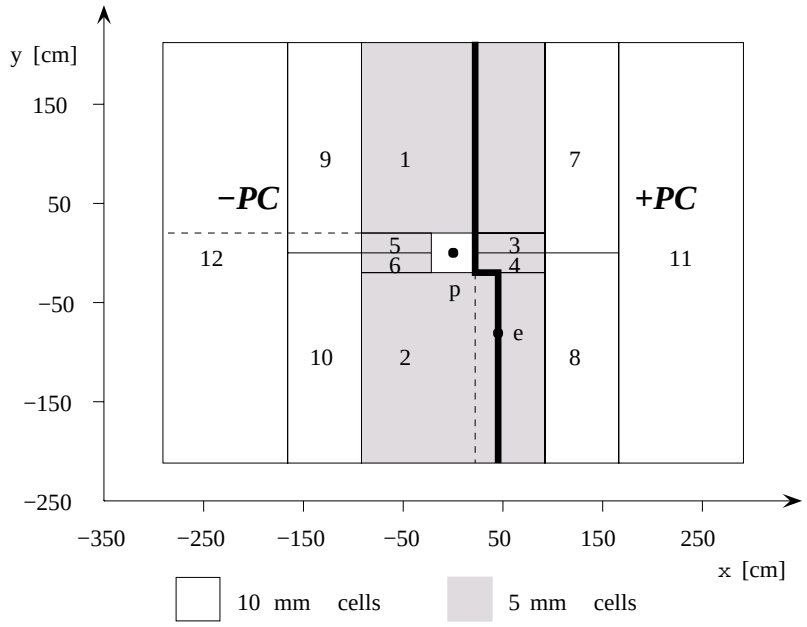

Figure 3.3: Subdivision of a typical plane in the PC part of OTR. The thick line represents the division between +PC and −PC which are mounted on two separate support frames.

3.3 Global alignment methods

In this section I will describe the three methods used for global alignment of HERA-B. The first two are based on single tracks, either by comparing the segments behind the magnet with those in front of the magnet directly, or by using the Runge Kutta tracking method to bring the parameters of the segments in front of the magnet to the point behind the magnet and then compare them with the parameters of the segment there.

3.3.1 Method 1: Direct comparison of the segments

The most straightforward method is the comparison of the components that are all located entirely behind or entirely in front of the magnetic field. In this case the directions and positions of the components can be compared directly. A typical example is the ECAL-OTR comparison, where both components are located behind the magnet. In the OTR track segments information about both the position and direction is obtained, while in ECAL, with reconstructed clusters only the position information is available. By linearly prolongating the OTR segment to the z coordinate of the ECAL reconstructed cluster, the two positions can be compared. When plotting the residuals, a peak superimposed on a smooth combinatorial background is obtained, which allows us to fit a simple linear (or at most quadratic) background function and a Gaussian peak.

The segments behind the magnet can also be directly compared with those in front of the magnet in the non-bending direction. The assumption made is that the amount of bending in this plane is very small compared to the resolution. This certainly is true when comparing the VDS and OTR segments in the non-bending y direction, because of the poor resolution of the OTR in this direction.

Also in the bending direction (x) certain direct comparisons of the segments in front of the magnet with those behind the magnet can be made. In the first approximation it would be expected that the VDS and OTR segments intersect at a certain point on the central plane of the magnet (Fig. 3.4). Detailed calculations show that the z of the intersection depends weakly on the direction coefficients of the two segments (t_{x_1} and t_{x_2}):

$$z_0 = z_1 + \frac{z_2 - z_1}{2} \frac{2}{1 + \frac{\sqrt{1+t_{x_1}^2}}{\sqrt{1+t_{x_2}^2}}}, \tag{3.1}$$

where t_{x_1} is the direction coefficient of the segment in the VDS and t_{x_2} is the direction coefficient of the segment in the OTR.

With both direction coefficients below 0.1, the maximal deviation from the central plane of the magnet is below $0.5\ \mathrm{cm}$ (Fig. 3.5).

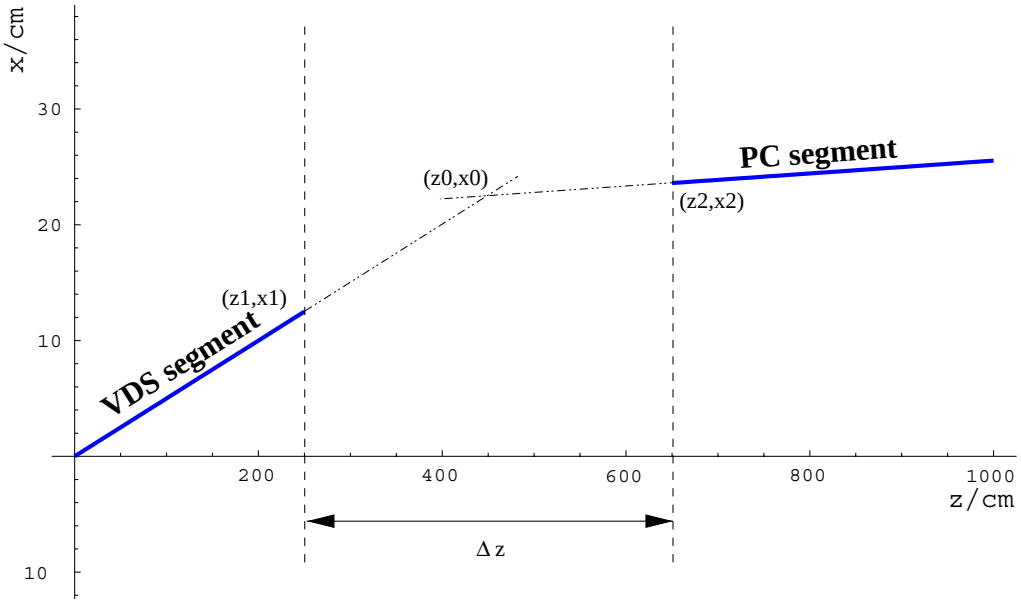

Figure 3.4: z_0 of the intersection of VDS and OTR segments. Pairs of VDS and OTR segments belong to the same reconstructed track.

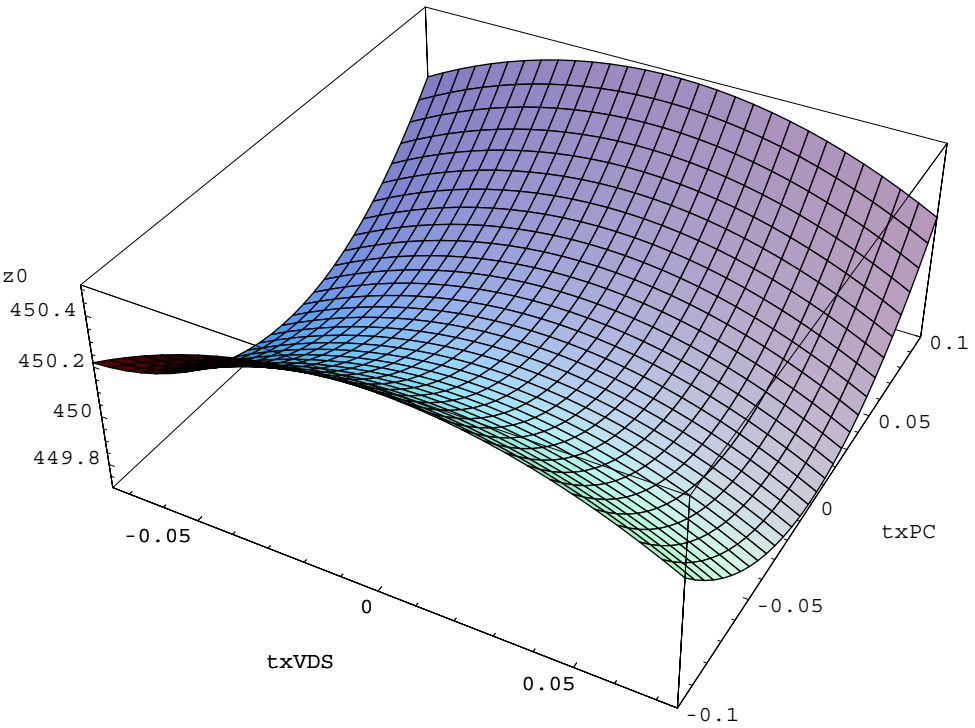

Figure 3.5: z_0 of the intersection of VDS and OTR segments as a function of t_x of VDS and OTR segments.

3.3.2 Method 2: Using Runge-Kutta tracks

For the purpose of global alignment a procedure to construct tracks that would depend on as few parameters as possible was established. The procedure of constructing such tracks is described in some more detail in the next section. With such tracks various distributions can be studied. A subset of these distributions, along with the distributions from method 1, is described in Section 3.4.1.

The tracks constructed in the standard reconstruction package of ARTE (and known as RTRA's) are not the best choice for global alignment because each of them is an average of all the corresponding segments from different parts of the detector. Thus, the following procedure was chosen for constructing the tracks: Matches of VDS and OTR segments were used, as provided by the MARPLE package [27]. Since it is decided to keep all true tracks and to have wide matching cuts to get a background which can be fitted easily (see Section 3.4.2), a modified broader MARPLE matching intervals were engaged. The matching intervals in x and y were modified to the following values:

$$\Delta_x : 2.57\mathrm{cm} \rightarrow 3.0\mathrm{cm}$$

$$\Delta_y : 5.65\mathrm{cm} \rightarrow 20.0\mathrm{cm}$$

From these matched RTRA tracks only the VDS segment is taken and tracked to the fixed plane (at $z = 750$ cm) in the PC section of the tracker. For this tracking a Runge-Kutta based routine (`rk5clip_`) is employed, which is implemented in the standard HERA-B reconstruction software. The routine takes into account the full knowledge of the magnet field. As a first approximation for the momentum of the track the momentum obtained from RTRA fit is used. At $z = 750$ cm the difference in x (dx) between the tracked VDS segment and the OTR segment extrapolated to $z = 750$ cm is evaluated. The correction for the momentum is then evaluated using the relation between the displacement and magnetic field integral:

$$d(p^{-1}) = \frac{dx}{(z - z_0) e \int_{Z_{min}}^{Z_{max}} B \cdot dz}, \tag{3.2}$$

with

$$z_0 = 450\mathrm{cm}; \quad \mathrm{e}\int_{\mathrm{Z_{min}}}^{\mathrm{Z_{max}}} \mathrm{B}\cdot\mathrm{dz} = 0.635\mathrm{GeV/c},$$

which holds approximately for the HERA-B magnet. Because this is not the exact magnet parameterization an iterative procedure is used. Now the same VDS segment with the corrected momentum is prolonged to $z = 750\mathrm{cm}$ and the next momentum correction is calculated. The procedure is repeated until the desired accuracy is reached. For the results presented in this chapter the condition $\Delta_x(z = 750\ \mathrm{cm}) < 0.005\ \mathrm{cm}$ was used, which is usually met in a few steps (Fig. 3.7). To summarize, in construction of the tracks in the way described above the VDS segment position and direction and the OTR segment position only are used.

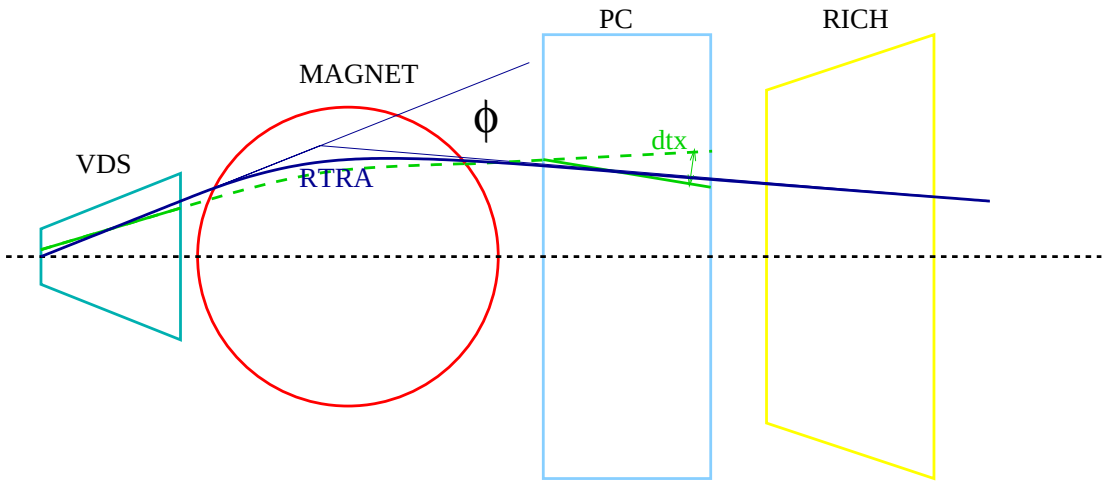

Figure 3.6: Matches are taken from RTRA. Then, the new momentum is determined (Fig. 3.7).

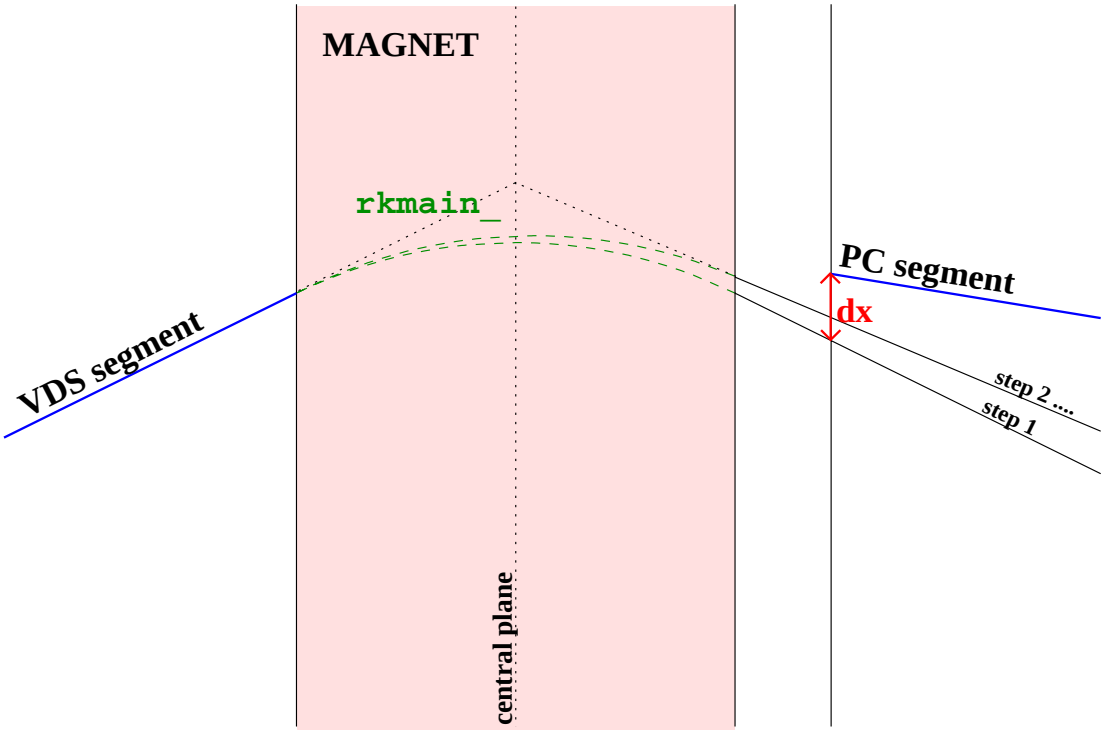

Figure 3.7: VDS segment is tracked to $z = 750\ \mathrm{cm}$ with ARTE built in routine. There it is compared with the OTR segment. From the deviation in x the momentum correction is evaluated. The procedure is iterated until the desired accuracy is reached. The true position is usually hit in a few steps.

3.3.3 Method 3: Using two body decays

The only way to determine the shear dt_x and the stretch f_z is to get the track momentum information from elsewhere. We chose to constrain the momentum of the tracks by using the muon tracks coming from the decays of the J/Ψ resonance. To determine the sensitivity of such a track sample to the above transformations, a J/Ψ sample was reconstructed and the effect on the width and position of the J/Ψ peak was observed, when shearing or stretching the detector. Note that shearing and stretching transformation only change the momentum of the tracks. Thus, it was possible to simulate the effect offline by studying the mass of the reconstructed J/Ψ mesons according to the change in the momentum of the two decay tracks (the effects will be estimated later in this section). Intuitively it is expected that changing t_x (thus decreasing one and increasing the other track momenta) would leave the mass unchanged (Fig. 3.8(a)). Further it is expected that by putting the components in the right positions would give the best resolution, hence a minimum in the width distribution (Fig. 3.8(b)). By stretching (shrinking) the detector in z, the momentum of both tracks is simultaneously increased (decreased), which in the same way changes the mass of J/Ψ mesons (Fig 3.9(a)). The width is not sensitive to stretching (Fig 3.9(b)).

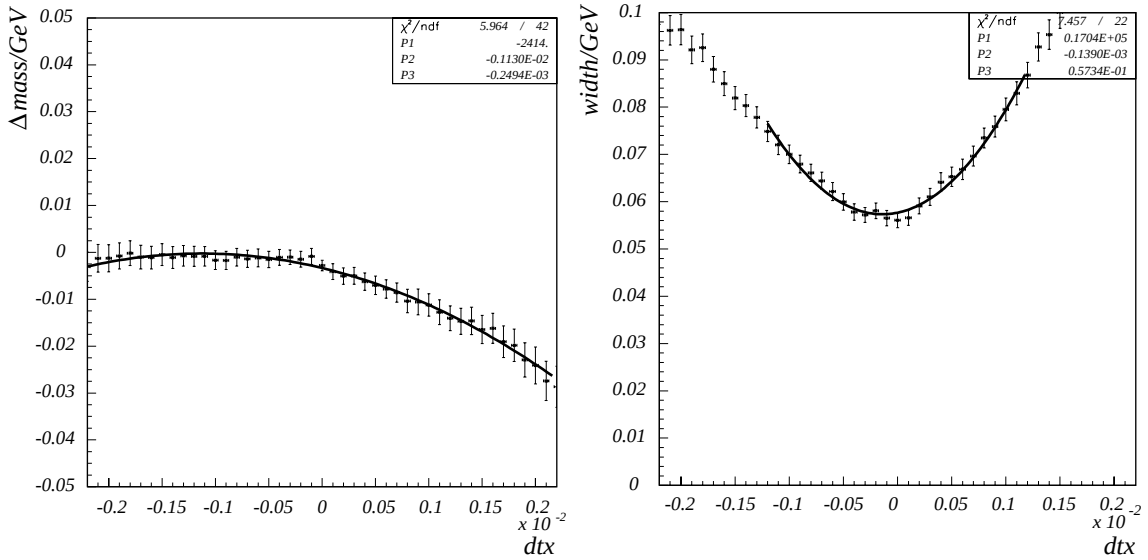

(a) (b)

Figure 3.8: Variation of the mass (a) and the width (b) of J/Ψ peak with changing the dt_x of the OTR.

The procedure gets more complicated when the tracker is divided into 2 halves. In most cases one of the tracks of the decaying particle goes to +OTR and the other to $-$OTR. However there still exist some J/Ψ mesons which decay entirely into $-$OTR, which has much larger occupancy than +OTR (Fig. 3.3). First the t_x and f_z for the $-$OTR is fixed with such J/Ψ mesons in the way described above. Then the rest of the J/Ψ meson sample can be used to determine the parameters of the +OTR.

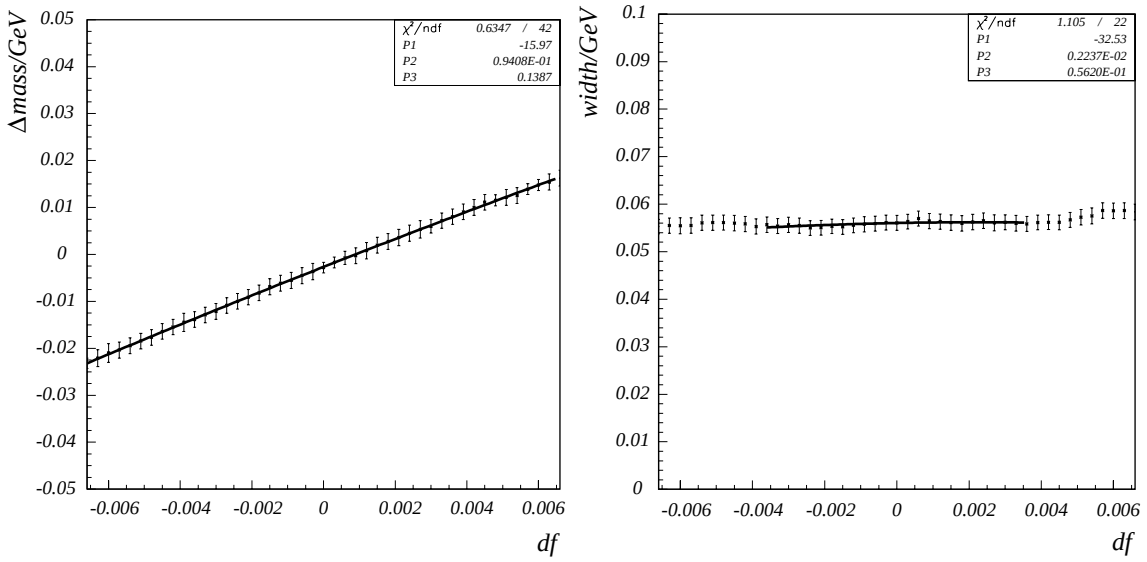

(a) (b)

Figure 3.9: Variation of the mass (a.) and the width (b.) of J/Ψ peak with changing the f_z of the OTR.

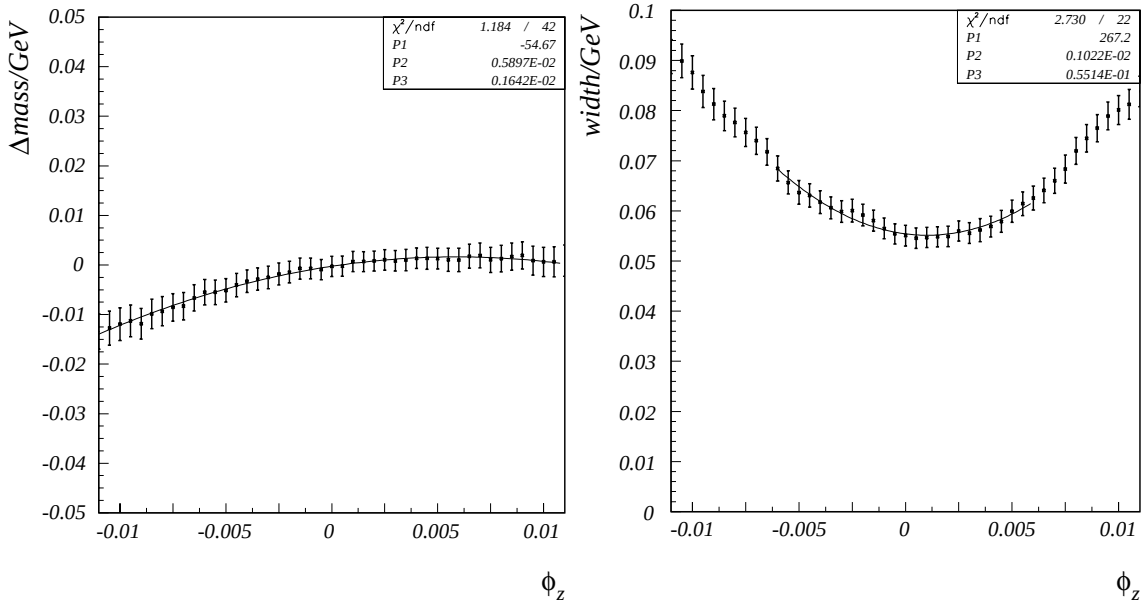

(a) (b)

Figure 3.10: Variation of the mass (a) and the width (b) of J/Ψ peak with changing the angle of rotation around z axis, φ_z, of the OTR. The angles necessary for the same effect on the width as the shearing transformation in dt_x are typically 10 times larger.

In the following I will estimate the effect of the transformations on the two body decay invariant mass. Denoting the 4-momentum of the first track by $p_1^\mu = (E_1, \vec{p}_1)$ and the second by $p_2^\mu = (E_2, \vec{p}_2)$, the invariant mass of the system is $M^2 = (E_1 + E_2)^2 - (\vec{p}_1 + \vec{p}_2)^2$. In case of $J/\Psi \rightarrow \mu\mu$ and $J/\Psi \rightarrow ee$ the mass of the two particles produced is much smaller than its momentum ($m_{1,2} << \vec{p}_{1,2}$). Because of the relatively large Lorentzian boost factors of the particles produced in the HERA-B, the opening angle is also small, such that the mass of J/Ψ candidate can be approximated with the following formula:

$$M^2 = p_1 p_2 \vartheta^2, \tag{3.3}$$

where ϑ is the opening angle between the two tracks, and p_1, p_2 are their momentum magnitudes. The momenta of the tracks are determined by the kink angle, i.e. the difference in slopes in OTR and in VDS ($t_{x_{OTR}} - t_{x_{VDS}}$). They are thus affected by shearing and stretching transformations of the components, which both change the t_x of the segments. On the other hand, the momenta are not affected at all by other global transformations, and the misalignment in the other parameters would just reduce the matching efficiency, or would require wider matching cuts. The opening angle ϑ is determined by VDS only. Multiple scattering in VDS contributes to the error in determination of the opening angle, and along with the multiple scattering in the tracker also contributes to wrong momentum assignment. The global transformations of shearing and stretching change only the momenta of the tracks which are determined by the kink angle φ:

$$\frac{1}{p} = \frac{q\varphi}{e\int_{Z_{min}}^{Z_{max}} B \cdot dz}, \tag{3.4}$$

where q denotes the charge of the particle.

If the shearing transformation is done to the whole OTR, the magnitude of momentum p of a single track will change in the following way due to the change in the kink angle ($d\varphi = dt_x$):

$$\frac{dp}{p} = -\frac{qp \cdot dt_x}{e\int_{Z_{min}}^{Z_{max}} B \cdot dz}$$

and thus the formula for the mass (3.3) becomes:

$$M^2 = M_0^2 \left(1 - \frac{q_1(p_1 - p_2)dt_x}{e\int_{Z_{min}}^{Z_{max}} B \cdot dz}\right) \tag{3.5}$$

where $M_0^2 = p_1 p_2 \vartheta^2$.

It can be assumed that the distribution of $p_1 - p_2$ is symmetric around 0. because the positive and negative particles have approximately the same momentum distributions (dN/dp). Because of that, the mean of the mass distribution does not change with changing the t_x of the OTR (in the first order approximation). In the mass formula (3.5) the momentum of the second track can be replaced with a function of the momentum of the first track:

$$p_2 = \frac{M_0^2}{p_1 \vartheta^2}$$

which gives us for the mass formula the following:

$$M^2 = M_0^2 \left(1 - \frac{q_1(p_1 - \frac{M_0}{p_1 \vartheta^2})dt_x}{e\int_{Z_{min}}^{Z_{max}} B \cdot dz}\right)$$

The width is narrowest when the OTR is in the nominal position. Any shear for dt_x out of this position would broaden the mass distribution. For results using real data see Fig. 3.28.

In case of stretch in the z direction for a factor of $f_z = 1 + df_z$, the momentum of a track changes in the following way:

$$\frac{dp}{p} = df_z$$

The mass of the resonance increases when the detector is stretched and decreases when the detector is shrunk:

$$M^2 = M_0^2(1 + 2df_z)$$

In case only the part behind the magnet (OTR) is stretched and the part in front of the magnet (VDS) is untouched the effect is just two times smaller (for the results see 3.4.4). The width of the mass distribution does not change noticeably with stretching:

$$\sigma_M \approx \sigma_{M_0}$$

The rotation around the z axis also changes the momentum slightly. In case the OTR on the downstream side of the magnet is rotated for a certain small angle φ_z the slope $t_{x_{OTR}}$ changes as $t_{x_{OTR}} = \cos(\varphi_z)t^0_{x_{OTR}} + \sin(\varphi_z)t^0_{y_{OTR}} \approx t^0_{x_{OTR}} + \varphi_z t^0_{y_{OTR}}$. The kink angle changes for the same amount, thus the momentum of each track changes according to the following formula:

$$\frac{dp}{p} = -\frac{p \cdot dt_y \cdot \varphi_z}{e\int_{Z_{min}}^{Z_{max}} B \cdot dz}$$

The mass formula (3.3) changes due to the change in the track momenta:

$$M^2 = M_0^2 \left(1 - \frac{(p_1 \cdot t_{y_1} + p_2 \cdot t_{y_2})\varphi_z}{e\int_{Z_{min}}^{Z_{max}} B \cdot dz}\right) \tag{3.6}$$

Again it can be assumed that the distribution of $p_1 \cdot t_{y_1} + p_2 \cdot t_{y_2}$ is symmetric and that the rotation around z does not change the mass of the reconstructed J/Ψ candidate (in the first order approximation). The results of changing the rotation angle on the data are presented in Figs. 3.10(a) and 3.10(b).

In the lowest order, when the momentum is determined only based on the kink of the track in the magnetic field, other global transformation (dx, dz, dy and dt_y) do not change the mass distribution. They only change the amount of right and wrong matches because the matching is based on these variables. In the real reconstruction, the momenta of tracks are obtained from the track fit, and may change with the transformations mentioned at the beginning of the paragraph (dx, dz, dy and dt_y). This effect is of higher order and if the procedure of global alignment is repeated a few times it converges to the nominal position.

3.4 Analysis of the data

3.4.1 Reference plots for methods 1 and 2

There exists a large set of possible residual distributions, among which it is very important to find the distributions which give us the most information about shifts of the component. It is also essential that the distribution is clean and can be fitted well. The shifts were determined from the following correlation reference plots (Fig. 3.11, 3.12):

1. Difference in the t_x of the Runge-Kutta track (see Section 3.3.2) and the t_x of the OTR segment, versus the t_x of the Runge-Kutta track. This determines the relative dx and φ_z of the components on each side of the magnet.

2. Difference in y of VDS and OTR segments at $z = 750$ cm. The dy was determined.

3. Difference in t_y of the Runge-Kutta track and OTR segment versus the t_x of the OTR segment. The relative VDS-OTR dt_y, φ_z can be determined.

4. Difference in x of OTR segment and ECAL cluster versus x of the ECAL cluster. A hint about the OTR dt_x and f_z compared to the ECAL is obtained. The parameters are very dependent on the determination of z coordinate of the cluster, which has bad resolution.

5. The z of intersection of the VDS and OTR segments versus inverse kink angle. Relative VDS-OTR dx and dz can be determined.

6. Difference in t_x of the Runge-Kutta track and OTR segment versus t_x of the OTR segment. The relative VDS-OTR dx and dz can be determined.

Each reference plot (either for the whole OTR or just for one side) gives us two parameters: the slope k and the value at $x = 0$, the neutral term n. Both are connected with displacements, as indicated in the table below, and illustrated in App. A.

plot no.	slope k	neutral term n
1	$k = 1.5 \cdot (\mathbf{d}\varphi_\mathbf{z})_{\mathbf{OTR-VDS}}$	$n = 0.0034 \cdot \mathbf{dx}_{\mathbf{OTR-VDS}}$
2		$n = -\mathbf{dy}_{\mathbf{OTR-VDS}}$
3	$k = (\mathbf{d}\varphi_\mathbf{z})_{\mathbf{OTR-VDS}}$	$n = (\mathbf{dt_y})_{\mathbf{OTR-VDS}}$
4	$k = 1 - (\mathbf{f_z})_{\mathbf{OTR-ECAL}}$	$n = 890 \cdot (\mathbf{dt_x})_{\mathbf{OTR-ECAL}}$
5	$k = \mathbf{dx}_{\mathbf{OTR-VDS}}$	$n = \mathbf{dz}_{\mathbf{OTR-VDS}}$
6	$k = 0.0034 \cdot \mathbf{dz}_{\mathbf{OTR-VDS}}$	$n = 0.0034 \cdot \mathbf{dx}_{\mathbf{OTR-VDS}}$

Table 3.1: Relations between the linear fit parameters (k and n) and different parameters of component transformations.

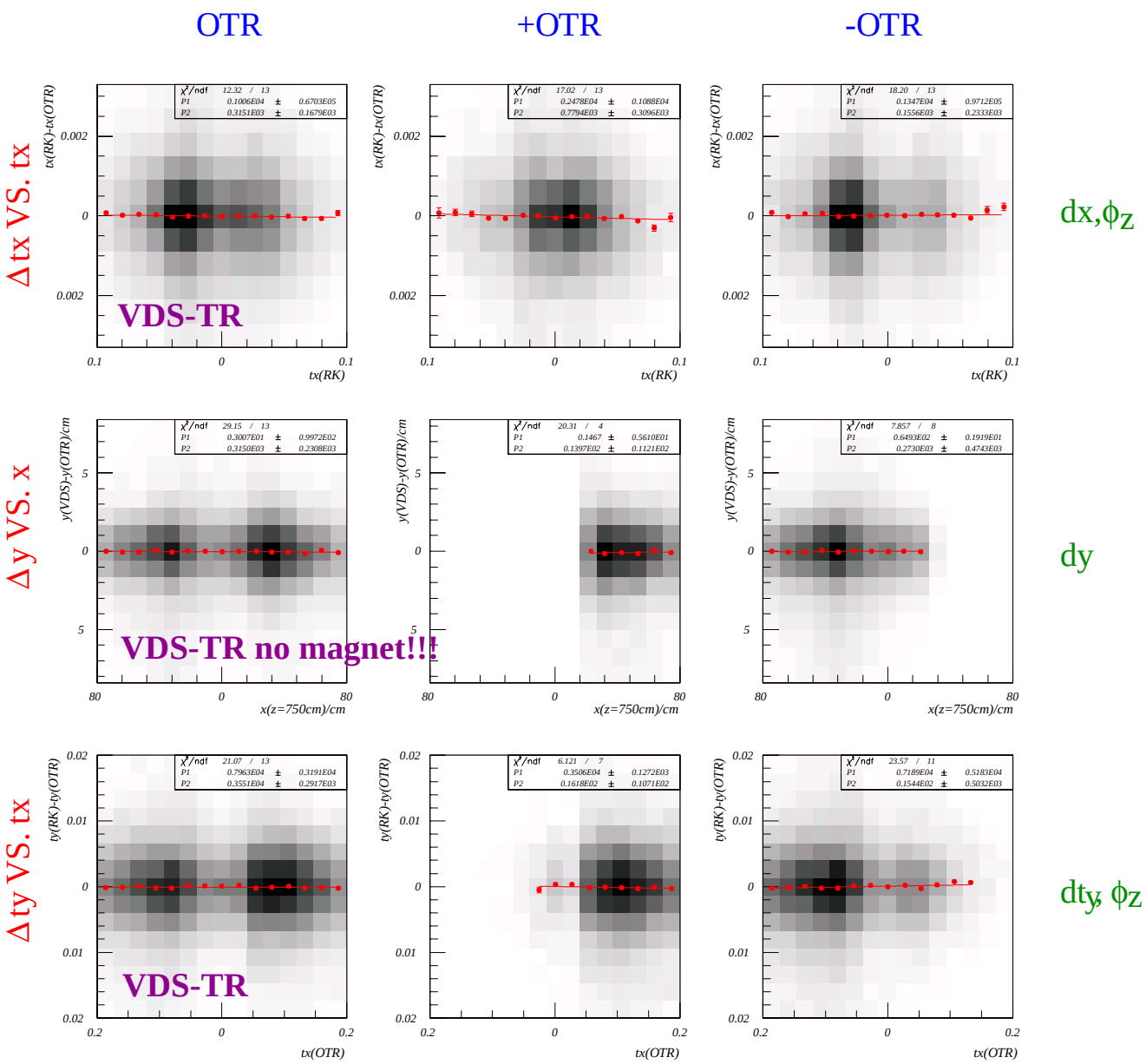

Figure 3.11: Reference plots 1-3. The Monte Carlo simulated data were used to produce these plots. From the errors of the fits to the two parameters of the linear function, the limit of the reachable accuracy of methods 1 and 2 can be estimated. 25000 events were used to produce these plots. See also Table 3.1. 'No magnet' label on plots means that that the plot was obtained with direct comparison of the two segments, and no magnet propagation was used.

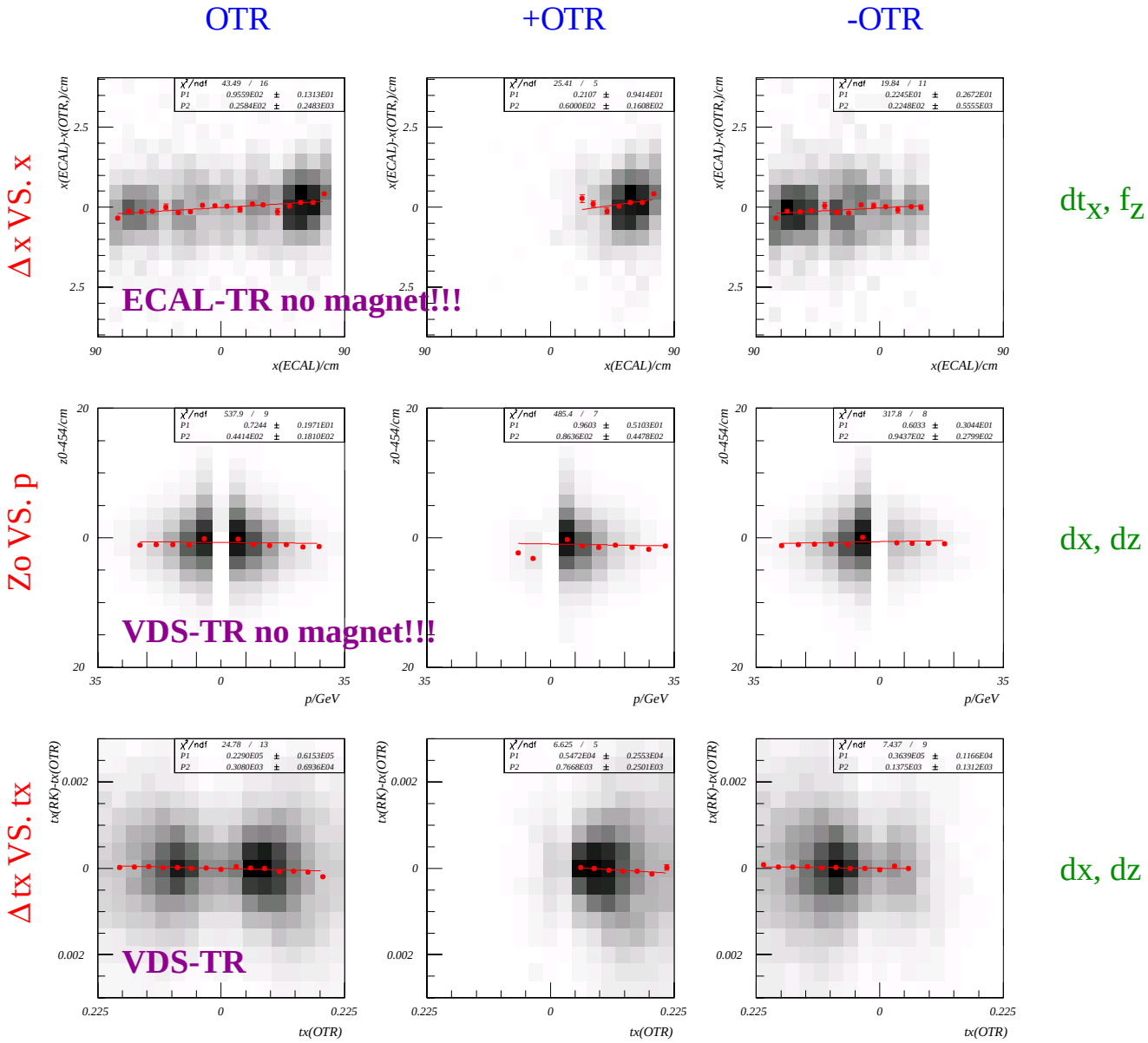

Figure 3.12: Reference plots 4-6. See also Table 3.1.

3.4.2 Fitting

For fitting of the 2 dimensional distribution corresponding to a certain reference plot separate vertical slices were fitted with a Gaussian function plus a polynomial (usually a linear function). The fitted means and r.m.s. widths of the Gaussians in each slice define points, trough which a strait line was fitted. Uncertainty of the fit comes mainly from limited statistics. By increasing the statistics the errors on the parameters would of course be reduced. Usually a sample of a few times 10000 events was taken, which suffices for the accuracy of the parameters as mentioned in Section 3.4.3.

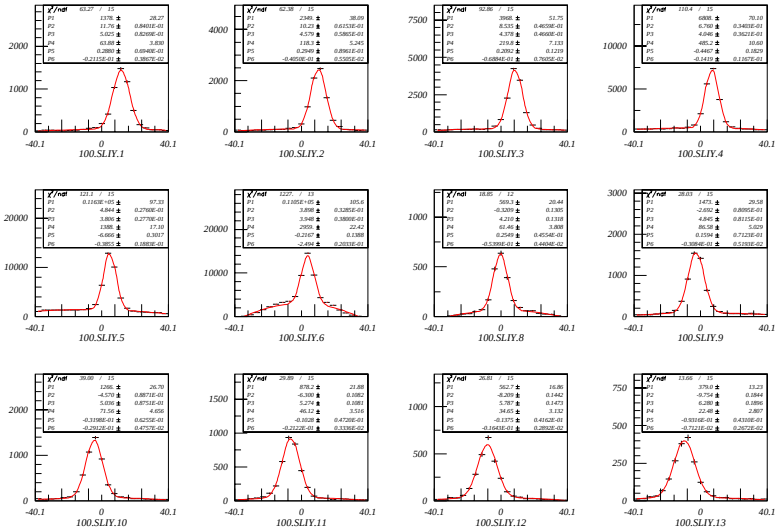

Figure 3.13: Fitted single vertical slices of the two dimensional distribution in Fig. 3.14. The results of the fits ate displayed together with a distribution in Fig. 3.14.

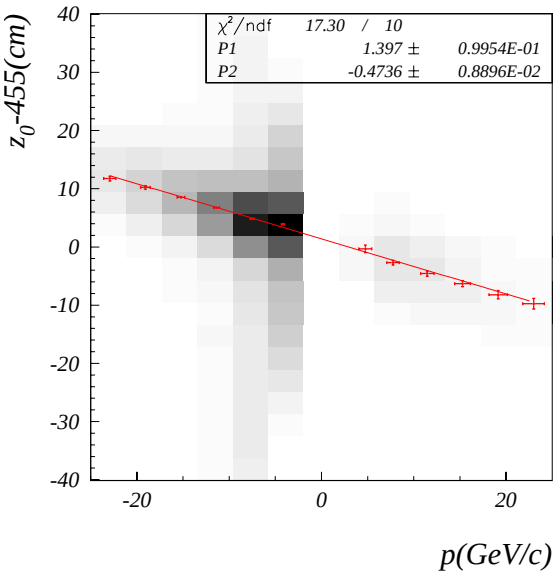

Figure 3.14: An example of fitting of two dimensional distribution.

3.4.3 Checks of the methods 1 and 2 on the MC simulated data

To test our algorithms, a misaligned MC data sets were required. The misalignment was introduced in the following way: simulated track intersection points with detector planes (technicaly known as MIMP's) were moved for chosen amounts in certain directions. Then these points were digitized, reconstructed, and analyzed. The shifts calculated in this way agree with the shifts that were introduced very well. It was also proved that the shifts are quite independent of each other, i.e. the shift or slope in a given reference plot is caused by a single transformation only (see also Table 3.1).

For example, in the first test, the whole OTR (the MIMP's) was moved for 0.3 cm in x. The plots change very drastically. By comparing the fitted constants of the shifted MC (Fig 3.16) to those of the nominal MC (Fig. 3.15) the shifts were calculated, for which the OTR should be moved. The only nonzero shift so calculated is the shift dx which is calculated to be from 0.297 cm to 0.300 cm for different measurements, i.e. from different distributions (error of the fit is below 0.005 cm). All other parameters determined in this way are below the error obtained from the fit.

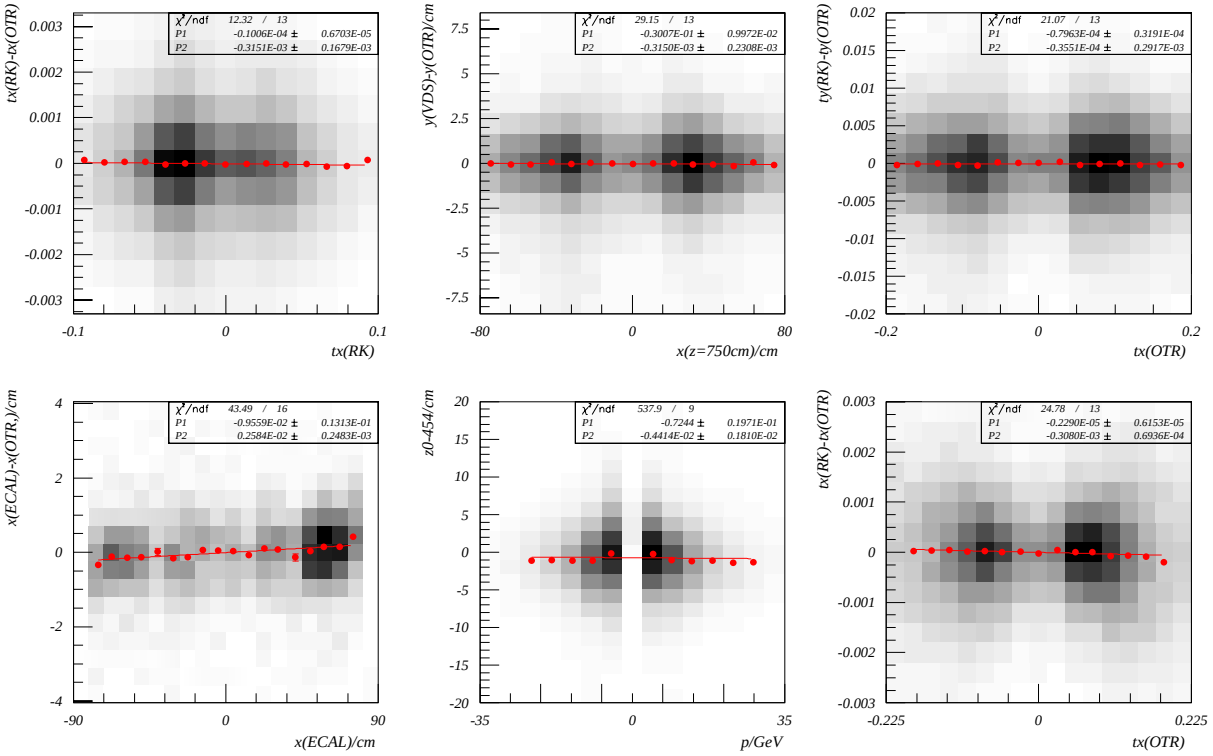

Figure 3.15: Reference plots for ideal, nominal MC data set. Only OTR is compared with VDS. For ITR plots look very similar, the difference being mainly in the scales. Only the plots for whole OTR are shown.

There existed some worries that transforming the +OTR and −OTR parts (see Fig. 3.3) separately is analogous to some other transformation which acts on the OTR as a whole. To disprove that, the shifts were applied to −OTR only (for an exaggerated shift of $+0.3$ cm and

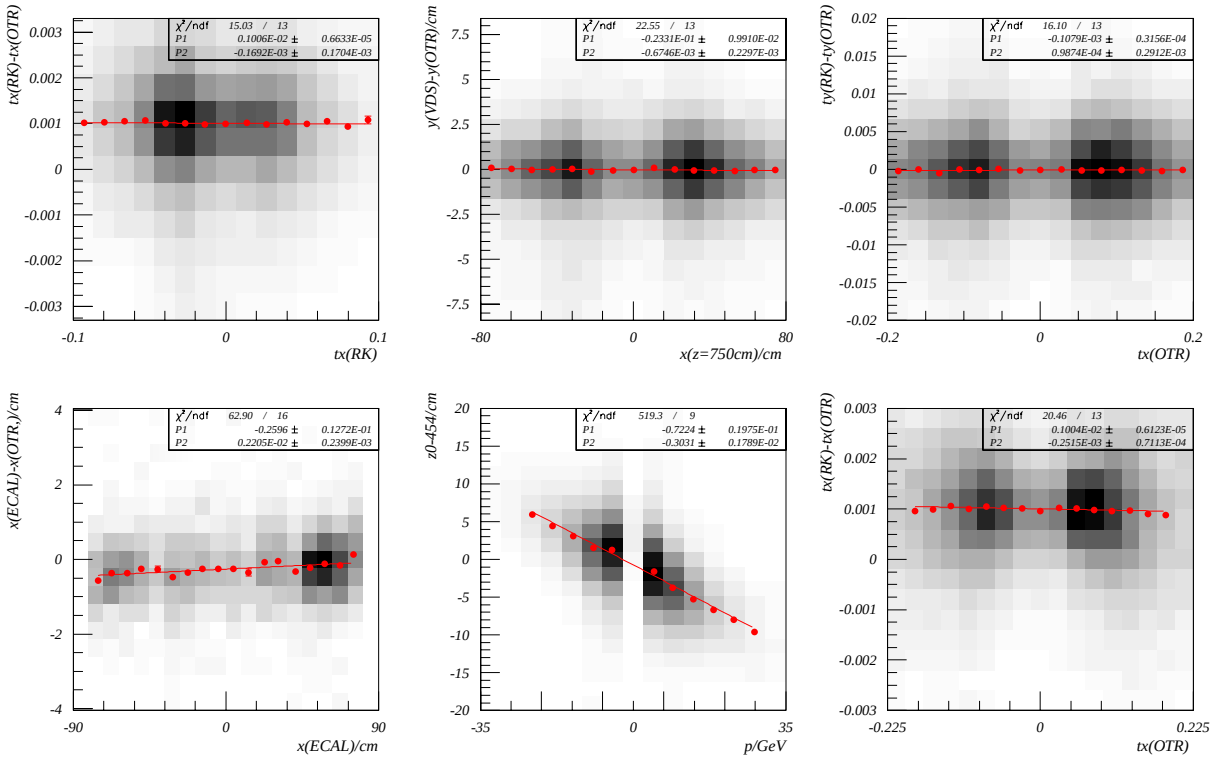

Figure 3.16: Reference plots for the MC data set shifted for 0.3 cm in x. Only the plots for whole OTR are shown.

for a more realistic $+0.03$ cm). The exaggerated shift once again is only for the illustrative purposes in order to see the effect of the shift by observing the plots and not for studying the fit numbers. With the smaller shift one has to study the numbers carefully.

From Figs. 3.17 and 3.18 one can see that the reference plots for the +OTR part do not get spoiled and the plots for $-$OTR give exactly the shift of this part of the detector. It is also obvious that the misalignment of one half can be corrected by moving the whole detector for a sort of an average shift. The average is closer to $-$OTR shift than to +OTR shift because the $-$OTR occupies more than half of the phase space covered by OTR. Of course, if the whole OTR would be corrected for an average shift, the difference between +OTR and $-$OTR would remain the same.

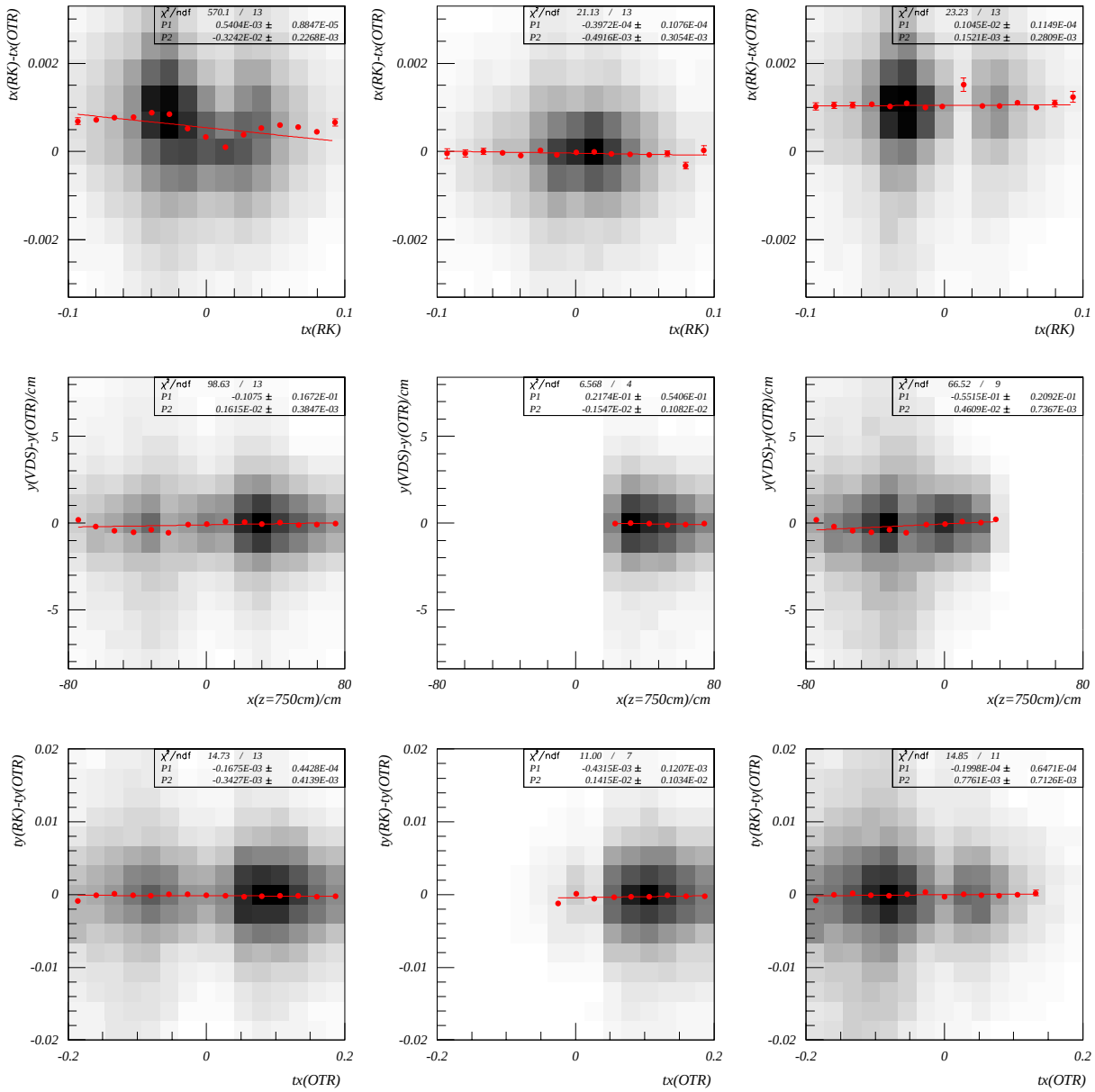

Figure 3.17: Reference plots 1-3. In the MC simulated data the $-$OTR is shifted for 0.3 cm in x. The first column $-$ all tracks, second column $-$ only tracks going to the +OTR region, third column $-$ only tracks going to the $-$OTR region.

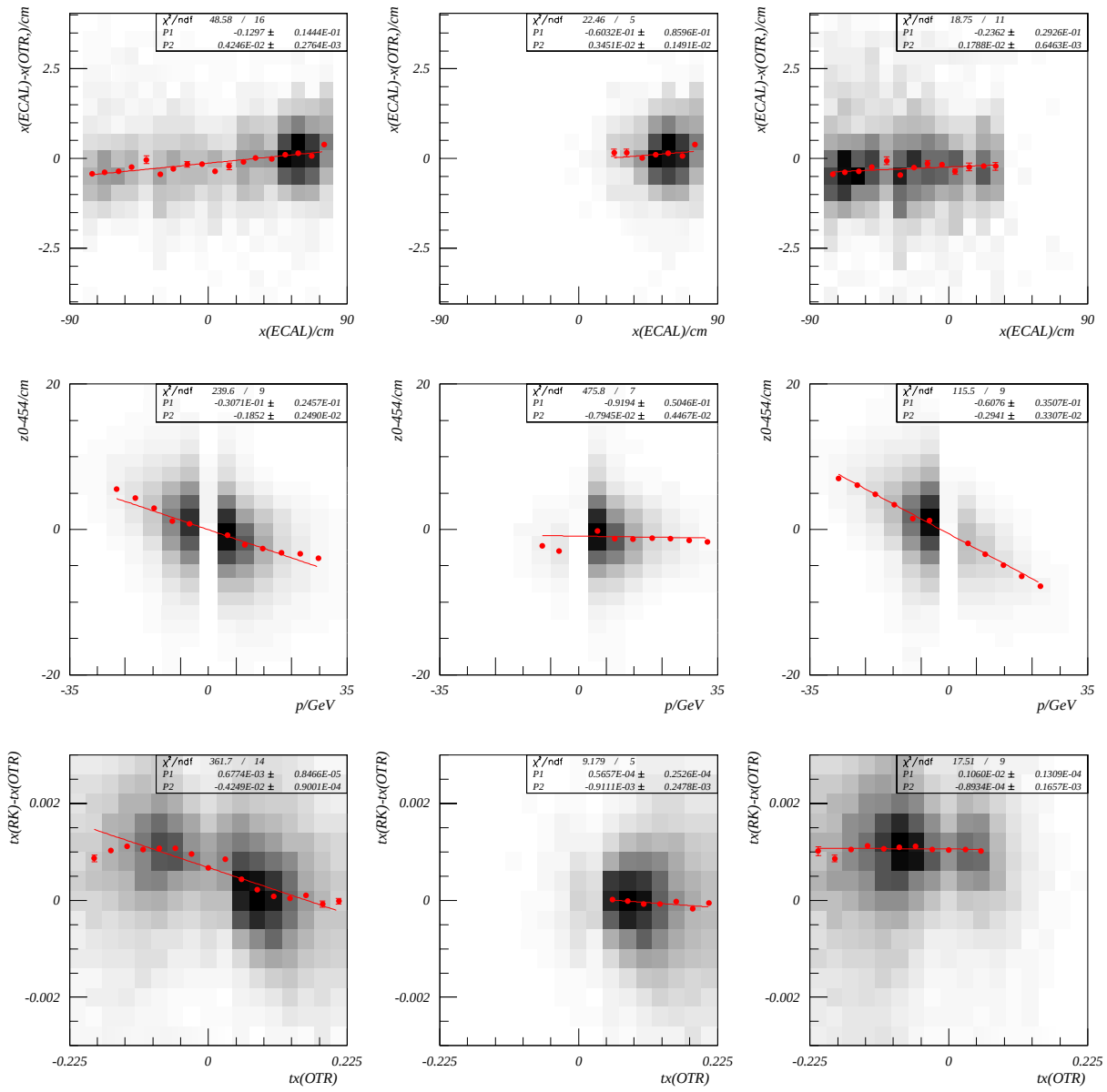

Figure 3.18: Reference plots 4-6. In the MC simulated data the $-$OTR is shifted for 0.3 cm in x. The first column – all tracks, second column – only tracks going to the +OTR region, third column – only tracks going to the $-$OTR region.

Accuracies of determined global alignment parameters From the reference plots 12 fit parameters are obtained, when OTR is not split into two halves, +OTR and −OTR, and 24 fit parameters in case the OTR is split. From these fit parameters the shifts of the components can be approximately determined. The determined shifts are burdened with errors which they inherit from the parameters of the fit. In the following table the shifts and their accuracies are shown (for a sample of 25000 Monte Carlo simulated events).

plot no.	shift	OTR	+OTR	−OTR	final effect on J/Ψ
1	$dx_{OTR-VDS}$	0.004 cm	0.006 cm	0.004 cm	$---$
	$d\phi_{zOTR-VDS}$	$0.3\ 10^{-3}$	$0.5\ 10^{-3}$	$0.4\ 10^{-3}$	negligible
2	$dy_{OTR-VDS}$	0.02 cm	0.1 cm	0.04 cm	$---$
3	$dt_{yOTR-VDS}$	$0.06\ 10^{-3}$	$0.2\ 10^{-3}$	$0.1\ 10^{-3}$	$---$
	$d\phi_{zOTR-VDS}$	$0.6\ 10^{-3}$	$2.\ 10^{-3}$	$1.\ 10^{-3}$	negligible
4	$dt_{xOTR-ECAL}$	$0.03\ 10^{-3}$	$0.2\ 10^{-3}$	$0.06\ 10^{-3}$	negligible
	$df_{zOTR-ECAL}$	$0.5\ 10^{-3}$	$3.\ 10^{-3}$	$1.\ 10^{-3}$	$\Delta M \approx 1$ MeV
5	$dx_{OTR-VDS}$	0.004 cm	0.009 cm	0.006 cm	$---$
	$dz_{OTR-VDS}$	0.04 cm	0.1 cm	0.06 cm	$---$
6	$dx_{OTR-VDS}$	0.004 cm	0.015 cm	0.007 cm	$---$
	$dz_{OTR-VDS}$	0.04 cm	0.1 cm	0.08 cm	$---$

Table 3.2: The accuracies as determined form the fitted parameters based on different reference plots from Figs. 3.11 and 3.12. The accuracy of adjusting the whole OTR as well as the accuracy of adjusting only one side (-OTR or +OTR) is shown. In the last column the impact on the J/Ψ peak of changing the parameter for the amount in the 3rd column is specified. The only parameters that affect the J/Ψ peak are dt_x, df_z and φ_z, the others affect the process of matching only.

3.4.4 Real data 2000

In this section the results obtained with the data acquired in the summer of 2000 will be presented. First, the improvement based on the first two methods described in Sections 3.3.1 and 3.3.2 will be presented. Only the results obtained with the outer part of the main tracker (OTR) will be shown for illustration. Next, the improvements based on the third, momentum based, method will be shown.

Results with the methods 1 and 2 For an orientation of the improvement of the global alignment using the methods 1 and 2 the reference plots for run 16784 are shown in Figs. 3.19 and 3.20 for the original knowledge of the global alignment (known as the key 0 version of the alignment database) and in Figs. 3.21 and 3.22 for the last global alignment version (which corresponds to key 17), used also for the third reprocessing. On the plots in this paragraph only the hits in OTR were used, the reconstruction of the ITR was totally switched off. The local alignment and calibration is in both cases kept constant and corresponds to the best knowledge of key 17. Run 16784 is a di-lepton run from the summer 2000 data-taking. The mentioned comparison would make perfect sense if none of the internal alignments or calibrations would depend on the global alignment. This is not true especially in the case of determining the $r(t)$ where global tracks (VDS-OTR tracks) are used. It is still believed that the given picture reflects the improvements due to global alignment more accurately than when comparing the results obtained using key 0 for all the calibration and alignment with the results obtained with key 17. In such a way the net improvement due to all changes in alignment and calibration would be obtained.

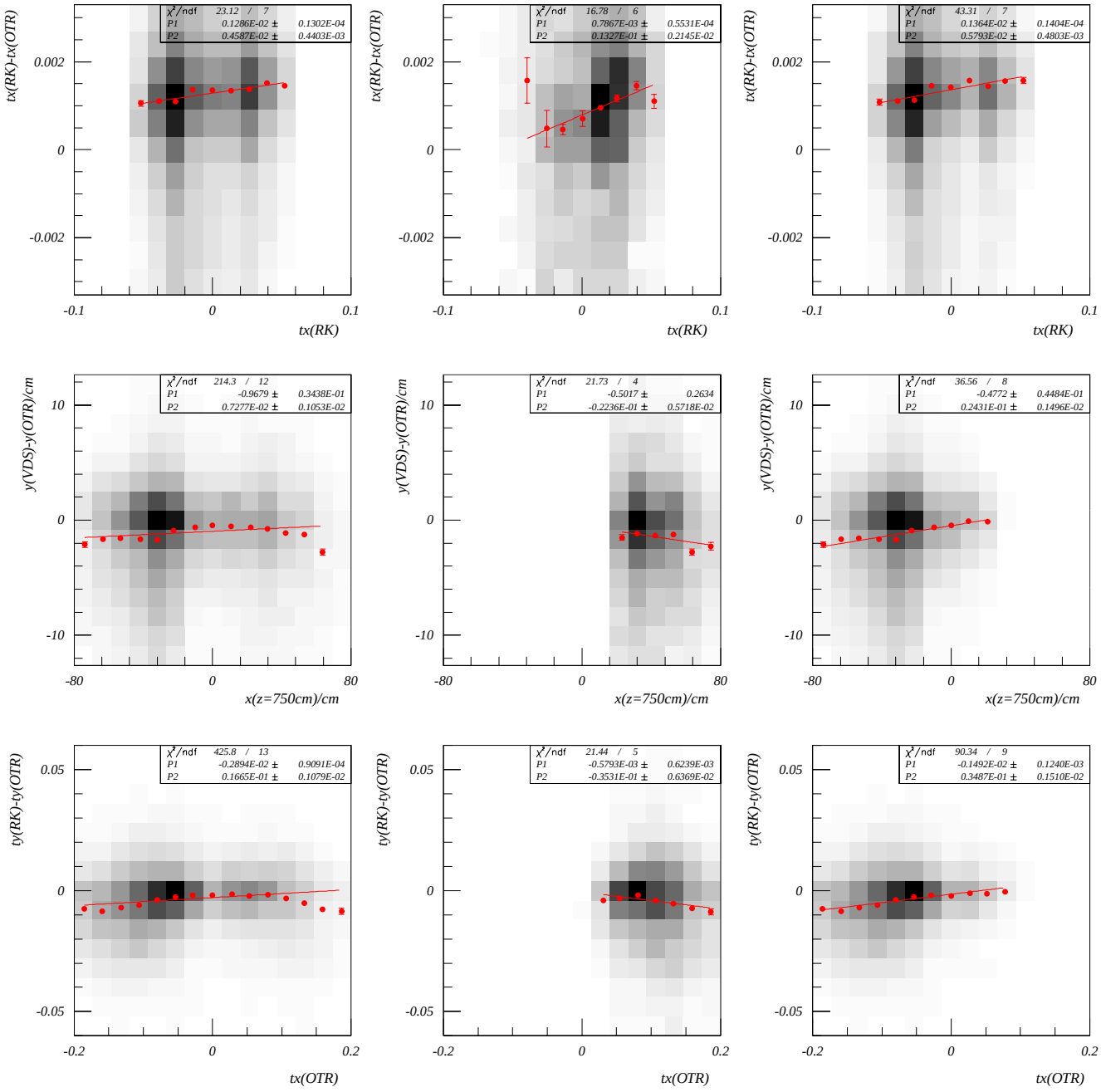

Figure 3.19: The first three reference plots for the run 16784 using key 0 for the global alignment. The local alignment and calibration assume key 17. The ITR reconstruction is switched off.

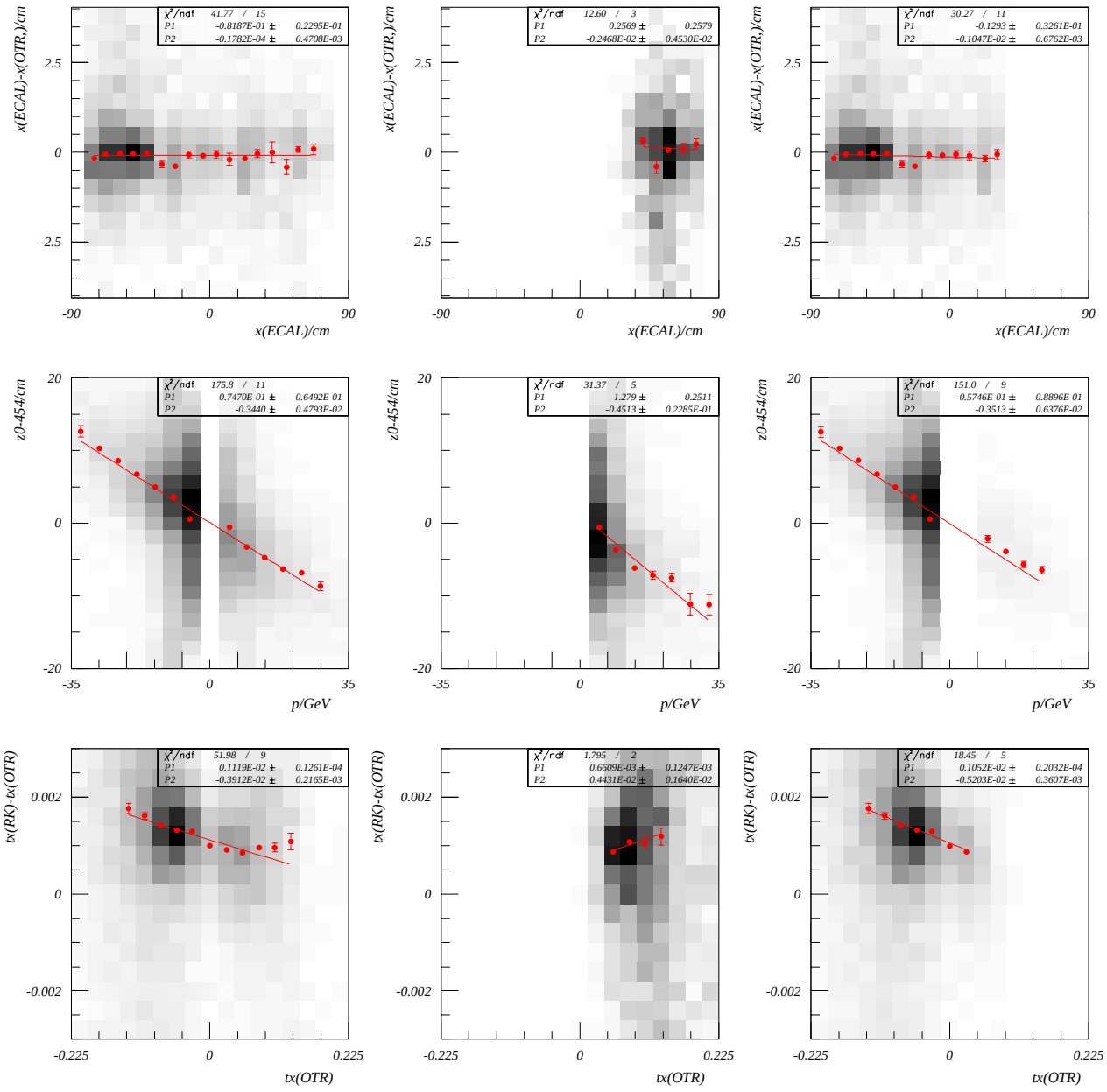

Figure 3.20: The second three reference plots for the run 16784 using key 0 for the global alignment. The local alignment and calibration assume key 17.

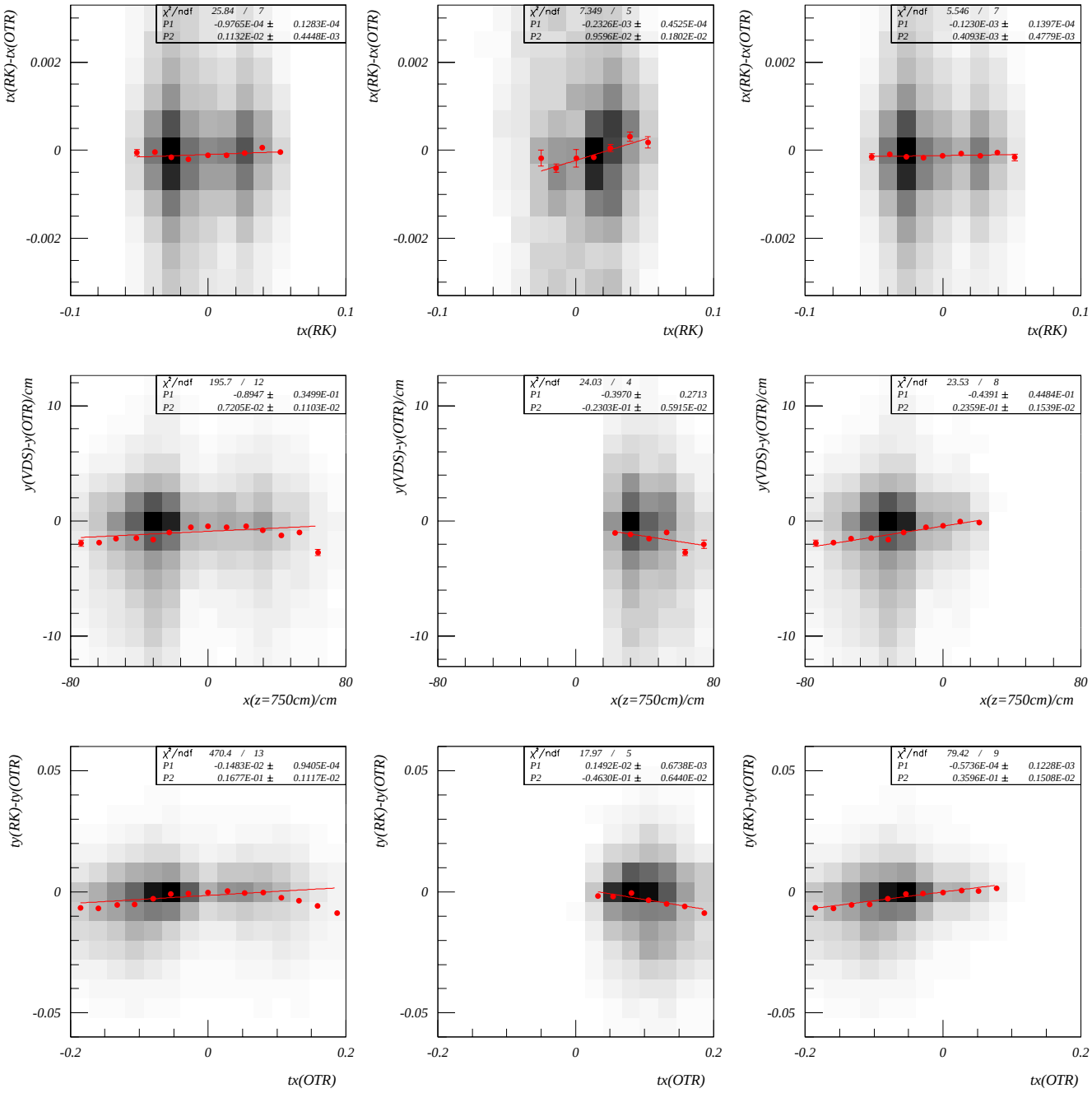

Figure 3.21: The first tree reference plots for the run 16784, using the new global alignment of key 17. The biggest improvement compared to Fig. 3.19 is especially visible in t_x change (the upper three plots).

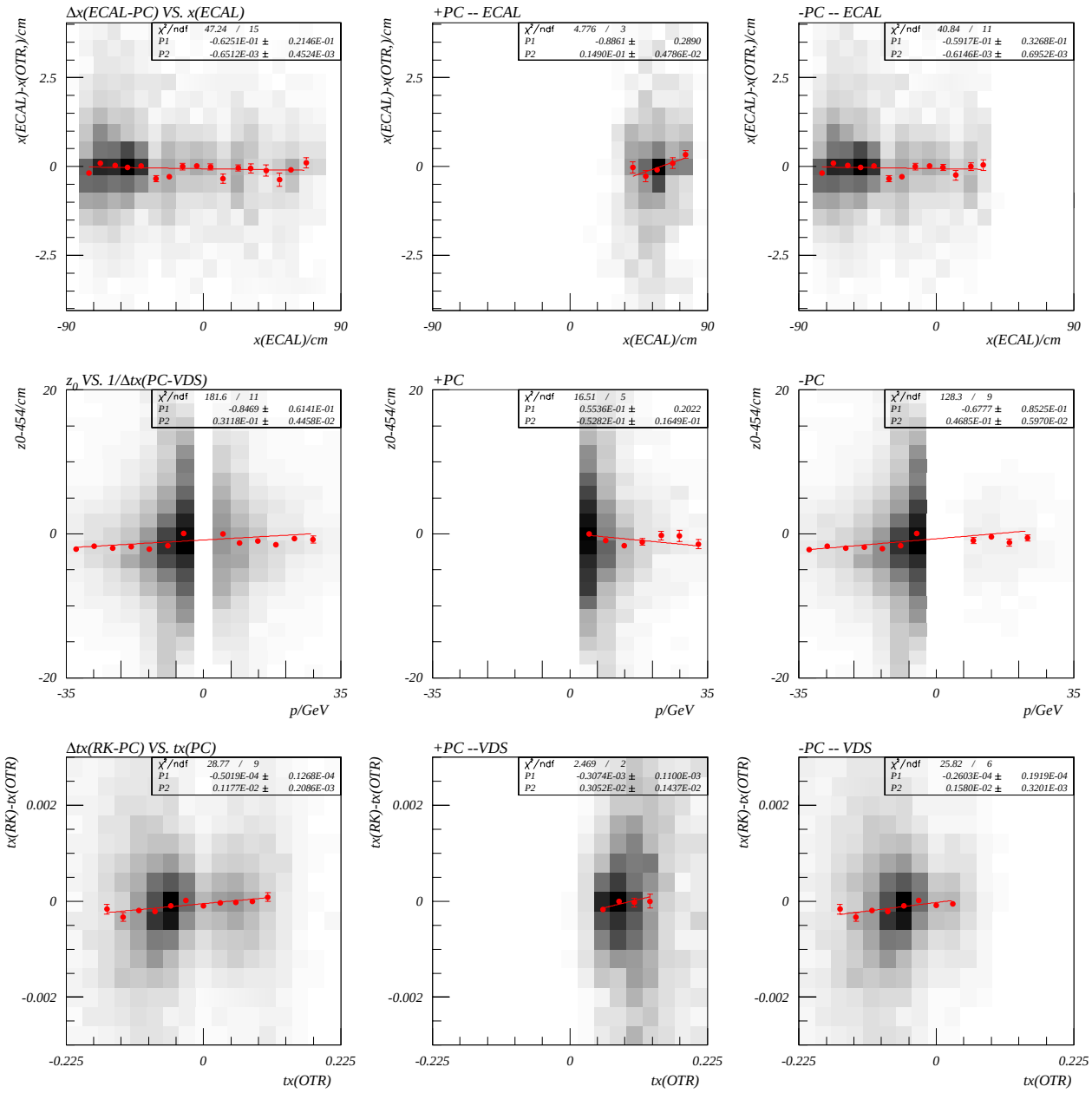

Figure 3.22: The second tree reference plots for the run 16784, using the new global alignment of key 17. The biggest improvement compared to Fig. 3.20 is especially visible in the lower six plots, due to x and z corrections. The upper three plots which show matching of OTR with ECAL stay unspoiled.

Physical signals In this section I show the impact on the J/Ψ signal by changing the t_x and f_z of the OTR which is divided into +OTR and $-$OTR as shown on Fig. 3.3. The sample of J/Ψ mesons used contained approximately 2000 selected J/Ψ events. The sample was reconstructed with the best global alignment for that run at current knowledge (the same global alignment which corresponds to key 17 version of the database and was used for the 3rd reprocessing).

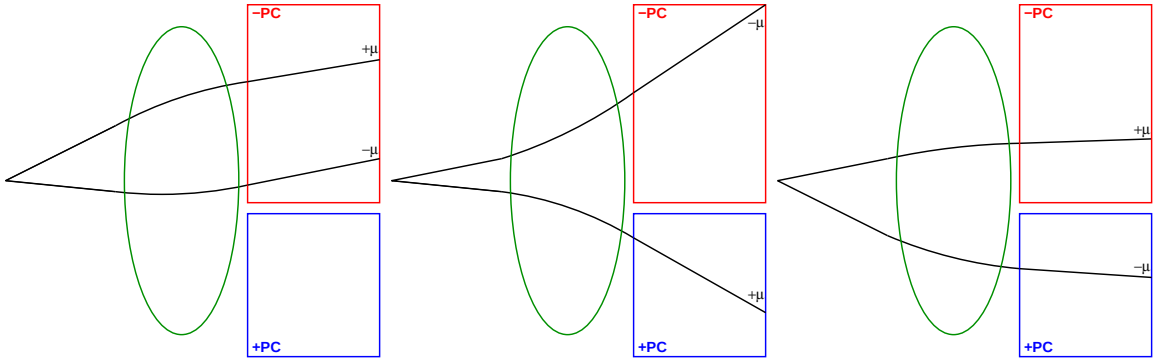

(a) (b) (c)

Figure 3.23: There are three subsamples of the J/Ψ sample with both muons having the hits only on one side of the OTR. They are: both muons are completely on the $-$OTR side (a), the negative muon going into $-$OTR and the positive into +OTR (b) and the case where the negative muon goes into +OTR and the positive into $-$OTR (c). There is virtually no events with both muons going into +OTR, because of its smaller size. There is also a lot of J/Ψ mesons where at least one muon crosses the border between the sides.

First the subsample of J/Ψ mesons was taken, which have all the hits (technically known as HITB's) belonging to both muon tracks in the -OTR side of the OTR (Fig. 3.23(a)). Changing the t_x changes mostly the with of the peak (see Fig. 3.24). The t_x was shifted for -0.3 mrad to hit the minimum of the width distribution (Fig. 3.24(b)). In the next stage the f_z parameter was changed for the same subsample. The $-$OTR was shrunk for a factor of approximately 0.997 (Fig. 3.25(a)). Following the above procedure the parameters dt_x and f_z were fixed for the $-$OTR part of the tracker. The changes in the parameters just mentioned are of the order of the error and are not significant.

In the next step another subset of J/Ψ mesons was considered, which decay into a $+\mu$ going into +OTR and $-\mu$ going in $-$OTR region of OTR (Fig. 3.23(b)). Again it was demanded that all the HITB's belonging to the track came from one side of the OTR part of tracker. Using the t_x and f_z of the $-$OTR as determined in the previous two steps, the t_x and f_z of the +OTR were changed, and the change of the mass and the width of the current sample was observed. The t_x was again fixed to minimize the width of the sample (Fig. 3.26(b)). Note also, that with changing the t_x of only one track and leaving the t_x of the other unchanged, mass changes a lot. To fit the width best, hardly any shift in t_x is needed. The mass is already very close to the nominal $m_{J/\Psi} = 3.097$ GeV. In the next step the f_z of the +OTR was changed to fit the nominal mass of the subsample. Almost no change in the f_z was needed (Fig. 3.27(a)).

In the procedure described quite some portion of the selected J/Ψ mesons was left out, e.g.

the sample where $+\mu$ goes into $-$OTR and $-\mu$ goes into +OTR region of OTR (Fig. 3.23(c)) and also all the J/Ψ mesons which decay into muons of which at least one hits both +OTR and $-$OTR. In the following two steps all the selected J/Ψ mesons were included and first the t_x of whole OTR was changed and then the f_z of the whole OTR to fit the best width and the nominal mass of the selection (Figs. 3.28 and 3.29).

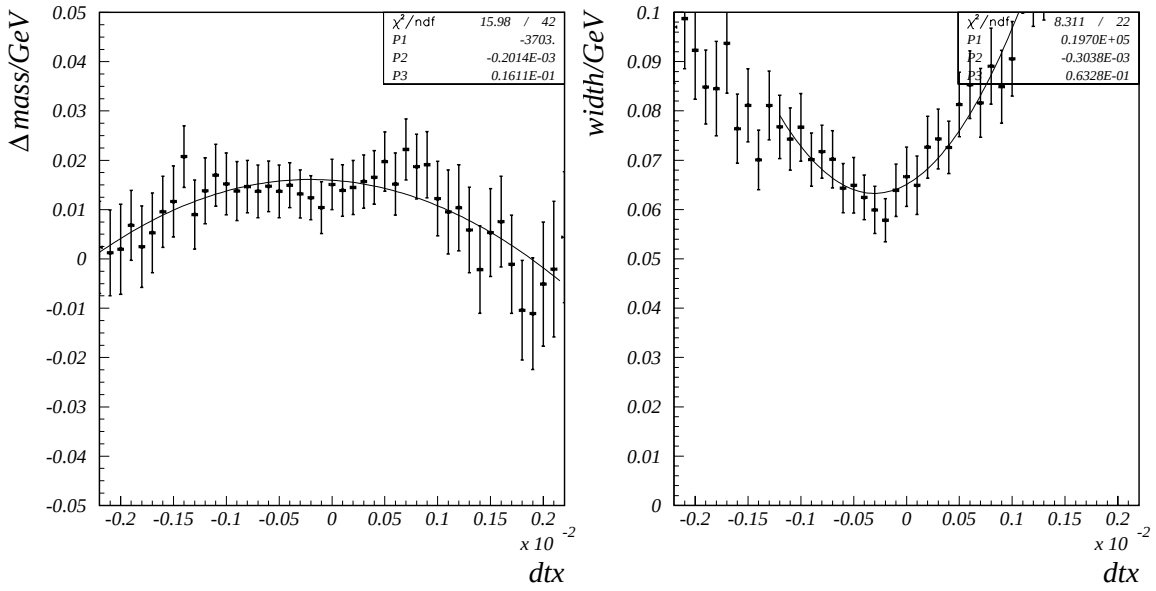

(a) (b)

Figure 3.24: Variation of the mass (a) and the width (b) of J/Ψ peak with changing the dt_x of the $-$OTR only. The subset of J/Ψ mesons is used with both muons having the hits in the $-$OTR only (Fig. 3.23(a)).

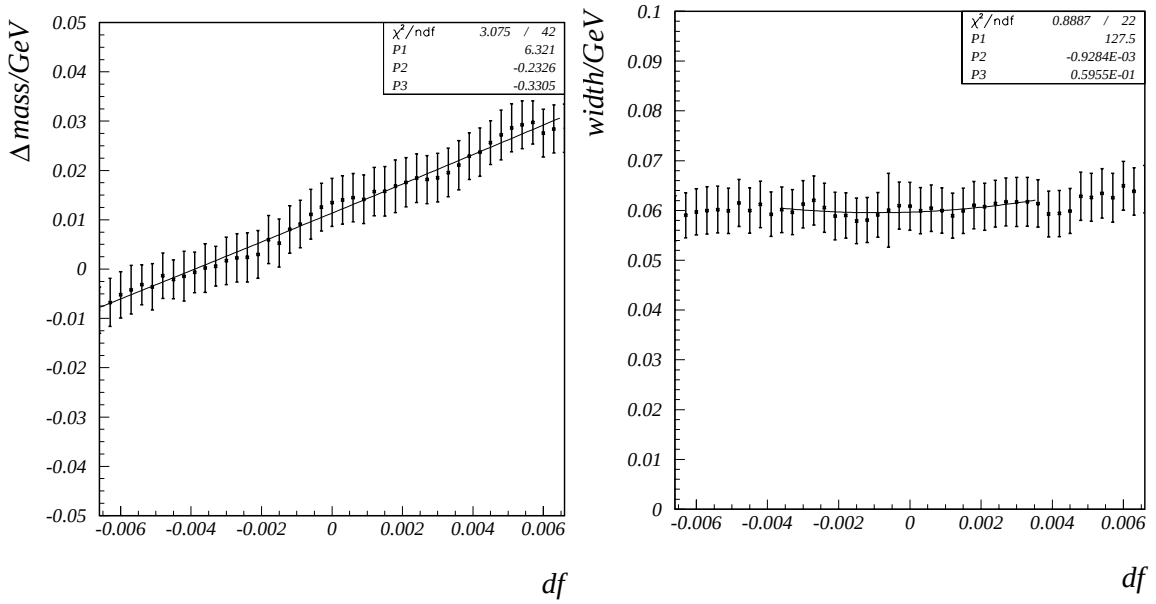

(a) (b)

Figure 3.25: Variation of the mass (a) and the width (b) of J/Ψ peak with changing the f_z of the $-$OTR only. The subset of J/Ψ mesons is used with both muons having the hits in the $-$OTR only (Fig. 3.23(a)).

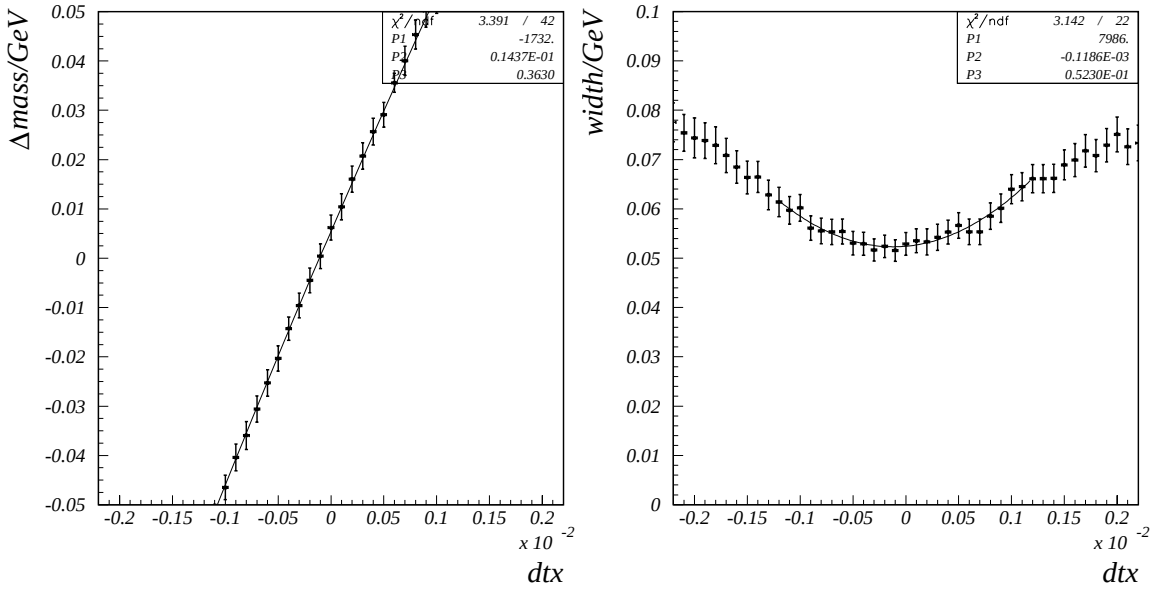

(a) (b)

Figure 3.26: Variation of the mass (a) and the width (b) of J/Ψ peak with changing the dt_x of the +OTR only. The subset of J/Ψ mesons is used which have the positive μ going to the +OTR and the negative going to the $-$OTR (Fig. 3.23(b)).

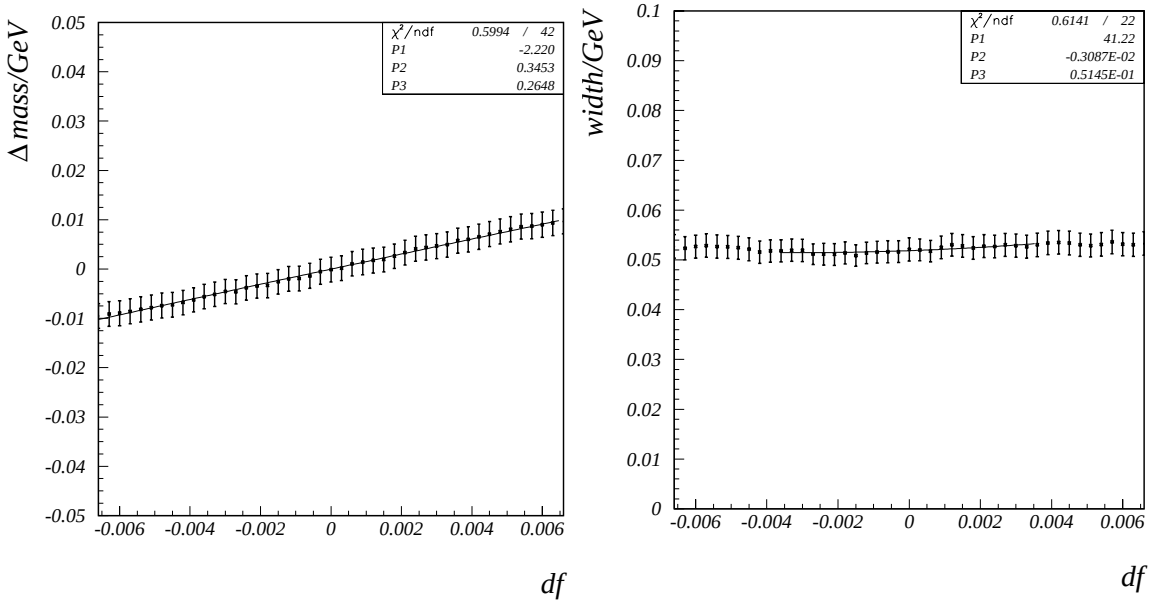

(a) (b)

Figure 3.27: Variation of the mass (a) and the width (b) of J/Ψ peak with changing the f_z of the +OTR only. The subset of J/Ψ mesons is used which have the positive μ going to the +OTR and the negative going to the $-$OTR (Fig. 3.23(b)).

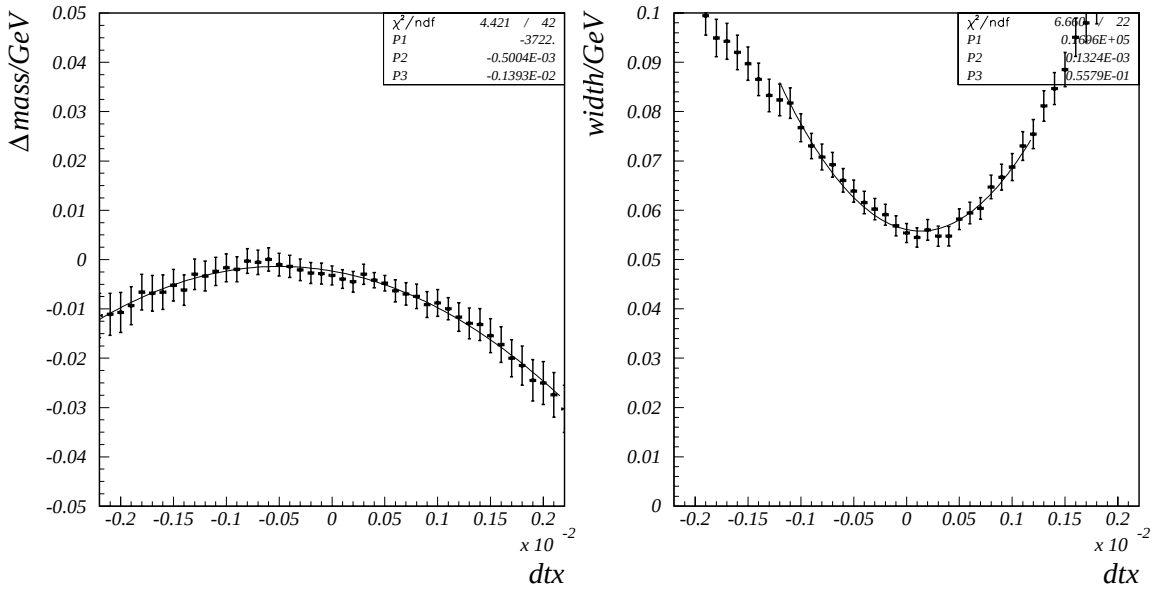

(a) (b)

Figure 3.28: Variation of the mass (a) and the width (b) of J/Ψ peak with changing the dt_x of the whole OTR. The whole selection of J/Ψ mesons is used.

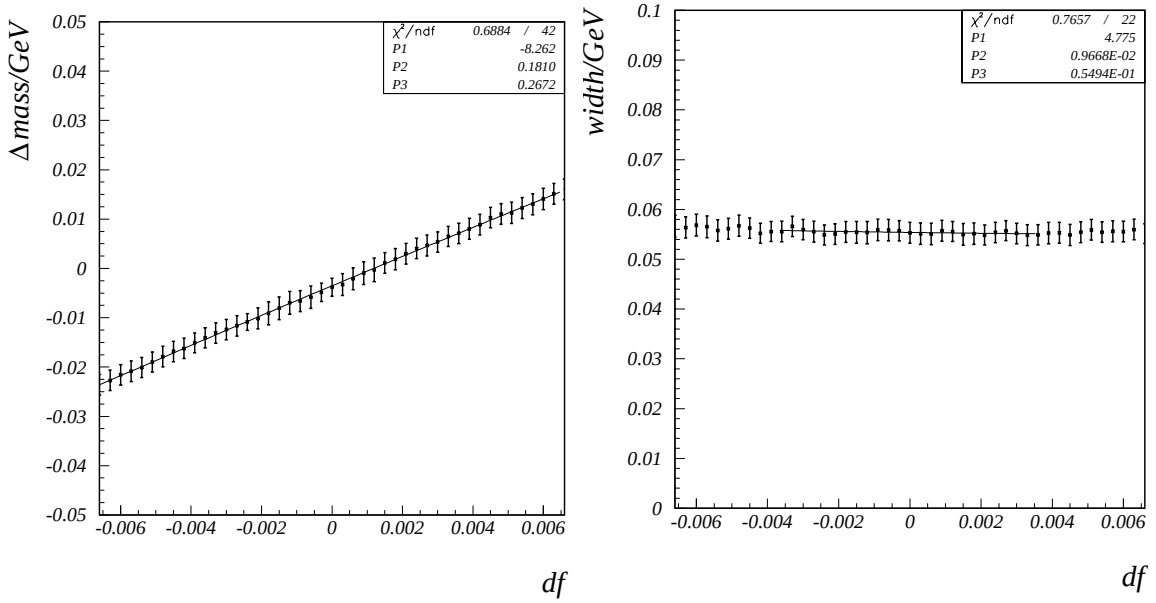

(a) (b)

Figure 3.29: Variation of the mass (a) and the width (b) of J/Ψ peak with changing the f_z of the whole OTR. The whole selection of J/Ψ mesons is used.

3.5 Alignment without magnetic field

In 2002 some data were taken with the magnet turned off. It turns out that the remnant field which is present in this case can be neglected. The complicated curved track geometry as discussed so far, is simplified in this case to straight lines. The procedure of alignment can be simplified and the whole HERA-B spectrometer aligned in one step. The clear advantages of such a procedure were illustrated already some time ago by using Monte Carlo simulated data [28], but the measurement was unfortunately carried out only recently. The improvement on real data is dramatic as can be seen from the comparison of Figs. 3.30 and 3.31. Fig. 3.30 shows how much the local alignment of the spectrometer, based on curved tracks, can be improved with global alignment, as discussed in this section. Fig. 3.31, on the other hand, shows the results obtained using the alignment based on the data taken in magnet off mode. This alignment was checked with the global alignment procedure, and no global shifts were found to be necessary to improve the reconstruction.

We conclude that it is of high importance to regularly perform alignment checks with data collected without magnetic field. The global alignment procedure with magnetic field, as described in this section should then be used for the alignment checks and improvements, especially in the long periods between the two adjacent data samples recorded with magnet turned off. It turns out that these periods should not be to frequent due to a complicated procedure of ramping down and up the magnetic field in the dipole magnet of the HERA-B spectrometer and also due to possible interference with the data taking of the other three experiments at the HERA accelerator.

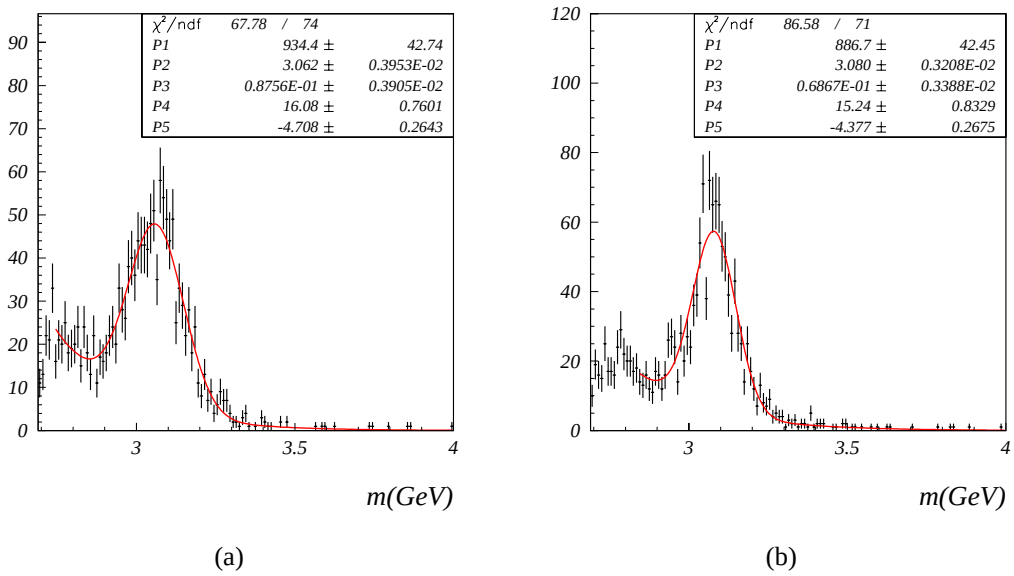

Figure 3.30: The invariant mass distribution for a sample containing J/Ψ meson decays. (a) corresponds to no global alignment corrections, while (b) corresponds to the globally aligned detector. The width ($\sigma = P3$) decreases when the global alignment is applied.

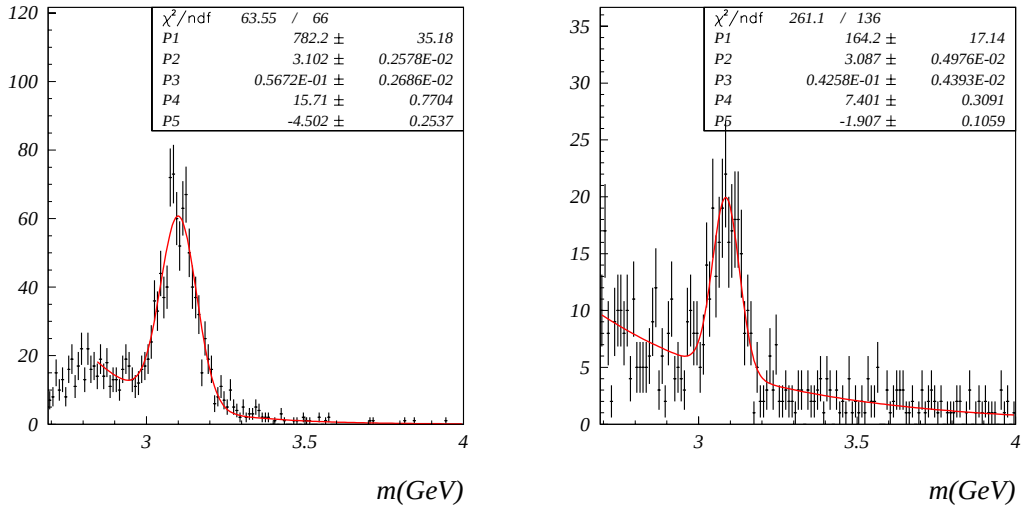

(a) (b)

Figure 3.31: (a) the same sample as in Fig. 3.30(a) was reprocessed with the alignment obtained based on the data taken with the magnet turned off. The slight decrease in the number of reconstructed J/Ψ's ($N = P1$) can be due to different alignment used for triggering and reconstruction. The width ($\sigma = P3$) is narrower than that in Fig. 3.30. (b) shows one of the recent data samples where already the alignment used for data taking was based on the magnet off data.

4 The performance of the RICH counter

4.1 Angular resolution

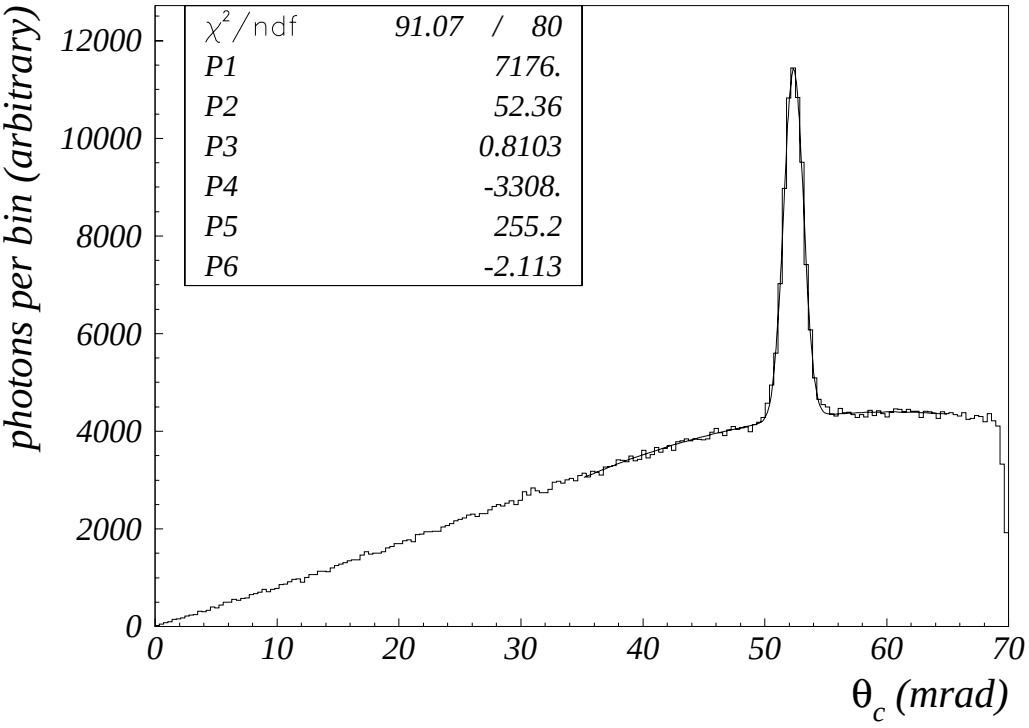

Figure 4.1: Single photon resolution for M16 PMTs: distribution of the measured Cherenkov angle for individual hits in the case of muons (from J/Ψ decays) with momenta above 40 GeV/c. The background below the peak comes from wrong track-photon combinations.

As already discussed in Section 2.6, one of the crucial parameters of the RICH counter is the resolution in the measurement of the Cherenkov angle of individual photons. This resolution was determined in the following way. A histogram was filled, for each track of known identity within a given momentum interval, with the photon hits at their corresponding reconstructed Cherenkov angles. The signal hits belonging to the track should show up as a peak, as shown in Fig. 4.1, which was produced by using the high momentum muons from the J/Ψ meson decay. Such distributions were fitted with a Gaussian function and polynomial background for each

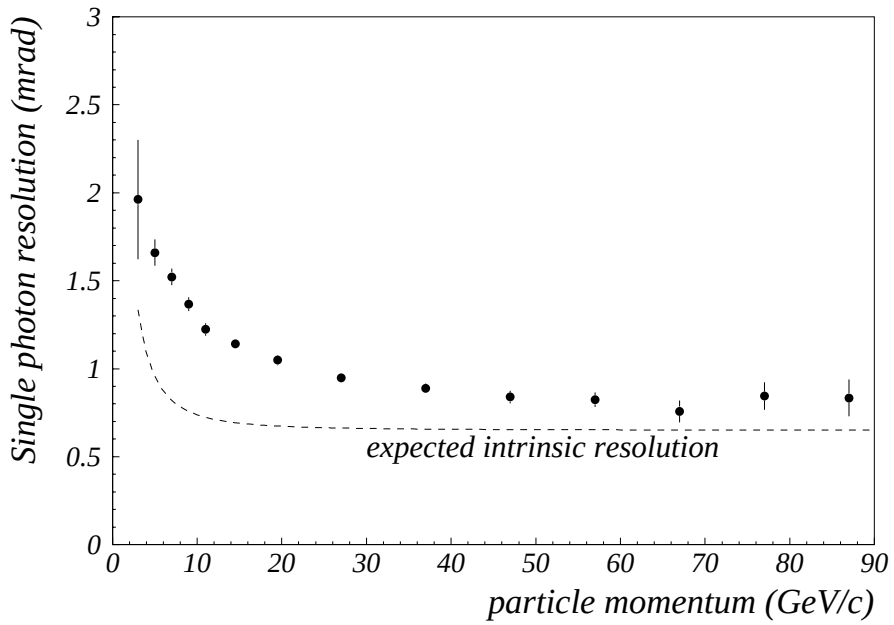

Figure 4.2: The measured single photon Cherenkov angle resolution versus particle momentum for the region covered by M16 photomultiplier tubes.

momentum interval, and the single photon resolution was identified with the r.m.s. width of the Gaussian function. The resulting momentum dependence of the single photon resolution is shown in Fig. 4.2. As expected, the single photon resolution depends on the particle momentum. For the high momentum tracks the resolutions of 0.81 mrad and 1.0 mrad were measured for the regions covered by M16 and M4 PMTs, respectively. The difference between the measured single photon resolution and the expected intrinsic resolution (as shown in Fig. 4.2) is attributed to the error in the measurement of the charged particle trajectory, which was not taken into account in the calculation of the expected Cherenkov angle uncertainty.

Note that the particle identification capabilities are affected also by the high multiplicity of rings in a single event. Typically 50 overlapping rings are present in an event. As a result, channel occupancies in some regions are as large as 25%. In such an environment the resolution in Cherenkov angle measurement of a track does not simply scale with the inverse of the square root of the number of the Cherenkov photons radiated by that track.

To illustrate its capabilities, the particle identification of the RICH detector was tested on a sample of measured data. For each track the Cherenkov angle distribution was fitted with a maximum likelihood method. Fig. 4.3 shows the resulting bands for different particles in the plot of reconstructed Cherenkov angle versus momentum. While it is obvious that e.g. pions can well be separated from kaons at least up to $35\ \mathrm{GeV}$, the separation capabilities will be discussed in detail in the next section.

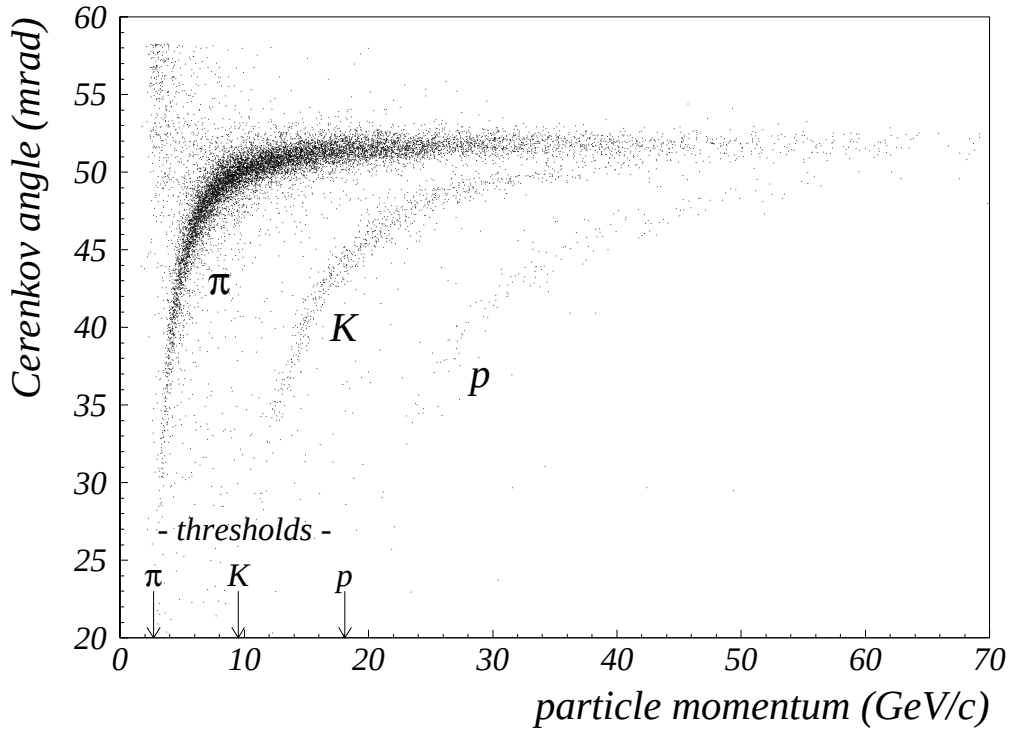

Figure 4.3: Reconstructed Cherenkov angle versus particle momentum. Bands for pions, kaons and protons are clearly visible.

4.2 Particle identification performance

For further use in physics analysis the particle identity information is stored in form of likelihoods for individual identity hypotheses. To determine these likelihoods, an extended likelihood method is used [29], combined with the expectation-maximization algorithm. The method is described in detail in [30, 31]. The first step in the method is the calculation of the Cherenkov angle for all track-photon pairs with the Cherenkov angle smaller than 70 mrad. The extended likelihood probabilities are calculated for 6 possible hypotheses for the identity of a track: *electron*, *muon*, *pion*, *kaon*, *proton* and *other*. The last one represents the case, where the distribution of Cherenkov angles of photons for a given track is consistent with the background. The resulting likelihood probabilities are normalized so their sum equals to one, and thus have the range of values between 0 and 1. The cut on the value of the appropriate likelihood enriches the sample of the selected tracks. For easier use, three levels of selection are defined in the standard reconstruction software. The levels are set to 0.05 (*soft*), 0.50 (*medium*) and 0.95 (*hard*) for pion selection and 0.05 (*soft*), 0.30 (*medium*) and 0.95 (*hard*) for kaon or proton selection.

To determine the efficiencies and mis-identification probabilities from the measured data, an a priori knowledge of particle types is required. For this purpose the following reconstructed decays were used:

- $K^0_S \to \pi^+\pi^-$, as a source of charged pions,

- $\Lambda \to p\pi^-$ and $\bar{\Lambda} \to \bar{p}\pi^+$, as a source of protons, anti protons and pions, and
- $\phi(1020) \to K^+K^-$, as a source of kaons.

For the first two decays a very clear signal in the invariant mass plot is obtained by cutting on the secondary vertex distance and removing the reflections (Λ, $\bar{\Lambda}$ in K^0_S, and similarly for Λ and $\bar{\Lambda}$). The ϕ mesons, on the other hand, decay immediately thus the signal quality can not be improved by cutting on its decay distance or on the impact parameters of decay products. The combinatorial background is large, since the K pair produced in the decay is typically accompanied by 10 other particles. To reduce this background, one of the particles was used to tag the decay by identifying it as a kaon and applying a transverse momentum cut. The other one was used for efficiency and mis-identification evaluation. In all cases, the number of particles of a given type surviving the selection criteria, and the number of all particles of the same type in a selected momentum bin were obtained by fitting a Gaussian plus a linear function to the invariant mass plots.

The results are presented in Fig. 4.4. At medium selection criteria, kaon identification efficiency for momenta between 10 GeV/c and 70 GeV/c is in a range from 60% to 80%, with typically about 5% pion mis-identification probability. The corresponding proton identification efficiency for momenta from 20 GeV/c to 70 GeV/c has values in a range between 60% and 80% with less than 5% pion mis-identification probability. In the region between pion and kaon (proton) Cherenkov threshold, the efficiencies are 65% for kaons (from 5 GeV/c to 10 GeV/c) with 16% pion mis-identification, and from 60% to 80% for protons (momentum region between 5 GeV/c and 20 GeV/c) with 15% pion mis-identification. Below 5 GeV/c the performance is degraded due to track direction uncertainty caused by multiple Coulomb scattering, and a small number of Cherenkov photons.

From Figs. 4.5 and 4.6, it is seen that the inclusion of the requirement that both tracks are identified, improves the signal to background ratio in the $\phi \to K^+K^-$ and $\Lambda \to \pi^- p$ decays.

4.3 RICH identification and alignment

From Fig. 4.2 it is easy to conclude that there is a very tight connection between the alignment of the spectrometer and the performance of the RICH counter. This will be further examined in this section. In Fig. 4.4 the efficiency and fake probabilities for identification of π, K and p obtained with an earlier version of calibration are shown, while in Fig. 4.7 the same data reprocessed with better alignment and calibration are presented. In both figures the results for the three standard identification cuts (see previous section) are shown. The improvement is obvious, specially for the efficiency of kaon identification.

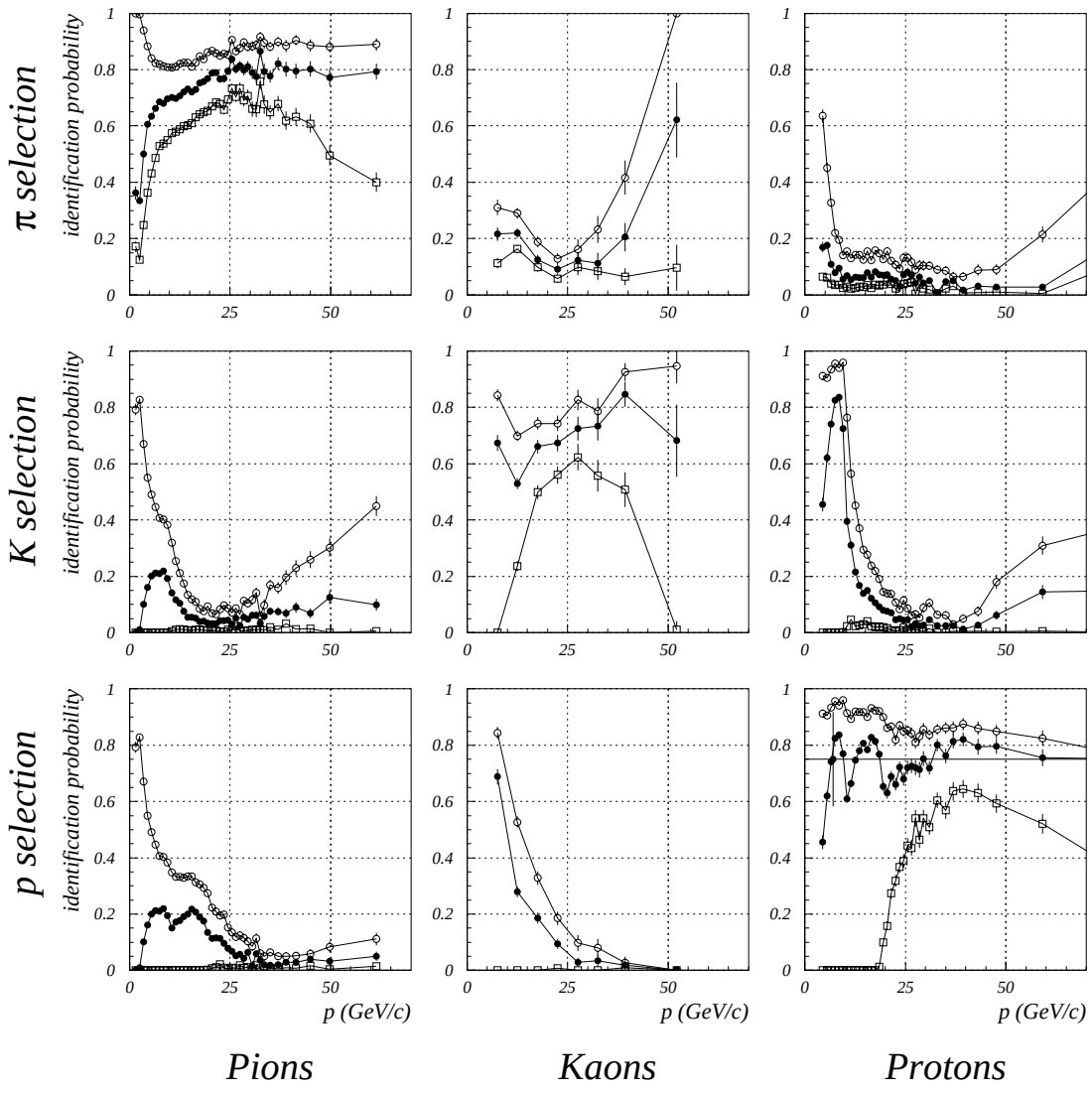

Figure 4.4: Momentum dependent identification probability plots for soft (open circles), medium (full circles) and hard (open squares) selections. Plots on the diagonal show the efficiency and off-diagonal plots show the mis-identification probability. Plots correspond to an older versions of global and RICH alignment.

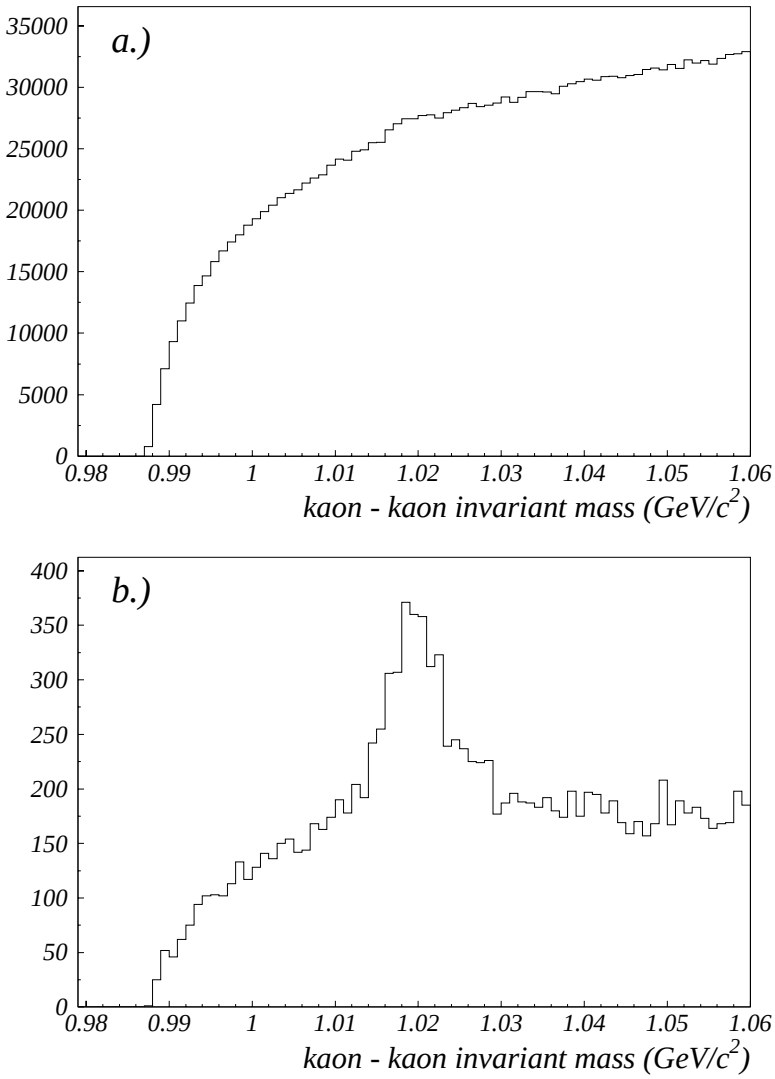

Figure 4.5: Improvement of signal to background for invariant mass distribution of $\phi \to K^{+} K^{-}$: a.) before and b.) after applying hard selection on both kaons.

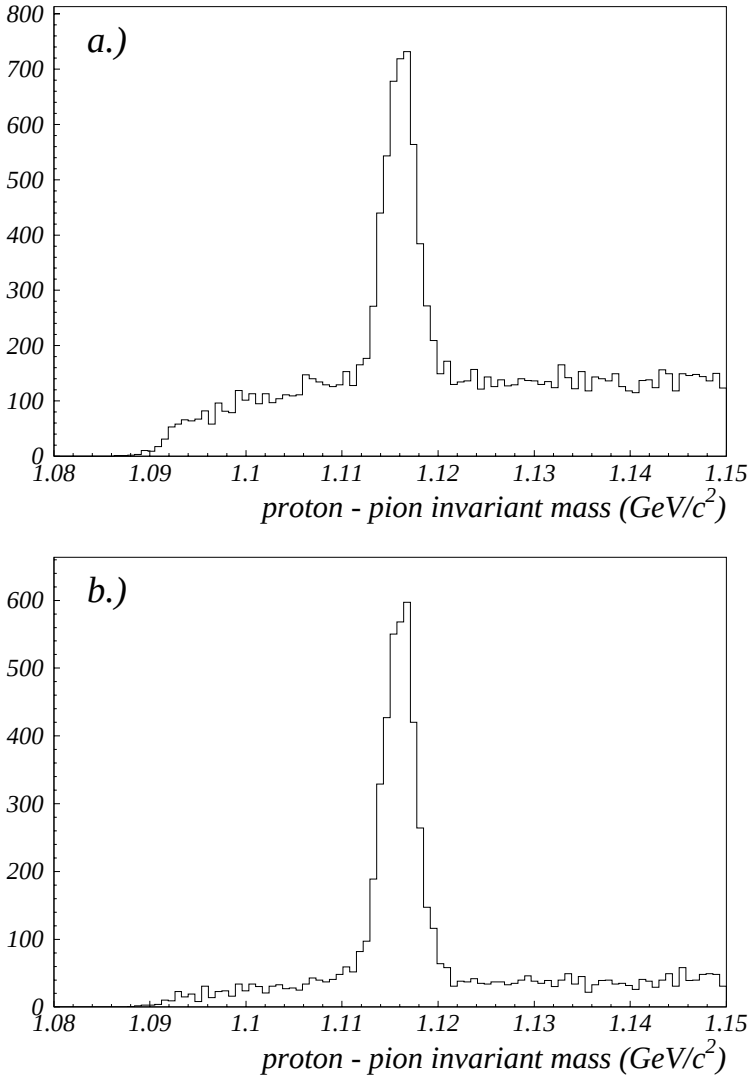

Figure 4.6: Improvement of signal to background for invariant mass distribution of $\Lambda \to \pi^- p$ in the kinematic region where the $K^0_S \to \pi^+\pi^-$ hypothesis cannot be excluded: a) no particle identification, b) for the positively charged particle, the proton likelihood was required to exceed the pion likelihood.

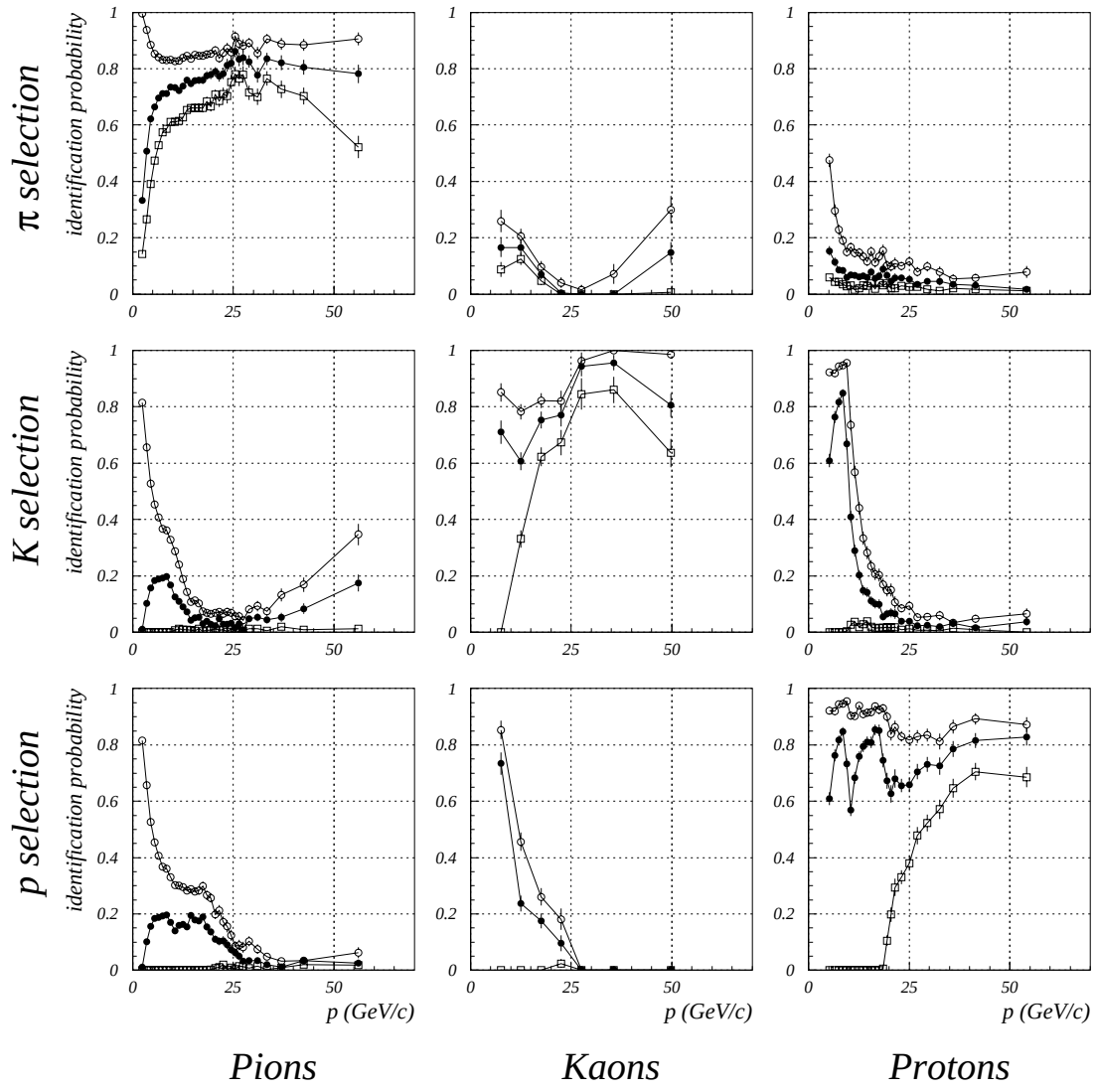

Figure 4.7: Efficiency matrix for the reprocessing with beter alignmnet and calibration.

Performance of RICH particle identification in 2002 data set In the next chapter, a specific cut on the RICH particle identification likelihood of 0.5 ($lrk > 0.5$) is used. Fig. 4.8(a) shown the efficiency of kaon identification and Fig. 4.8(b) the probability of pion being falsely identified as kaon, both for the chosen likelihood cut. The efficiency for kaon identification is in the range of $70 - 85\%$ and the pion 'fake' probability is around 2%. Since the data were recorded very recently, only an early version of alignment and calibration was available, and the particle identification performance is expected to improve with better alignment and calibration.

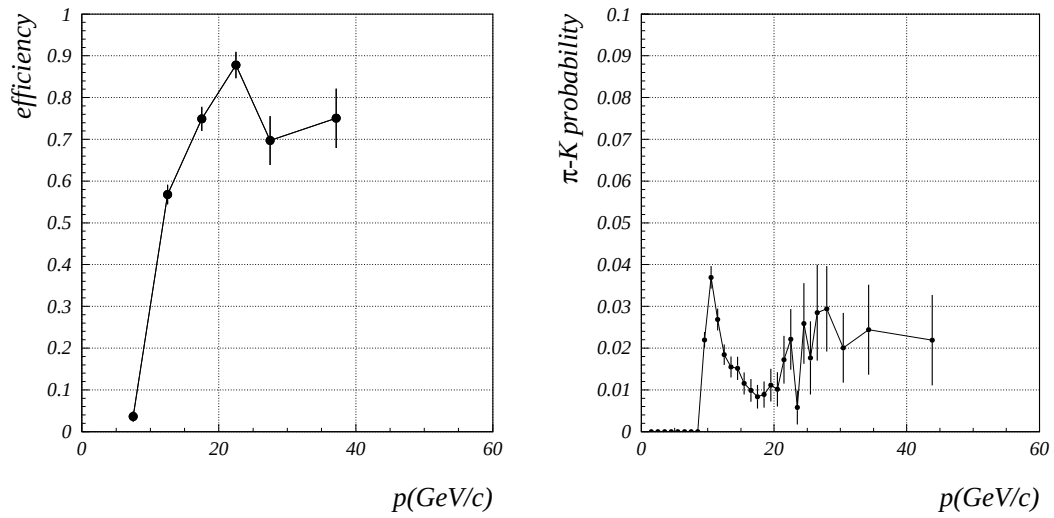

(a) (b)

Figure 4.8: Efficiency of kaon being identified as kaon (a) and probability of pion being identified as kaon (b) using the RICH particle identification likelihood cut of $lrk > 0.5$. The plot (a) is obtained from a sample of $\phi \to KK$ decays reconstructed in the data sample used in the analysis presented in the next Chapter. The source of pions in (b) were the $K_s \to \pi^+\pi^-$ and $\Lambda \to p\pi^-$ (and c.c.) decays.

5 Measurement of the production cross section

5.1 Introduction

Heavy flavor production Heavy quark production processes are good tests of perturbative quantum chromo dynamics (QCD) theory, where the production of heavy flavor quarks is calculable as long as their masses are sufficiently large. If this is true, the low energy hadronization effects are small, and the perturbative QCD can be used to predict the cross section.

On one hand the perturbative QCD seems to describe the experimental data of the top quark production cross section well, while the agreement for bottom and even more for charm production is less good, though it is unfair to state that the theory does not agree with the experiment at all, due to experimental, as well as theoretical errors. In order to increase the significance of the deviation (or optimistically - to decrease the value of deviations) between experiment and theory both errors should be decreased, clearly one task being to measure the production cross section more accurately.

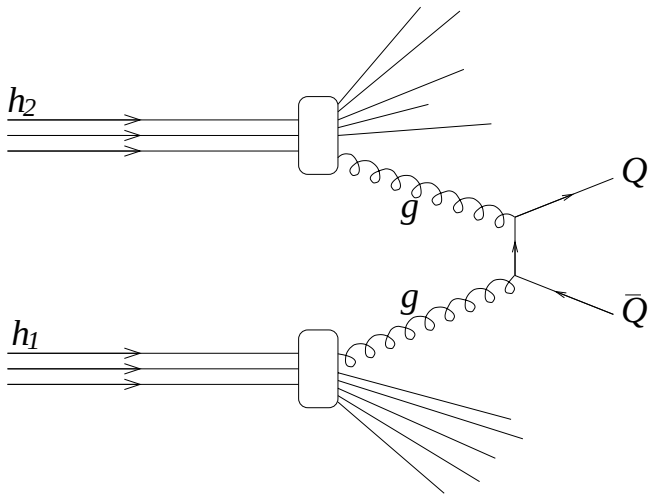

Figure 5.1: Schematic diagram of a typical heavy quark hadroproduction process $h_1 + h_2 \to Q\bar{Q} + X$.

The heavy quark production cross section in the collision of hadrons is described in the theoretical framework of the Improved Parton Model. The Factorization theorem states that the hadron cross section can be factorized into the partonic density function and the partonic cross

section, so the hadron cross section can be written in the following form:

$$\sigma(s,\tau) = \sum_{AB} \int dx_1 dx_2 p_{1A}(x_1,Q^2) p_{2B}(x_2,Q^2) \sigma_{AB}(x_1 x_2 s,\tau),$$

here $\tau = Q^2/s$ is the scaling variable, p_{1A} and p_{2B} are generic parton (A and B) density functions in the hadron h_i and σ_{AB} is the partonic cross section for the process $A + B \rightarrow Q\bar{Q} + X'$. Note that σ_{AB} is calculable in the perturbative QCD theory. The partonic density function, on the other hand, is measured experimentally, for example with lepton hadron deep inelastic scattering at certain Q^2, and can then be scaled via Altarelli-Parissi evolution equation which reads for parton-quark density function $q_i(x,Q^2)$:

$$\frac{d}{dt} q_i(x,Q^2) = \frac{\alpha_s(Q^2)}{2\pi}\big(q_i \otimes P_{qq}\big) + \frac{\alpha_s(Q^2)}{2\pi}\big(g \otimes P_{qg}\big).$$

Here $(q \otimes P) = \int_x^1 dy \frac{q(y,Q^2}{y} P\big(\frac{x}{y}\big)\big)$, and P is the splitting function. For parton-gluon density function a similar expression is obtained:

$$\frac{d}{dt} g(x,Q^2) = \frac{\alpha_s(Q^2)}{2\pi}\big(\sum_i (q_i + \bar{q}_i) \otimes P_{gq}\big) + \frac{\alpha_s(Q^2)}{2\pi}\big(g \otimes P_{gg}\big)$$

There exist, however, ambiguities in the theoretical calculations due to different choices of renormalization and regularization schemes of QCD gauge theory, for the purpose of which the parameter Λ_{QCD} has to be introduced. Λ_{QCD} is a function of Q^2 and changes discretely when going over the mass threshold for $Q\bar{Q}$ pair production, in order that the QCD 'running coupling' (α_s) stays continuous. Its value also depends on the choice of the scheme. The calculations of higher order radiative corrections to the leading order (tree level diagrams) are of order Q/Λ_{QCD} and $\log^{(2,1)}(Q/\Lambda_{QCD})$. In case of charm and bottom production these radiative terms are large, and thus the corrections to the theoretical predictions are expected to be large, too.

The process of factorizing the partonic density function into long distance and short distance effects also contributes a scale factor μ_f (in the calculation often the choice $\mu_f = \Lambda_{QCD}$ is used), which determines the order of non-perturbative correction effects (typically suppressed by μ_f/m_Q). One of such non-perturbative effects is the fragmentation process, in which the heavy quark is combined with the light sea quarks to form a hadron. This process is governed by the fragmentation distribution of the fraction of hadron momentum brought by the heavy quark. In the $m_Q \rightarrow \infty$ limit this contribution is 1, but the charm and bottom case is far from that regime [37].

The theoretical prediction for the charm quark pair production $c\bar{c}$ can be found in [36] computed at NLO order in QCD, and in [38], where the calculation of the effects of soft-gluon resummation was done at NLL order, the later giving slightly higher cross section values. In Fig. 5.2 theoretical prediction for the behavior of $c\bar{c}$ and $b\bar{b}$ cross section as a function of the beam energy (from [36]) is depicted together with existing experimental data. The prediction for $c\bar{c}$ quark pair production cross section at HERA-B energies for the favorable $m_c = 1.5\ \mathrm{GeV}$ is in the range:

$$\sigma_{c\bar{c}} = (9 - 71)\ \mu\mathrm{b},$$

where the variation is due to a choice of the QCD scale. A measurement of the production cross section in the region covered by the HERA-B spectrometer ($E_0 = 920$ GeV) is therefore highly desirable to pin down these theoretical ambiguities.

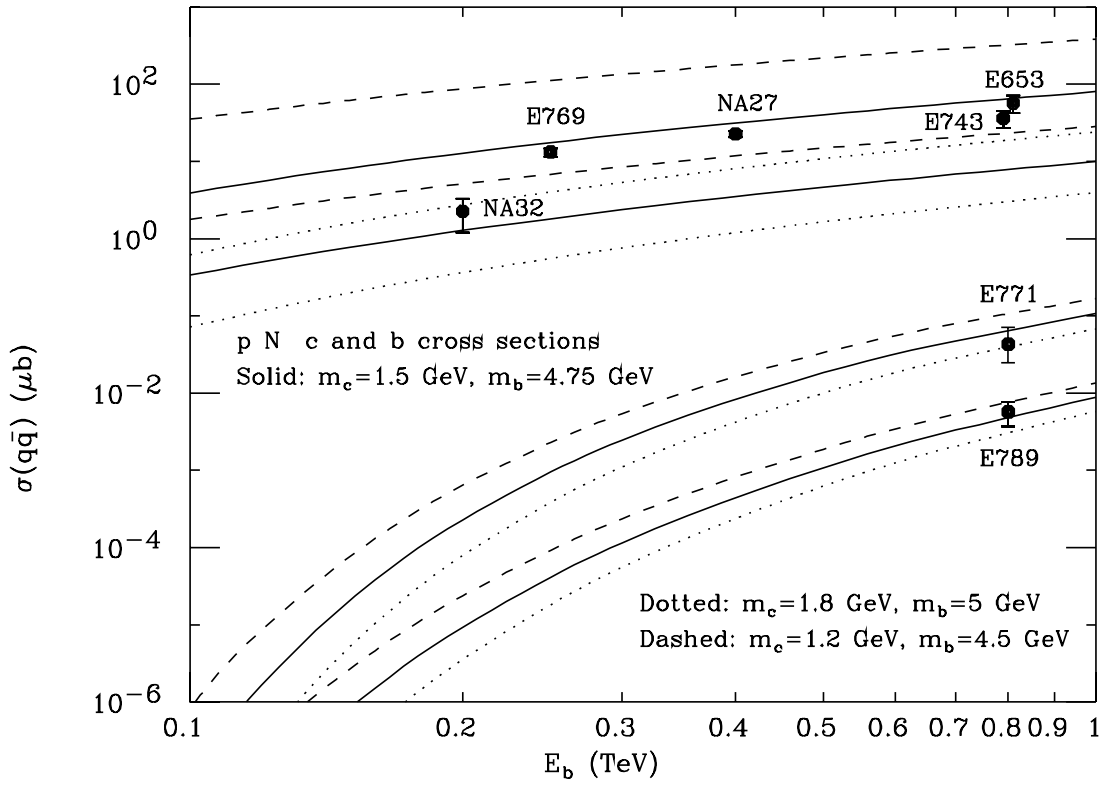

Figure 5.2: Summary of $c\bar{c}$ and $b\bar{b}$ production cross section [36], theoretical predictions and published measurements.

Nuclear effects. A nucleus can be naively represented as a sphere made of nucleons. The volume of the nucleus increases linearly with number of nucleons - atomic number A, while its two dimensional projection increases with the power of $2/3$ of A. In case the probability of nucleon nucleon reaction is high (close to 1), it is expected that the probability for nucleon nucleus interaction increases similarly as the geometrical cross section, i.e. as $A^{2/3}$. On the other hand, when the probability of nucleon nucleon interaction is small, it is naively expected that the probability of nucleon nucleus interaction increases linearly with A. In practice, the power of A has to be measured for individual processes. The cross section for a reaction, which is proportional to the probability for reaction to occur, is commonly parameterized by the following expression:

$$\sigma = \sigma_0 A^{\alpha}, \tag{5.1}$$

where σ is the total cross section per nucleus, and σ_0 is the cross section per nucleon. If $\alpha = 1$, there is no suppression or enhancement due to nuclear effects, $\alpha < 1$ means suppression and $\alpha > 1$ enhancement.

In the case of proton nucleon inelastic interactions, the power was determined experimentally at different proton beam energies than the energies covered by HERA-B. It was scaled to the proton beam energy of HERA-B [33],

$$\alpha_{inel} = 0.7111 \pm 0.0011.$$

Thus:

$$\sigma_{inel}(pN) = \sigma_{0,inel}(pN)\, A^{0.7111 \pm 0.0011}.$$

Note that this value of α is not far away from the simplistic estimate of $\alpha = 2/3$ coming from the geometric cross section of the spherical nucleus, as if the nucleus would seem as a hard shell.

The charm production cross section is expected to be tree orders of magnitude smaller than the inelastic one, thus also the probability for producing charm in nucleon nucleon collision is small. Hence we expect the suppression of charm production to be small, such that α is close to unity. Consequently, this means the charm production is relatively enhanced at higher A values compared to the inelastic events.

As far as the charm production is concerned, the following two measurements of the α parameter are available. The experiment E789 at Fermilab measured the α parameter for neutral D meson production for the collisions of protons with energies of $800\ \mathrm{GeV}$ against two different targets, made of beryllium and gold [34],

$$\alpha_{D^0,\bar{D}^0} = 1.02 \pm 0.03_{stat} \pm 0.02_{syst} \tag{5.2}$$

Recently, the A dependence was also estimated at HERA-B for the J/Ψ production cross section [35]. Two different α constants were determined, one for $J/\Psi \to \mu\mu$ and the other for $J/\Psi \to ee$ channel, in a slightly different kinematical range. Since the measurements are compatible within errors, we cite the average:

$$\alpha_{J/\Psi} = 0.996 \pm 0.037 \tag{5.3}$$

By taking for the $c\bar{c}$ production cross section a value of $\sigma_{c\bar{c}} = 50\mu b$ [36], and setting $\alpha = 1$, we would expect that each 1000 inelastic interactions contain the following numbers of interactions that produced a $c\bar{c}$ pair: 2.3 in case of the target made of carbon (A=12) and 5.2 in case the target is made of tungsten (A=184). Taking into account the efficiencies (see Section 5.4.6) and the branching ratios of the reactions that we study, we expect in 10^7 events to have couple of 10 events of interest, which we are able to fully reconstruct.

In the present analysis cross section was determined for the production of neutral D^0 meson, charged excited D^{*+} meson as well as for the production of the $c\bar{c}$ quark pair. Furthermore, an estimate of the α parameter in the production of neutral D^0 mesons was given.

5.2 Experimental cross section determination

Experimentally a collision of two particles is usually described in terms of cross section, which is a measure of the probability of reaction to occur. Integrated luminosity connects the cross section σ and number of reactions N that occurred with the following formula:

$$\sigma = \frac{N}{\mathcal{L}}, \tag{5.4}$$

where $\mathcal{L}$ is the integrated luminosity. The event could be any reaction of interest, for example the neutral D^0 meson decay into K and π mesons, or it could be the most ordinary inelastic interaction event.

The inelastic cross section for the HERA-B environment was evaluated in [33], and was used in the present analysis to determine the luminosity of the collected data. This is quite a simple way to determine the luminosity but it was estimated that the introduced error is well below the statistical error so far. For the further analysis with higher statistics a proper more sophisticated luminosity determination should be considered (as also discussed in [33]), but the corresponding luminosity values are not available yet for the recently collected data. We will therefore use the following expression obtained from Equation 5.4 for the luminosity estimate:

$$\mathcal{L} = \frac{N_{inel}}{\sigma_{inel}} = \frac{N_{inel}}{\sigma_{inel,0} A_{inel}^{\alpha}}, \tag{5.5}$$

where N_{inel} corresponds to the number of inelastic interactions, σ_{inel} and $\sigma_{inel,0}$ to the inelastic cross section per nucleus and per nucleon respectively, and α_{inel} describes the nuclear suppression of inelastic interactions.

In the following argument the decay $D^0 \rightarrow K\pi$ will be used for illustration, but the formulae are valid for any chosen event type. The produced number of chosen particles (D^0) has to be measured in order to calculate the production cross section. Usually the decay products of a chosen decay channel of the primary particle are measured (K and π). Thus the number of reactions is reduced by the branching ratio, a fraction in which the chosen particle decays via the chosen decay channel ($B(D^0 \rightarrow K\,\pi)$). Furthermore, the decays that are finally reconstructed are only a fraction of all that have actually occurred, due to the limited detector acceptance and reconstruction algorithm efficiencies. The number of primary particles that decayed in the decay channel and are actually reconstructed (e.g. $N_{detected}(D^0 \rightarrow K\,\pi)$) is linked to the number of the particles that have been produced (e.g. $N_{total}(D^0)$) with the following expression:

$$N_{detected}(D^0 \rightarrow K\,\pi) = N_{total}(D^0)\, B(D^0 \rightarrow K\,\pi)\, \epsilon_{geo}\, \epsilon_{reco}\, \epsilon_{cuts}, \tag{5.6}$$

where $B(D^0 \rightarrow K\,\pi)$ is the branching ratio for the specified decay channel. The imperfectness of the detector and reconstruction can be factorized into: ϵ_{geo} geometric acceptance, ϵ_{reco} reconstruction efficiency and ϵ_{cuts} the efficiency of our selection cuts. Geometric and reconstruction efficiencies were estimated in Section 5.4.6. The geometric efficiencies for K and π from the D^0 decay is summarized in the table 5.1. Note that there is quite a difference between the total

geometric efficiency ϵ_{geo} and the VDS only geometric efficiency ϵ_{geo}^{VDS}. This is also due to missing inner part of the main tracker (ITR), which was not ready yet at the time of data taking (due to a long start up periods). Note also that this factorization of efficiencies is somewhat artificial, since they are correlated. In fact, in the cross section estimation (Section 5.5) we will use the combined efficiency ϵ_{ana}.

	ϵ_{geo}	ϵ_{geo}^{VDS}
K	0.44	0.58
π	0.32	0.44
D^0	0.17	0.30

Table 5.1: Geometric efficiencies (ϵ_{geo}) of the K and π track comming from the decay of D^0 meson (based on Monte Carlo simulation). D^0 corresponds to the demand that both tracks are in the acceptance. ϵ_{geo}^{VDS} represent geometric efficiency of the VDS subdetector.

By combining Eqs. 5.6, 5.5 and 5.4 the production cross section $\sigma_P(D^0)$ is obtained:

$$\sigma_P(D^0) = \frac{N_{detected}(D^0 \rightarrow K\ \pi)\ \sigma_{inel,0}\ A^{\alpha_{inel}}}{B(D^0 \rightarrow K\ \pi)\ N_{inel}\ \epsilon_{geo}\ \epsilon_{reco}\ \epsilon_{cuts}} \tag{5.7}$$

Denoting the D^0 production cross section per nucleon with $\sigma_{0,P}(D^0)$ and taking into account the A dependence of the cross section, which was parameterized in Equation 5.1, the nucleonic production cross section can be written as:

$$\sigma_{0,P}(D^0) = \frac{N_{detected}(D^0 \rightarrow K\ \pi)\ \sigma_{inel,0}\ A^{\alpha_{inel}-\alpha_{D^0}}}{B(D^0 \rightarrow K\ \pi)\ N_{inel}\ \epsilon_{geo}\ \epsilon_{reco}\ \epsilon_{cuts}}, \tag{5.8}$$

where α_{D^0} corresponds to suppression/enhancement parameter for D^0 production.

It is expected that α varies with Feynman's variable x_F, which is approximately:

$$x_F \approx \frac{2p_{z\ cms}}{\sqrt{s}},$$

with $p_{z\ cms}$ the momentum component along the beam direction in the center of mass system and $\sqrt{s}$ is the center of mass energy, being $\sqrt{s} = 42.6\ \mathrm{GeV}$ at present for the HERA-B experiment. x_F is used to describe different kinematic regimes. The average x_F for the measurement in [34] was close to zero, $\langle x_F \rangle = 0.03$. In the present analysis we have assumed that α has the same value since x_F is close to zero as well, as can be seen from the x_F distribution for the reconstructed D^0 decays (Fig. 5.3). The x_F values in [35] were in the similar range as ours, too.

The data considered in the analysis was taken with two different target wires, which were made of carbon (C, A=12.0) and tungsten (W, A=184). In the Table 5.2 the inelastic cross section for the two setups is summarized based on [33].

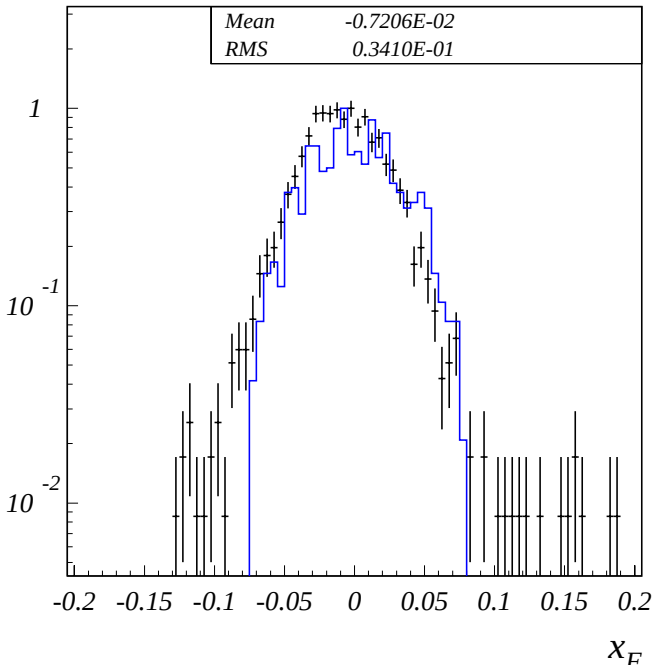

Figure 5.3: Kinematical x_F distribution for the D^0 candidates in reconstructed data (black with error bars) and Monte Carlo sample (blue). Narrow region is due to reconstruction and cuts applied (note that for data the distribution is mainly due to the background but it is still similar). Vertical scale is arbitrary.

material	$\sigma_{inel}(mb)$
C	255.1 ± 2.4
W	1775 ± 19
per nucleon	43.55 ± 0.40

Table 5.2: The inelastic cross section at HERA-B conditions. The values for C and W wires are cited as well as the nucleonic inelastic cross section.

To calculate the cross section for the $c\bar{c}$ production, from the measured D^0 production cross section, the fractions F of $c\bar{c}$ pair hadronizes into different species of charmed hadrons and charmonium states have to be known. The $c\bar{c}$ production cross section can then be determined from a single particle species production cross section and these fraction by the following expression:

$$\sigma_{c\bar{c}} = \frac{\sigma_{D^0}}{F_{D^0}} = \frac{\sigma_{D^{*+}}}{F_{D^{*+}}}$$

In the Table 5.3 we summarize the fractions at which different open charm particles are produced, in the model used for Monte Carlo generation of simulated data. The event generation in HERA-B Monte Carlo simulation is described in [20], and is based on PYTHIA [21] and FRITIOF [22] packages.

particle (+anti p.)	fraction per $c\bar{c}$ pair
D^0	1.19
D^+	0.49
D^{*+}	0.51

Table 5.3: Fractions of D mesons produced per $c\bar{c}$ pair as determined from the Monte Carlo simulated sample.

The present analysis is limited to two decay channels: $D^0 \to K^-\pi^+$ and $D^{*+} \to D^0\pi^+ \to K^-\pi^+\pi^+$. The branching ratios were taken from [32]. They are listed in Table 5.4.

reaction	B
$D^0 \to K^-\pi^+$	$(3.80 \pm 0.09)\%$
$D^{*+} \to D^0\pi^+$	$(67.7 \pm 0.5)\%$
$D^{*+} \to D^0\pi^+ \to K^-\pi^+\pi^+$	$(2.57 \pm 0.09)\%$

Table 5.4: Branching ratios of the reactions of interest for the present analysis.

5.3 Data sample

The HERA-B spectrometer came into operation in the late spring of 2000. The first data was taken that year till the September 2000 shutdown, while not all commissioning problems were yet solved. The next data taking period came only in the year of 2002. Till the fall of this year majority of the commissioning problems were solved and data taking started with much higher efficiency. The number of recorded events in the year 2002 already untill this thesis was completed surpasses considerably the one from the year 2000. Data samples are of a few different types depending on the trigger setup used for data taking (see Section 2.10). The candidates for the open charm production studies are the sample taken in the single lepton trigger mode in August 2000 and the sample taken in the interaction trigger mode, where almost only the empty events were rejected. In this section we will present arguments for our choice of the 2002 interaction trigger sample over the 2000 single lepton trigger sample.

5.3.1 Single lepton trigger data sample

Chronologically the first interesting sample to study the open charm production was the sample of data taken in August 2000 in the single lepton trigger mode, where the track with the highest trnsverse momentum (p_t) that left signal in muon chambers or in electromagnetic-calorimeter (ECAL) was considered for triggering. If such a track had p_t higher than $1\ \mathrm{GeV/c}$ (or in some cases $1.5\ \mathrm{GeV/c}$), the trigger was fired. It was expected that the enhancement of the signal was substantial.

The single lepton trigger data of August 2000 consists of runs with run numbers between 17116 and 17266, including the two. There is around $4\ 10^6$ events recorded in the sample which is divided in two subsamples: the runs with run numbers from 17116 to 17137 were taken in a single muon mode, i.e. triggering only on muon track candidates. The runs between run number 17242 and 17266 were taken in the combined muon and electron mode, triggering on both muon and electron track candidates. The target rate was set at approximately 2MHz, which would mean (assuming that all bunches are equally populated) that the number of interactions per bunch crossing would be distributed according to Poisson distribution with a mean of approximately $\mu = 0.2$. Effectively, the trigger selected only the events that deposit some signal in the spectrometer, thus rejecting the events without an interaction.

The enhancement of the signal in the triggered events can be estimated with a simple consideration. For the qualitative estimate only the data acquired with the single muon trigger will be considered. The desired signal events in this case are the events containing a reaction that produced a $c\bar{c}$ quark pair. On the other hand, the single muon trigger was set to accept all events having at least one track satisfying the condition in the muon chambers and having a large enough transverse momentum. The condition in the muon chambers is satisfied by a coincidence of hits in two consecutive super-layers of the muon system in the corresponding channels (a sort of projective geometry is employed). We approximated the trigger condition by requiring that the candidate track has muon particle identification likelihood with a value larger than 0. The survival probabilities of the Monte Carlo generated events with one $c\bar{c}$ quark pair decay, as well as of the events from Monte Carlo sample with 1 inelastic interaction were studied (see Fig. 5.4). All events were required to have at least one muon candidate, i.e. at

least one particle was required to be identified as a muon in the MUON chambers. For the p_t cut the muon candidate with the highest p_t value was considered. By dividing the two survival probabilities we get the enhancement factor (Fig. 5.5). It could be seen that the enhancement is the biggest at p_t of approximately $1\ \mathrm{GeV/c}$, but also that it does not exceed a factor of 3. That would mean that the single muon triggered data sample would be $2-3$ times richer with charm containing events than the simple inelastic interaction sample.

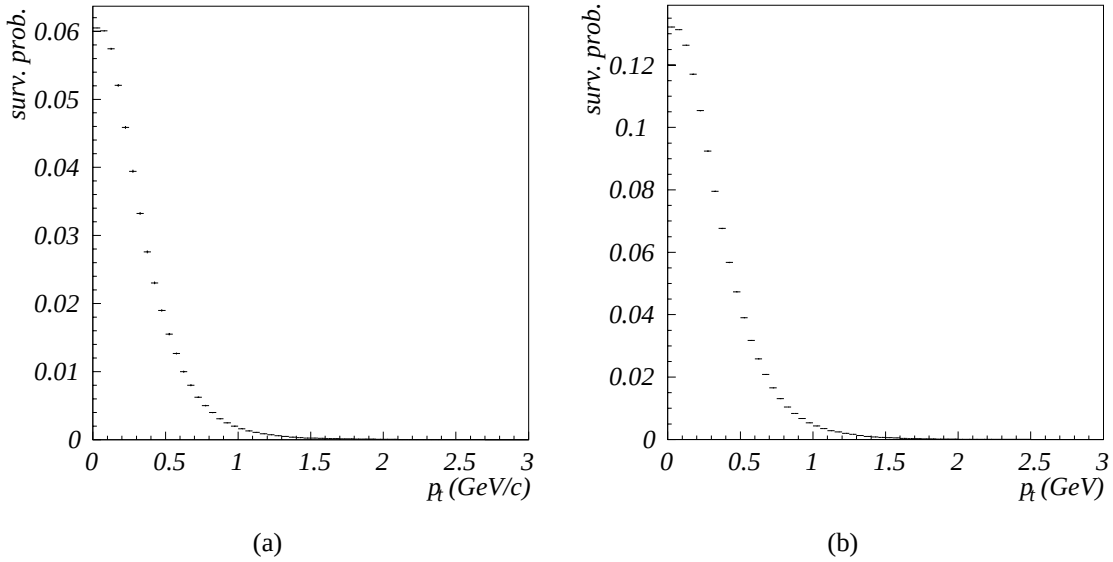

(a) (b)

Figure 5.4: Survival probabilities as a function of the cut on p_t of the muon candidate for the inelastic interaction event (a) and for an event with reaction that produced a $c\bar{c}$ pair (b) .

Unfortunately the occupancies in the sub-detectors such as RICH in the single lepton data sample indicate that the trigger selected events were populated much above the expectation for an average event with 1 inelastic interaction. This could indicate that the trigger preferably selected events with higher multiplicities. The occupancies in RICH approximately match with those of Monte Carlo generated events with $1+\langle 2\rangle$ inelastic interaction events, where $\langle 2\rangle$ stands for a number generated according to Poisson distribution with mean value equal 2. The survival probabilities for such events are higher than for the events with just 1 interaction generated, thus causing a decrease of the enhancement of charm (see Fig. 5.6).

With this simple consideration it becomes clear that in the $4\ 10^6$ events of single lepton data it is not expected to find much more $c\bar{c}$ containing events than in the inelastic interaction sample of comparable size. If the triggered sample were chosen for the present analysis, an additional difficulty would be to properly evaluate the trigger efficiency and enhancement, which would bring additional uncertainty into the interpretation of results. In addition, the events that passed the single lepton trigger have a higher multiplicity than average events, which tends to increase the combinatoric background and the rate of unrealistic, fake, tracks.

Just for comparison we estimate the enhancement factor for the events containing the decay of J/Ψ mesons into charged muons over the inelastic interaction events. Again we took the $1+\langle 2\rangle$ inelastic interaction sample for the background estimation. Particles identified as

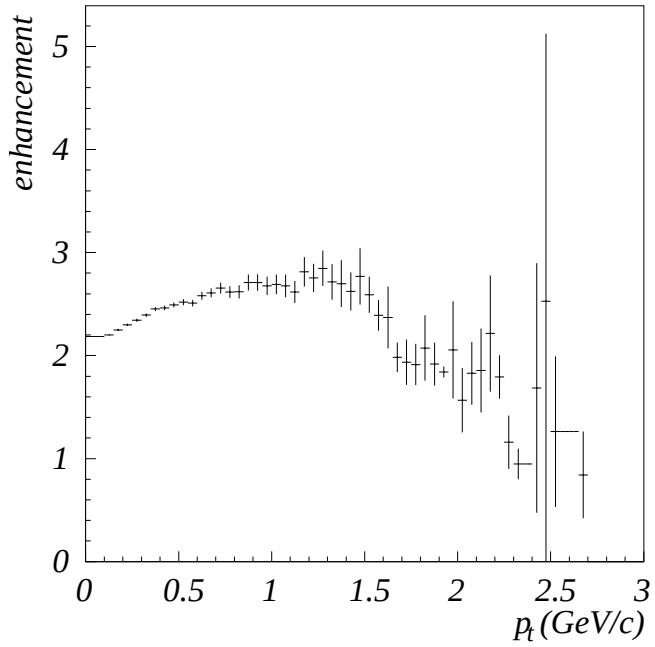

Figure 5.5: Enhancement of charm in the single muon triggered events as a function of p_t cut on the muon candidate with the biggest p_t in the event.

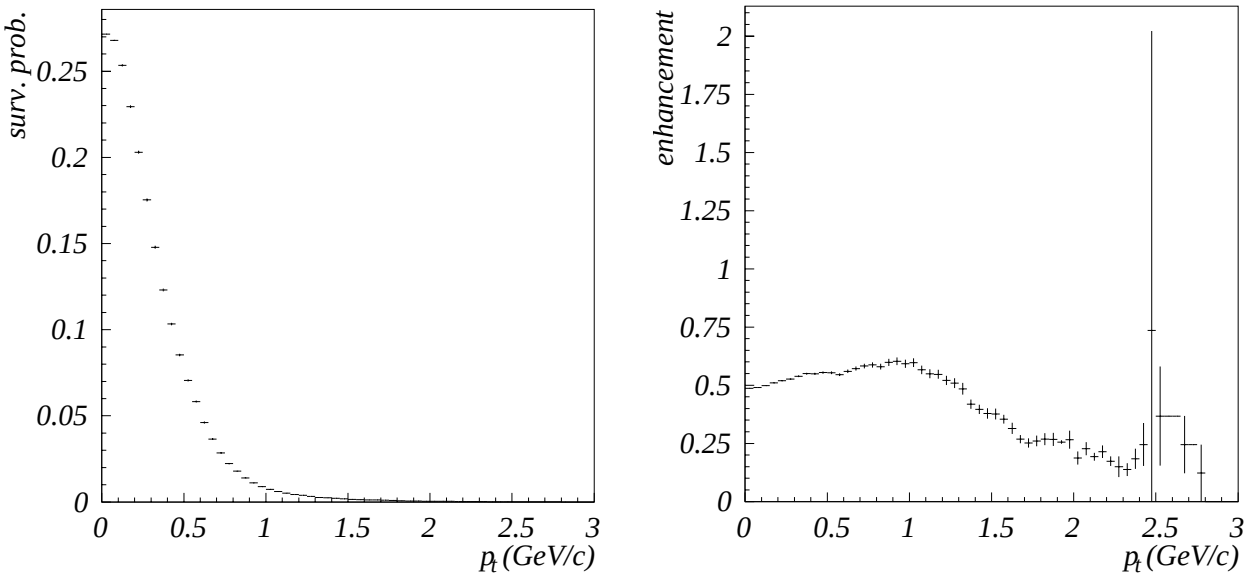

(a) (b)

Figure 5.6: Survival probabilities for the inelastic interaction event 6(a) with 1 interaction plus 2 Poisonially distributed interactions. The occupancies of such events match approximately the occupancies of the single lepton triggered data sample. The enhancement could no longer be called enhancement 6(b).

muons in events containing the J/Ψ meson decay have a much higher p_t than an average muon

identified particles in $c\bar{c}$ events (see Fig. 5.7). This indicates that high p_t trigger is much more efficient for enhancing J/Ψ mesons than the general $c\bar{c}$ events. In the general $c\bar{c}$ events the 'fake' muons are almost as energetic as the real ones, while in the events containing J/Ψ mesons, the muons from the J/Ψ mesons have typically much higher p_t than the rest of the particles which leave a signal in the muon system. Note that majority of 'fake' muons are real muons that come from the decays of kaons and pions.

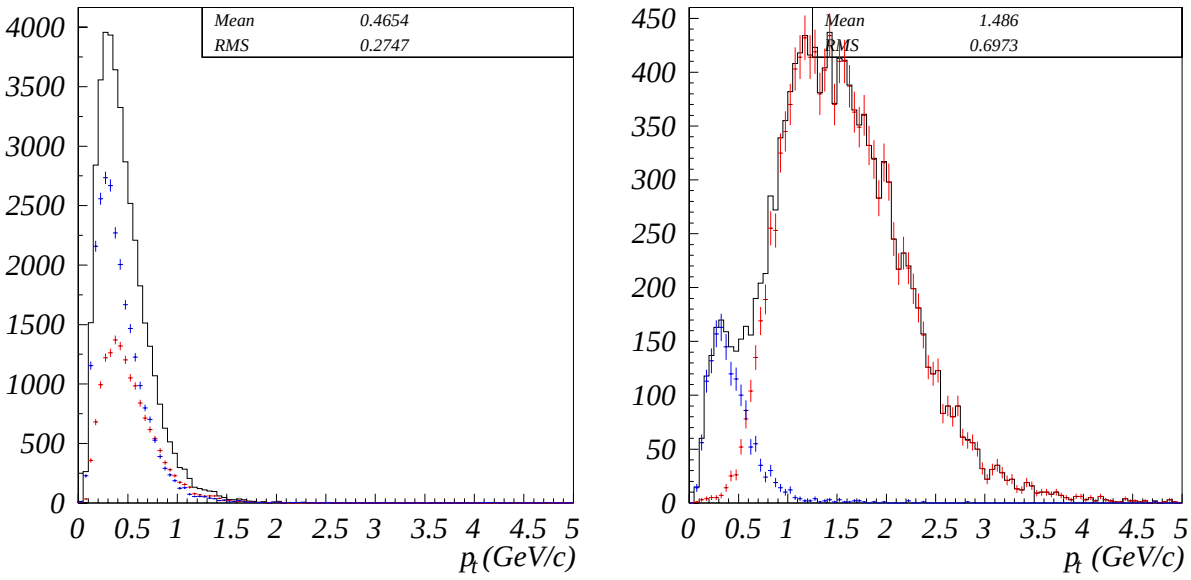

(a) (b)

Figure 5.7: Distribution of events over p_t of the muon candidate in a general $c\bar{c}$ (a) event and in an event containing a J/Ψ meson decay (b). Full histogram indicates all particles identified as muons, red are particles that correspond to a generated muon true track, and blue correspond to the muon identified tracks, that did not correspond to a muon true track immediately after the interaction (they could come from a muon main tracker segment falsely matched with a VDS segment, or from particles that decayed into muons, i.e. from K and π).

In Fig. 5.8 the survival probability for events containing a J/Ψ meson is plotted together with the enhancement factor for such events compared to the $1+\langle 2\rangle$ inelastic interaction sample, all based on Monte Carlo simulation. The direct J/Ψ meson cross section is approximately five orders of magnitude smaller than the cross section for inelastic interaction events. The enhancement at a p_t cut of 1 GeV/c is approximately 30. Taking into account the ratio of cross section for J/Ψ production over the inelastic cross section this would result in about 400 produced J/Ψ mesons in $1.4\ 10^6$ events recorded with single muon trigger. This number is in reasonable good agreement with the 300 J/Ψ mesons in this sample (see Fig. 5.9), in particular if the μ pair reconstruction efficiency is taken into account.

Two independent analyses ([39], [13]) already made use of the single lepton triggered data sample collected in 2000. In [13] the production cross sections was determined for the produc-

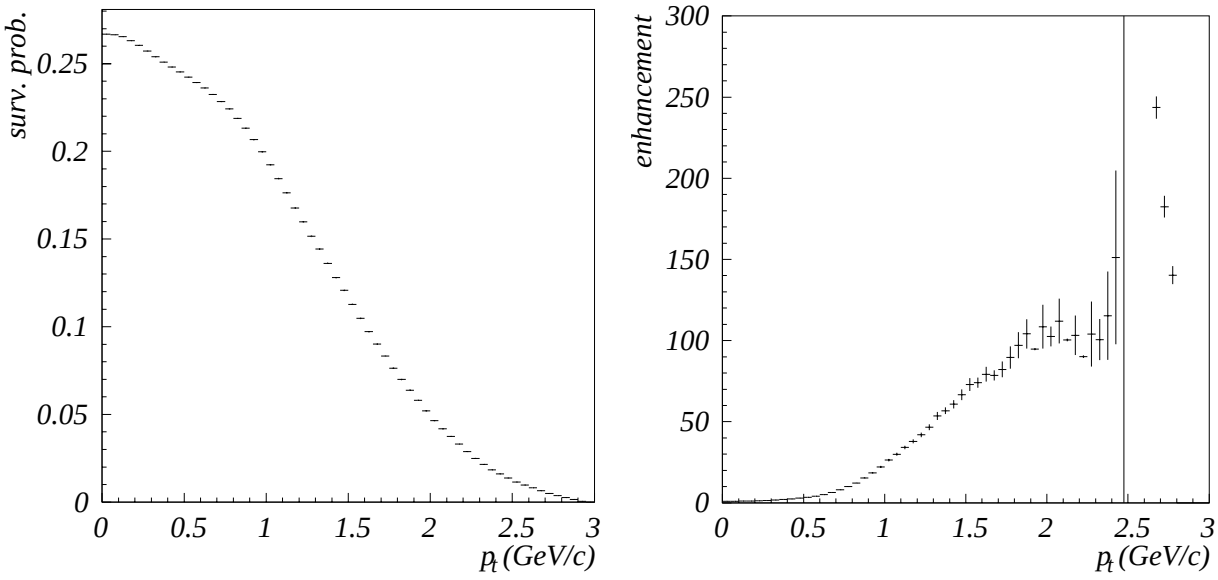

(a) (b)

Figure 5.8: Survival probabilities for events containing a J/Ψ meson decay (a). The enhancement of such event over the inelastic interaction background ($1 + \langle 2 \rangle$) is quite large (b).

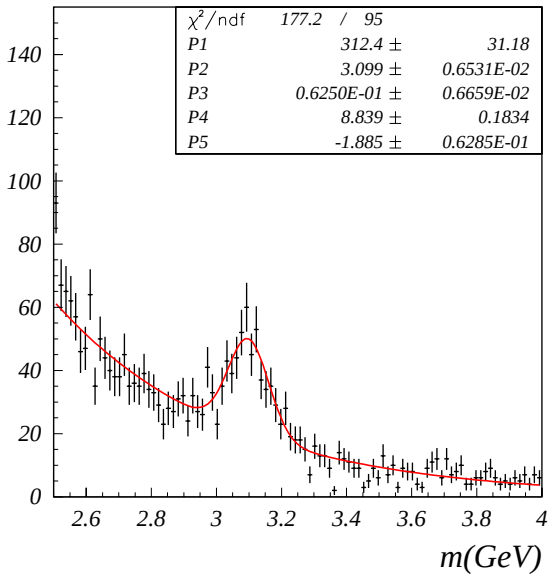

Figure 5.9: Invariant mass of $\mu^+\mu^-$ pairs as found in the single lepton triggered sample. The fitted peak corresponds to about 300 reconstructed J/Ψ mesons.

tion of neutral D^0 mesons, charged D^+ mesons and for the $c\bar{c}$ quark pairs,

$$\sigma_{D^0+\bar{D}^0} = 80 \pm 27_{stat} \pm 61_{syst} \mu b/nucleon$$

$$\sigma_{D^+ + D^-} = 52 \pm 20_{stat} \pm 39_{syst} \mu b/nucleon$$
$$\sigma_{c\bar{c}} = 39 \pm 10_{stat} \pm 21_{syst} \mu b/nucleon$$

In analysis [39] the ratio of D^0 and D^+ production cross sections was determined,

$$R = \frac{\sigma_{D^+}}{\sigma_{D^0}} = 1.08 \pm 0.62$$

5.3.2 2002 inelastic interaction data

Due to a relatively poor enhancement in the single lepton data, ambiguities when estimating trigger efficiency, and its relatively poor statistics, we decided to present the analysis based on 2002 interaction trigger data sample which was already quite substantial ($16.4\ 10^6$ events were already reconstructed when this thesis was finalized). This was done despite some initial difficulties in the new reconstruction and not yet fully calibrated and aligned spectrometer for this particular run period. The data analyzed in this chapter was collected during the fall of 2002, when the HERA accelerator was finally recommisioned and the HERA-B spectrometer become operational with performance superseding the level of the year 2000. The first two runs (19170 and 19179) were taken with one target inserted. The target material was carbon, C (A=12.0), in run 19170, and tungsten, W (A=184), in run 19179. The run 19185 had both targets present. The run statistics is summarized in the Table. 5.5.

run	N	wire no.	target name	material
19170	7006974	2	below 1	C $(A = 12.0)$
19179	2419759	3	inner 1	W $(A = 184)$
19185	7009010	2,3	b 1,i 1	C, W
	4.4M	2	below 1	C
	2.6M	3	inner 1	W
total	**16435743**			

Table 5.5: Summary of the data analyzed. N is the number of all events recorded, and were required to satisfy the interaction trigger condition.

The trigger condition was set to accept all events in which more than 20 hits were found in the RICH detector. The probability for an inelastic interaction event not to satisfy the trigger condition was determined on an inelastic Monte Carlo sample. Since the data were recorded at an interaction rate of $1\ \mathrm{MHz}$, the number of interactions per event was generated in accordance with a Poissonian distribution with a mean of $\mu = 0.1$. The resulting escape probability P_{esc} is depicted in Fig. 5.10 as a function of increasing number of RICH hits required. The efficiency of the trigger η is then:

$$\eta = 1 - P_{esc} = 0.937,$$

and has to be taken into account when estimating the number of inelastic interaction at the target:

$$N_{inel} = \frac{N_{inel}^{trgd}}{\eta}, \tag{5.9}$$

In the real data the number of detected hits in RICH detector could be affected by hot and dead channels, that are not properly masked out in the reconstruction. We estimate that η parameter is not affected for more than $\%$ level and we will disregard this uncertainty in the following analysis.

Since the interaction triggered data sample was taken at a target rate of approximately $1\ \mathrm{MHz}$, the probability of two or more interactions to happen in the same event is small. Ac-

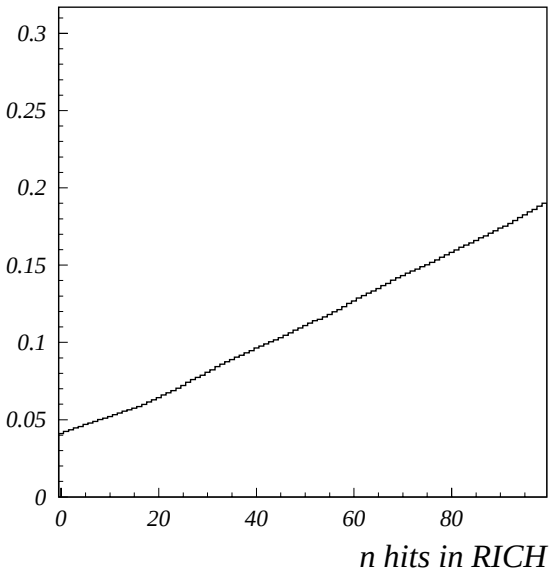

Figure 5.10: The probability of a inelastic interaction event to produce less than n hits in RICH subsystem. At $n = 20$ this probability is 0.063.

cording to the Poisson statistics the probabilities for having 0, 1 and more than one interactions in a single event are:

$$w_N = \frac{\bar{N}^N}{N!} e^{-\bar{N}},\ w_0 = 0.9048,\ w_1 = 0.0905,\ w_{N>1} = 0.0047.$$

Since virtually all empty events are rejected with the interaction trigger and all non-empty accepted, the ratio between the events with more than 1 interaction compared to those with exactly one in our sample is approximately $w_{N>1}/w_1 = 0.05$.

5.4 Reconstruction

In this section the reconstruction applied in the present analysis will be explained. Different cuts and their efficiencies will be discussed.

5.4.1 Track selection

HERA-B is a hadron fixed target experiment where high energetic protons collide against target nucleons. In such an environment a large amount of particles are generated which leave numerous hits in the spectrometer. These hits are of various types. The task of reconstruction is to transform these low level detector responses into tracks. A track is a hypothesis for a charged particle including the information of its momentum and spatial trajectory. The momentum measurement comes from the determination of the kink of the track in the magnetic field of HERA-B dipole magnet. Simplistically (if the magnetic field were uniform) the momenta are approximated with Equation 3.4. In reality the magnetic field of HERA-B is approximated with a magnetic field table which was determined by measurements at different points of the dipole magnet.

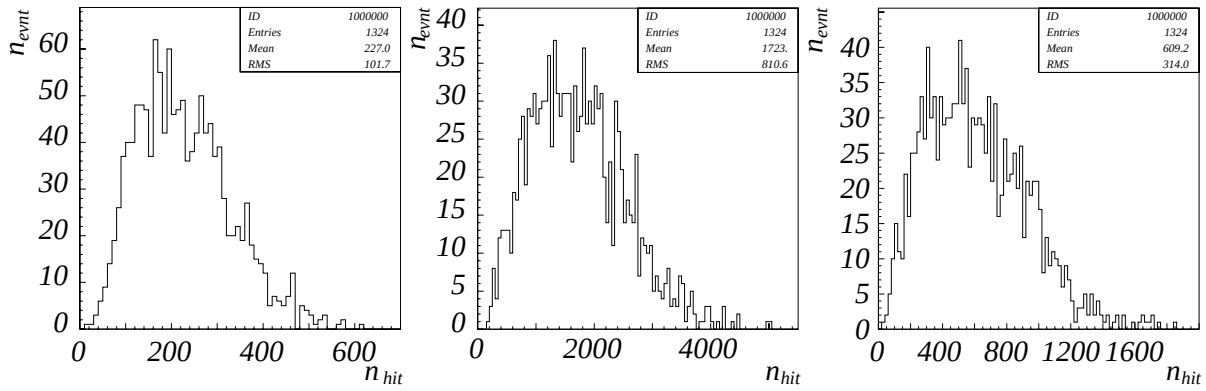

(a) (b) (c)

Figure 5.11: Number of hits per selected event in VDS, OTR and RICH sub-detectors (MC simulated sample).

It is crucial to correctly match the track segments downstream from the magnet, in the outer and inner trackers (main tracker), with those upstream from the magnet, in the vertex detector (VDS). In the standard reconstruction procedure track segments which meet the cuts of the matching criteria are combined into reconstructed tracks (see [27]). The segments in the main tracker are used only once, whereas the segments in the vertex detector are allowed to be used more than once, thus leaving also some fake tracks.

In the present analysis a track selection routine was used which selected the tracks in such a way that each segment was used at most once. First all track candidates with less than 6 reconstructed hits in the vertex detector and less than 11 hits in the main tracker were rejected. In case more than one remaining track was found with the same track segment, only the one with a better figure of merit (Q) was accepted. Q is defined as:

$$Q = n_{hits}^{VDS} + n_{hits}^{main} - \frac{\chi^2_{track}}{n_{df,track}},$$

where n_{hits}^{VDS} and n_{hits}^{main} are the number of hits in the vertex detector and number of hits in the main tracker respectively, χ^2_{track} and $n_{df,track}$ are the χ^2 and number of degrees of freedom of the track fit. The performance of such a track selection is summarized in Table 5.6 where the composition of reconstructed K and π are shown, as determined on simulated data. Tracks were sorted into 3 groups: true, the reconstructed track had the closest Monte Carlo track which corresponds to the chosen particle; wrong match, the reconstructed track is a wrong match of two segments; fake, the reconstructed track has a closest Monte Carlo track which does not correspond to the chosen particle.

particle	true	wrong match	fake
K	0.84	0.03	0.13
π	0.73	0.04	0.23

Table 5.6: Track quality for the reconstructed K and π candidates that were combined into D^0 candidates, as determined for a simulated data (a sample containing the decay of $D^0 \to K\pi$ in each event was used). The selection criteria is the particle identification cut on kaon, the opposite charges of reconstructed K and π, cut on the track to vertex distance of $0.025cm$ for both tracks and mass window cut.

5.4.2 Vertex reconstruction

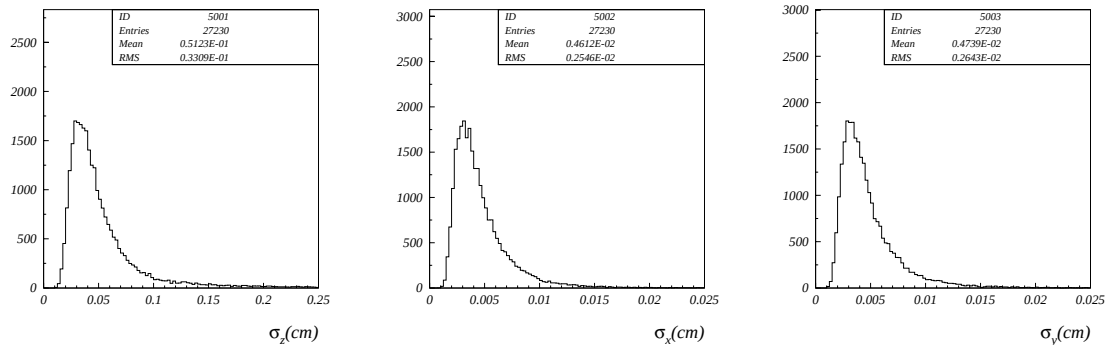

(a) (b) (c)

Figure 5.12: Distribution of events as a function of the resolutions of the fitted primary vertex in z (a), x (b) and y (c) directions, as determined on the simulated inelastic events.

Primary vertex After the track subsample in a given event was selected, according to procedure described in Section 5.4.1, the primary vertex was reconstructed. We first note that typical

primary vertex resolutions are $50\ \mu\mathrm{m}$ in the two transversal directions and $500\ \mu\mathrm{m}$ in the longitudinal direction along the proton beam direction for the standard reconstruction method (see Fig. 5.12). The target wire position, however, can be determined with much higher precision than a single reconstructed primary vertex, since it is expected that the target wire remains at the same coordinates (it moves perpendicular to the beam, but very slowly, to keep the interaction rate at the preset value). To reconstruct the target wire position, the position of primary vertices from many events can be averaged, obtaining the resolutions on the position of the wire much better than those of single primary vertex, especially in the direction perpendicular to the target wire. Thus, for determining the position of the primary interaction vertex, a combination was used of the position of the current reconstructed primary vertex ($\vec{P}^0_{prim} = (x^0_{prim}, y^0_{prim}, z^0_{prim})$) in the direction along the target wire, and the position of the target wire ($\vec{P}_{wf} = (x_{wf}, y_{wf}, z_{wf})$) in the other two directions. A special target reconstruction algorithm, also called the 'wire-following' algorithm, is described in Appendix E. In the present analysis two wires were used, 'inner 1' and 'below 1' (see Table 5.5), for which the primary vertex position was determined as follows:

$$\vec{P}^{\text{below 1}}_{prim} = (x^0_{prim}, y_{wf}, z_{wf}) \quad \text{for below 1}$$

and

$$\vec{P}^{\text{inner 1}}_{prim} = (x_{wf}, y^0_{prim}, z_{wf}) \quad \text{for inner 1.}$$

The primary vertex covariance matrix $\mathbf{V_{prim}}$ was similarly determined from the primary vertex reconstruction in the direction along the target wire and from the wire following procedure (see Appendix E) in the two directions perpendicular to the target wire. For example, in the case of the 'below 1' wire, which is oriented along x axis, σ_x was determined from the primary vertex fit (σ^{prim}_x), while σ_y and σ_z were determined from wire following resolution ($\sigma^{wf}_{y,z}$) and the intrinsic resolution of the target ($\sigma^{intrin}_{y,z}$). The covariance matrices were assumed to have a diagonal form. For the two different target wires used in the present analysis they are:

$$\mathbf{V}^{\text{below 1}} = \begin{Vmatrix} (\sigma^{prim}_x)^2 & 0 & 0 \\ 0 & (\sigma^{wf}_y)^2 + (\sigma^{intrin}_y)^2 & 0 \\ 0 & 0 & (\sigma^{wf}_z)^2 + (\sigma^{intrin}_z)^2 \end{Vmatrix}$$

and

$$\mathbf{V}^{\text{inner 1}} = \begin{Vmatrix} (\sigma^{wf}_x)^2 + (\sigma^{intrin}_x)^2 & 0 & 0 \\ 0 & (\sigma^{prim}_y)^2 & 0 \\ 0 & 0 & (\sigma^{wf}_z)^2 + (\sigma^{intrin}_z)^2 \end{Vmatrix},$$

where σ^{intrin}_z are the intrinsic resolutions of the target wires due to their spatial dimensions (see E.1).

Number of primary vertices A cut on the decay distance is crucial for improving the signal to background ratio in long lived D meson decays. It is important to reconstruct the primary and secondary vertex position to highest possible accuracy. To avoid ambiguities such as assigning the wrong primary interaction point to the secondary decay vertex, only events with single primary vertices were accepted. In case of a multi wire run we allowed that more primary

vertices are reconstructed if there is not more than 1 on each target wire. The events with two primary vertices reconstructed on the same target wire were rejected. For the distribution of events over the number of primary vertices reconstructed see Fig. 5.13(a).

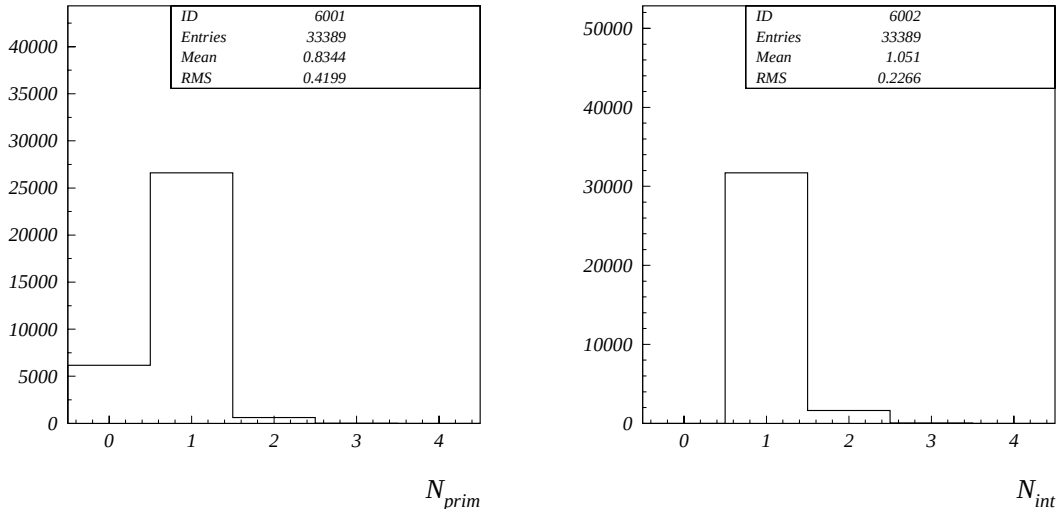

(a) (b)

Figure 5.13: Number of reconstructed primary vertices in MC sample with 0.1 interaction generated according to the Poisson distribution (a). In (b) the distribution of the number of generated interaction is shown. Only event with more than 0 interactions generated are plotted.

Secondary vertex After the primary vertex was reconstructed, pairs of tracks were selected as candidates for the K and π coming form the secondary decay vertex of D^0. The tracks from the selected pairs were required to have opposite charge. The two tracks were combined in the secondary vertex point, and fitted with the standard Grover package [41] for vertex reconstruction. The vertex was accepted if the distance of each track to the fitted vertex did not exceed $0.025\,\mathrm{cm}$. Furthermore the χ^2 probability of the secondary vertex was required to exceed 0.1.

Decay distance significance Decay distance is crucial to distinguish relatively rare events containing decays of the particles which are long lived, including charmed hadrons, from the inelastic interaction background. The number of surviving reconstructed D^0 mesons with increasing the decay distance cut can be found in Fig. 5.14.

The reconstructed primary vertices as well as secondaries are distributed with known resolution and target wire dimensions. Since the resolution depends on the event kinematics, simply cutting on spatial decay distance neglects some useful information. Therefore a cut on the significance of the decay distance S_{dd} was used instead, which is defined by the following equation:

$$S_{dd}^2 = \vec{d}^{\,T}\mathbf{V^{-1}}\vec{d}. \tag{5.10}$$

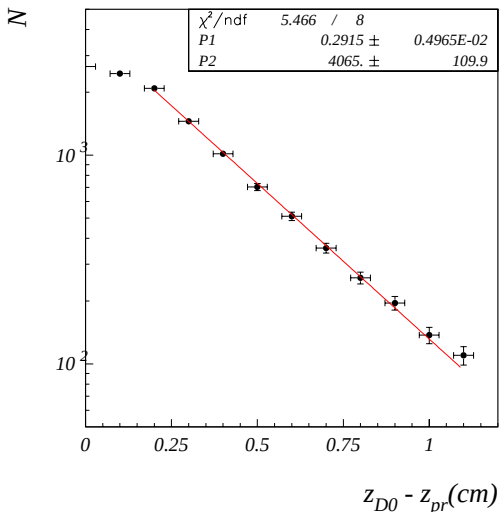

Figure 5.14: Number of surviving D^0 with increasing cut on decay distance for the signal Monte Carlo sample.

Here $\vec{d}$ is the 3D vector connecting the secondary to the primary vertex, and $\mathbf{V}$ is the sum of the primary vertex and secondary vertex covariance matrices:

$$\vec{d} = \vec{P}_{sec} - \vec{P}_{prim},$$

$$\mathbf{V} = \mathbf{V_{sec}} + \mathbf{V_{prim}}.$$

The secondary vertex covariance matrix $\mathbf{V_{sec}}$ was obtained form the vertex fit, while the primary vertex covariance matrix $\mathbf{V_{prim}}$ was determined both from the primary vertex reconstruction in the direction along the target wire and from the wire following procedure in the other two directions, as described at the beginning of this section.

The $S/\sqrt{B}$ ratio behavior with increasing decay distance significance cut is presented in Fig. 5.15(b). The signal was taken from D^0 Monte Carlo sample and the background from interaction triggered real date sample. A significance cut of 6 was used in order to optimize the $S/\sqrt{B}$ ratio.

5.4.3 Particle identification

Particle identification, based on the RICH detector, was used for identifying stable hadrons. The majority of tracks traversing the RICH detector are pions, thus cutting on the pion identification likelihood does not improve much the signal to background ratio. On the other hand, RICH is very efficient in separating kaons from the majority of pions (as we have seen in Section 4). We set the cut value of the RICH particle identification likelihood for kaons to 0.5 (with the RICH likelihood $lrk > 0.5$).

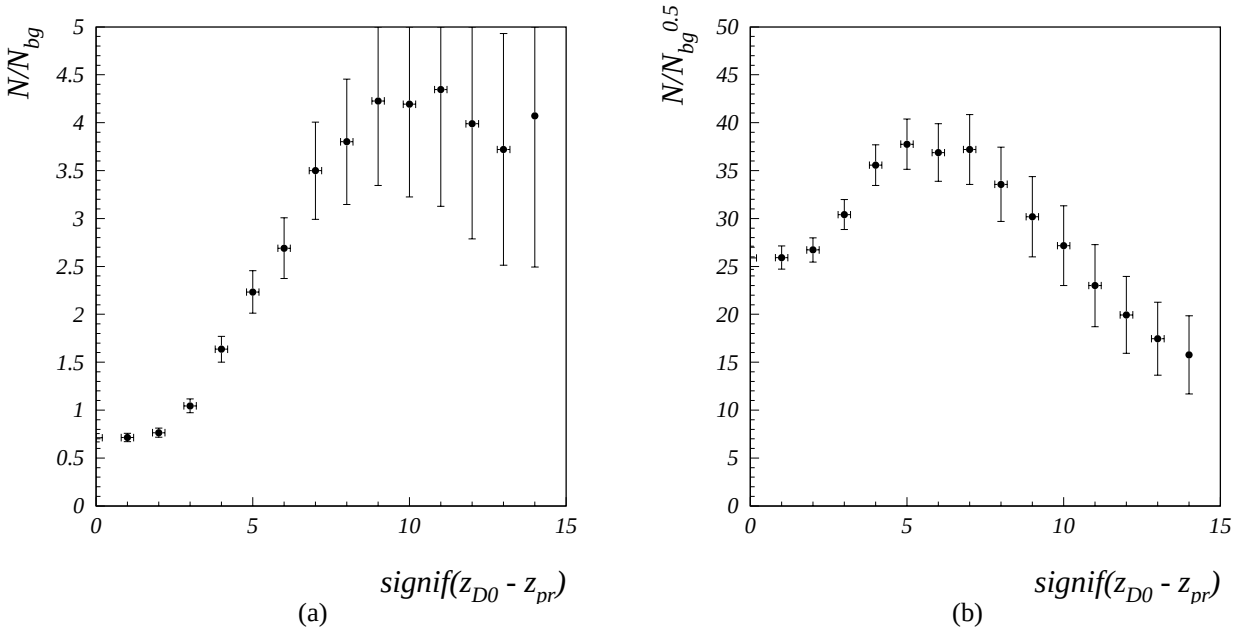

Figure 5.15: Optimization of the cut on the decay distance significance. S/B (a) and $S/\sqrt{B}$ (b), where signal (S) was taken from MC generated events and background from inelastic interaction real data. From (b) we see that a cut on the significance S_{dd} around 6 is the optimal. In the analysis, e.g. in the Fig. 5.19, we applied this cut.

5.4.4 Reconstruction of $D^0 \to K\pi$

In the case of D^0 two body decay into K and π, the kaon candidate was first identified in the RICH detector. It was then required that the charge of the pion is opposite to that of the kaon. No additional cut was applied on the kaon candidate. Since the majority of particles are pions their positive identification in RICH does not improve signal over background ratio. However, the pion track candidate was required to have momentum larger than $8\ \mathrm{GeV/c}$, to get rid of the low energy track background. The significance of the impact parameter (the impact parameter divided by its error) to the primary vertex of the pion was required to be larger than 2, to reject the combinatoric background coming from pions which are mostly produced directly at the primary vertex. The D^0 decay vertex candidate was reconstructed using standard Grover package [41] and was required to be separated from the target wire by more than $2\ \mathrm{mm}$. In addition, the significance of primary vertex to secondary vertex distance was required to be larger than 6, as described in the Section 5.4.2. The two tracks were required to be closer to the vertex than 0.25mm. The cuts applied in the analysis of the decay channel $D^0 \to K\pi$ are summarized in the Table 5.7.

quantity	cut value
number of primary vertices in event	$= 1$
coordinates of wire used	in $\perp$ direction
particle identification	
K: lrk	> 0.5
π: $lre + lrmu + lrpi$	> 0.05
momentum cuts	
K (due to particle id.)	$\gtrsim 10\ \mathrm{GeV/c}$
π	$> 8\ \mathrm{GeV/c}$
impact parameter	
$b/\sigma_b(\pi)$	> 2
secondary vertex	
$prob(\chi^2, N_{df})$	> 0.1
$z_{sec} - z_{prim}$	$> 0.2\ \mathrm{cm}$
S_{dd}	> 6
π, D^0 distance	$< 0.025\ \mathrm{cm}$
K, D^0 distance	$< 0.025\ \mathrm{cm}$

Table 5.7: Summary of selection criteria and cuts applied in reconstruction of $D^0 \to K\pi$.

5.4.5 Reconstruction of $D^{*+} \to D^0\pi^+ \to K^-\pi^+\pi^+$

The sum of masses $m(D^0) + m(\pi)$ is only about $6\ \mathrm{MeV}$ smaller than the rest mass of D^{*+} meson, $2.010\ \mathrm{GeV}$. The main discrimination of signal against background in the present analysis, due to specific kinematics of the decay, comes from the mass difference:

$$q = m(K\pi\pi) - m(K\pi) - m(\pi), \tag{5.11}$$

which peaks close to zero and has a very small width. The peak is narrow due to the fact that the errors in calculating invariant mass of three particles (in D^{*+} case) and two particles (D^0) are highly correlated, and therefore cancel to a large extent. These errors are due to different imperfections in track and vertex reconstruction (momenta, direction, alignment, calibration). The combinatorial background has a threshold at the q value of 0.

The π from the D^{*+} decay (it will be called slow pion and labeled π_s) and D^0 have very little energy in the D^{*+} rest frame. Their momenta in the rest frame of D^{*+} can be calculated:

$$p_{D^0} = p_{\pi^+} = \sqrt{(m^2_{D^{*+}} - (m_{D^0} + m_{\pi^+})^2)(m^2_{D^{*+}} - (m_{D^0} - m_{\pi^+})^2)} = 30\ \mathrm{MeV}$$

This is also the maximum transverse momentum p_t of D^0 and π_s relative to the D^{*+} direction. The typical Lorentzian boost factors (γ) of D^{*+} mesons are around 15, which means that both decay products, π_s and D^0, fly very close to the original direction of D^{*+}. The maximal angle between π_s and D^{*+} direction can be estimated as a ratio of the maximal p_t and p of the pion in the HERA-B frame which is approximately 0.014. The distributions of reconstructed angles for signal tracks from Monte Carlo simulated sample and for the interaction triggered data acquired are compared in Fig. 5.16. The upper limit for the angle between π_s and D^{*+} is slightly higher than the above estimate due to the reconstruction resolution. Furthermore, it turns out that the momenta of the kaon (K) and the slow pion (π_s) can be combined into another quantity m_{wrong} (Fig. 5.17 compares the Monte Carlo simulated signal tracks with the acquired data sample), which can also be useful for improving the signal.

In the present analysis we decided to reconstruct the D^0 candidates using the same cuts as for the reconstruction of $D^0 \to K^-\pi^+$ described in the last section, we only loosen a cut on the decay distance significance from 6 to 3. We then combine the D^0 candidates with π_s candidate tracks, for which the distance to the D^0 reconstructed vertex was smaller than $0.025\ \mathrm{cm}$. The candidate for the slow pion π_s has to pass, according to the above discussion, very close to the D^0 decay vertex. At the maximal π_s D^{*+} opening angle and a decay distance of $1\ \mathrm{cm}$, the impact parameter of π_s to the D^0 vertex would be of the order of the secondary vertex resolution.

The cuts applied in the analysis of $D^{*+} \to D^0\pi^+ \to K^-\pi^+\pi^+$ are summarized in the Table 5.8.

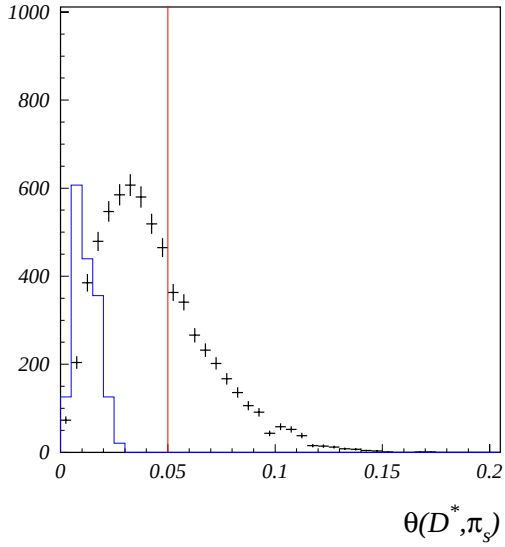

Figure 5.16: The angle between D^{*+} and π_s (direct π from D^{*+} decay) directions as reconstructed for signal tracks from Monte Carlo simulated sample (blue histogram) and from interaction triggered data (black histogram with error bars).

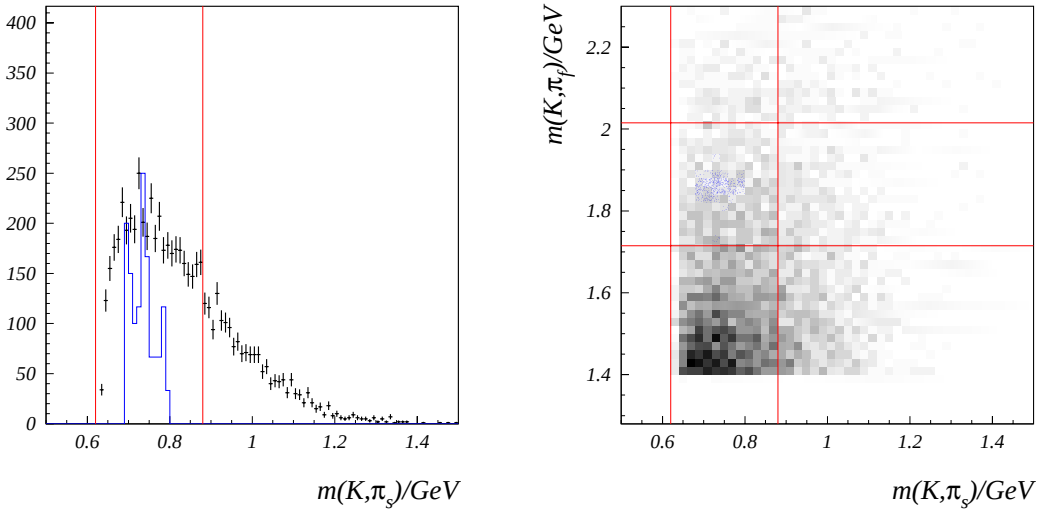

(a) (b)

Figure 5.17: (a) Invariant mass of $K\ \pi_s$ combination, where the kaon form D^0 decay is combined with the slow pion from D^{*+}. The signal tracks form narrow distribution between 0.7 GeV and 0.8 GeV. (b) two dimensional distribution showing the D^0 meson reconstructed mass versus the invariant mass of $K\ \pi_s$ combination. In both diagrams blue indicates the signal Monte Carlo tracks and black (gray) the interaction triggered data acquired.

quantity	cut value
number of primary vertices in event	$= 1$
coordinates of wire used	in $\perp$ direction
particle identification	
lrk	> 0.5
$lre + lrmu + lrpi$ for π_f	> 0.05
momentum cuts	
K (due to particle id.)	$\gtrsim 10$ GeV/c
π_f	> 8 GeV/c
impact parameter b/σ_b	
π_f	> 2
secondary vertex	
$prob(\chi^2, N_{df})$	> 0.1
$z_{sec} - z_{prim}$	> 0.2 cm
S_{dd}	> 3
π_f, D^0 distance	< 0.025 cm
K, D^0 distance	< 0.025 cm
π_s (slow pion) momentum	1 GeV/c $<$ p < 7.5 GeV/c
π_s to D^0 distance	< 250 μm
$\theta(D^{*+}, \pi_s)$ opening angle	< 50 mrad
K, π_f invariant mass	$\lvert m(K, \pi_f) - 1.83 \text{ GeV}\rvert < 0.15$ GeV
K, π_s invariant mass	$\lvert m(K, \pi_s) - 0.75 \text{ GeV}\rvert < 0.13$ GeV

Table 5.8: Summary of selection criteria and cuts applied in reconstruction of $D^{*+} \to D^0\pi_s^+ \to K^-\pi_f^+\pi_s^+$. π_s labels relatively slow pion which comes from the D^{*+} decay and π_f the pion from the subsequent D^0 decay.

5.4.6 The Analysis Efficiency

In this analysis D^0 decays into K and π and D^{*+} decays into K and two π's were reconstructed. The selections described above were applied. The overall analysis efficiency (ϵ_{ana}) consists of: geometrical acceptance (ϵ_{geo}), reconstruction efficiency (ϵ_{reco}) and the efficiency of our cuts (ϵ_{cuts}) applied to improve signal over background. The ϵ_{ana} can be estimated with their product:

$$\epsilon_{ana} \approx \epsilon_{geo}\, \epsilon_{reco}\, \epsilon_{cuts}$$

which amounts to a value of an order of 1%. However, because the possible correlations between the three efficiencies, the analysis efficiency, ϵ_{ana}, is properly determined by using the above described analysis on the Monte Carlo signal sample. In the simulation the number of generated D^0 mesons that decayed into K and π is known. The number of chosen decays that are reconstructed in the same sample by applying the same cuts as in the analysis of real data can also be determined, and the corresponding overall efficiency is determined as the ratio of the two numbers. In Fig. 5.18 the reconstructed $D^0 + c.c.$ and $D^{*+} + c.c.$ are shown. The numbers of reconstructed decays are gathered in the Table 5.9 and are used to determine the analysis efficiencies.

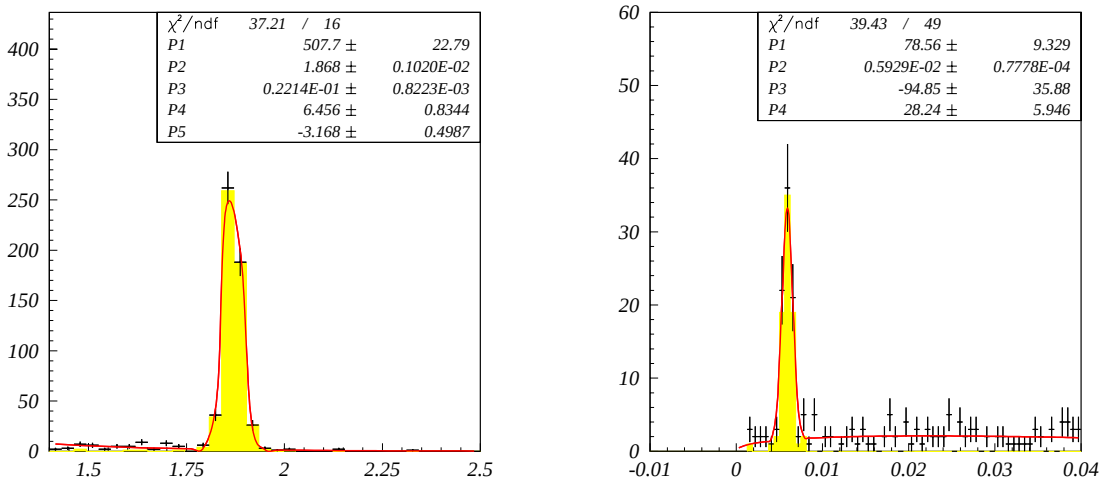

(a) (b)

Figure 5.18: The reconstructed D^0 and D^{*+} decays after all the analysis cuts (both particle and c.c. are included) obtained from Monte Carlo sample with $D^0 \to K\pi$ decay simulated in each event. In yellow only the tracks coming from the actual decay products of the two decays are considered.

reaction	N_{gen}	N_{ana}	ϵ_{ana}
$D^0 \to K^-\pi^+$+c.c.	71160	508 ± 23	0.00714 ± 0.00032
$D^{*+} \to K^+\pi^-\pi^-$+c.c.	27213	78.56 ± 6.9	0.00289 ± 0.00034

Table 5.9: Overall analysis efficiency ϵ_{ana} is determined from the Monte Carlo simulated reactions. N_{gen} is the number of reactions generated, N_{ana} the number of reactions which were reconstructed using the same analysis chain as in the real data case and their ratio $\epsilon_{ana} = \frac{N_{ana}}{N_{gen}}$ is the overall efficiency of the analysis.

5.5 Real data

Table 5.5 summarizes the data sample used in the present analysis and their different target settings. In the next two sections the two chosen channels as reconstructed from that sample will be described. The errors on the measured values were assumed to be uncorrelated.

5.5.1 $D^0 \to K\pi$

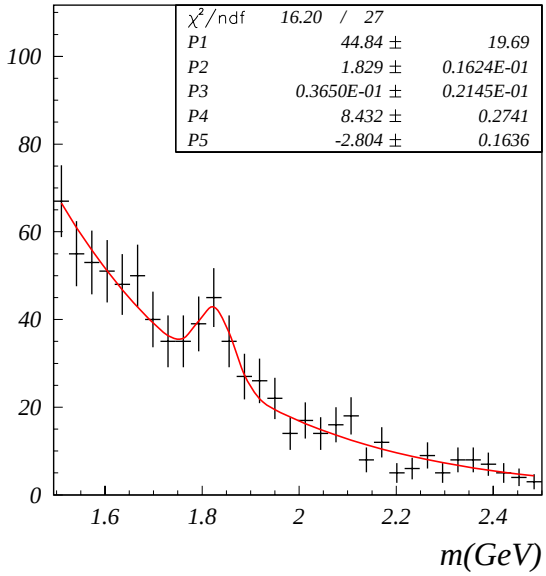

Figure 5.19: Reconstructed $D^0 \to K\pi$ decays from the runs 19170, 19179 and 19185 with over 16 million interaction triggered events.

In Fig. 5.19 the mass distribution is fitted with a Gaussian function to model the signal and exponential function as an estimate of the background. In Fig. 5.20 the D^0 peak is plotted for each target material separately. The numbers of reconstructed D^0 decays are summarized in Table 5.10, where in the last column the total production cross section for D^0 are computed according to Equation 5.7 with taking into account Equation 5.9.

A	wire	N_{inel}^{tgrd}	$N_{det}(D^0)$	$N_{tot}(D^0)$	$\sigma_P(D^0)/mb$
12.0	'below 1'	11.4M	22 ± 9	81200 ± 36500	$\mathbf{1.70 \pm 0.75}$
184	'inner 1'	5.0M	26 ± 10	96000 ± 37500	$\mathbf{31.9 \pm 12.5}$
total		16435743	45 ± 20	166000 ± 74000	

Table 5.10: D^0 meson production cross section.

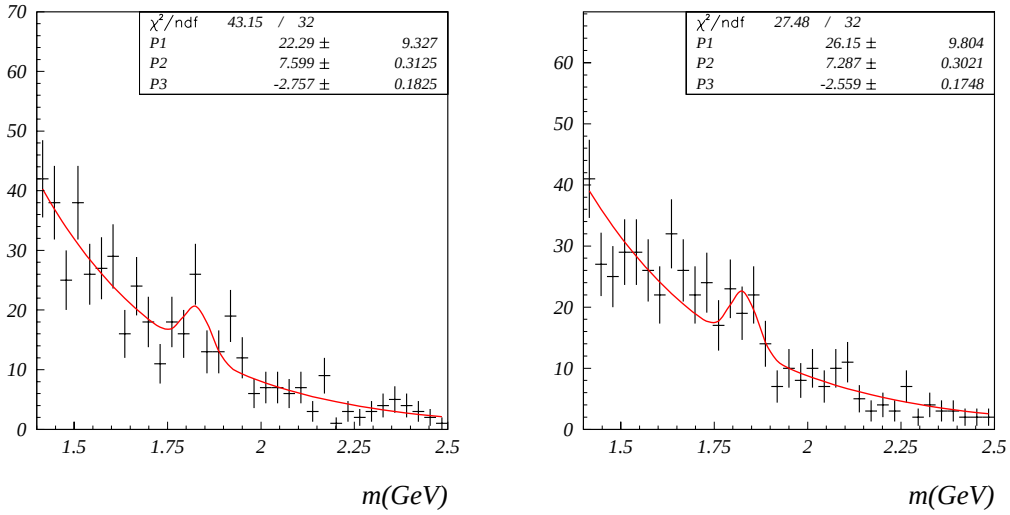

(a) (b)

Figure 5.20: Reconstructed $D^0 \to K\pi$ decay of D^0 mesons produced at (a) carbon wire (A=12.0) and at (b) tungsten wire (A=184). In the fit only the number under the Gaussian was fitted with assumed values of mass and width from the overall fit in Fig. 5.19.

The D^0 production cross section per nucleon is determined by (see Equation 5.1):

$$\sigma_{0,P}(D^0) = \frac{\sigma_P(D^0)}{A^{\alpha_{D^0}}} \tag{5.12}$$

Now we assume a certain value of α based on discussion in Section 5.2 where two estimates were given in Equations 5.2 and 5.3. The resulting cross section is given in the Table 5.11.

A	wire	$\sigma_P(D^0)/\mathrm{mb}$	$\sigma_{0,P}(D^0)/(\mu\mathrm{b/nucleon})$	
			$\alpha_{D^0} = 1.02 \pm 0.04$	$\alpha_{D^0} = 0.996 \pm 0.037$
12.0	'below 1'	1.70 ± 0.75	136 ± 56	144 ± 60
184	'inner 1'	31.9 ± 12.5	157 ± 60	178 ± 76
average			$\mathbf{147 \pm 41}$	$\mathbf{159 \pm 48}$

Table 5.11: Summary of the measured D^0 production cross section per nucleon. The errors are dominated by available statistics.

We can also fit the α_{D^0} to be consistent with our result, i.e. that $\sigma_{0,P}(D^0)$ in Equation 5.12 is independent of the material used. Thus:

$$\frac{\sigma_{P,W}(D^0)}{A_W^{\alpha_{D^0}}} = \frac{\sigma_{P,C}(D^0)}{A_C^{\alpha_{D^0}}},$$

where indices W and C indicate the material used. We get:

$$\alpha_{D^0} = \ln \frac{\sigma_{P,W}(D^0)}{\sigma_{P,C}(D^0)} / \ln \frac{A_W}{A_C}. \tag{5.13}$$

By taking $A_C = 12.0$ and $A_W = 184$ the following expression results:

$$\alpha_{D^0} = \alpha_{inel} + \frac{\ln N_{det,W}/N_{det,C}}{2.730} + \frac{\ln N_{inel,C}/N_{inel,W}}{2.730} = 1.07 \pm 0.20,$$

which is consistent with 1, as well as with both cited numbers in Equations 5.2 and 5.3.

For comparison of our result with the theoretical prediction we will use the $\alpha_{D^0} = 1.02 \pm 0.04$ as measured by the E789 experiment at Fermilab [34]. The D^0 production cross section per nucleon is then $\sigma_{0,P}(D^0) = 147 \pm 41$. The $c\bar{c}$ pair production cross section is determined by taking into account an average number of $F_{D^0} = 1.19$ D^0 mesons produced per $c\bar{c}$ pair (see Table 5.3):

$$\sigma_{0,P}(c\bar{c}) = \frac{\sigma_{0,P}(D^0)}{1.19} = (124 \pm 34)\ \frac{\mu\text{b}}{\text{nucleon}},$$

which is at the upper limit of the theoretical prediction. The result is presented in Fig. 5.21 together with theoretical predictions and existing measurements.

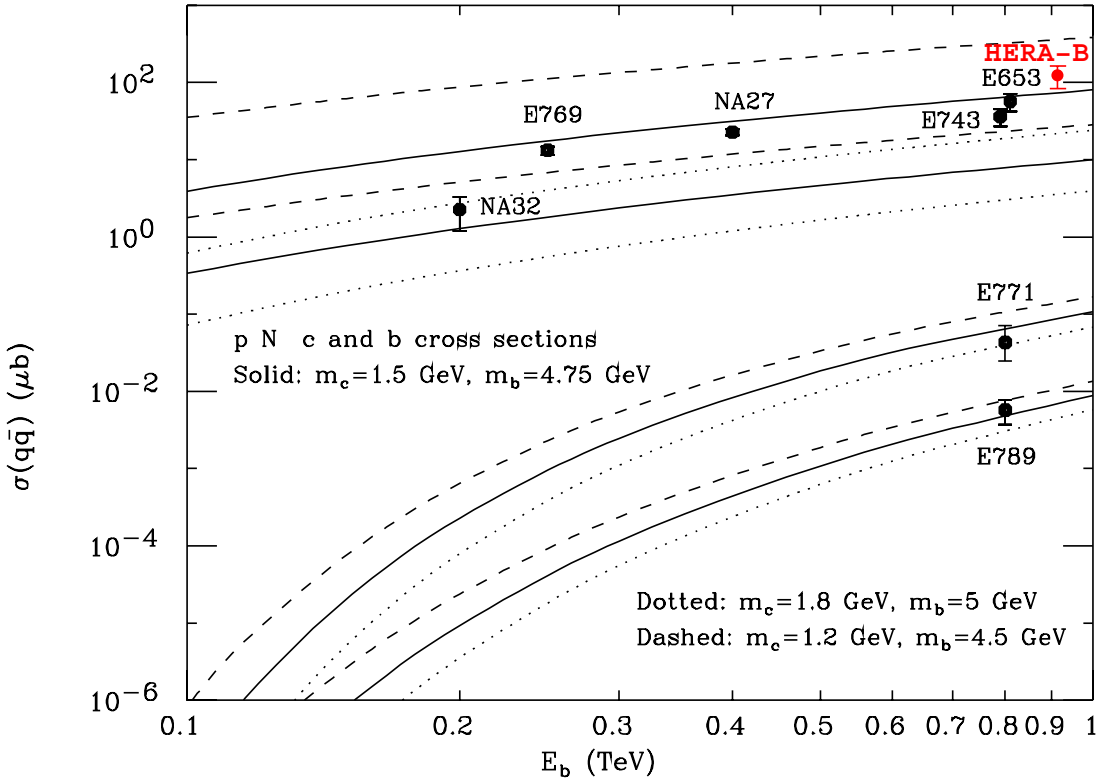

Figure 5.21: Our result for $c\bar{c}$ production cross section shown together with theoretical predictions and published measurements [36].

5.5.2 $D^{*+} \to D^0\pi^+ \to K^-\pi^+\pi^+$

Again the efficiency of the analysis was estimated by using Monte Carlo simulation, $\epsilon_{ana}(D^{*+}) = 0.00289 \pm 0.00034$. The charged D^{*+} meson candidates reconstructed in the selected data sample (see Table 5.5) are plotted in the Figs. 5.22 and 5.23. In this case the threshold behaviour of the combinatorical background was modeled by sum of a square root and linear function and the signal was approximated with a Gaussian function. The results are summarized in the Table 5.12 which utilizes the Eqs. 5.7 and 5.9, with obvious replacements, for derivation of the cross section value from the number of reconstructed candidates ($N_{det}(D^{*+})$). In the last row of the table we assumed the same value of the α parameter in production of D^{*+} as in the case of D^0 ($\alpha_{D^0} = 1.02 \pm 0.036$). The average production cross section per nucleon is:

$$\sigma_{0,P}(D^{*+}) = (158 \pm 63)\ \frac{\mu\mathrm{b}}{\mathrm{nucleon}}.$$

A	wire	N_{inel}^{tgrd}	$N_{det}(D^{*+})$	$N_{tot}(D^{*+})$	$\sigma_P(D^{*+})/\mathrm{mb}$	$\sigma_{0,P}(D^{*+})\ /(\mu\mathrm{b/nucl.})$
12.0	'below 1'	$11.4\ 10^6$	7.9 ± 3.8	2700 ± 1300	2.4 ± 1.2	177 ± 87
184	'inner 1'	$5.0\ 10^6$	5.4 ± 3.8	1900 ± 1300	26 ± 18	118 ± 84
total		16435743	13.3 ± 5.3	4600 ± 1800		$\mathbf{158 \pm 63}$

Table 5.12: Summary of measured charged D^{*+} meson production cross section.

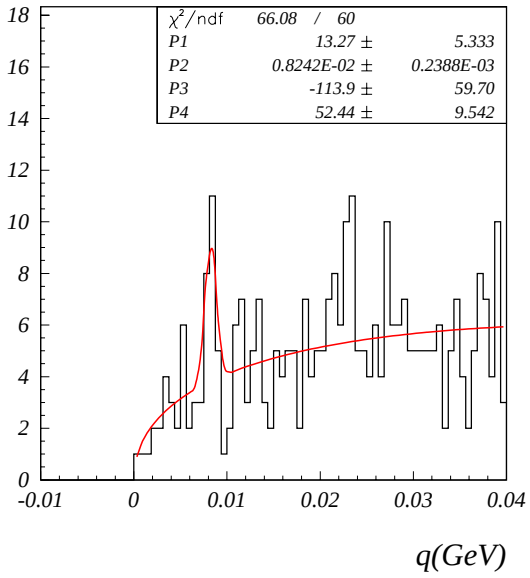

Figure 5.22: Reconstructed $D^{*+} \to D^0\pi \to K\pi\pi$ decays in the runs 19170, 19179 and 19185 with over 16 million interaction triggered events.

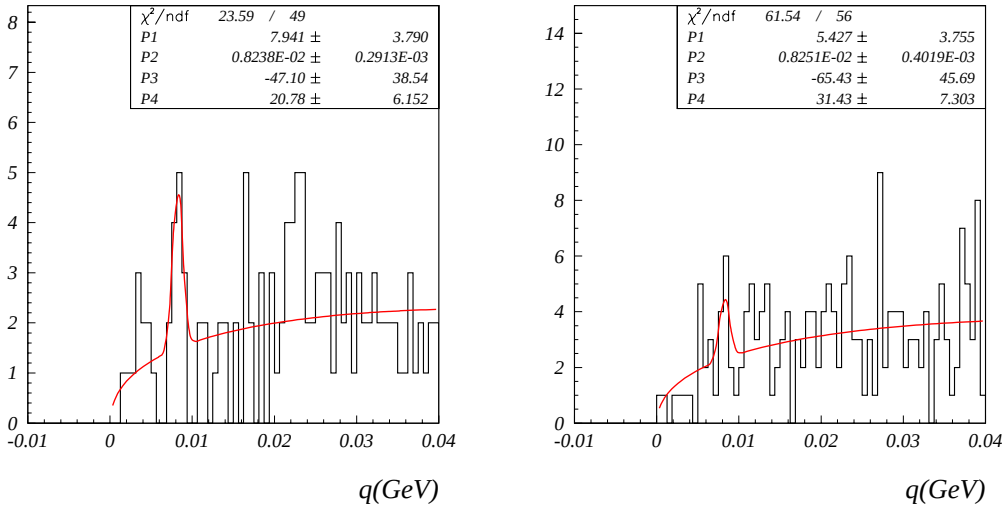

(a) (b)

Figure 5.23: Reconstructed $D^{*+} \to D^0\pi \to K\pi\pi$ decays of charged D^{*+} (and D^{*-}) mesons produced at (a) carbon wire (A=12.0) and at (b) tungsten wire (A=184).

5.6 Systematic error evaluation

In this section three different contributions to the systematic error in the cross section measurement are evaluated.

Monte Carlo acceptance The overall acceptance for the two decays discussed in Section 5.5 was determined from the Monte Carlo simulated sample, which was generated using slightly different geometry from the present geometry of the HERA-B spectrometer. Especially superlayers 7 and 8 of the VDS detector were positioned further away from the proton beam in the geometry used for simulation compared to the positions used in the real data acquisition. Thus the efficiency estimated based on the Monte Carlo sample is too small. In Figs. 5.24 and 5.25 the acceptances for the two different geometries are compared for superlayers 7 and 8 respectively.

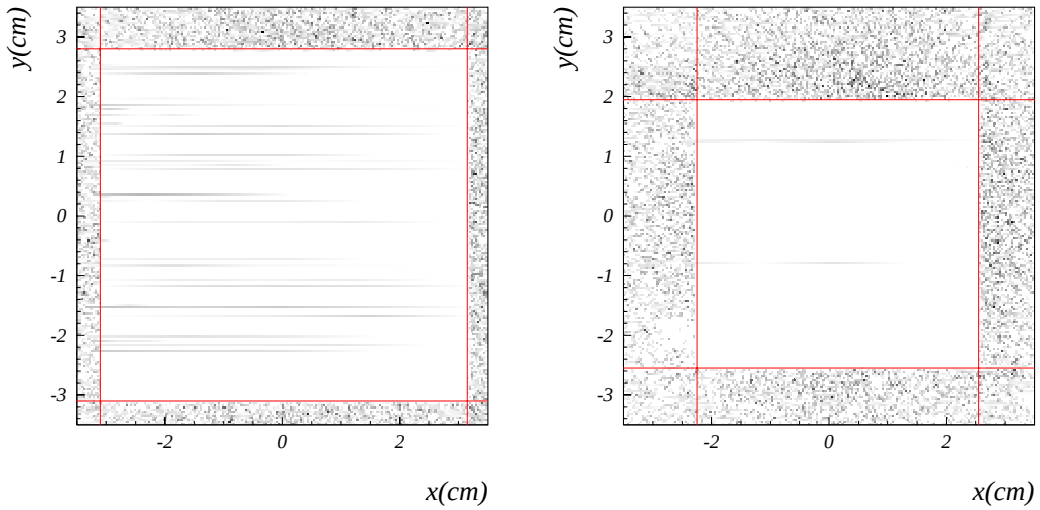

(a) (b)

Figure 5.24: The inner part of the acceptance for superlayer 7 of the VDS detector as used in geometry for Monte Carlo simulation (a) and in recording the real data (b).

To estimate the variation of the geometric acceptance, the effect was simulated by demanding that the D^0 and D^{*+} decay tracks have associated more than 6 reconstructed hits in the VDS detector and more than 10 reconstructed hits in the OTR part of the main tracker. If the tracks with less than 6 hits in VDS detector pass the region of the acceptance difference in superlayers 7 or 8, then 4 or 2 additional hits were assigned to the corresponding track, respectively. The relative increase in the fraction of the decays that survive the analysis cuts is 0.03, which would cause a similar decrease in the value of D^0 and D^{*+} production cross section.

In the similar way the slow pion, π_s, from decay of the charged D^{*+} can be treated. In this case the effect is larger, as expected, due to small transversal momentum of this pion,

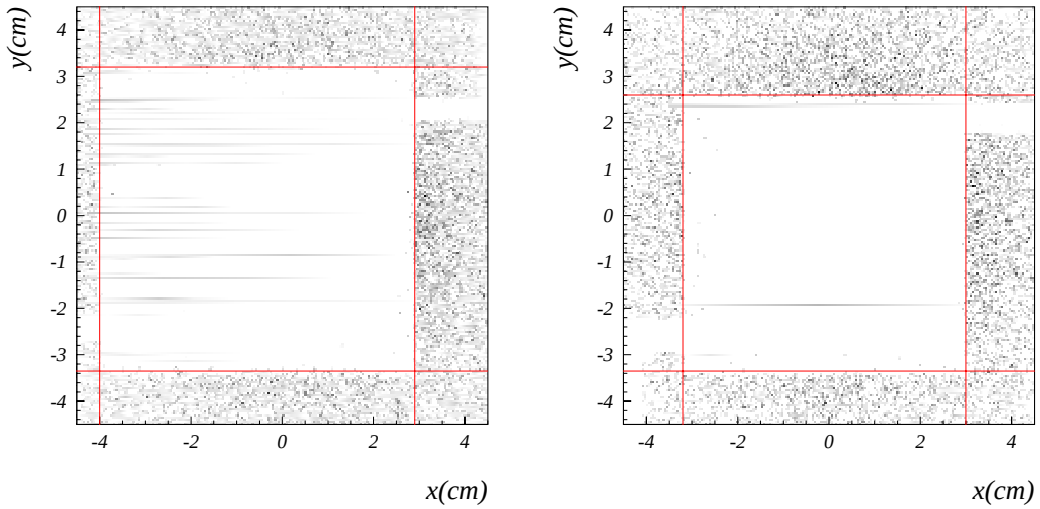

(a) (b)

Figure 5.25: The inner part of the acceptance for the superlayer 8 of the VDS detector as used in geometry for Monte Carlo simulation (a) and in recording the real data (b).

which tends to escape the inner border of acceptance. The D^{*+} production cross section would decrease for 0.07. It turns out that this effects is almost uncorrelated with the increase in the D^0 acceptance.

RICH particle identification The analysis efficiency was obtained based on the efficiency of reconstruction of the $D^0 \rightarrow \pi K$ decay in the Monte Carlo simulated sample. The RICH was used for kaon particle identification in the presented analysis with certain efficiency ϵ_{RICH}, which contributes to the overall analysis efficiency. It is expected that this efficiency degrades with the increasing occupancy, because of the higher overlap of the rings on the photon detector. The typical occupancies of the RICH subdetector for events that passed the analysis cuts are much larger than the RICH occupancies reproduced in the Monte Carlo signal sample, and it is much closer to the occupancy (see Fig. 5.26) that is generated by mixing 1 inelastic interaction event with the number of inelastic events generated according to the Poisson distribution with the mean equal to 2 (such sample is usually labeled '$1 + \langle 2 \rangle$').

Thus we expect that the efficiency for particle identification in the RICH was overestimated when used for calculating the production cross sections. The effect is seen on the Fig. 5.27, where the identification efficiency for kaons is shown for the signal Monte Carlo sample, and for a sample of simulated $1 + \langle 2 \rangle$ inelastic events. The first was used in determining the analysis efficiency, ϵ_{ana}, while the latter describes the RICH occupancy in the real data better and is thus closer to the RICH efficiency in the real data analysis. The ratio of both is the scale factor with which ϵ_{ana} decreases and consequently the value of the cross section increases. By taking the ratio of the two particle identification efficiencies the plot in Fig. 5.28 is obtained, which shows

the relative decrease of the ϵ_{RICH} value for 0.09. This would cause a similar relative increase in the cross section. As a consistency check we compare in Fig 5.29 the kaon identification efficiency as determined from $\phi \rightarrow KK$ decays on the real data (run 19170), to the kaon identification efficiency determined on signal MC simulated data (Fig5.27(a)) scaled by the factor 0.91 as derived from Fig. 5.28. The scaled efficiency seems to reproduce the measured one quite well.

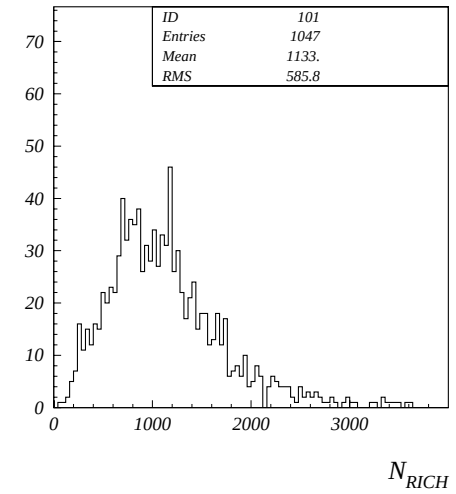

(a)

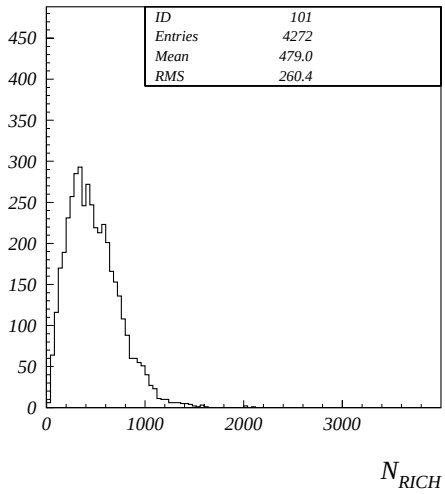

(b)

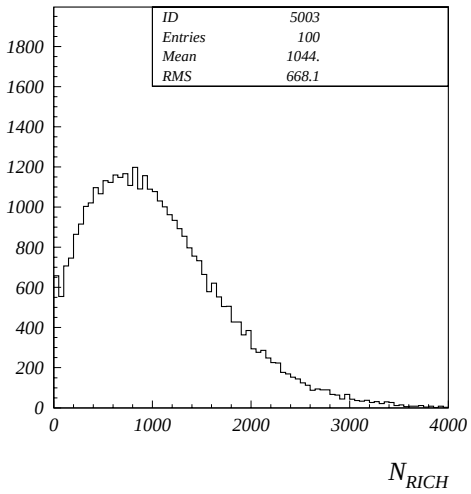

(c)

Figure 5.26: Number of hits reconstructed in the RICH subdetector for the real data events that passed the analysis cuts (a), for the Monte Carlo simulated events containing neutral D^0 decay (b) and for the events with $1 + \langle 2 \rangle$ inelastic interaction simulated.

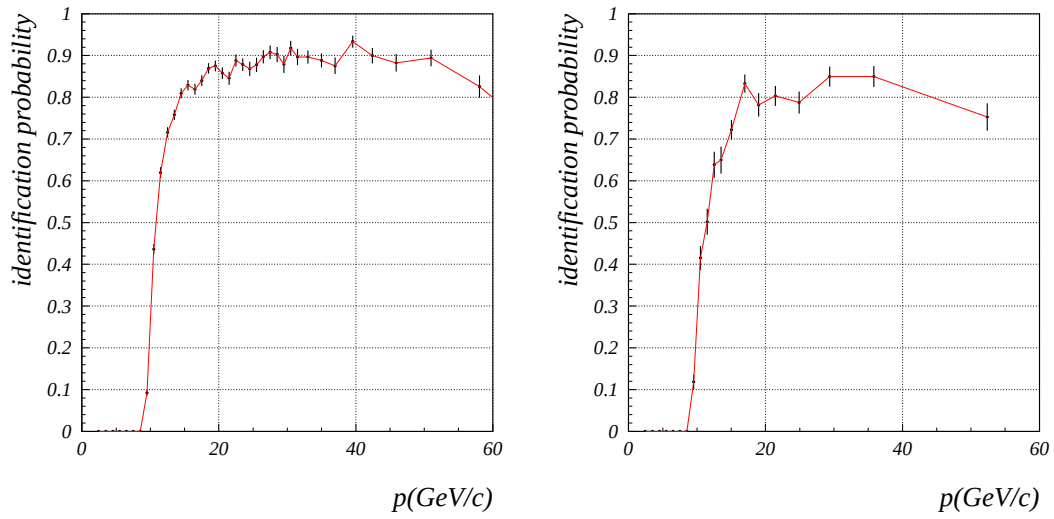

(a) (b)

Figure 5.27: The RICH particle identification efficiency for the signal Monte Carlo reconstructed sample (a). In (b) the $1 + \langle 2 \rangle$ inelastic interaction simulated sample was reconstructed, which matches much better the occupancy of the RICH detector in the case of real data.

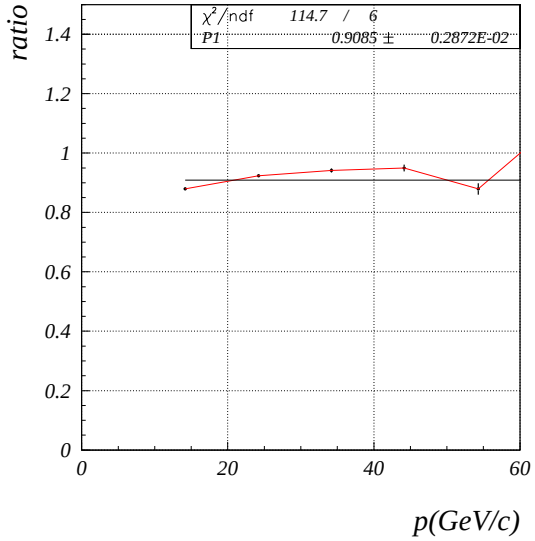

Figure 5.28: The ratio of the two identification efficiencies in Fig. 5.27

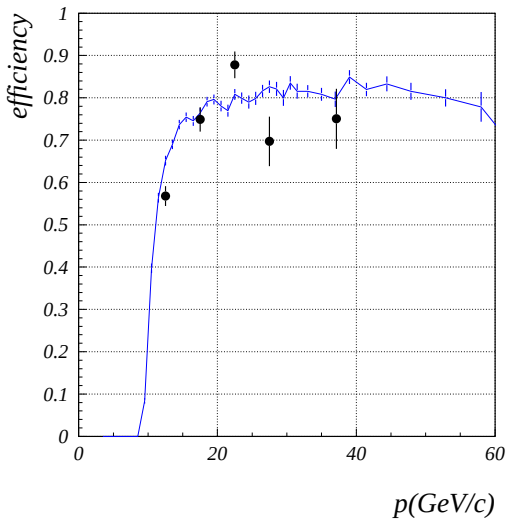

Figure 5.29: Kaon identification efficiency as determined from $\phi \rightarrow KK$ decays on the real data (run 19170) compared to the kaon identification efficiency determined on signal MC simulated data (Fig5.27(a)) scaled by the factor 0.91 as derived from Fig. 5.28. Blue points connected with a line correspond to the scaled MC and black points to the real data.

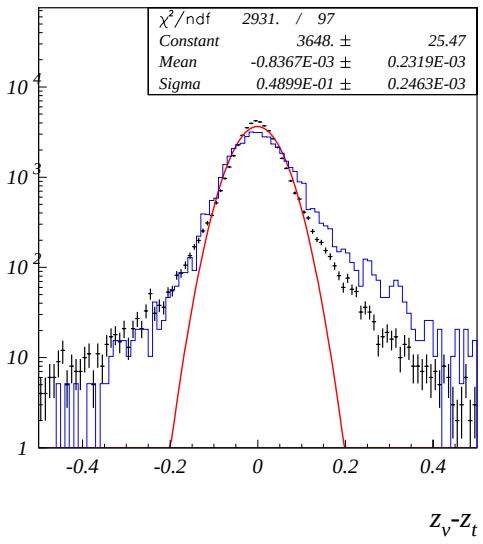

Figure 5.30: The distribution of the difference in z direction of the reconstructed primary vertex and target obtained with the wire-following procedure. The points with error bars correspond to the real data, the full histogram to the Monte Carlo simulated data and the curve to the Gaussian fit to the real data.

Decay distance In the present analysis one of the crucial cuts was the cut on the decay distance significance, S_{dd}, as defined in Eq. 5.10. It turns out that the primary vertex resolution, and consequently the reconstructed wire position resolution, on Monte Carlo data is worse than the corresponding resolution on the real data (see Fig. 5.30). Consequently the significance cut applied to Monte Carlo is stronger than the same cut applied to the real data. The optimal S_{dd} cut was determined in Fig 5.15, and the value of 6 was used in the analysis, as well as in the efficiency determination from the Monte Carlo simulated data.

To estimate the resulting effect on the cross section determination, the following procedure was applied. First note that in addition to the significance cut, we have also applied a cut on the minimal decay distance of the D^0 vertex to the primary of 0.2 cm. The effect of the significance cut would be reduced if we increase the decay distance cut. If the significance cut would cause the same effect on Monte Carlo as it does on the real data, the cross section value would be independent of the decay distance cut. In Fig. 5.31 two cases are shown, first for the value of S_{dd} set to 6 in both real and Monte Carlo simulated data, and the second where this value was changed to 5.5 for the Monte Carlo case. This latter seems to be more consistent with a constant value. The cross section value is in this case reduced by 18 μb which corresponds to a decrease by 12%.

External sources In the determination of cross section values we used some external measurements by themselves burdened with errors (statistical or systematic). They also contribute to the systematic error of our measurement. These values are the branching ratios (listed in Table 5.4), the parameters describing the nuclear effects α_{D^0} (see Eq. 5.2) and α_{inel} (Table 5.2) and finally the inelastic cross section value (see Table 5.2). In calculating the net effect of these

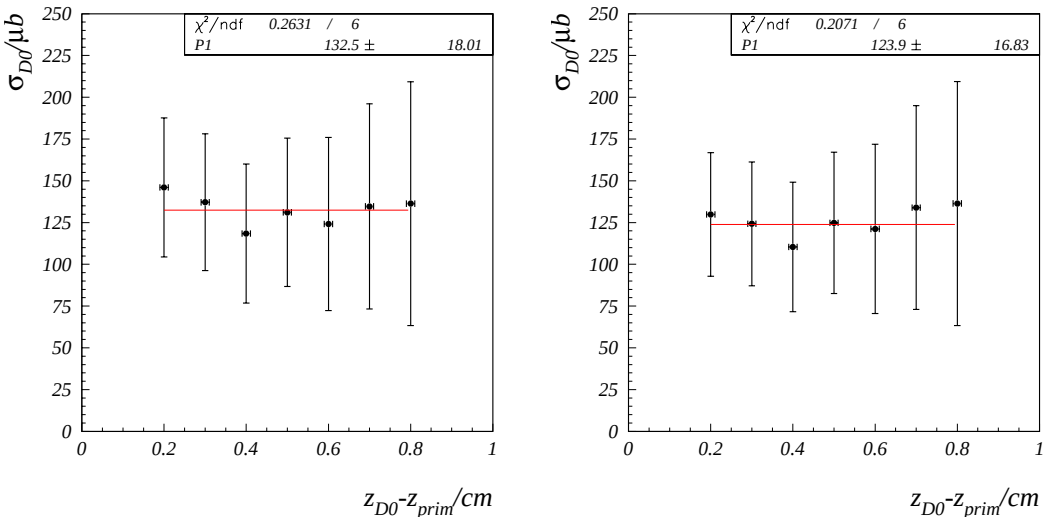

(a) (b)

Figure 5.31: Variation of D^0 production cross section with increasing cut on the decay distance. In (a) the decay significance cut $S_{dd} = 6$ was used for real and Monte Carlo data, while in (b) the significance cut was changed to $S_{dd} = 5.5$ for Monte Carlo case.

contributions for the measurement on C and W target wire separately it was assumed that the errors are uncorrelated. Note that the effect of error in α parameter is much more pronounced in the case of W than it is in the case of C target wire, due to its larger A number. In determining the total systematic error due to external sources we assumed the total correlation in this error made in the two cases of different target materials and was estimated to be $\pm 15\%$ in the case of D^0 and $\pm 13\%$ in the case of D^{*+} production cross section.

The total systematic error was determined by summing all the above effects in the following way. First the systematic errors, listed in Table 5.13, were assumed to be uncorrelated. The relative values were summed in squares separately for negative and for positive contributions. Note that the effects described above cancel out in the determination of parameter α that describes the nuclear dependence of the cross section (see Eq. 5.13).

The D^0 meson production cross section becomes:

$$\sigma_{0,P}(D^0) = (147 \pm 41^{+25}_{-28}) \, \frac{\mu\mathrm{b}}{\mathrm{nucleon}}. \tag{5.14}$$

The D^{*+} meson production cross section amounts to:

$$\sigma_{0,P}(D^*) = (158 \pm 63^{+25}_{-32}) \, \frac{\mu\mathrm{b}}{\mathrm{nucleon}}. \tag{5.15}$$

Finally, the $c\bar{c}$ quark pair production cross section as derived from the D^0 meson production

source	rel. error in $\sigma_{0,P}(D^0)$	rel. error in $\sigma_{0,P}(D^{*+})$
VDS geometrical acceptance D^0	-0.03	-0.03
VDS geometrical acceptance π_s	—	-0.07
RICH ϵ	$+0.09$	$+0.09$
decay distance significance	-0.12	-0.12
external sources	± 0.15	± 0.13
net effect	$^{+0.17}_{-0.19}$	$^{+0.16}_{-0.20}$

Table 5.13: Systematic errors in the cross section measurement.

cross section is:

$$\sigma_{0,P}(c\bar{c}) = (124 \pm 34^{+21}_{-24}) \, \frac{\mu\mathrm{b}}{\mathrm{nucleon}}, \tag{5.16}$$

where the theoretical uncertainty in the fragmentation fraction (see Table 5.3) was not taken into account.

6 Summary

The present thesis is a part of the advanced commissioning stage of the HERA-B spectrometer. Three issues are discussed, overall alignment of the whole spectrometer, the calibration of one of the crucial components, the Ring Imaging Cherenkov Counter (RICH), and finally, a measurement of the D^0 and D^{*+} production cross section.

The three methods used for overall ('global') alignment are reviewed and some typical results are shown. The results show a sizeable improvement introduced by the global alignment both in the geometrical track based residuals, as well as in physical signals, such as the J/Ψ meson two muon decay. The magnet-off data collected in 2002 brought the HERA-B alignment to the next level of accuracy. The procedure of global alignment with magnet on remains essential for checking the quality of the alignment and for eventually aligning the spectrometer in the long periods of data taking between two consecutive data samples taken in magnet off mode.

The particle identification performance of the RICH detector was determined on the sample of recorded two body decays of hadrons, $\phi \to K^+K^-$, $\Lambda \to \pi p$ and $K^0_S \to \pi^+\pi^-$, where the identity of the decay product is known. For performance of particle identification an accurate knowledge of the particle trajectories is essential. It was shown that with improvements in alignment, and consequently in the determination of the particle track parameters, the RICH performance improves significantly.

Finally, the cross section was measured for the production of D^0 mesons at two targets made of carbon and tungsten. Its average value is $\sigma_{0,P}(D^0) = (147 \pm 41^{+25}_{-28}) \mu\mathrm{b/nucleon}$. The $c\bar{c}$ quark pair production cross section based on this number is: $\sigma_{0,P}(c\bar{c}) = (124 \pm 34^{+21}_{-24})\ \mu\mathrm{b/nucleon}$, which is consistent with extrapolated measurements at lower energies, and seems to favor values at the higher range of the theoretical predictions. The nuclear effects in the D^0 production process were estimated by comparing the production cross section on two different wire materials and result in an estimate of the α parameter, $\alpha_{D^0} = 1.07 \pm 0.20$. The production cross section of charged excited D^{*+} meson was measured to be $\sigma_{0,P}(D^*) = (158 \pm 63^{+25}_{-32})\ \mu\mathrm{b/nucleon}$.

It is worth noting that with the expected sizeable increase in the number of recorded events, these measurements will become precise enough to discriminate among different parameter sets, used in theoretical predictions.

A A simplified model: approximation of homogenous magnetic field

To illustrate the relation between various quantities a simplified picture is given. It assumes the uniform magnetic field integral independent on the entrance and exit angles of the track from and to the magnetic field. In this case we can draw certain conclusions analytically, which helps us in understanding different distributions (see below).

In order to determine the displacements of the detector parts in front of the magnet and those behind the magnet, we have to estimate the effect of a single affine transformation on the tracks. This tells us how and which distributions would change with a given transformation. The discrepancies between the extrapolated VDS segment and the segment behind the magnet have in general a functional dependence on parameters of each segment. In the lowest order approximation we would expect this dependence to be linear. For example, the difference between tx of the PC segment and the tx of the VDS extrapolated segment should be:

$$tx_{PC} - tx_{VDS}|_{z=z_{match}} = k \cdot tx_{PC} + n \tag{A.1}$$

the parameters k and n are obtained from the fit as described in Section 3.4.2.

In the following plots we show the true position of the segment in blue and the position of the segment as reconstructed in red.

A.1 Translation for Δz

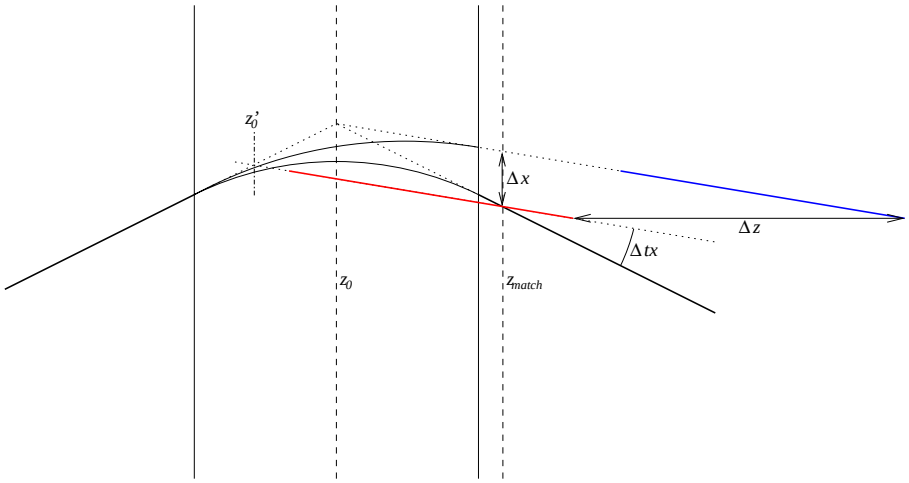

$$\Delta x = tx\Delta z$$

$$\Delta tx = \frac{\Delta z}{z_{match} - z_0} tx$$

The translation in z contributes to the slope (k) of the reference distribution 6 and to the shift (n) of the reference distribution 5 of Table 3.1. z_0' designates the intersection of the reconstructed PC and VDS segments.

A.2 Translation for Δx

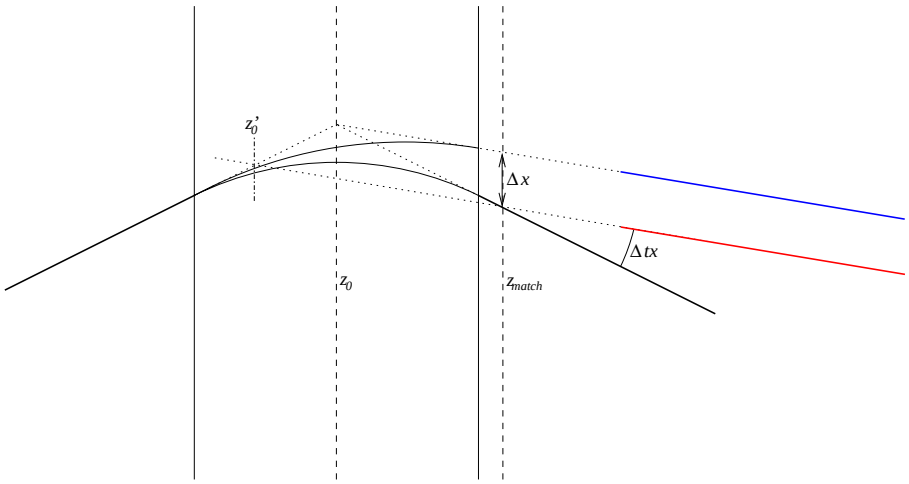

$$\Delta tx = -\frac{\Delta x}{z_{match} - z_0}$$

Translation in x contributes to the neutral term (n) of the distribution 6 in Table 3.1. It also contributes to the slope (k) of the distribution 5 and to n of the distribution 1 of the same table. Again, z_0' designates the intersection of the reconstructed PC and VDS segments.

A.3 Stretching for a factor f

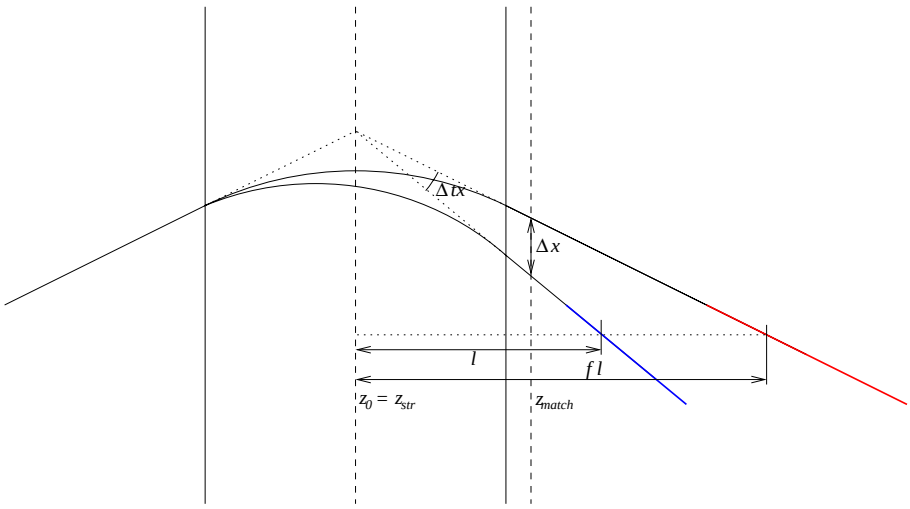

$$\Delta tx = (1 - 1/f)tx$$

$$\Delta x = (z_{str} - z_{match})(1 - 1/f)tx$$

If we choose the reference z_{str} to be z_0 the stretching causes only the change in the momentum. Thus, the amount of stretching can't be determined using single tracks. This also means that stretching with the reference at the mid point of magnet do not affect any of the reference plots of Section 3.4.1.

A.4 Shear for Δtx

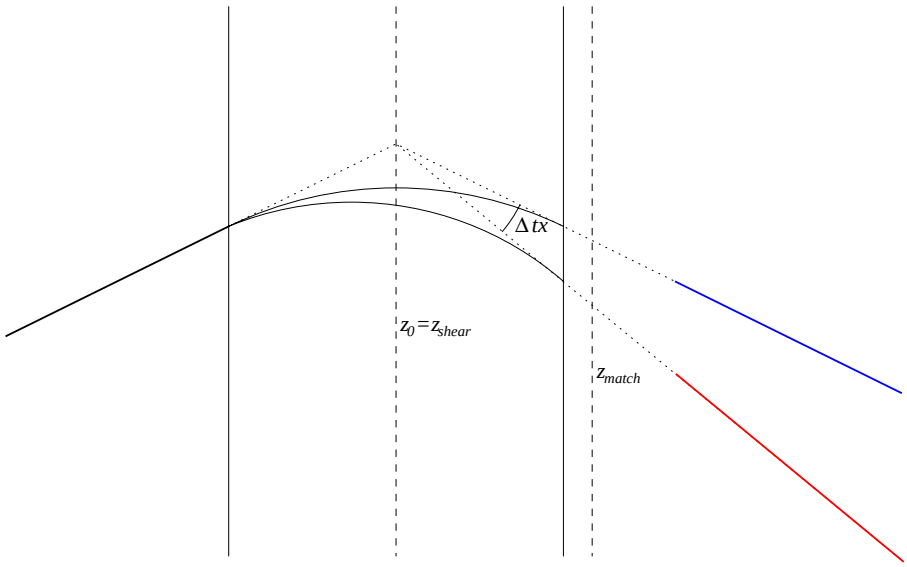

In case when we choose z_{shear} to be the mid point of the magnet z_0 we realize that shearing do not affect any of our reference distributions in Section 3.4.1. It only affects the momentum.

A.5 Rotation for an angle φ around z axis

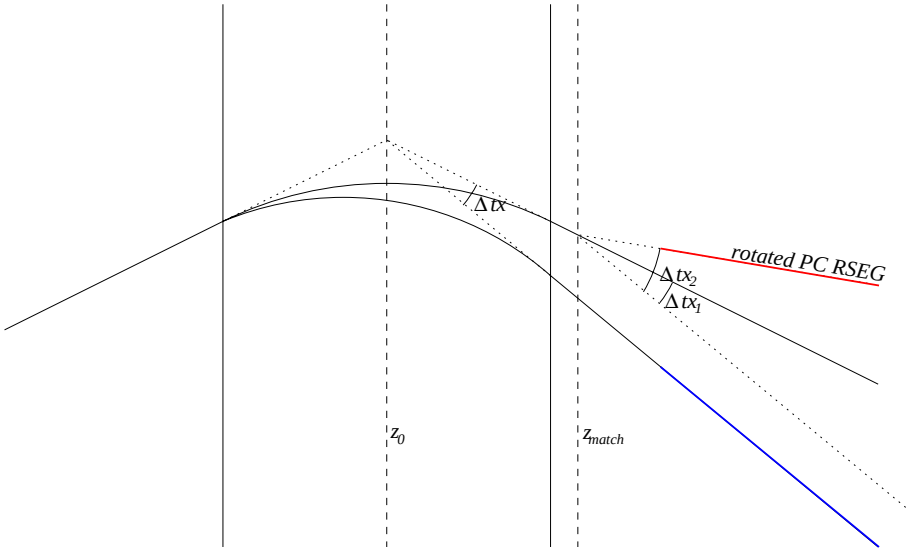

$$\begin{bmatrix} x \\ y \end{bmatrix}' = \begin{bmatrix} \cos(\varphi) & -\sin(\varphi) \\ \sin(\varphi) & \cos(\varphi) \end{bmatrix} \begin{bmatrix} x \\ y \end{bmatrix} \approx \begin{bmatrix} x - \varphi y \\ y + \varphi x \end{bmatrix}$$

$$\Delta tx_1 = \frac{\varphi y}{z_{match} - z_0}$$

$$\Delta tx_2 = \varphi ty$$

$$\Delta tx = \Delta tx_1 - \Delta tx_2 = \frac{\varphi y}{z_{match} - z_0} - \varphi ty = -\varphi \frac{z_0}{z_{match} - z_0} ty$$

The rotation around the beam-pipe causes Δtx to depend on ty (y).

A.6 Translation for Δy and shear for Δty

The interpretation of results in the y (non-bending) direction is much simpler. The translation and shear can be directly interpreted. Unfortunately the y direction is not as important as the x direction and has very poor resolution in PC.

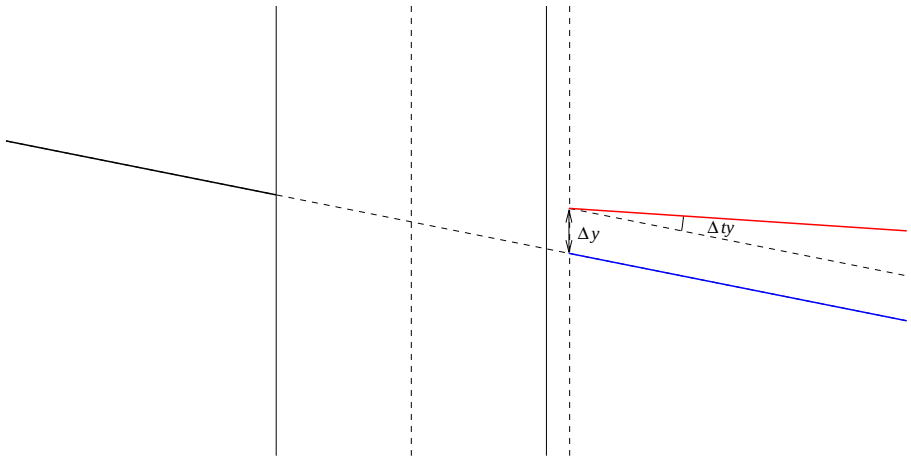

B Implementation of global transformations in the analysis code

The global alignment transforms single detector modules stored in the so called GEDE tables of the main HERA-B analysis framework, ARTE. A single component is treated as a bulk. The planes inside this bulk are transformed according to the transformations defined by the 7 parameters in the ACGA table (see Section C). The code where we do the transformations is in `acGlobalAlignmentForGEDE.C` of `alca` directory of ARTE. You can find the part where the transformations are done also in Section B.1. We can describe the transformations with mathematical formulas. We will designate the vector of displacement with $d\vec{X}$. It is calculated from the parameters dx, dy, dz, dtx, dty and fz in the ACGA table in the following way:

$$d\vec{X} = \begin{Vmatrix} dx \\ dy \\ dz \end{Vmatrix} + \begin{Vmatrix} dtx \cdot (z - z_0) \\ dty \cdot (z - z_0) \\ (fz - 1) \cdot (z - z_0) \end{Vmatrix} \tag{B.1}$$

z_0, the reference z position which we need for the shearing and stretching transformations, is also obtained from the ACGA table.

The stereo angle of the GEDE plane (α) is first changed for the angle defined in the ACGA rotation matrix ($R(\varphi_z)$). Please note that the rotation matrix in ACGA table is used only to describe the rotation around the z axis and could be in principle replaced by a single parameter but is kept like this for backward compatibility.

$$\alpha' = \alpha + \varphi_z \tag{B.2}$$

α' and α are the new and the old stereo angles of the GEDE plane.

The vector $d\vec{X}$ is then rotated into the local system of GEDE. We will label this transformation as $R_{loc}(\alpha')$. It is a simple rotation around the z axis with reference point $(x, y) = (0, 0)$:

$$R_{loc}(\alpha') = \begin{Vmatrix} \cos(\alpha') & \sin(\alpha') & 0 \\ -\sin(\alpha') & \cos(\alpha') & 0 \\ 0 & 0 & 1 \end{Vmatrix}$$

The transformed vector of displacements is then added to the coordinates of the GEDE, labeled as $\vec{X}$:

$$\vec{X}' = \vec{X} + R_{loc}(\alpha') d\vec{X} \tag{B.3}$$

vector $\vec{X}'$ represents the new GEDE positions. Both $\vec{X}$ and $\vec{X}'$ are in local GEDE coordinates.

B.1 Transformation code

The following section of the code shows the part where the actual transformations are applied. They differ slightly for VDS on one hand and OTR/ITR on the other (see “detector specific updates” below).

```
//-------------------------------------------------------------
// transformation
// new GEDE rot matrix: Gnew = A * G
//-------------------------------------------------------------

  l=0 ;
  for (int i=0; i<3; i++){
    for (int j=0; j<3; j++){
      GEDErotnew[i][j] = 0.0;
      for (int k=0; k<3; k++){
        GEDErotnew[i][j] += ACGArot[i][k] * GEDErot[k][j];
      }
      (*gede)->rot[l++] = GEDErotnew[i][j];
    }
  }

//-------------------------------------------------------------
// transformation
// new position : Rnew = R + Gnew**-1 * dr
//-------------------------------------------------------------

  float dz0, dr[3], drRot[3];

  dz0 = 0.5*((*gede)->zmin+(*gede)->zmax)+(*acga)->dz-(*acga)->z;

  dr[0] = (*acga)->dx + (*acga)->dtx * dz0;
  dr[1] = (*acga)->dy + (*acga)->dty * dz0;
  dr[2] = (*acga)->dz + ((*acga)->fz - 1.) * dz0;

  for (int i=0; i<3; i++){
    drRot[i] = 0.0;
    for (int j=0; j<3; j++){
      drRot[i] = drRot[i] + GEDErotnew[j][i] * dr[j];
    }
  }
```

```
  (*gede)->xmin = (*gede)->xmin + drRot[0];
  (*gede)->xmax = (*gede)->xmax + drRot[0];
  (*gede)->ymin = (*gede)->ymin + drRot[1];
  (*gede)->ymax = (*gede)->ymax + drRot[1];
  (*gede)->zmin = (*gede)->zmin + drRot[2];
  (*gede)->zmax = (*gede)->zmax + drRot[2];

  (*gede)->sxmn = (*gede)->sxmn + drRot[0];
  (*gede)->sxmx = (*gede)->sxmx + drRot[0];
  (*gede)->symn = (*gede)->symn + drRot[1];
  (*gede)->symx = (*gede)->symx + drRot[1];


//-----------------------------------------------------------------
// detector specific updates
//-----------------------------------------------------------------

  if ((*gede)->cmp == 1){ //VDS
    (*gede)->xfw[0] = (*gede)->cos*(*gede)->sxmn
                     -(*gede)->sin*(*gede)->symn + (*gede)->xfw[1];
  }

  if ((*gede)->cmp == 2 || (*gede)->cmp == 3){ //OTR/ITR
    for (int i = 0 ; i < (*gede)->nsl ; i++) {
      (*gede)->xfw[i] = (*gede)->xfw[i] + drRot[0] ;
      (*gede)->zfw[i] = (*gede)->zfw[i] + drRot[2] ;
      (*gede)->y1w[i] = (*gede)->y1w[i] + drRot[1] ;
      (*gede)->y2w[i] = (*gede)->y2w[i] + drRot[1] ;
    }
  }
```

C ACGA table

The ACGA table is the table where all parameters of the transformations related to the global aliment of HERA-B are stored. Each component corresponds to a row in the ACGA table. It has several fields: detector component ID - cmp, displacement in x, y and z directions - dx, dy and dz, shearing angles in yz and xz planes - dtx and dty, scale factor in z direction - fz, reference z position for shearing and stretching - $z0$ and 9 component rotation matrix $r1 - r9$.

In the global alignment scheme the HERA-B spectrometer is divided into several components. They are listed in the following table along with their corresponding component id's:

component ID	GLAL component
$0x00000001$	VDS
$0x00000002$	OTR +PC
$0x00010002$	OTR $-$PC
$0x00020002$	OTR +TC
$0x00030002$	OTR $-$TC
$0x00040002$	OTR +MC
$0x00050002$	OTR $-$MC
$0x00000003$	ITR PC +x+y
$0x00010003$	ITR PC $-$x+y
$0x00020003$	ITR PC +x$-$y
$0x00030003$	ITR PC $-$x$-$y
$0x00040003$	ITR TC +x+y
$0x00050003$	ITR TC $-$x+y
$0x00060003$	ITR TC +x$-$y
$0x00070003$	ITR TC $-$x$-$y
$0x00080003$	ITR MC +x+y
$0x00090003$	ITR MC $-$x+y
$0x000A0003$	ITR MC +x$-$y
$0x000B0003$	ITR MC $-$x$-$y
$0x04000000$	RICH[§]
$0x00000005$	$\mathrm{RICH_{up}}$
$0x00010005$	$\mathrm{RICH_{down}}$
$0x00000007$	ECAL

C.1 ACGA tables for different periods

Bellow there is a collection of different ACGA tables valid for different runs and periods, starting with the default ACGA table which was valid for keytable version 0. For the convenience the numbers representing dtx, dty are in mrad. In the database they would appear in rad. Also the rotation matrix is represented with $\sin(\varphi)$ only, where the φ represents the angle of rotation around z axis. The number is multiplied with a factor of 1000 for convenience.

../hbook/ACGA.KEY0.TXT								
cmp	dx	dy	dz	dtx	dty	fz	$z0$	$\sin(\varphi) * K$
$RICH$	0.0000	0.0000	0.0000	-0.2160	-0.5339	1.0000	0.0000	-0.0000
VDS	0.0085	0.0790	0.0000	0.6799	0.4350	1.0000	-0.7000	-5.8100
PC	0.0000	-0.8000	0.0000	0.0000	-0.7000	1.0000	1344.0000	-0.0000

../hbook/ACGA/ACGA.KEY11.TXT								
cmp	dx	dy	dz	dtx	dty	fz	z0	$\sin(\varphi) * K$
$RICH$	0.0000	0.0000	0.0000	-0.2500	-0.2300	1.0000	0.0000	-0.0000
VDS	0.0085	0.0790	0.0000	0.6799	0.4350	1.0000	-0.7000	-5.8100
PC	0.0000	-0.1000	0.0000	-0.1200	-2.5000	1.0000	700.0000	-0.0000
TC	0.0000	-0.1000	0.0000	-0.1200	-2.5000	1.0000	700.0000	-0.0000
0x00000010	-1.8000	-0.9000	0.0000	0.0000	0.0000	1.0000	0.0000	-0.0000
0x00000040	0.0000	-0.1000	0.0000	-0.1200	-2.5000	1.0000	700.0000	-0.0000

../hbook/ACGA/ACGA.KEY13.run1-run17062.TXT								
cmp	dx	dy	dz	dtx	dty	fz	z0	$\sin(\varphi) * K$
VDS	0.0085	0.0790	0.0000	0.6799	0.4350	1.0000	-0.7000	-2.8100
$+PC$	0.0600	0.2500	0.0000	-0.1200	-2.5000	0.9990	700.0000	-0.0000
$-PC$	-0.1000	-0.1000	0.0000	-0.1200	-2.5000	1.0010	700.0000	-0.0000
$+TC$	-0.1000	-0.1000	0.0000	-0.1200	-2.5000	1.0000	700.0000	-0.0000
$-TC$	-0.1000	-0.1000	0.0000	-0.1200	-2.5000	1.0000	700.0000	-0.0000
$RICH_{dn}$	0.0000	0.0000	0.0000	-0.2500	-0.2300	1.0000	0.0000	-0.0000
$RICH_{up}$	0.0000	0.0000	0.0000	-0.2500	-0.2300	1.0000	0.0000	-0.0000
$ECAL$	-1.8000	-0.9000	0.0000	0.0000	0.0000	1.0000	0.0000	-0.0000
$RICH$	0.0000	0.0000	0.0000	-0.2500	-0.2300	1.0000	0.0000	-0.0000

../hbook/ACGA/ACGA.KEY13.run17063-.TXT								
cmp	dx	dy	dz	dtx	dty	fz	z0	$\sin(\varphi) * K$
VDS	0.0085	0.0790	0.0000	0.6799	0.4350	1.0000	-0.7000	-2.8100
$+PC$	-0.1540	0.0900	0.0000	-0.1200	-2.5000	0.9990	700.0000	-0.0000
$-PC$	-0.2260	-0.2600	0.0000	-0.1200	-2.5000	1.0010	700.0000	-0.0000
$+TC$	-0.2700	-0.2600	0.0000	-0.1200	-2.5000	1.0000	700.0000	-0.0000
$-TC$	-0.2700	-0.2600	0.0000	-0.1200	-2.5000	1.0000	700.0000	-0.0000
$RICH_{dn}$	0.0000	0.0000	0.0000	-0.2500	-0.2300	1.0000	0.0000	-0.0000
$RICH_{up}$	0.0000	0.0000	0.0000	-0.2500	-0.2300	1.0000	0.0000	-0.0000
$ECAL$	-1.8000	-0.9000	0.0000	0.0000	0.0000	1.0000	0.0000	-0.0000
$RICH$	0.0000	0.0000	0.0000	-0.2500	-0.2300	1.0000	0.0000	-0.0000

../hbook/ACGA/ACGA.KEY14.1-17062.TXT								
cmp	dx	dy	dz	dtx	dty	fz	z0	$\sin(\varphi) * K$
VDS	0.0085	0.0790	0.0000	0.6799	0.4350	1.0000	-0.7000	-2.8100
$+PC$	0.0600	0.2500	0.0000	-0.1200	-2.5000	0.9990	700.0000	-0.0000
$-PC$	-0.1000	-0.1000	0.0000	-0.1200	-2.5000	1.0010	700.0000	-0.0000
$+TC$	-0.1000	-0.1000	0.0000	-0.1200	-2.5000	1.0000	700.0000	-0.0000
$-TC$	-0.1000	-0.1000	0.0000	-0.1200	-2.5000	1.0000	700.0000	-0.0000
$RICH_{dn}$	0.0000	0.0000	0.0000	-0.2500	-0.2300	1.0000	0.0000	-0.0000
$RICH_{up}$	0.0000	0.0000	0.0000	-0.2500	-0.2300	1.0000	0.0000	-0.0000
$ECAL$	-1.8000	-0.9000	0.0000	0.0000	0.0000	1.0000	0.0000	-0.0000
$RICH$	0.0000	0.0000	0.0000	-0.2500	-0.2300	1.0000	0.0000	-0.0000

../hbook/ACGA/ACGA.KEY14.17063-.TXT								
cmp	dx	dy	dz	dtx	dty	fz	z0	$\sin(\varphi) * K$
VDS	0.0085	0.0790	0.0000	0.6799	0.4350	1.0000	-0.7000	-2.8100
$+PC$	-0.1540	0.0900	0.0000	-0.1200	-2.5000	0.9990	700.0000	-0.0000
$-PC$	-0.2260	-0.2600	0.0000	-0.1200	-2.5000	1.0010	700.0000	-0.0000
$+TC$	-0.2700	-0.2600	0.0000	-0.1200	-2.5000	1.0000	700.0000	-0.0000
$-TC$	-0.2700	-0.2600	0.0000	-0.1200	-2.5000	1.0000	700.0000	-0.0000
$RICH_{dn}$	0.0000	0.0000	0.0000	-0.2500	-0.2300	1.0000	0.0000	-0.0000
$RICH_{up}$	0.0000	0.0000	0.0000	-0.2500	-0.2300	1.0000	0.0000	-0.0000
$ECAL$	-1.8000	-0.9000	0.0000	0.0000	0.0000	1.0000	0.0000	-0.0000
$RICH$	0.0000	0.0000	0.0000	-0.2500	-0.2300	1.0000	0.0000	-0.0000

../hbook/ACGA/ACGA.KEY17.16784.ITR-beta.OTR-V3a1.JPSI.TXT								
cmp	dx	dy	dz	dtx	dty	fz	z0	$\sin(\varphi) * K$
VDS	0.3180	0.2770	0.0000	0.6800	0.4350	1.0000	454.0000	-2.2400
$+PC$	-0.0100	0.0560	-0.4000	0.1000	-2.7500	1.0002	454.0000	-0.0000
$+TC$	-0.0100	0.0560	-0.4000	0.1000	-2.7500	1.0002	454.0000	-0.0000
$-PC$	-0.0200	0.3060	-1.9100	0.0000	-1.5500	1.0019	454.0000	-0.0000
$-TC$	-0.0200	0.3060	-1.9100	0.0000	-1.5500	1.0019	454.0000	-0.0000
ITR	0.3300	1.0000	-2.8300	-0.5400	-4.2000	1.0000	454.0000	-0.0000
$RICH$	0.0000	0.0000	0.0000	-0.2500	-0.2300	1.0000	0.0000	-0.0000

../hbook/ACGA/ACGA.KEY17.17063-.ITR-alfa.OTR-beta.TXT								
cmp	dx	dy	dz	dtx	dty	fz	z0	$\sin(\varphi) * K$
VDS	0.3180	0.2770	0.0000	0.6800	0.4350	1.0000	454.0000	-2.2400
$+PC$	-0.1340	0.0560	-0.8000	0.0000	-1.9500	1.0012	454.0000	-0.0000
$+TC$	-0.1340	0.0560	-0.8000	0.0000	-1.9500	1.0012	454.0000	-0.0000
$-PC$	-0.1110	0.3060	-1.7900	0.0000	-1.8500	1.0040	454.0000	-0.0000
$-TC$	-0.1110	0.3060	-1.7900	0.0000	-1.8500	1.0040	454.0000	-0.0000
ITR	0.2400	0.0000	-2.9000	-0.3000	-3.3000	1.0000	454.0000	-0.0000
$RICH$	0.0000	0.0000	0.0000	-0.2500	-0.2300	1.0000	0.0000	-0.0000

D Magnet chambers

Given the nature of the internal alignment of magnet chambers which are aligned to VDS at the beginning of the magnet and to the PC at its end we have to treat their transformations differently. If we move the PC part for a certain amount in x, we have to move a part of MC which touches PC for the same amount while keeping the part touching VDS at rest. A simple shear is also not the right thing, since the direction of the tracks (tx) should also match. We decided to use the next simplest transformation to a linear transformation. The magnet chambers are transformed in a way that the direction and position of the VDS segment at its entrance to the magnet are the same as the direction and position of the magnet segment at the beginning of the magnet. An additional requirement is that at the point of exit from the magnet, the magnet segment matches the PC segment in position. We parameterized such a transformation as $A(z - z_1)^2 + B(z - z_0) + C$, where $z_0 = 250$ cm is the entry point of the magnet.

Since the magnet chambers were removed from the HERA-B spectrometer, their alignment lost all importance. The code is still there in case someone wishes to do it on the old data.

E Wire following

In what follows a new wire following procedure will be presented. It was developed because we have noticed that the standard wire following procedure, based on the Grover vertexing package [41], failed in case of multi-wire run, where more than one target wire were used simultaneously, for example in a two-wire run 19185, which is a part of the present analyzed data. It appeared as if the two reconstructed targets swop their places over extended periods of time. Thus a new wire following algorithm was written [40], which is described in this section.

A typical resolution in reconstruction of primary vertices in the direction of the beam-pipe (z) is about $500\ \mu\mathrm{m}$, while the resolution in the transversal directions are about $50\ \mu\mathrm{m}$ (see Fig. 5.12, based on Monte Carlo simulated data). On the other hand, it is quite obvious that primary interactions happen in the target wires, which are of different shapes and dimensions. In the present analysis the data taken with 2 different wires was analyzed. They were 'below 1' and 'inner 1' target wires, as they are named in the HERA-B, due to their relative position with respect to the HERA spectrometer ring (see Fig. 2.5). Their characteristics are gathered in Table E.1, where also the spatial dimensions (Δx, Δy and Δz) are given in the directions perpendicular to the wires. In the last three columns the intrinsic spatial resolution of the primary vertex, if assigned to the target wire, is given in these directions (σ_x^{intrin}, σ_y^{intrin} and σ_z^{intrin}). In all cases this resolution is better than the one cited at the beginning of this paragraph.

name	orientation	material	$\Delta x/\mathrm{cm}$	$\Delta y/\mathrm{cm}$	$\Delta z/\mathrm{cm}$	σ_x^{intrin}	σ_y^{intrin}	σ_z^{intrin}
below 1	horizontal	C $(A = 12.0)$	—	0.01	0.05	—	0.0029	0.014
inner 1	vertical	W $(A = 184)$	0.005	—	0.005	0.001	—	0.001

Table E.1: Summary of the characteristics of the two wires used for data taking of the data sample analyzed. The 'below 1' wire is actually a strip, while 'inner 1' is a wire with circular cross section.

E.1 Primary vertex reconstruction

First the primary vertices were found on the basis of all tracks having the segment in the VDS detector. The quality of the track used in primary vertex finding and fitting was improved with track selection as described in Section 5.4.1. The intersections of the selected tracks with planes at the geometrical z positions of target wires were calculated and histogramed in two dimensions with the bin width of $400\ \mu\mathrm{m}$ on an event by event basis. In the search of clusters the following criterion was used: two bins belong to the same cluster only if they are neighboring bins (see Fig. E.1).

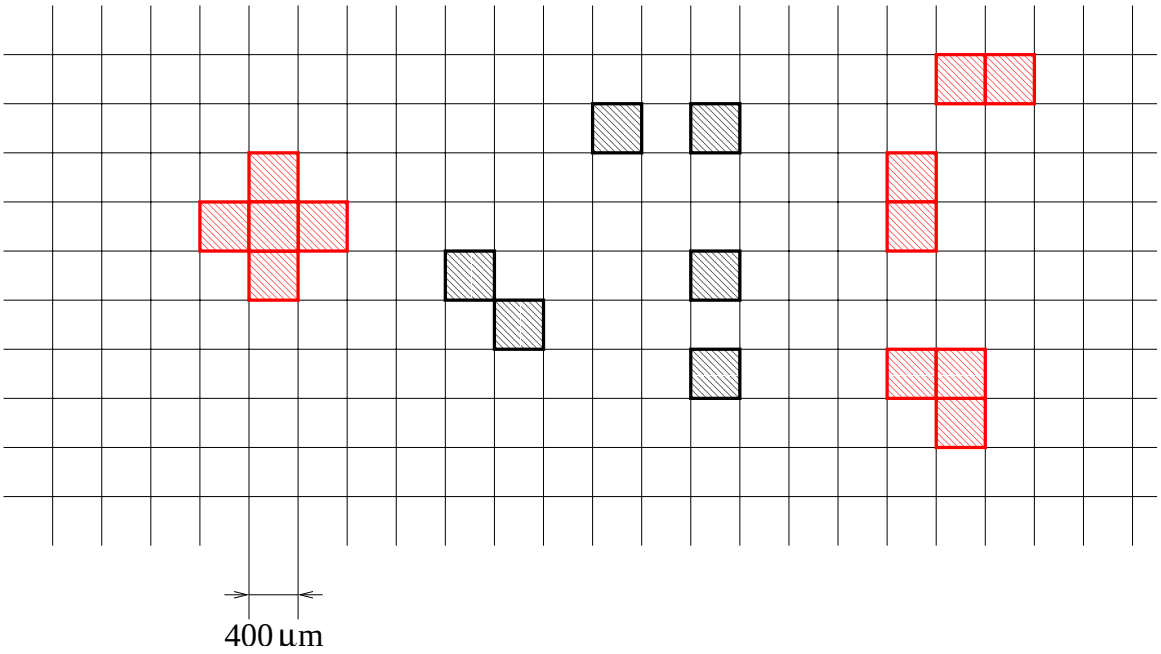

Figure E.1: Schematic representation of the 2D histogram where the track intersection points with plane at z of each target wire was filled. Each shaded square represent a bin which was intersected by at least one track. There are 4 patterns marked red which would be recognized as a primary vertex candidate if the number of tracks in one cluster is higher than the threshold required (in our case higher than 4). In the black boxes the threshold would have to be met individually, i.e. .

Each track was then assigned to one cluster only with the procedure of expectation maximization [42]. From the histograms described above a new set of histograms were filled with weights for each track, which were defined as:

$$w_i^j = \frac{n_i^j}{\sum_k n_i^k},$$

where the lower index (i) represents the track and the upper (j and k) runs over the target planes. These histograms were than used to produce a new set of histograms by the same procedure. This was iterated a few times. When the tracks were assigned to the planes, their weights were reset to 1 for the final set of histograms, which defined the clusters for vertex fitting.

The track belonging to the same cluster were used in the calculation of the vertex point. The best vertex was found to be the one which minimizes the χ^2, calculated in the following manner:

$$\chi^2 = \sum_{i=1}^{N} \left(\frac{x_v - x_i(z_v)}{\sigma^2_{x_i}(z_v)} + \frac{y_v - y_i(z_v)}{\sigma^2_{y_i}(z_v)} \right), \tag{E.1}$$

where $\vec{X} = (x_v, y_v, z_v)$ is the vertex point, while vector $\vec{X}^t(z_v) = (x_i(z_v), y_i(z_v), tx_i, ty_i)$ defines the coordinates ($x_i(z_v)$ and $y_i(z_v)$) and slopes (tx_i and ty_i) of the track at the intersection with the plain defined by $z = z_v$. The slopes were not changed. $\sigma_{x_i,y_i}(z_v)$ are the errors of the track coordinate determination propagated to $z = z_v$. They correspond to square roots of the

diagonal elements of the track covariance matrices $\mathbf{V^t}$. Since at first the exact vertex position is not known, the covariance matrix of each track $\mathbf{V}_i^t$ was first propagated to the $z = z_t$, position of the target. The new covariance matrices were calculated by the following propagation:

$$\mathbf{V}_i^t(z_t) = \mathbf{F}_i^T \mathbf{V}_i^t(z_0) \mathbf{F}_i,$$

where $\mathbf{F}_i$ are the track transport matrices defined as:

$$\mathbf{F}_i = \begin{Vmatrix} 1 & 0 & dZ_i & 0 \\ 0 & 1 & 0 & dZ_i \\ 0 & 0 & 1 & 0 \\ 0 & 0 & 0 & 1 \end{Vmatrix},$$

dZ_i being the difference in the target z position and the z position of the beginning of the track: $dZ_i = z_t - z_{0,i}$. The track points were linearly propagated to the same $z = z_t$:

$$x_i(z_t) = x_i(z_0) + tx_i dZ_i$$

$$y_i(z_t) = y_i(z_0) + ty_i dZ_i$$

With differentiating Eq. E.1 against the coordinates of the vertex, a system of linear equations is obtained, which can be written in the matrix form:

$$\mathbf{A}\vec{X} = \vec{b},$$

where $\vec{X}$ is the vertex point defined above,

$$\vec{b} = \left\| \sum_{i=1}^N \frac{x_i(z_v) - tx_i z_v}{\sigma^2_{x_i}(z_v)}, \sum_{i=1}^N \frac{y_i(z_v) - ty_i z_v}{\sigma^2_{y_i}(z_v)}, -\sum_{i=1}^N \left(\frac{(x_i(z_v) - tx_i z_v) tx_i}{\sigma^2_{x_i}(z_v)} + \frac{(y_i(z_v) - ty_i z_v) ty_i}{\sigma^2_{y_i}(z_v)} \right) \right\|$$

and

$$\mathbf{A} = \begin{Vmatrix} \sum_{i=1}^N \sigma_{x_i}^{-2}(z_v) & 0 & -\sum_{i=1}^N \frac{tx_i}{\sigma^2_{x_i}(z_v)} \\ 0 & \sum_{i=1}^N \sigma_{y_i}^{-2}(z_v) & -\sum_{i=1}^N \frac{ty_i}{\sigma^2_{x_i}(z_v)} \\ -\sum_{i=1}^N \frac{tx_i}{\sigma^2_{x_i}(z_v)} & -\sum_{i=1}^N \frac{ty_i}{\sigma^2_{x_i}(z_v)} & \sum_{i=1}^N \left(\frac{tx_i^2}{\sigma^2_{x_i}(z_v)} + \frac{ty_i^2}{\sigma^2_{y_i}(z_v)} \right) \end{Vmatrix}$$

The system is solved by inverting the matrix A,

$$\vec{X} = \mathbf{A}^{-1}\vec{b}$$

Since instead of the exact z_v vertex position an approximation was used (the first one being z_t) for covariance matrix and track propagation, the result after the inversion and multiplication with $\vec{b}$ is again only an approximation, and the procedure has to be repeated to reach the desired resolution.

E.2 Wire position

In the wire following procedure only the primary vertices were used, which had 10 or more tracks associated. Instead of determining the absolute coordinate the relative deviation from the position measured by the physical target movements was determined. In the next argument we will explain the averaging technique used. By u we will denote the relative coordinate in any direction.

The averaging of the position of the target wire was done with a low-pass filter of the 1^{st} order, which is defined by the equation:

$$\tau_f \frac{d\bar{u}(t)}{dt} + \bar{u}(t) = u(t),$$

where τ_f defines the time scale of the filter, $\bar{u}(t)$ is the average at time t and $u(t)$ is the current measurement at that time. This equation can be discretized and then reads:

$$\tau_f \frac{\bar{u}_k - \bar{u}_{k-1}}{T_s} + \bar{u}_k = u_k, \tag{E.2}$$

T_s being the interval between two measurements, u_k and u_{k-1}, which was put in our case to $T_s = 1$, meaning that the u_{k-1} and u_k represent the two adjacent measurements, or in other words, that τ_f is measured in units of T_s. The filter Eq. E.2 then reads:

$$\tau_f(\bar{u}_k - \bar{u}_{k-1}) + \bar{u}_k = u_k.$$

Solving this for $\bar{u}_k$ in terms of $\bar{u}_{k-1}$ and u_k the following expression is obtained:

$$\bar{u}_k = \frac{\tau_f}{\tau_f + 1}\bar{u}_{k-1} + \frac{1}{\tau_f + 1}u_k \tag{E.3}$$

In the starting time interval of $2\tau_f$ (i.e. for $k \leq 2\tau_f$) the wire position is obtained by averaging the primary vertex position:

$$\bar{v}_k = \frac{u_k + (k-1)\bar{v}_{k-1}}{k} \quad (k \leqq 2\tau_f),$$

From $k > 2\tau_f$ the wire position is calculated according to Eq. E.3, using $\bar{u}_{2\tau_f+1} = \frac{\tau_f}{\tau_f+1}\bar{v}_{2\tau_f} + \frac{1}{\tau_f+1}u_k$ as an initial approximation.

The events of data taken are stored in files. Since the events are treated by a processor farm which consumes different amount of CPU time for different events, they are stored non-consequentially. The interval in which events are mixed is of the order of 1000 events, which means that event 1 can come in the worst case as thousandth in a row. The time constant was deliberately set below this number to $\tau_f = 50$, so that averaging was done over number of events of order of 50, as they were read from the file (and have primary vertices with more than 10 tracks). Please note that 1000 events, even less 50, is much shorter interval as the typical interval in which the wire moves noticeably (for the amount of reconstructed wire resolution), and furthermore note that each wire is expected to move only towards and away from the beam,

so the z coordinate should not change at all (if neglecting the thermal expansion of the VDS vessel, changing alignment of VDS,...).

The spread of the primary vertices around the exact target position can be estimated using the current filtered average (Eq. E.3):

$$(\sigma_p^k)^2 = \frac{\tau_f}{\tau_f + 1}(\sigma_p^{k-1})^2 + \frac{1}{\tau_f + 1}(u_k - \bar{u}_k)^2$$

The resolution of the relative target position σ_u^k is better since it is the result of averaging. It turns out to be:

$$\sigma_u^k = \frac{\sigma_p^k}{\sqrt{2\tau}}$$

E.3 Performance

Using the above described algorithm, the primary vertices and targets were reconstructed in single wire runs as well as in the multi wire runs. Here an example of run 19185 with over $7\ 10^6$ events is presented. In Figures E.2 and E.3 the reconstructed position of primary vertex as a function of the event number is shown as well as the reconstructed wire position. The comparison between target and primary vertex position is shown also on Fig. E.4, in a short interval when the target did not move noticeably. The superior resolution of the target position is obvious.

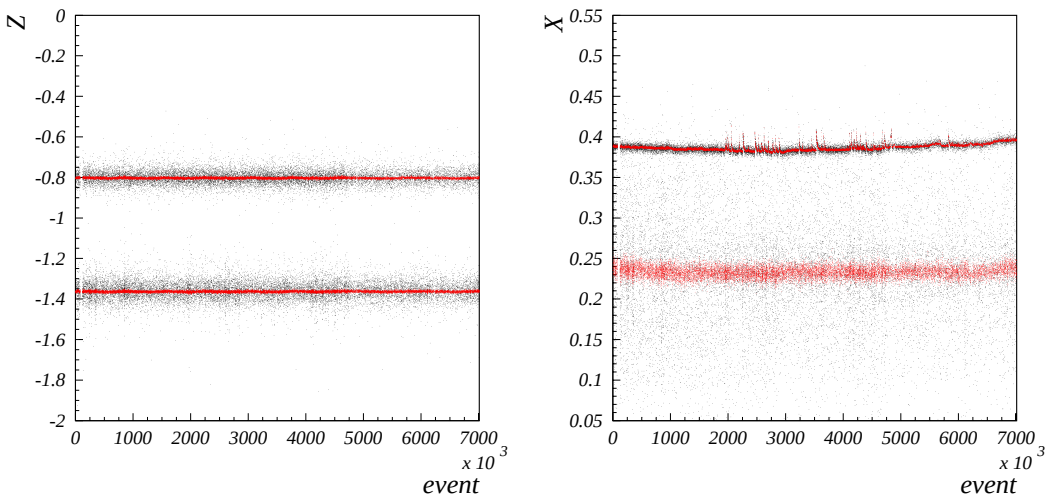

(a) (b)

Figure E.2: Reconstructed primary vertices are shown as black dots. The red represent the reconstructed wire position using the algorithm described in the previous section. (a) shows the reconstructed z coordinates of the primary vertex and the target and (b) the x coordinate. The gap in the event number at the beginning is due to corrupted data file.

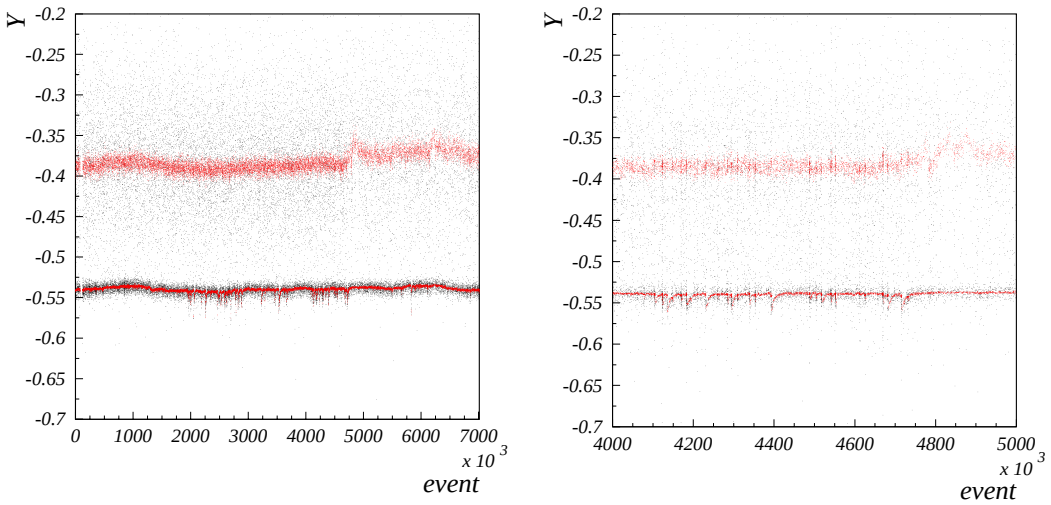

(a) (b)

Figure E.3: The same as in Fig. E.2. Here y coordinate is shown in (a) and (b). From (b), where only a fraction of events is shown, it can be seen that the spikes in the wire position are typically couple of 10000 events wide.

The wires in run 19185 were made of carbon $A = 12.0$ and tungsten $A = 184$. It is expected that the interactions of protons with heavier nuclei have higher multiplicities, which is observed also in HERA-B data (see Fig. E.5). Due to higher multiplicity, i.e. due to a larger number of tracks, the primary vertex reconstructed on the tungsten has better resolution, as can be seen in Fig. E.6. The wire following algorithm was tested also on the Monte Carlo simulated data, and agrees well with the real data. There is a small deviation in the resolution of the single primary vertex, which is worse in the case of Monte Carlo data (see Fig. E.7).

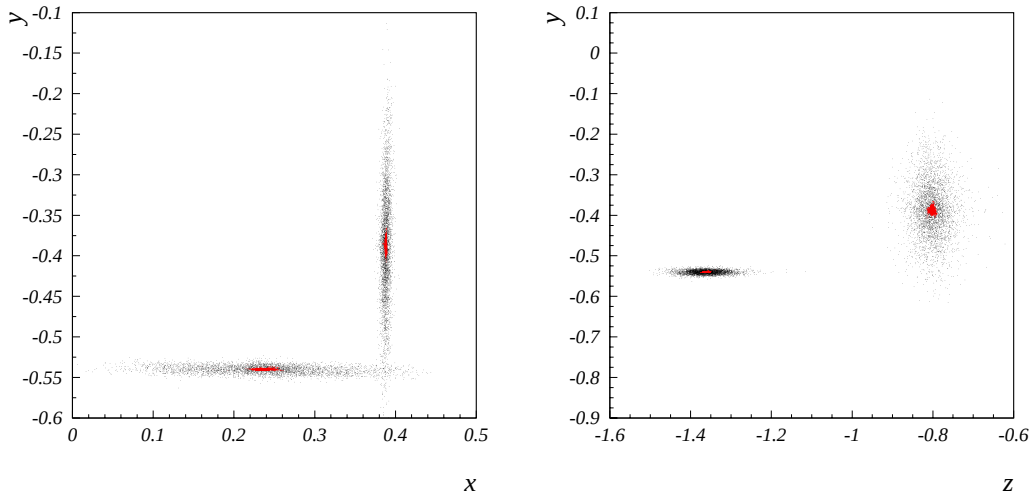

(a) (b)

Figure E.4: The reconstructed primary vertex (black dots) and target positions (red dots). The positions are plotted for short period (events with numbers from 10000 to 10300), in which the target movement was not noticeable.

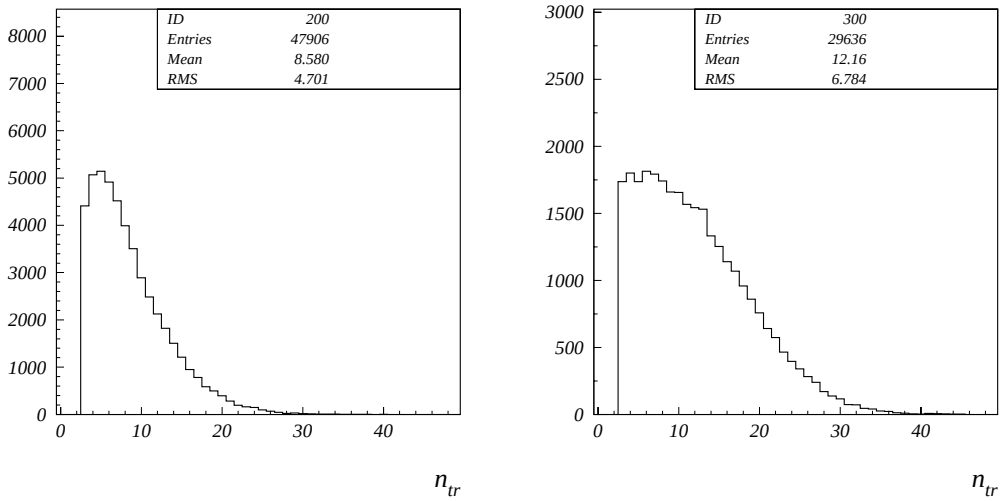

(a) (b)

Figure E.5: The track multiplicity of the inelastic events recorded with carbon (a) and tungsten target wires (b).

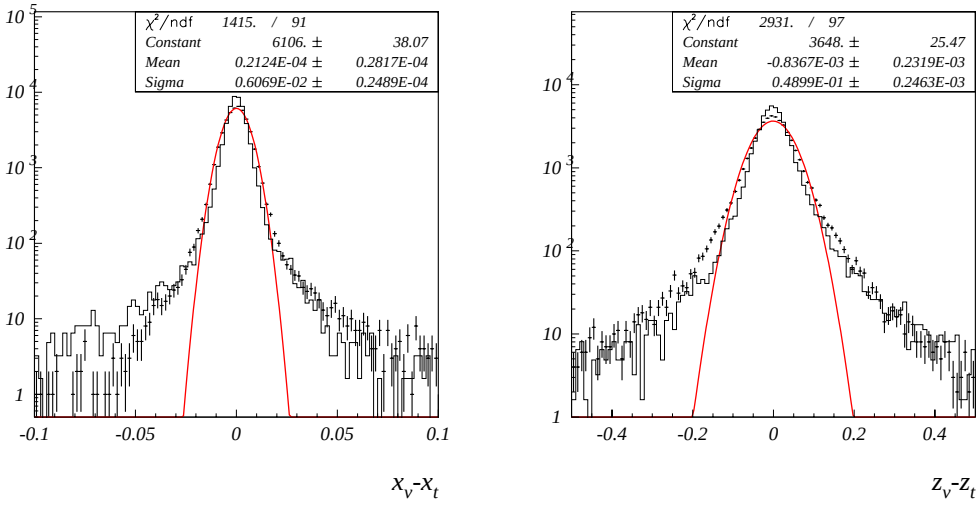

(a) (b)

Figure E.6: The distribution of the difference in the reconstructed primary vertex position and target position obtained with wire-following procedure. The histograms with error bars correspond to the primary vertex reconstructed on the carbon wire and the histograms without error bars correspond to the tungsten wire. The fit corresponds to the tungsten wire.

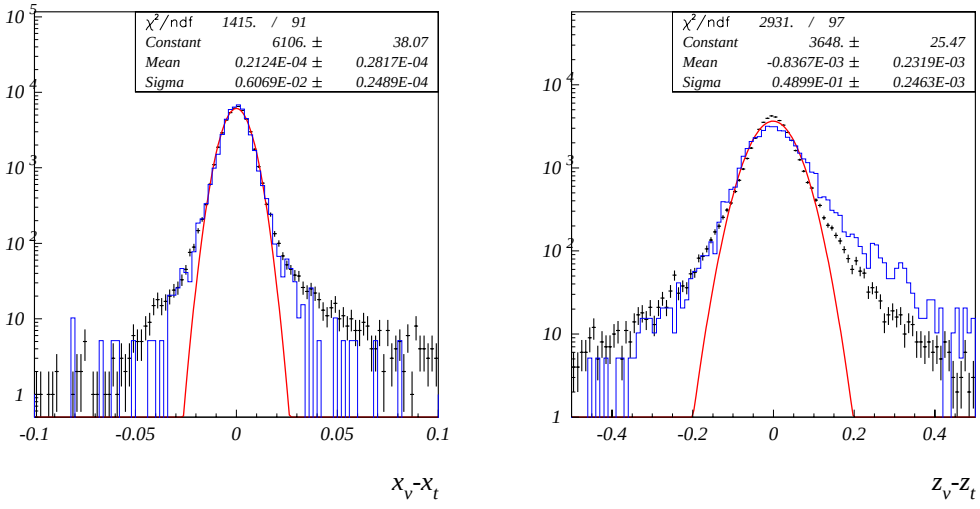

(a) (b)

Figure E.7: The distribution of the difference in the reconstructed primary vertex position and target position obtained with wire-following procedure. Black histogram with error bars correspond to the real data, blue histogram to the Monte Carlo simulated data and red curve to the Gaussian fit to the real data.

Povzetek doktorskega dela

Študij redkih procesov pri razpadu kvarkov b in c se je izkazal kot zelo pomembno orodje fizike osnovnih delcev. Meritve zahtevajo velik vzorec izmerjenih razpadov mezonov B in D, ki jih lahko zberemo pri trkih hitrih protonov ob mirujočo tarčo. Ta način zbiranja podatkov smo uporabili pri poskusu HERA-B ob trkalniku HERA na institutu DESY v Hamburgu.

Pričujoče doktorsko delo je del uvodnih meritev poskusa HERA-B, ko je potrebno merske napravo pripraviti na delovanje v neprijaznem radioaktivnem okolju, jo umeriti in izvesti prve meritve. Doktorsko delo je razdeljeno na tri dele, določitev krajevne umeritve celotne merske naprave, umeritev ene bistvenih komponent, števca obročev Čerenkova (zanj uporabljamo kratico RICH, Ring Imaging Cherenkov), in na koncu meritev preseka za tvorbo mezonov D^0 in D^{*+}.

Poskus HERA-B

Na inštitutu DESY (Deutsches Elektronen Synchrotron) v Hamburgu deluje trkalnik HERA, kjer v nasprotnih smereh krožijo gruče elektronov in protonov. Poskus HERA-B izkorišča protone z energijo 920 GeV, ki trkajo ob mirujočo tarčo vsakih 96 ns. Z analizo identitete in kinematičnih lastnosti delcev, ki nastanejo ob teh trkih, želijo pri tem poskusu raziskovati redke pojave v fiziki težkih mezonov [1]. Zaradi velike energije protonov leti večina nastalih delcev pod majhnim kotom glede na smer protonskega žarka. Zato je merilna naprava načrtovana tako, da pokriva 220 mrad $\times$ 160 mrad prostorskega kota, kar zadošča za detekcijo večine nastalih delcev.

Poskus HERA-B je bil prvotno zgrajen za meritev kršitve simetrije CP v razpadnem kanalu $B^0 \; ali \; \bar{B}^0 \rightarrow J/\psi \; {K_s}^0 \rightarrow l^+l^-\pi^+\pi^-$. Razpad mezona B v J/ψ in K_S pusti v merilni napravi značilno sled, ki jo sestavljajo par visokoenergijskih leptonov z invariantno maso J/ψ ter par visokoenergijskih pionov z invariantno maso K^0 in mestom nastanka, premaknjenim za tipično 1m glede na tarčo (slika I). Omenjeni razpad je tako eksperimentalno in teoretično najprimernejši za opazovanje kršitve simetrije CP. Merska naprava HERA-B (slika II) je optimizirana za njegovo zaznavo. Izkazalo se je, da omenjenega razpadnega kanala z zelo majhnim razvejitvenim razmerjem zaradi tehničnih težav pri izgradnji zelo zapletenega prožilnega sistema ne bo mogoče izvesti v načrtovanem času.

Pomemben cilj poskusa HERA-B pa je še vedno meritev preseka za nastanek težkih kvarkov b in c. Verjetnost, da se iskani dogodek zgodi, je tipično mnogo redov velikosti manjša, kot da se zgodi za nas nezanimiva neelastična reakcija med protonom in jedrom. Zato potrebujemo veliko število zajetih dogodkov in učinkovit prožilni sistem, ki z veliko večjo verjetnostjo proži, ko se

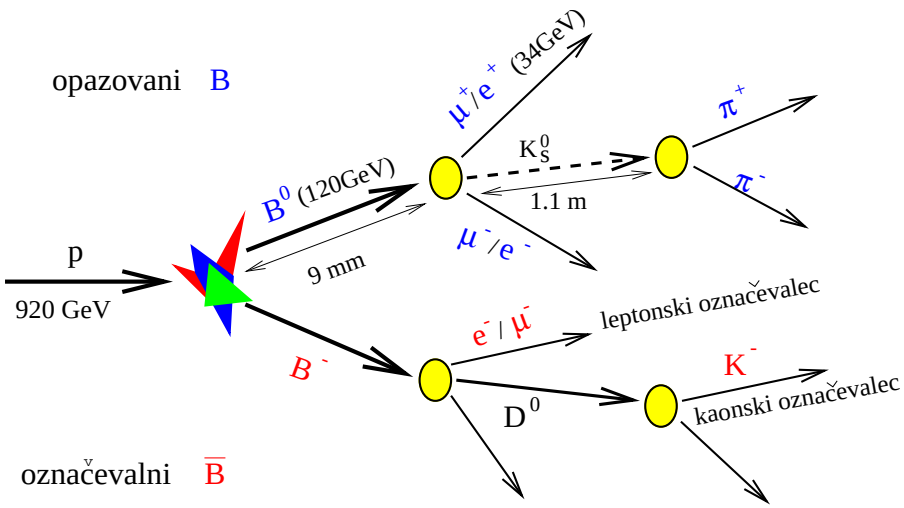

Slika I: Razpad $\mathrm{B}^0 \to \mathrm{J}/\psi\,\mathrm{K_s}$ s tipičnimi vrednostmi za gibalne količine in razpadne razdalje.

zgodi iskani dogodek, kot v primeru neelastične reakcije med protonom in jedrom. Za reakcije, ki potečejo ob trkih, je značilno veliko število sledi nabitih delcev v končnem stanju. Med njimi moramo izbrati le nekaj sledi, ki pripadajo iskanemu razpadu. Tipičen primer je prikazan na sliki III. Sledi nabitih delcev zaznajo v različnih sledilnih sistemih. Detektor verteksov, sestavljen iz silicijevih mikropasovnih detektorjev, je postavljen takoj za žično tarčo in omogoča natančno določitev začetnih sledi delcev in točk, v katerih nekateri delci, na primer mezoni B in D, razpadejo. V magnetnem polju dipolnega magneta se poti nabitih delcev ukrivijo, kar zaznamo v glavnem sledilnem sistemu na drugi strani magneta. To nam omogoča določitev gibalnih količin delcev. Da zmanjšamo prispevek naključnih kombinacij delcev iz ozadja, ki se lahko slučajno sestavijo v invariantno maso blizu masi tistega razpadlega delca, ki ga iščemo, imamo na voljo še sisteme za identifikacijo delcev. S števcem obročev Čerenkova lahko uspešno ločujemo med nabitimi kaoni, protoni in večinskimi pioni na širokem področju gibalnih količin. Elektromagnetni kalorimeter lahko uspešno ločuje elektrone in fotone od ostalih delcev. Za debelim železnim zidom, ki prepusti skoraj samo mione (in seveda nevtrine), so postavljeni merilniki mionov, ki določijo, ali je sled pred železnim zidom pripadala mionu ali kateremu drugemu nabitemu delcu.

Krajevna umeritev merilne naprave

Ključni del zagonskega obdobja merilne naprave je njena krajevna umeritev. Predmet tega poglavja je krajevna umeritev celotne merilne naprave, ki jo bom imenoval globalna umeritev, v nasprotju z lokalno umeritvijo, kjer določijo umeritev posameznega dela merilne naprave. Opisal bom metode, ki sem jih uporabil za določitev globalne umeritve. Najprej bom opisal dve metodi, kjer umeritev določim iz posameznih sledi delcev. Izkaže se, da samo na podlagi posameznih sledi delcev ne moremo določiti vseh parametrov, zato sem uporabil še tretjo metodo, kjer sem preučeval dvodelčne razpade delcev.

Z globalno umeritvijo je potrebno dele merilne naprave, ki so predhodno dobro lokalno

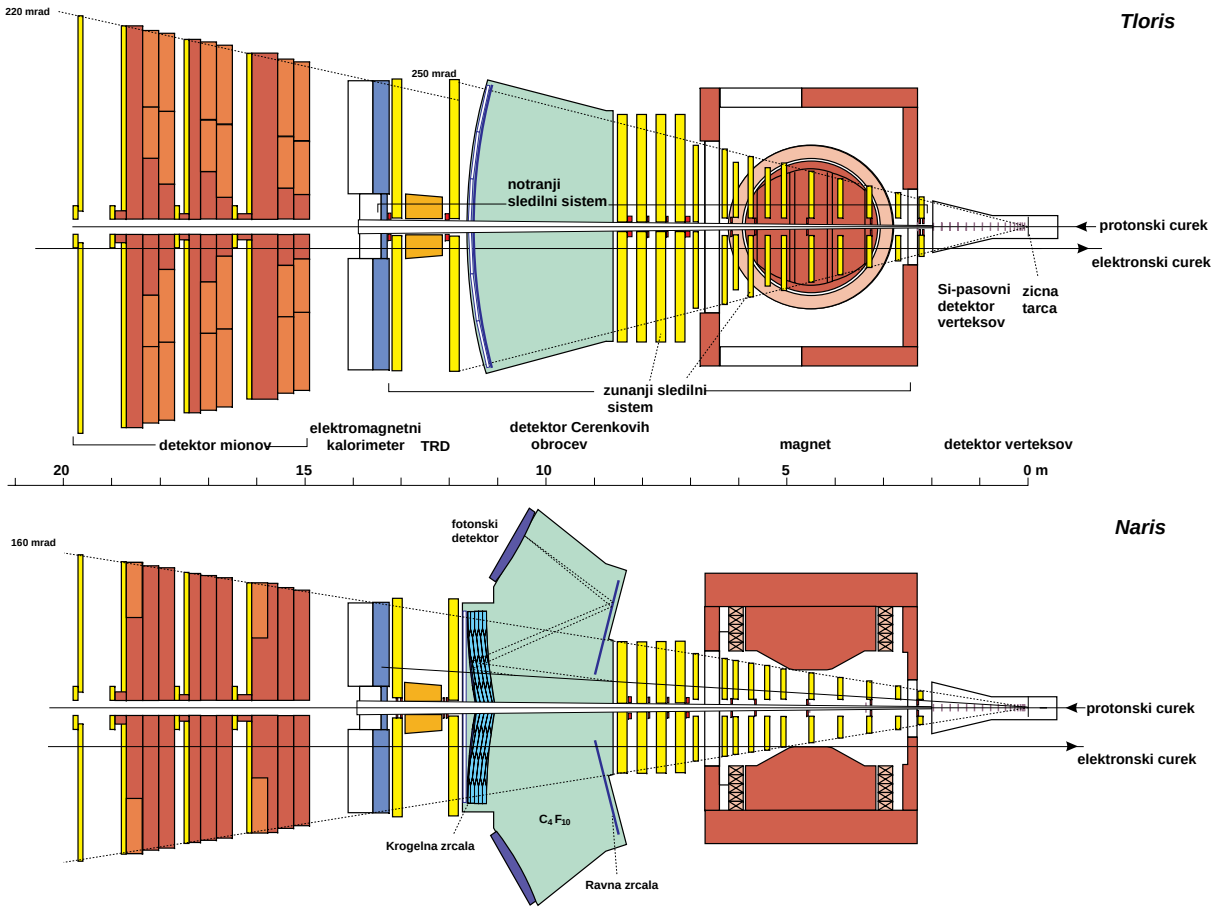

Slika II: Prikaz vodoravnega in navpičnega vzdolžnega prereza merilne naprave HERA-B.

umerjeni, skladno sestaviti. Merilno napravo HERA-B smo razdelli na več delov:

- detektor razpadnih točk, verteksov, s kratico VDS, ki se nahaja pred dipolnim magnetom,
- dipolni magnet, s katerim določimo gibalno količino delcem,
- glavni sledilni sistem, ki je sestavljen iz zunanjega (OTR) in notranjega (ITR) dela. Pri globalni umeritvi smo glavni sledilni sistem še dodatno razdelili na del, ki se nahaja pri pozitivnih vrednostih koordinate x, in na del, ki se nahaja pretežno na delu z negativnimi koordinatami x,
- elektromagnetni kalorimeter (ECAL) in
- detektor mionov (MUON).

Neposredna primerjava delov sledi Za globalno krajevno umeritev sem uporabil tri postopke, ki se med seboj dopolnjujejo. Pri prvih dveh postopkih sem primerjal odstopanja izmerjenih delov sledi med seboj. Pri prvem postopku sem to primerjavo naredil direktno, pri drugem pa sem

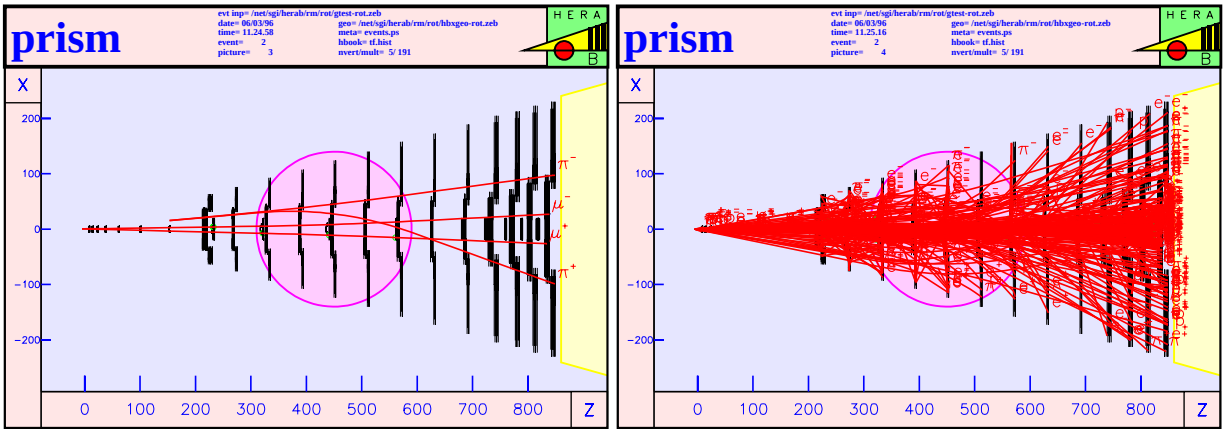

Slika III: V eksperimentu HERA-B bomo iskali dogodke, ki bodo v detektorju pustili značilne sledi. Žal pa je en tak dogodek skrit v množici nezanimivih dogodkov, ki prispevajo k velikemu ozadju meritve. Na sliki je simuliran dogodek brez ozadja (levo) in z ozadjem vrste reakcij, ki jih povzročijo sekundarni delci (desno).

sledi delcev propagiral skozi navpično usmerjeno magnetno polje z metodo Runge-Kutta. Izbral sem porazdelitve, ki sem jih prilagajal in določil premike posameznih delov merilne naprave.

Podatki, na podlagi katerih sem določil krajevno umeritev merilne naprave, so bili posneti z vključenim magnetnim poljem (v smeri ozi y), zato sem neposredno lahko primerjal dele sledi za magnetom s tistimi pred njim samo v določenih smereh. Poleg neposredne primerjave projekcij delov sledi na ravnino zy, ki jih linearno podaljšamo do iste vrednosti koordinate z (vzdolž smeri protonskega žarka), lahko tudi primerjamo koordinato z točke, v katerih se dva dela sledi sekata v ravnini zx. Ta točka je v prvem približku sredina magneta, bolj natančno pa:

$$z_0 = z_1 + \frac{z_2 - z_1}{2} \frac{2}{1 + \frac{\sqrt{1+t_{x_1}^2}}{\sqrt{1+t_{x_2}^2}}},$$

kjer sta s t_{x_1} in t_{x_2} označena smerna koeficienta delov sledi pred in za magnetom.

Runge-Kutta postopek Pri drugem postopku sem del sledi pred magnetom z metodo Runge-Kutta propagiral skozi magnetno polje na drugo stran, kjer sem njen položaj primerjal z delom iste sledi za magnetom. Iz razlike v smeri x sem potem izračunal popravek k gibalni količini, ki ob ponovni propagaciji skozi magnetno polje istega dela sledi pred magnetom bolje zadane točko v delu sledi za magnetom (slika IV). Z nekaj iteracijami sem prišel do željene natančnosti, potem pa sem lahko primerjal smerne koeficiente t_x delov obeh sledi za magnetom (dela sledi pred magnetom, propagiranim skozi magnetno polje in dela sledi za magnetom).

Uporaba razpadov Z do sedaj opisanima postopkoma ne moremo dobro določiti vse premike delov merilne naprave. Po opisanih postopkih je namreč merilna naprave še vedno lahko 'zlomljena' na sredini magnetnega polja, kar v prvem približku samo sistematsko spremeni velikost gibalnih količin, katerih prave vrednosti ne poznamo. Za dodatno določitev gibalne

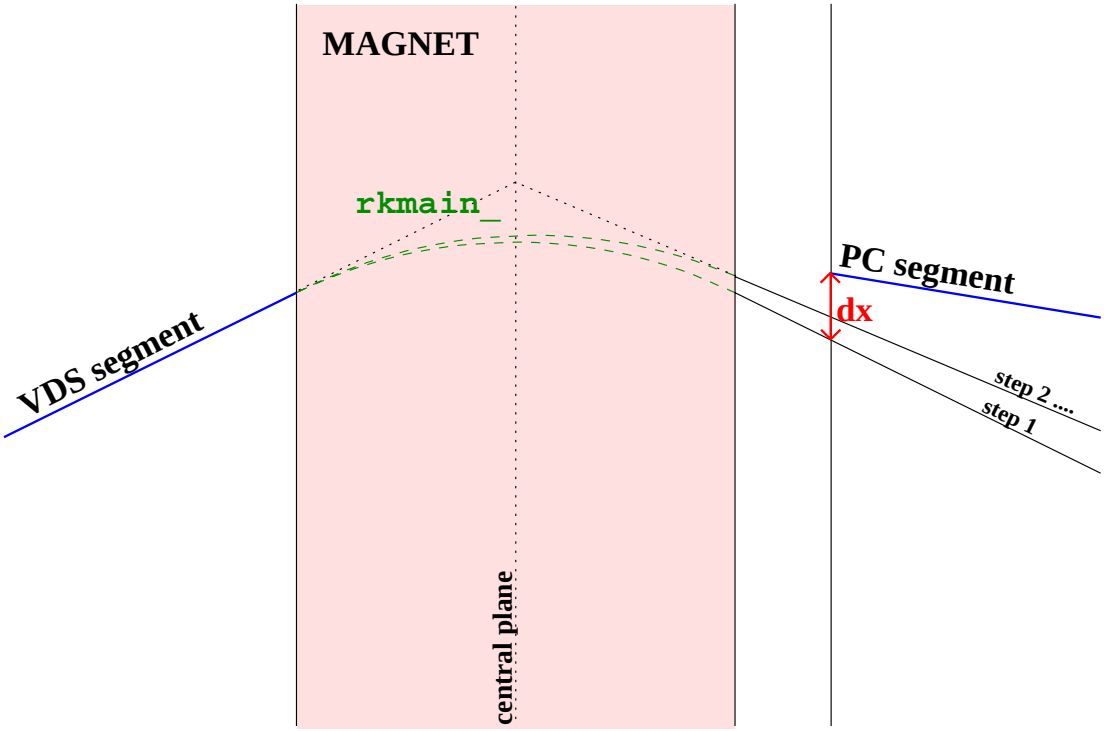

Slika IV: Del sledi pred magnetom je propagiran skozi magnetno polje z metodo Runge-Kutta. Pri tem zgrešimo del sledi za magnetom. V parih korakih dosežemo željeno natančnost s popravljanjem gibalne količine, ki jo uporabimo za Runge-Kutta propagacijo.

količine lahko uporabimo vzorec dvodelčnih razpadov, kjer vemo, da se morata gibalni količini sestaviti v maso razpadlega delca.

Analiza podatkov Metode so bile preizkušene na simuliranih podatkih, kjer sem ugotovil, da se premiki, izračunani po zgornjih treh postopkih, zelo dobro ujemajo s tistimi, ki sem jih predhodno namerno povzročil pri simulaciji dogodkov.

Postopke sem nato uporabil za krajevno umeritev podatkov, zajetih z magnetnim poljem. Primeri izboljšave so prikazani na slikah V in VI, kjer so prikazana odstopanja sledi pred magnetom od tistih za magnetom (os y) kot funkcija različnih količin (prikazano na oseh x). Ta odstopanja se v idealni simulaciji skladajo s konstanto $y = 0$. Očitno je, da so porazdelitve na sliki VI (po umeritvi) veliko bliže temu kot tiste na sliki V (pred umeritvijo).

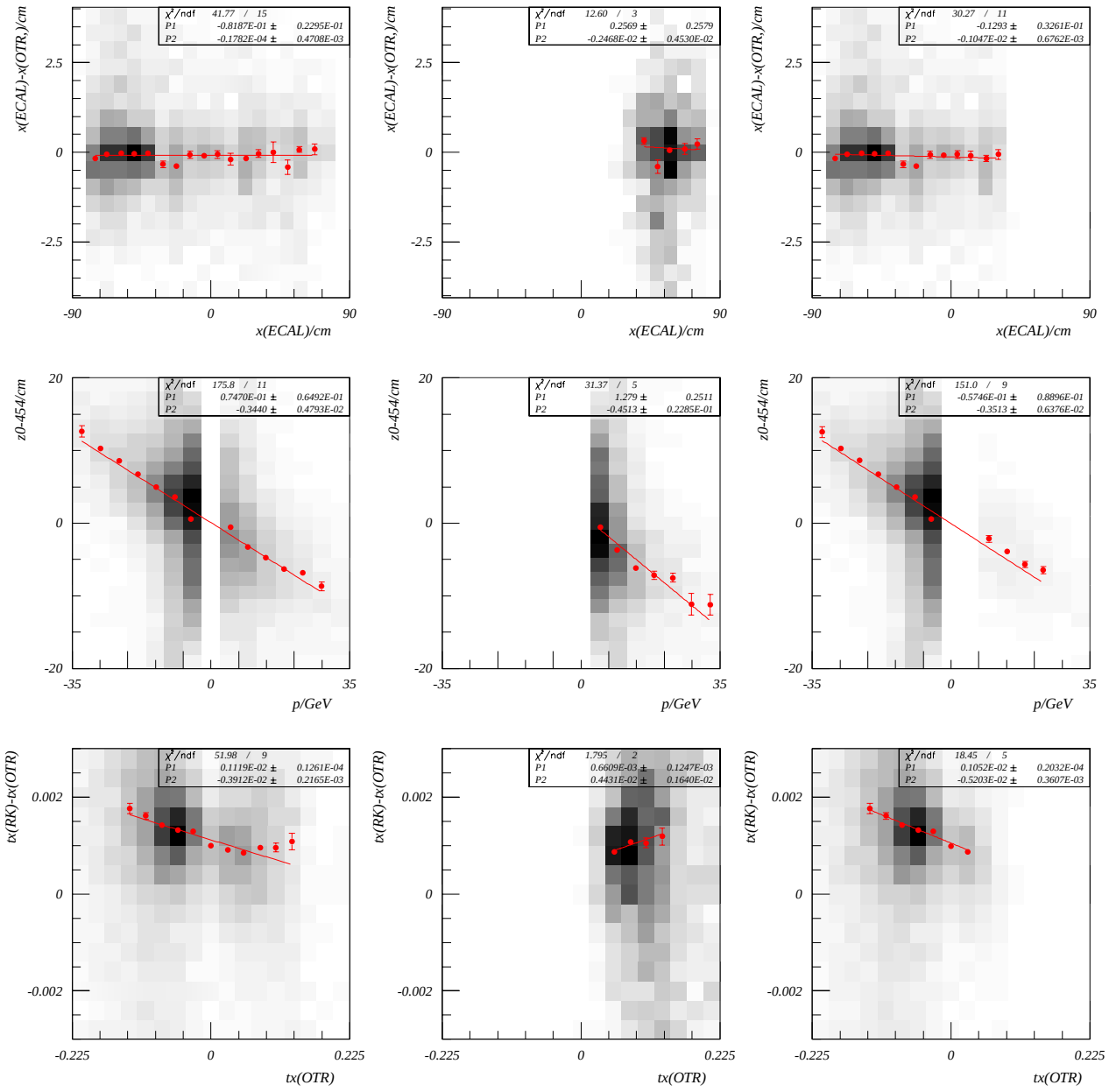

Slika V: Na slikah so prikazani trije primeri porazdelitev pred globalno krajevno umeritvijo. V drugem in tretjem stolpcu, je glavni sledilni sistem razdeljen na pozitivno in negativno polovico po smeri x.

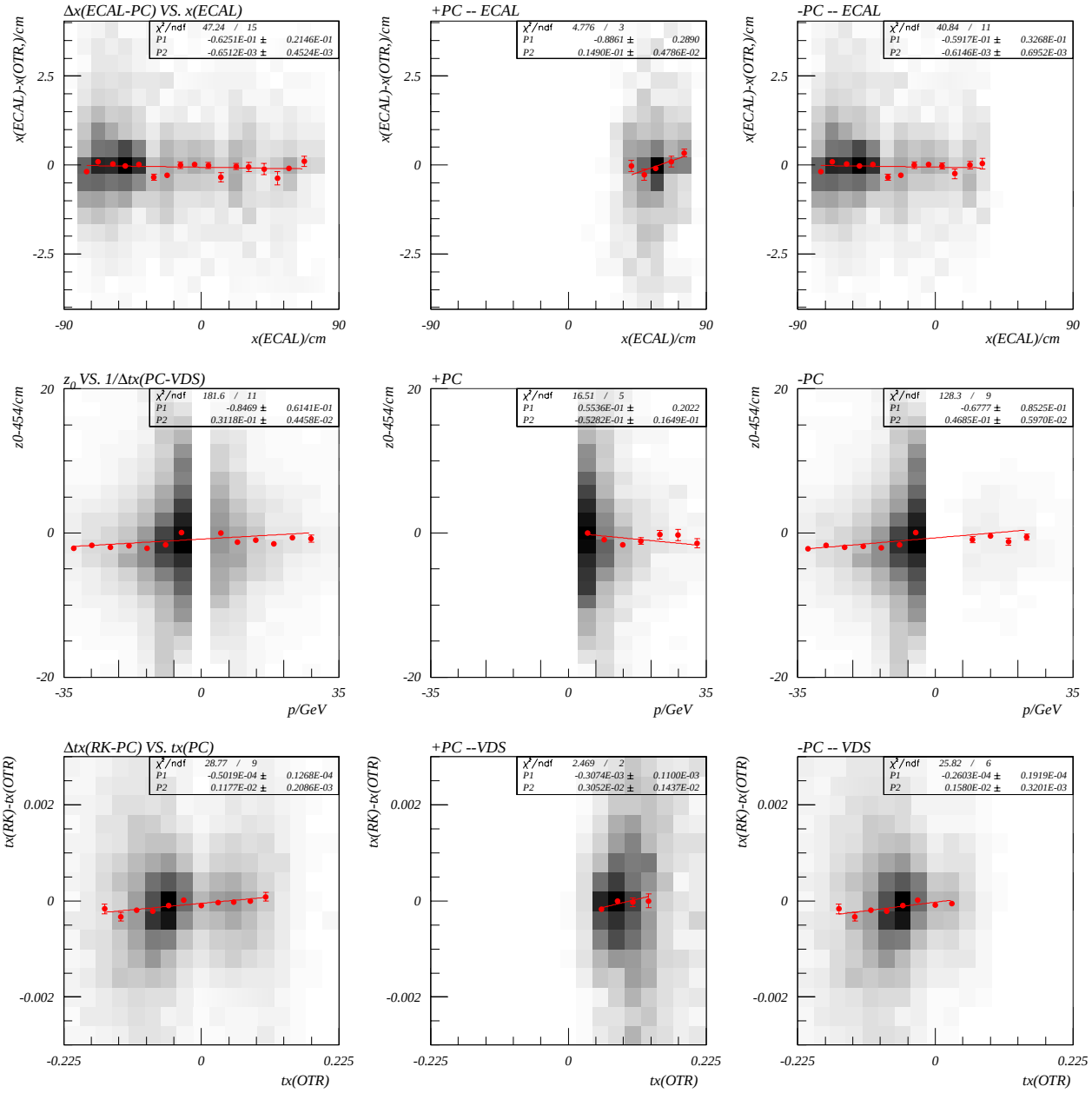

Slika VI: Na slikah so prikazani trije primeri porazdelitev po globalni krajevni umeritvi. Relativen popravek glede na porazdelitve na sliki V je očiten.

Tretji postopek za krajevno umeritev sem preizkusil na vzorcu razpadov $J/\Psi \to \mu\mu$. Na sliki VII, je prikazana izmerjena invariantna masa mionskega para pred umeritvijo in po njej.

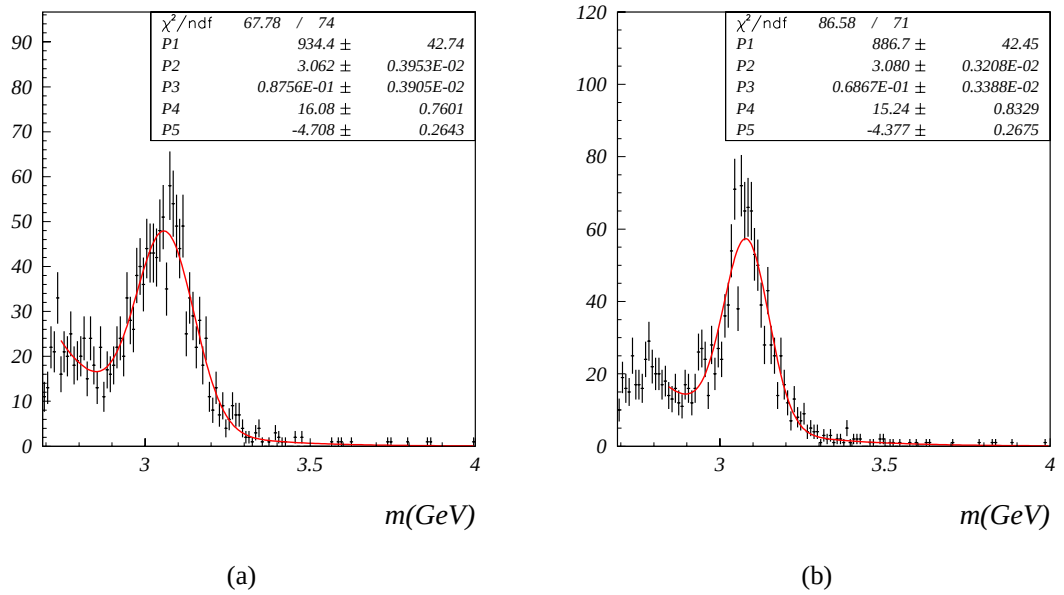

(a) (b)

Slika VII: Porazdelitev dogodkov po invariantni masi mionskega para. Vrh ustreza pravim razpadom mezonov J/Ψ: (a) ustreza podatkom pred postopkom globalne umeritve in (b) po njem. Širina vrha, t.j. ločljivost pri meritvi mase, se zelo izboljša ($\sigma = P3$).

Delovanje števca obročev Čerenkova

Da sem določil eno bistvenih lastnosti števca obročev Čerenkova, natančnost pri določitvi smeri fotonov, sem narisal histogram razlik med smerimi fotonov in delcev, ki fotone izsevajo. Na sliki VIII je prikazan primer take porazdelitve za mione, ki so nastali pri razpadu J/Ψ in imajo gibalno količino nad $40\ \mathrm{GeV}$.

Identifikacija delcev Pri rekonstrukciji dogodkov uporabljamo RICH za identifikacijo nabitih hadronov, predvsem za ločevanje kaonov in protonov od pionov. Za uspešno ločevanje je potrebno tudi dobro poznavanje smeri sledi delcev, ki sevajo fotone Čerenkova. Učinkovitost identifikacije sem ocenil na podlagi vzorcev razpadov, $\phi \to K^+K^-$, $\Lambda \to \pi p$ in $K^0_S \to \pi^+\pi^-$, ki so mi služili kot izvor kaonov, protonov in pionov. Na slikah IX in X so prikazane učinkovitosti za njihovo identifikacijo in verjetnosti za njihovo napačno identifikacijo. Slika IX je narejena pred globalno umeritvijo in umeritvijo števca Čerenkova, kjer so bili določeni premiki posameznih okledal optičnega sistema tega detektorja, slika X pa po opravljenih obeh umeritvah. Razlika je najbolj očitna v primeru učinkovitosti za identifikacijo kaonov.

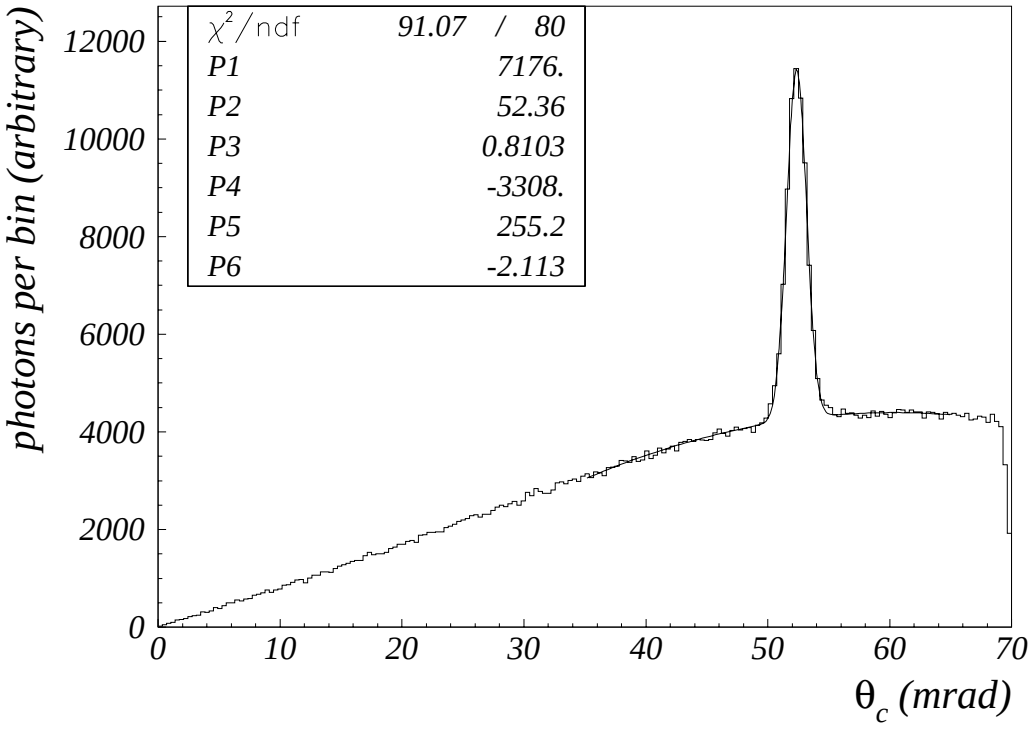

Slika VIII: Porazdelitev fotonov po kotu med njihovo smerjo in smerjo sledi delca. Vrh ustreza fotonom Čerenkova, ki pripadajo mionskim sledem iz razpada $J/\Psi \to \mu\mu$

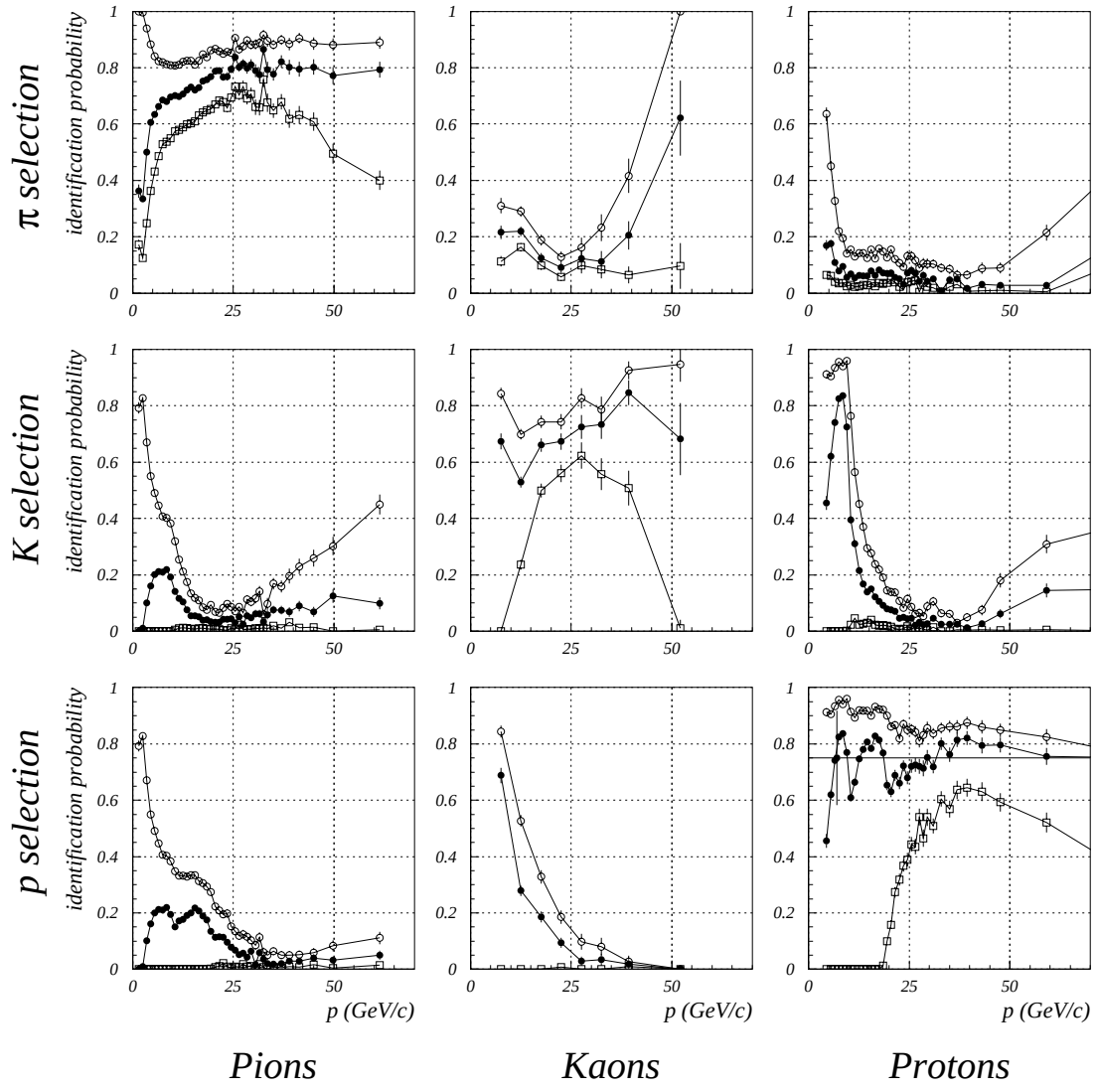

Slika IX: Diagrami prikazujejo stanje pred umeritvijo za tri standardne reze. Na diagonalnih diagramih je prikazana učinkovitost za identifikacijo π, K in p, izvendiagonalni diagrami pa kažejo verjetnost za napačno identifikacijo. Prazni kvadratki ustrezajo šibkim rezom, polni krogci srednje močnim in prazni krogci močnim identifikacijskim rezom.

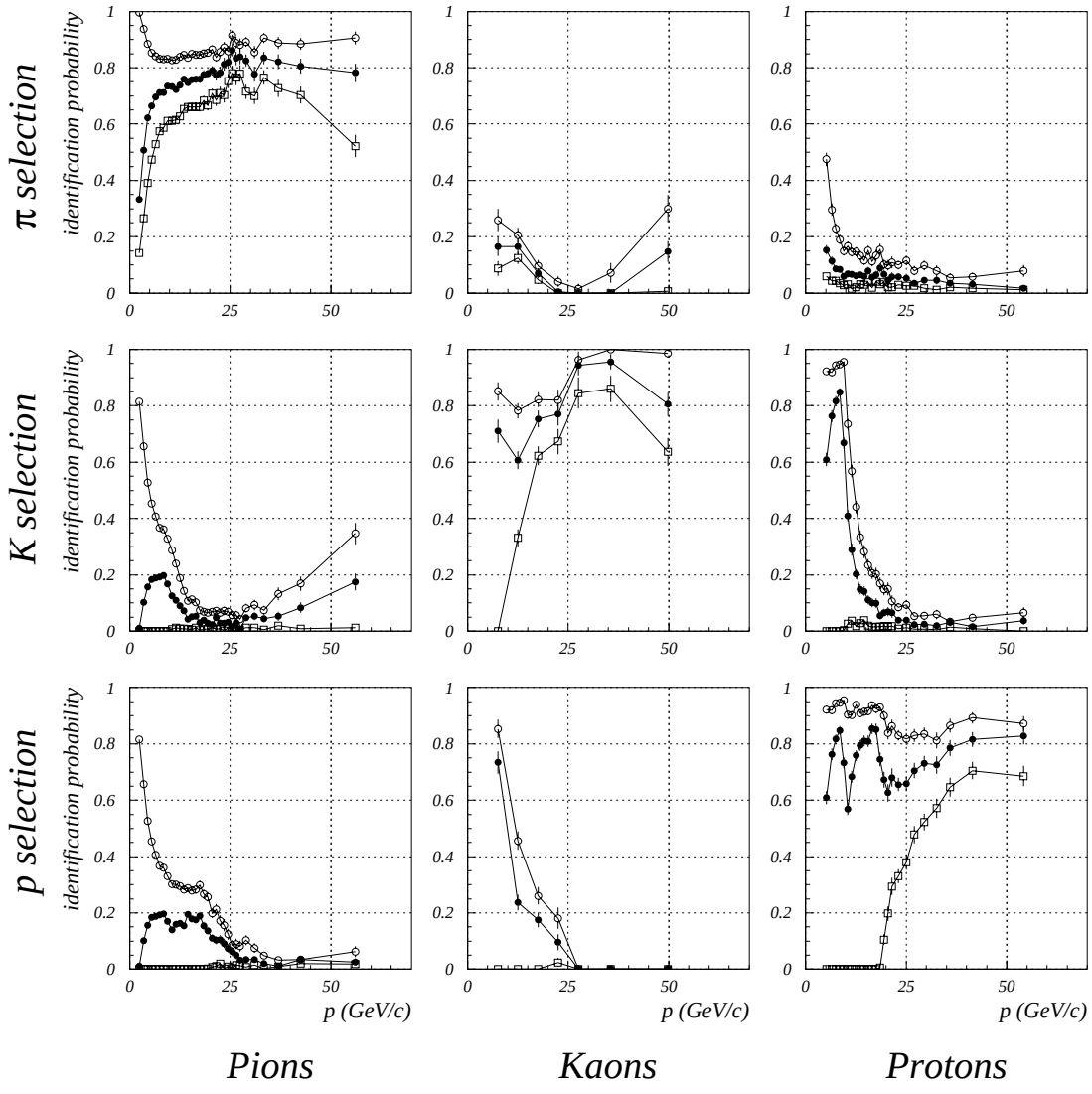

Slika X: Diagrami prikazujejo stanje po umeritvi. Na diagonalnih diagramih je prikazana učinkovitost za identifikacijo π, K in p, izvendiagonalni diagrami pa kažejo verjetnost za napačno identifikacijo.

Meritev preseka za nastanek mezonov D^0 in D^{*+}

Procesi, v katerih nastanejo težki kvarki, so pomemben test veljavnosti teorije perturbativne kvantne kromodinamike (pQCD). V tej teoriji so ti preseki izračunljivi, če je le masa kvarka dovolj velika in so prispevki z majhnim prenosom energije zanemarljivi. Računi potekajo v okviru izboljšanega partonskega modela, s predpostavko, da velja faktorizacijski izrek, ki pove, da lahko presek razdelimo na produkt partonskega preseka, ki se ga da izračunati, in partonskih oblikovnih faktorjev, ki pa jih lahko izmerijo v drugih procesih.

Teoretična ocena preseka za tvorbo kvarka t, se dobro prilega izmerjeni vrednosti. Večje razlike obstajajo med teoretično napovedjo in meritvijo za tvorbo kvarka b in kvarka c, kjer pridejo bolj do izraza prispevki z majhnim prenosom energije. Parameter Λ_{QCD}, ki ga dobimo zaradi renormalizacije v kvantni kromodinamiki, ni natančno določen, vpliva pa bistveno na končno vrednost izračunanega preseka.

Oblikovne faktorje kvarkov faktorizirajo na teoretično izračunljive kratkosežne in dalekosežne prispevke, ki jih je potrebno izmeriti. Tudi v tem procesu dobimo dodaten parameter, ki je slabo določen. V primeru, ko je masa kvarka zelo velika ($m_Q \to \infty$), je napaka na oblikovnem faktorju zanemarljiva. Masa kvarka c je daleč od te limite, zato so pri teoretski napovedi preseka za tvorbo kvarka c napake relativno velike, napoved pa je zelo odvisna od izbire parametrov, kot so Λ_{QCD}, faktorizacijska skala in masa golega kvarka. Meritev preseka za nastanek kvarkov c lahko pomembno prispeva k določitvi pravega teoretskega modela in njegovih parametrov.

Teoretske napovedi za tvorbo težkih kvarkov so na primer zbrane v [36] in so prikazane skupaj z obstoječimi meritvami in tudi našim rezultatom na sliki XV, na koncu povzetka.

Merilna naprava HERA-B izkorišča trke hitrih protonov z jedri v mirujočih tarčah, ki so narejene iz različnih snovi z različnimi atomskimi števili A. Presek za posamezno reakcijo (σ) narašča z številom nukleonov v jedru. Ponavadi to odvisnost opišemo z naslednjo zvezo:

$$\sigma = \sigma_0 A^\alpha, \tag{I}$$

kjer je α parameter, ki je odvisen od vrste reakcije, σ_0 pa je presek za posamezen nukleon. Parameter α je bil določen za nastanek neelastičnih reakcij z jedri, $\alpha_{inel} = 0.7111 \pm 0.0011$, kar je le malo večja kot bi bil, če bi bil presek za reakcijo določen kar z geometriskim presekom jedra ($\alpha = 2/3$).

Parameter α je bil izmerjen tudi za procese za tvorbo mezonov D^0, vendar pri nekoliko nižji energiji vpadnih protonov, kot so energije pri eksperimentu HERA-B. Njegovo izmerjeno vrednost, $\alpha_{D^0,\bar{D}^0} = 1.02 \pm 0.03_{stat} \pm 0.02_{syst}$, sem upošteval pri meritvi preseka, ocenil pa sem tudi vrednost tega parametra, ki se najbolj sklada z našimi meritvami preseka za tvorbo D^0 mezonov na dveh tarčah iz različnih snovi, ogljika in volframa.

Presek za določeno reakcijo izmerimo tako, da preštejemo število teh reakcij, ki so potekle (N), in to število delimo z luminoznostjo $\mathcal{L}$:

$$\sigma = \frac{N}{\mathcal{L}}. \tag{II}$$

Luminoznost določimo s štetjem referenčnih reakcij, za katere poznamo presek. Pri meritvi, ki jo bom opisal, sem za določitev luminoznosti uporabil število neelastičnih reakcij in dobro

znani presek za njihovo tvorbo. Določil sem presek za tvorbo mezonov D^0 in mezonov D^{*+}. Pri meritvi preseka ze nastanek mezonov D^0 sem se omejil le na štetje dela nastalih mezonov, ki so razpadli v nabita pion π in kaon K. Ta delež označimo z $B(D^0 \rightarrow K\,\pi)$ in ima vrednost $(3.80 \pm 0.09)\%$ [32]. V primeru mezonov D^{*+} pa sem se omejil na razpade $D^{*+} \rightarrow D^0\pi^+ \rightarrow K^-\pi^+\pi^+$, katerih relativni delež je $(2.57 \pm 0.09)\%$ [32]. Lahko sem izmeril le majhen del omenjenih razpadov, ker merilna naprava ne pokriva celotnega prostora, kamor nastali delci letijo, in ker vseh posnetih razpadov tega tipa ne moremo zaznati pri analizi podatkov. To nepopolnost meritve opišemo z izkoristkom ϵ. Tako se presek za tvorbo mezonov D^0 zapiše:

$$\sigma_{0,P}(D^0) = \frac{N_{detected}(D^0 \rightarrow K\,\pi)\;\sigma_{inel,0}\;A^{\alpha_{inel}-\alpha_{D^0}}}{B(D^0 \rightarrow K\,\pi)\;N_{inel}\;\epsilon}.$$

Potenca $\alpha_{inel} - \alpha_{D^0}$ opiše razliko med vplivom jedrskih prispevkov pri tvorbi mezonov D^0 in pri neelastičnih reakcijah. Podobno bi zapisali tudi presek za nastanek mezonov D^{*+}.

Vrednosti izmerjenega preseka za tvorbo neelastičnih reakcij med protoni z energijo $920\ \mathrm{GeV}$ in jedri je zbran v naslednji tabeli:

snov	$\sigma_{inel}(mb)$
C	255.1 ± 2.4
W	1775 ± 19
na nukleon	43.55 ± 0.40

Veliko delcev, ki nastanejo v razpadih D^0 in D^{*+} mezonov, uide v prostor, ki ga merilna naprava ne pokriva ali pa ne pusti dovolj signala v delu merilne naprave, ki jo prečka. Veliko pa je kombinacij naključnih delcev, ki niso nastali v omenjenih reakcijah, njihova invariantna masa pa ima vrednost blizu pravi masi mezona D^0 ali D^{*+}. Takim naključnim kombinacijam pravimo kombinatorno ozadje, ki sem ga poskušal zmanjšati z rezi na raznih količinah, ki so relativno oplemenitili moj vzorec rekonstruiranih dogodkov. Skupni izkoristek teh prispevkov sem ocenil na simuliranih dogodkih, 0.00714 ± 0.00032 za razpade $D^0 \rightarrow K\pi$, in 0.00289 ± 0.00034 za razpade $D^{*+} \rightarrow K^-\pi^+\pi^+$.

Pri svoji analizi sem upošteval 16.4 miljona dogodkov z neelastičnimi reakcijami, 11.4 posnetih z ogljikovo tarčo in 5.0 miljona, ki so bili posneti s tarčo iz volframa. V teh dogodkih sem uspel rekonstruirati razpade nevtralnih mezonov D^0, ki so prikazani na slikah XI in XII. Vrednosti izmerjenega preseka za njihovo tvorbo so povzete v naslednji tabeli:

A	$\sigma_{0,P}(D^0)/(\mu\mathrm{b/nukleon})$
12.0	136 ± 56
184	157 ± 60
povprečje	$\mathbf{147 \pm 41}$

Za določitev preseka za tvorbo parov kvarkov, kvarka c in njegovega antikvarka $\bar{c}$, moramo določiti še povprečno število mezonov D^0, ki nastane iz para kvarkov $c\bar{c}$. Za vrednost tega parametra sem uporabil vrednost, ki sledi iz hadronizacijskega modela, ki je uporabljen pri simulaciji dogodkov. V povprečju nastane 1.19 mezona D^0 pri razpadu enega para kvarkov $c\bar{c}$. Iz vrednosti izmerjenega preseka za nastanek mezonov D^0, dobim $\sigma_{0,P}(c\bar{c}) = (124 \pm$

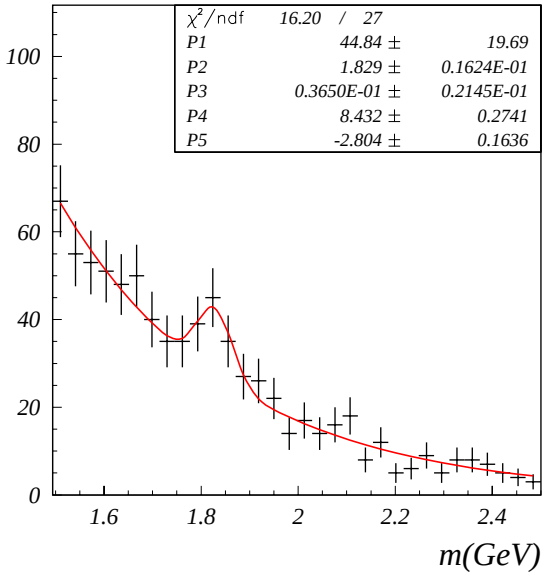

Slika XI: Rekonstruirani razpadi $D^0 \to K\pi$ iz vzorca 16.4 miljona neelastičnih reakcij.

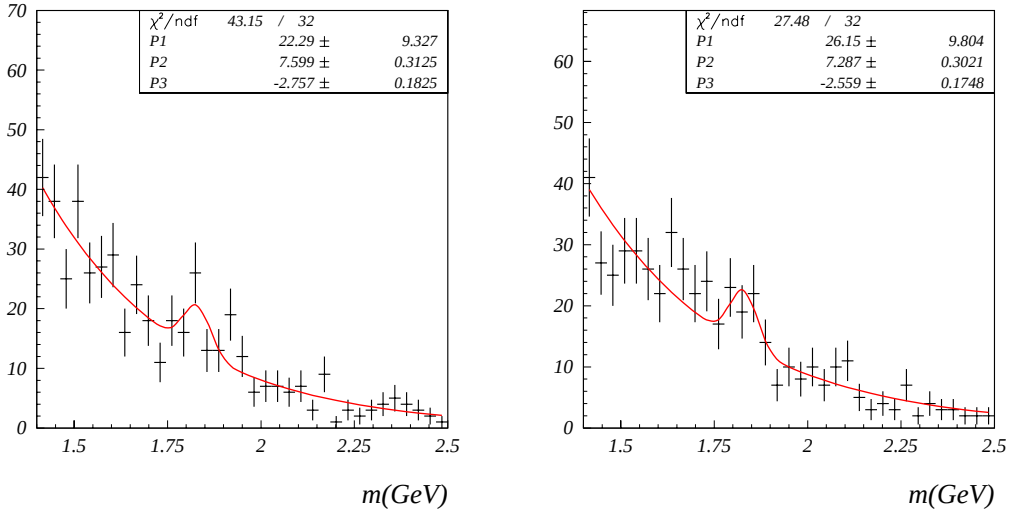

(a) (b)

Slika XII: Rekonstruirani razpadi $D^0 \to K\pi$ na (a) žici iz ogljika in (b) na žici iz wolframa.

34) $\frac{\mu\mathrm{b}}{\mathrm{nukleon}}$. Vrednost je narisana na sliki XV skupaj z nekaterimi drugimi meritvami in teoretskimi napovedmi.

Mezoni D^{*+} razpadejo najprej na mezona D^0 in π, ki imata skupaj skoraj tolikšno mirovno maso kot mezon D^{*+}. Ker ima D^{*+} veliko gibalno količino (tipični Lorentzov faktor je 15),

letita D^0 in π skoraj v isto smer. Rekonstruiral sem samo primere, ko je D^0 razpadel v K in π. Izkaže se da je pametno namesto invariantne mase D^{*+} sestaviti drugo količino, $q = m(K\pi\pi) - m(K\pi) - m(\pi)$, ker je mnogo bolje določena, ker odštevamo dve količini z zelo koreliranimi napakami. Na slikah XIII in XIV so prikazani razpadi mezonov D^{*+}, na podlagi katerih sem določil presek za tvorbo mezonov D^{*+}, $\sigma_{0,P}(D^*) = (158 \pm 63)\ \frac{\mu\mathrm{b}}{\mathrm{nukleon}}$.

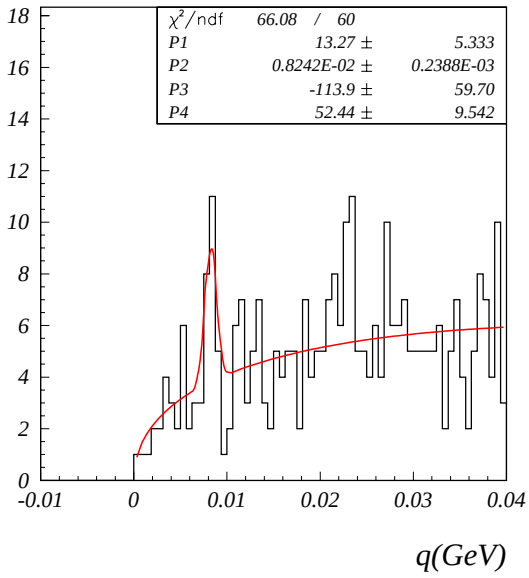

Slika XIII: Rekonstruirani razpadi $D^* \to D^0\pi \to K\pi\pi$.

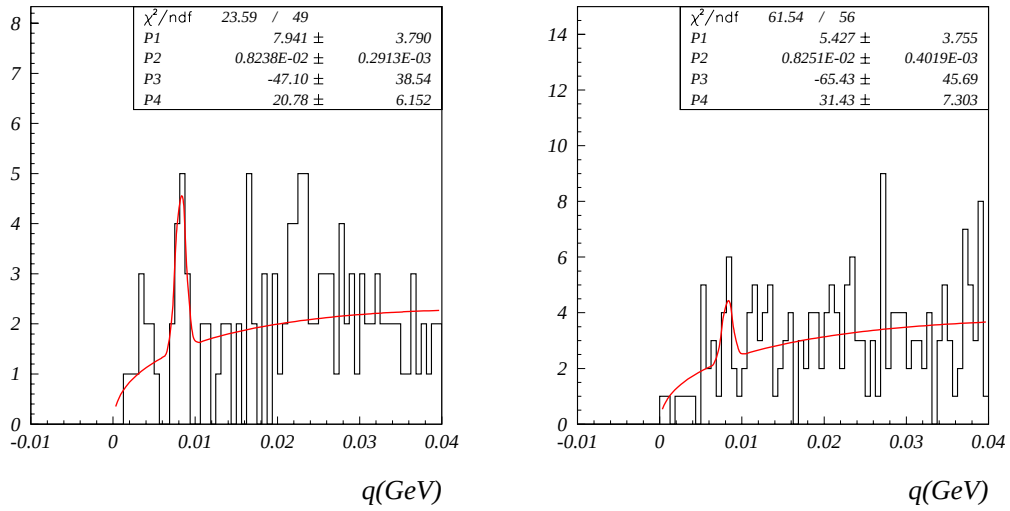

(a) (b)

Slika XIV: Rekonstruirani razpadi $D^* \to D^0\pi \to K\pi\pi$ na ogljikovi (a) in volframovi (b) tarči.

Zaključek

V disertaciji sem opisal tri bistvene dele raziskav, ki sem jih opravil v okviru svojega doktorskega dela, krajevno umeritev celotne merilne naprave HERA-B, umeritev števca obročev Čerenkova, ter na koncu meritev preseka za tvorbo mezonov D^0 in D^{*+}.

Opisal sem tri različne postopke za krajevno umeritvev celotne merilne naprave ob vključenem magnetnem polju, ki se med sabo dopolnjujejo. Rezultati na zajetih podatkih kažejo občutno izboljšanje po opravljeni umeritvi, kar je razvidno iz porazdelitev odstopanj sledi delcev in iz izmerjenih razpadov delcev, kot na primer iz razpada $J/\Psi \rightarrow \mu\mu$. V letu 2002 so bili zajeti tudi podatki, ko je bilo magnetno polje izkljopljeno. V tem primeru se postopek krajevne umeritve zelo poenostavi. Opisani postopki so še vedno zelo uporabni za krajevno umeritev merilne naprave v dolgih obdobjih med dvema vzorcema podatkov, posnetima brez magnetnega polja.

Delovanje detektorja obročev Čerenkova (RICH) sem določil na vzorcu razpadov, $\phi \rightarrow K^+K^-$, $\Lambda \rightarrow \pi p$ in $K^0_S \rightarrow \pi^+\pi^-$, kjer sem identiteto razpadlih delcev poznal. Za dobro ločevanje z RICH med njimi je potrebno dobro poznati smeri delcev. Pokazal sem, da se delovanje RICH izboljša z izbolšano krajevno umeritvijo merilne naprave.

Na koncu sem opisal meritev za nastanek mezonov D^0 in D^{*+}, na dveh različnih tarčah narejenih iz ogljika in volframa. Izmerjena vrednost preseka je za mezone D^0, $\sigma_{0,P}(D^0) = (147 \pm 41^{+25}_{-28})\mu\mathrm{b/nukleon}$. Iz te vrednosti sem izračunal presek za nastanek parov kvarkov $c\bar{c}$, $\sigma_{0,P}(c\bar{c}) = (124 \pm 34^{+21}_{-24})\ \mu\mathrm{b/nukleon}$, ki se ujema z ostalimi meritvami pri nižjih energijah, in ki leži na zgornjem področju teoretskih napovedi. Določil sem tudi parameter α, ki opiše jedrske prispevke pri tvorbi D^0 mezonov, $\alpha_{D^0} = 1.07 \pm 0.2$. Vrednost izmerjenega preseka za tvorbo mezonov D^{*+} je, $\sigma_{0,P}(D^*) = (158 \pm 63^{+25}_{-32})\ \mu\mathrm{b/nucleon}$.

Pri poskusu HERA-B načrtujejo zajeti še veliko večji vzorec podatkov, kot je bil na voljo pri opisani meritvi. Z večjim številom zapisanih dogodkov bodo napake na omenjenih meritvah presekov dovolj zmanjšale, da bo možno razlikovati med različnimi teoretskimi napovedimi.

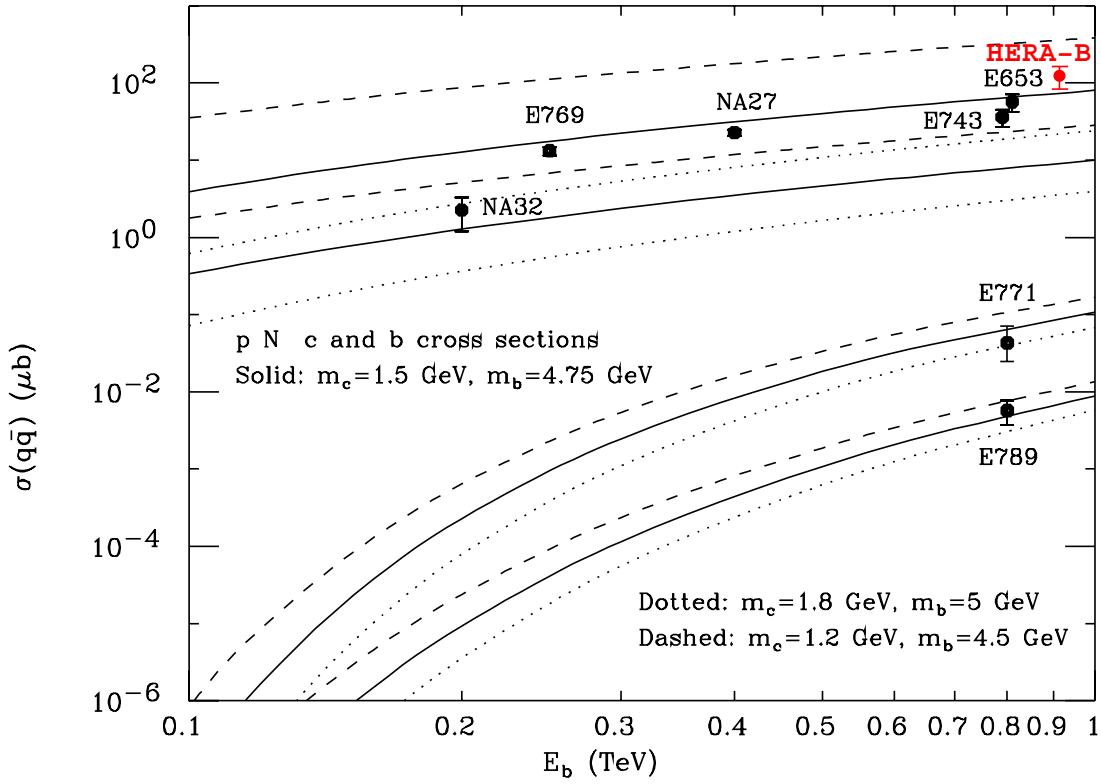

Slika XV: Naša meritev preseka za tvorbo kvarkov c. Zgornji set krivulj ustreza teoretskim napovedim za presek za nastanek kvarkov c, spodnji pa za kvarke b. Posamezne krivulje prikazujejo razpon teoretskih napovedi pri dani izbiri mase golega kvarka. Naša meritev je v zgornjem delu razpona teoretskih napovedi in se v okviru napak ujema z meritvami pri nekoliko nižjih energijah.

References

[1] T. Lohse et al., An Experiment to Study CP Violation in the B System Using an Internal Target at the HERA Proton Ring. Proposal, DESY-PRC 94-02 (1994)

[2] T. Lohse et al., An Experiment to Study CP Violation in the B System Using an Internal Target at the HERA Proton Ring. Design Report, DESY-PRC 95/01 (1995)

[3] I.Bigi, A.I.Sanda, CP violation in heavy flavor decays, Predictions and search strategies. Nucl. Phys., B (55 p), 1986

[4] The HERA-B collaboration, HERA-B Physics in 2001/2002.
DESY internal note, December 2000

[5] HERA-B Collaboration, Measurement of the $b\bar{b}$ Production Cross Section in 920 GeV Fixed-Target Proton-Nucleus Collisions.
DESY-02-076, May 2002., Submitted to Eur.J.Phys.C, hep-ex/0205106

[6] K. Ehret, Performance of the HERA B target and interference with HERA operation.
Near Beam Symposium Proceedings, FNAL Sept. 1997

[7] The HERA-B collaboration, HERA-B Report on status and prospects.
DESY-PRC 00-04, October 2000

[8] K. T. Knöpfle, Nucl. Instr. and Methods A368 (1995) 192.

[9] F. Sauli et al., IEEE Trans. Nucl. Sci. 44, 646, (1997)

[10] R. Pestotnik, Diploma Thesis, Univerza v Ljubljani, Fakulteta za matematiko in fiziko, Ljubljana (1996).

[11] D. Dujmić, K. Reeves, HERA-B RICH Note 97-182, Hamburg (1997).

[12] A. Gorisek, P. Križan, S. Korpar and M. Starič, Nucl. Instrum. Meth. A 433, 408 (1999).

[13] D. Dujmić: Ph. D. Thesis, Open Charm Production at HERA-B.
The University of Texas at Austin, December 2001

[14] Hamamatsu Data Sheets for R5900-M16 and R5900-M4 Photomultipliers

[15] P. Križan, S. Korpar, R. Pestotnik, M. Starič, A. Stanovnik, E. Michel, C. Oehser, W. Schmidt-Parzefall, A. Schwarz, T. Hamacher, D. Broemmelsiek, J. Pyrlik, Nucl. Instr. and Meth. in Phys. Res. A394 (1997) 27-34.

[16] S. Korpar et al., Nucl. Instr. and Meth. in Phys. Res. A478 (2002) 391-394; P. Križan, ICFA Instrum. Bull. 19 (1999) 3.

[17] S. Korpar et al., Nucl. Instr. and Meth. A 442 (2000) 316.

[18] M. Villa, ECAL Analysis Status update. HERA-B Note 99-1381999

[19] M. Dam et al., HERA-B Data Acquisition System, submitted to Elsevier Science, October 2002.

[20] J. Ivarsson, P. Kreuzer, T. Lohse, PYTHIA and FRITIOF: Event Generators for HERA-B. HERA-B Note 99-067

[21] T. Sjöstrand, Computer Physics Comm. 82 (1994) 74, hep-ph/9508391

[22] H. Pi, Computer Physics Comm. 71 (1992) 173.

[23] S. Nowak, HBGEAN

[24] Application software group, GEANT - Detector Description and Simulation Tool. CERN Program Library Long Writeup W5013, 1993

[25] A. Gorišek, S. Korpar, Status Report of Global Alignment of HERA-B. HERA-B Note 02-032

[26] A. Gorišek, S. Korpar, HERA-B Note 01-081

[27] O. Igorkina, http://www-hera-b.desy.de/subgroup/software/arte/MARPLE/index.html

[28] S. Kupper, A. Gorišek, Gobal alignment - MC with Magnet off. HERA-B Meeting 27. 02. 2002, Oral presentation

[29] P. Baillon, Nucl. Instr. and Meth. A 238 (1985) 341.

[30] M. Starič, P. Križan, Nucl. Instr. and Meth. in Phys. Res. A433 (1999) 279.

[31] R. Pestotnik, Ph.D. Thesis, University of Ljubljana (2001)

[32] K. Hagiwara et al. (Particle Data Group), Phys. Rev. D 66, 010001 (2002) (URL: http://pdg.lbl.gov)

[33] J. Carvalho et al., HERA-B Collaboration: Luminosity measurement in HERA-B. Preprint submitted to Elsevier Science, November 2002

[34] M. J. Leitch et al., Phys. Rev. Lett. 72, 16 (1994), 2542

[35] M. Bruinsma, Ph.D. Thesis, Utrecht, May 2002

[36] S. Frixione et al., hep-ph/9702287

[37] P. Nason, Heavy Flavour Production, Heavy Flavours 8, 1999

[38] R. Bonciani et al., hep-ph/9801375

[39] P. Conde Muiño, Ph.D. Thesis (in preparation), Hamburg 2002

[40] M. Staric, private communication.

[41] D. Emeliyanov et al., Grover, internal note.

[42] D. W. Townsend, M. Defrise, Image reconstruction methods in positron tomography. CERN 93-02 (1993) 34.

Izjavljam, da je disertacija rezultat samostojnega raziskovalnega dela.

Ljubljana, december 2002 Andrej Gorišek, univ. dipl. fiz.